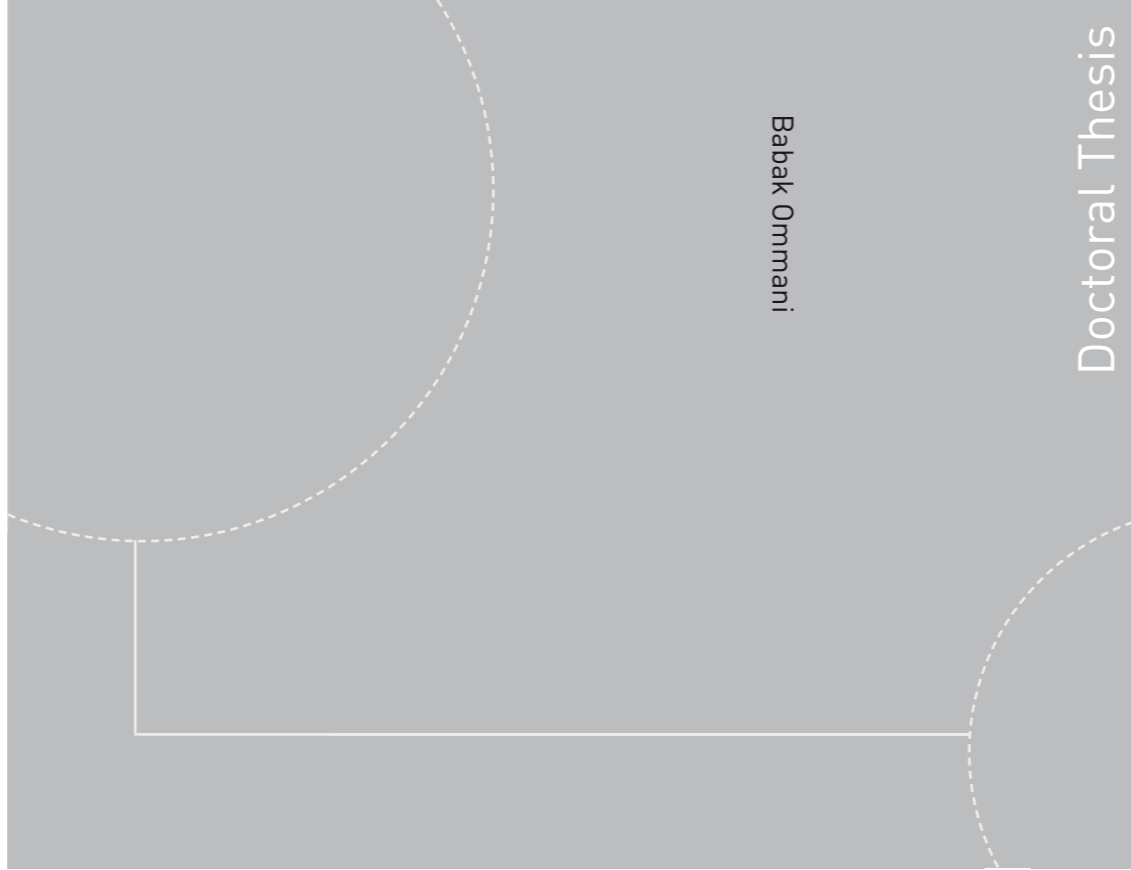


ISBN 978-82-471-4417-6 (printed version)
ISBN 978-82-471-4418-3 (electronic version)
ISSN 1503-8181



Doctoral theses at NTNU, 2013:155

Babak Ommani

Potential-Flow Predictions of a Semi-Displacement Vessel Including Applications to Calm-Water Broaching

Babak Ommani

Potential-Flow Predictions of a Semi-Displacement Vessel Including Applications to Calm-Water Broaching

Thesis for the degree of philosophiae doctor

Trondheim, May 2013

Norwegian University of Science and Technology
Faculty of Engineering Science and Technology
Department of Marine Technology



NTNU – Trondheim
Norwegian University of
Science and Technology

NTNU

Norwegian University of Science and Technology

Thesis for the degree of philosophiae doctor

Faculty of Engineering Science and Technology
Department of Marine Technology

© Babak Ommani

ISBN 978-82-471-4417-6 (printed version)

ISBN 978-82-471-4418-3 (electronic version)

ISSN 1503-8181

Doctoral Theses at NTNU, 2013:155



Printed by Skipnes Kommunikasjon as

*to my wife Neda
to my mother Roya
to my grandmother Maryam*

Abstract

As a marine vehicle's operational speed increases, hydrodynamic pressure plays an increasingly significant role in carrying the vessel's weight. The shift of importance from hydrostatic to hydrodynamic pressure may cause a vessel, which is stable at rest or low speeds, to become dynamically unstable at high speeds. The nature of the dynamic instability depends mainly on the vessel's type and speed. Among high speed vessels, semi-displacement mono-hulls are particularly susceptible to a non-oscillatory dynamic instability in sway, roll and yaw known as *calm water broaching*. This type of dynamic instability is the main reason why semi-displacement mono-hulls must not operate at Froude numbers higher than 1.2 (Lavis, 1980). The application of linear theory in predicting this type of instability motivated the present study.

A linear dynamic model of the vessel, including its hydrodynamic coefficients, is needed for the dynamic stability analysis. Prediction of these coefficients is a challenging problem, requiring the solution of the flow around an advancing, oscillating vessel. A three-dimensional boundary element solver was constructed for this purpose. The free-surface and body boundary conditions were linearized using Neumann-Kelvin linearization. Since the focus here is on high speed vessels, this type of linearization is chosen instead of the double-body linearization. Boundary surfaces were discretized using numerical grid generation methods. Elements ranging from constant to cubic were used to represent the surfaces. Rankine sources and dipoles were distributed on the boundaries. The solver was programmed in a way to allow for the implementation of different boundary integral formulations using elements with different distribution orders in a convenient and compact form.

The derivatives of the velocity potential on the body surface were calculated using shape functions. On the free surface, the direction of differentiation is known to be important, especially in the flow around high-speed vessels. Therefore, derivatives on the free surface were calculated using upstream finite difference operators to satisfy the radiation condition and avoid numerical instabilities. Semi-discrete Fourier analysis was used to investigate numerical dispersion and damping of a wave traveling on a discrete free surface with and without current. Different singularity distribution and differentiation methods were considered. Based on these studies, a set of practical guidelines were established to choose suitable differentiation methods and an appropriate number of elements for each problem, and assess the numerical accuracy of the results. Damping zones were introduced around the free surface boundaries in order to absorb the waves and ensure that the radiation

condition was satisfied in the time-domain analysis.

Three types of flow separation were accounted for indirectly in the present potential-flow solution: trailing edge flow separation by a vortex sheet method, transom stern flow separation by a hollow body model, and cross flow separation by a 2D+t drag model. A series of problems for non-separated potential flows with and without forward speed were solved both in the time-domain and steady-state. The results were validated against experimental and analytical data.

The flow around an advancing, surface-piercing flat plate with steady drift was investigated using steady-state and time-domain solvers as an example of the tail-separated flows. A 2D+t cross-flow drag model was adopted in order to consider the cross-flow separation effects, which turned out to be important. Then, the problem was extended by adding oscillatory motions to the surface-piercing plate. The hydrodynamic coefficients in sway, roll and yaw were calculated for a series of Froude numbers and oscillation frequencies. The results were validated against existing experimental and numerical data.

Next, the flow around monohull semi-displacement vessels was studied using linear theory. The dry transom stern effects were captured by introducing a hollow body model. The results were validated against experimental and numerical data in terms of free-surface elevation and steady vertical forces. The hollow body model was extended to solve the flow around an advancing semi-displacement vessel with constant drift angle. A simplified 2D+t cross-flow drag model explained the differences between numerical and experimental data. The hydrodynamic coefficients in heave were calculated using the extended hollow body model. This method captured the anticipated sharp drop in the values of added mass and damping close to the transom stern.

Finally, dynamic stability in sway-yaw and sway-roll-yaw was investigated using linear stability analysis. A semi-displacement vessel with documented instability issues was chosen for validation. The hydrodynamic properties of the vessel were simplified to those of a flat plate. A sensitivity study was carried out to assess the importance of different parameters in the vessel's dynamic stability. This simplified analysis predicted the presence of an instability around the reported unstable Froude number. The nature of the instability was, however, different than what has been reported in the literature. Further investigations are needed on this subject.

Acknowledgment

First and foremost, I would like to thank my supervisor, Prof. Odd M. Faltinsen. He, with his deep understanding of hydrodynamics, and his kind and patient personality, helped me a lot during this study. I learned from him, what does it mean to be a good researcher, and a good teacher. His contributions to this work are highly appreciated.

This study was financially supported by Norwegian Research Council, through Centre for Ships and Ocean Structures (CeSOS) at Norwegian University of Science and Technology (NTNU). I am thankful for their support. The coordinator, Prof. Torgeir Moan, and the executive staff of CeSOS are also thanked.

I would like to thank Dr. Yanlin Shao for all the detailed and long discussions we had on boundary element method. Dr. Claudio Lugni from INSEAN helped me by providing very valuable, and interesting, experimental data. His contributions to this work are highly appreciated. I am thankful to Prof. Masashi Kashiwagi from Osaka University, for providing me with his PhD dissertation and explaining it to me. The honorable members of my PhD-committee, Prof. Rene H.M. Huijsmans and Dr. Arne Nestegård, are thanked for their valuable comments, which improved the quality of the thesis. I am thankful to Erin E. Bachynski and Dr. Hossein Alimadadi for reading parts of this thesis and giving me valuable suggestions.

I would like to thank all of my classmates and colleagues at Marine Technology Department at NTNU. Special thanks go to, Maxime Thys and Reza Firoozkoobi, as my two friends and classmates, for all the problems we solved together. Moreover, Prof. Marilena Greco, Dr. Trygve Kristiansen, Arnt G. Fredriksen, Dr. Xu Xiang, Dr. Jikun You, Dr. Bjørn C. Abrahamsen, Morten D. Pedersen, Jacobus de Vaal, Dr. Hamid Amini, Ehsan Peymani, Dr. Madjid Karimirad, Mahmoud Etemaddar and Dr. Vahid Hassani, are thanked for all of the valuable discussions. I would like to thank my employer, MARINTEK, and especially, Halvor Lie, Ole David Økland, and Øyvind Hellan, for tolerating my regular absences during the final period of my study. Sigrid Bakken Wold, Dr. Reza Taghipour and Reza Mohseni are thanked for their helps from the beginning of my stay in Norway.

I am grateful to my mother, Roya, for her passion, patience and for always believing in me; my father, Mohammad Taghi, for his constant support and kindness; my brothers, Bamdad and Bahador, for all the games we played and still play. I would like to thank my newly born son, Nikan, for smiling at me every time he looks at me. His smiles kept me going during the last period of my work despite all problems. I am thankful to my mother, and specially, to my mother-in-law, Mehry,

for staying with us during the last couple of months of my study, and giving me the chance to finish this work.

At last but not least, I thank my wife, Fatemeh Neda, for standing beside me during all these years, in sickness and in health; for supporting me with her kindness, patience and understanding. We have been studying together for more than a decade. I am grateful to her for all of her scientific contributions to my works during these years, for all the discussions we had, the projects we finished, and for listening to me talking on and on about my work.

At the end, I dedicate this thesis to my lovely grandmother, Maryam, who passed away when I was writing the final parts of this thesis. She was constantly following up my progress since I entered elementary school, but did not last to see the end of this study. She will always be in my heart.

Babak Ommani,
Trondheim, May 31, 2013

Nomenclature

Abbreviations

2D	Two-dimensional
3D	Three-dimensional
ABM	Adams-Bashforth-Moulton method
BEM	Boundary Element Method
BIM	Boundary Integral Method
CFL	Courant-Friedrichs-Lewy condition
CG	Center of gravity
CPM	Constant Panel Method
DB	Double-Body linearization
FDM	Finite Difference Method
HOBEM	Higher Order Boundary Element Method
LCB	Longitudinal Center of Buoyancy, measured from mid-ship
MEL	Mixed Eulerian-Lagrangian method
NK	Neumann-Kelvin linearization
NURBS	Non-Uniform Rational B-Spline
RK	Runge-Kutta method

Bold symbols

δ	Local displacement vector of the ship's surface in the sea-keeping coordinate system
\mathbf{i}	Unit vector in x -direction
\mathbf{J}	Jacobian vector
\mathbf{n}	Normal vector pointing into the fluid
\mathbf{p}	A field point
\mathbf{q}	A source point
\mathbf{u}	Fluid velocity vector
\mathbf{U}_B	Vector of instantaneous body velocity

\mathbf{x}	Location vector, sea-keeping coordinate
ξ	Coordinates of source points
\mathbf{x}'	Location vector, body-fixed coordinate
$\boldsymbol{\eta}$	Vector of translational motions relative to the sea-keeping coordinate system
$\boldsymbol{\Theta}$	Vector of rotational motions relative to the sea-keeping coordinate system

Greek Letters

$\bar{\eta}_j$	Amplitude of motion in j th mode
$\bar{\phi}$	Base steady velocity potential
$\bar{\zeta}$	Steady base free-surface elevation
δ_{ij}	Kronecker delta function
Γ	Circulation
Λ	Aspect ratio
λ	Wave length
μ	Water's dynamic viscosity
ω	Oscillation frequency
Φ	Total velocity potential
ϕ	Perturbation velocity potential
ρ	Water's mass density
σ	Source strength in indirect boundary integral formulation
$\bar{\phi}$	Steady perturbation velocity potential
φ	Unsteady perturbation velocity potential
$\bar{\varphi}$	Amplitude of a harmonically oscillating perturbation velocity potential
ζ	Free-surface elevation

Mathematical Operators

\cdot	Dot-product
$\nabla \times$	Curl
∇	Gradient
$\nabla \cdot$	Divergence
∇^2	Laplacian
\times	Cross-product

Super-scripts

\sim	Continuous Fourier transform
$\hat{\sim}$	Semi-discrete Fourier transform

Roman Letters

A_W	Area of the water plane
\overline{BM}	Vertical distance of metacenter from the center of buoyancy
$D^{(tt)}$	Double differentiation operator in time
\mathcal{D}	Dipole integral
$\widetilde{\mathcal{W}}$	Continuous dispersion relation
$\widehat{\mathcal{W}}$	Discrete dispersion relation
\mathcal{E}	Element's surface
\mathcal{K}	Ship's form factor
$Fn_{\Delta x}$	Element Froude number
\overline{GM}	Transverse metacentric height
\overline{GM}_L	Longitudinal metacentric height
\overline{KB}	Vertical distance of the center of buoyancy from keel
\overline{KG}	Vertical distance of the center of gravity from keel
\overline{KM}	Vertical distance of metacenter from keel
u	Longitudinal component of wave number
\bar{u}	Non-dimensional longitudinal component of wave number
v	Transverse component of wave number
\bar{v}	Non-dimensional transverse component of wave number
\mathcal{T}	Non-dimensional time for 2D+t cross-flow drag model
C_M	Matrix of mapping coefficients
N_C	Number of collocation points
N_E	Number of elements
N_K	Number of knots
N_N	Element's number of nodes
N_P	Number of data points
N_{TN}	Total number of nodes
N_V	Total number of vertices
P_{tot}	Total pressure
\mathcal{C}	Solid angle
S_B	Body surface
\bar{S}_B	Mean body surface
S_F	Free surface
\bar{S}_F	Mean free surface
\mathcal{N}_j	Shape function for the j^{th} -node

S_H	Hollow surface
\mathcal{S}	Source integral
S_V	Vortex sheet
\bar{S}_V	Mean vortex sheet
S_{V+}	Upper side of vortex sheet
S_W	Area of the body wetted surface
A_T	Transom stern hollow shape coefficient
A_{jk}	Added mass coefficient in j^{th} mode due to motion in k^{th} direction
$B_j^{(m)(n)}$	Two-dimensional B-spline base function of order m and n at the vertex j
$b_j^{(m)}$	One-dimensional B-spline base function of order m at the vertex j
B_{jk}	Damping coefficient in j^{th} mode due to motion in k^{th} direction
C_B	Vessel's block coefficient
C_i	Damping/Amplification error in discrete waves
C_r	Dispersion error in discrete waves
C_W	Vessel's wave making resistance coefficient
C_{F0}	Flat plate's frictional coefficient
C_F	Effective frictional resistance coefficient
C_{jk}	Restoring coefficient in j^{th} due to motion in k^{th} direction
F_{CF}	Cross-flow force
Fn	Froude number
Fn_h	Transom stern Froude number
G	Green function, Rankine source
g	Gravitational acceleration
h_T	Transom stern draft
I_{jj}	Moment of inertia
I_{kj}	Product of inertia
I_w	Second transverse moment of the water plane area
J	Magnitude of Jacobian vector
k	Wave number
k_c	Continuous wave number
k_d	Discrete wave number
L	Characteristic length
M	Mass of the body
M_{CF}	Cross-flow moment

M_{jk}	Generalized mass matrix
N_{GP}	Number of Gauss points
p	Pressure relative to atmospheric pressure
p_a	Atmospheric pressure
Re	Reynolds number
S	Surface
t	Time
U	Mean forward velocity of the body
u, v, w	Velocities in x, y, z directions respectively
U_S	Tangential velocity at separation point
X, Y, Z	Earth-fixed coordinate system
x, y, z	Sea-keeping coordinate system
X_T, Y_T, Z_T	Transom stern coordinate system
z_B	Vertical position of the center of buoyancy
z_G	Vertical position of the center of gravity

Special Symbols

∇	Displaced volume
----------	------------------

Sub-scripts

\bar{s}_B	On mean body-surface
s_B	On body-surface
e	Related to element e

Contents

Abstract	iii
Acknowledgment	v
Nomenclature	vii
1 Introduction	1
1.1 Background and motivation	1
1.2 Scope and objectives of the present study	6
1.3 Overview of the previous related studies	7
1.4 Outline of the present study	12
1.5 Main contributions	14
2 Mathematical Formulation	17
2.1 Coordinate systems	17
2.2 Governing equations	19
2.3 Boundary conditions	20
2.4 Linearization around a steady base flow	22
2.4.1 Free surface	22
2.4.2 Body	23
2.4.3 Pressure	25
2.5 Double body linearization	25
2.6 Neumann-Kelvin linearization	26
2.7 Steady and unsteady problems	27
2.8 Equations of motion	28
2.9 Calculating forces and moments	32
2.10 Flow separation	34
2.10.1 Trailing edge flow separation	34
2.10.2 Transom stern flow separation	36
2.10.3 Cross-flow separation	38
2.11 Boundary integral formulation	41

3	Numerical Implementation	45
3.1	An overview on discretization methods	45
3.2	Constant panel method	47
3.2.1	Representing surfaces	47
3.2.2	Boundary element formulation	47
3.2.3	Calculating integrals	49
3.2.4	Calculating derivatives	50
3.2.5	De-singularization and collocation shift	51
3.3	Higher-order boundary element method	53
3.3.1	Representing surfaces	53
3.3.2	Boundary element formulation	55
3.3.3	Calculating integrals	57
3.3.4	Solid angles	61
3.3.5	Diagonal terms, indirect method	62
3.3.6	Calculating derivatives	63
3.4	B-spline method	63
3.4.1	Surface representation	64
3.4.2	Boundary element formulation	68
3.4.3	Calculating integrals	69
3.4.4	Solid angles	70
3.4.5	Derivatives	70
3.5	Notes on discretization methods	70
3.6	Time marching methods	71
3.6.1	Explicit/Implicit Euler	71
3.6.2	ABM4	72
3.6.3	Runge-Kutta	73
3.6.4	Choosing a time marching method	74
3.7	Free surface truncation	74
3.7.1	Steady problem, Radiation condition	74
3.7.2	Unsteady problem and damping zone	76
3.8	Solver scheme	78
3.9	Grid generation	79
3.9.1	Distributing points on boundaries	80
3.9.2	Algebraic surface grid generation	84
3.9.3	Elliptic surface grid generation	85
3.9.4	Paneling	86
3.10	Programming	86
4	Evaluation of discretization methods	91
4.1	Introduction	91
4.2	Zero forward speed (current)	95
4.2.1	Continuous time and discrete space	95
4.2.2	Continuous space and discrete time	97
4.2.3	Discrete time and space	98
4.3	Steady forward speed	100
4.3.1	Two-dimensional waves	101

4.3.2	Three-dimensional waves	104
4.4	Forward speed with oscillations	107
4.4.1	Continuous space and time derivatives	107
4.4.2	Harmonic waves with discrete spatial derivative	108
4.4.3	Fully discretized dispersion relation	110
4.5	Notes on temporal stability	111
4.6	Conclusions	113
5	Non-separated Flows	115
5.1	Introduction	115
5.2	A heaving semi-sphere on the free surface	115
5.3	Wave diffraction by a vertical cylinder	119
5.4	A traveling Kelvin source under the free surface	121
5.5	A Wigley hull with forward speed	124
5.6	A Wigley hull in forced heave oscillations	126
5.7	A series-60 vessel in forced heave oscillations	129
5.8	Conclusions	129
6	Tail-separated Flows	131
6.1	Introduction	131
6.2	Foil in infinite fluid	132
6.3	Plate with a drift angle	135
6.3.1	Formulation	136
6.3.2	Discretization and numerical implementation	141
6.3.3	Results and discussions	143
6.4	Plate in oscillatory sway and yaw motions	154
6.4.1	Formulation	155
6.4.2	Discretization	156
6.4.3	Results	157
6.5	Conclusions	168
7	Hydrodynamics of Semi-displacement Vessels	169
7.1	Introduction	169
7.2	Steady forward speed	170
7.2.1	Free surface elevation	171
7.2.2	Sectional vertical force	173
7.3	Forward motion with a drift angle	176
7.4	Heave oscillations	185
7.5	Conclusions	188
8	Dynamic Stability Analysis	189
8.1	Introduction	189
8.2	A case with observed dynamic instability	190
8.2.1	A model semi-displacement vessel	190
8.2.2	Hydrodynamic modeling	192
8.3	Sway-yaw dynamic stability analysis	199

8.3.1	Formulation	199
8.3.2	Analysis	200
8.3.3	Sensitivity study	203
8.4	Sway-roll-yaw dynamic stability	208
8.4.1	Formulation	208
8.4.2	Analysis	209
8.4.3	Sensitivity study	211
8.5	Conclusions	219
9	Summary and Future Works	221
9.1	Summary and conclusions	221
9.2	Suggestions for future works	226
	Bibliography	229
	Appendices	
	Appendix A Lagrangian polynomials and shape functions	241
A.1	4-points linear elements	241
A.2	8-points quadratic elements	241
A.3	9-points quadratic elements	242
A.4	12-points cubic elements	243
	Appendices	
	Appendix B Fourier transformations	245
B.1	Analytical solution for propagating waves in 3D	245
B.2	Fourier analysis	246
B.2.1	Continuous Fourier transform	246
B.2.2	Semi-discrete Fourier transform	246
B.2.3	Convolution theorem	247
B.2.4	Aliasing theorem	247
B.2.5	Fourier transform of the Rankine source function	247
B.2.6	Fourier transforms of B-spline base functions	249
B.2.7	Fourier transform of differential operators	251
B.3	Boundary integral formulation	252

Chapter 1

Introduction

1.1 Background and motivation

Marine vehicles can be categorized based on their operational speed. Length based Froude number, defined as $Fn = U/\sqrt{Lg}$, is used in practice to represent the vessel's speed (U) in a non-dimensional form where L is the vessel's length and g is the acceleration due to gravity. A vessel operating at $Fn > 0.4$ is generally referred to as a high-speed vessel (Faltinsen, 2005). The weight of the vessel is carried by the hydrodynamic and hydrostatic pressure. For $Fn < 0.4$, the hydrostatic pressure which gives the buoyancy force is dominant. The vessels operating in this condition are called *displacement* vessels. As Froude number increases, however, the relative importance of hydrodynamic pressure in carrying the vessel's weight increases. This can be explained simply by considering the fact that the hydrodynamic pressure is proportional to velocity squared. For vessels operating above Fn 1.2, it is the hydrodynamic pressure which mainly carries the vessel. Such vessels are called *planing* vessels. Between these two limits there is a range where both hydrostatic and hydrodynamic pressures are equally important. The vessels which operate in this range are known as *semi-displacement* vessels.

In addition to the operational Froude number, vessels can be categorized based on how their weight is supported at sea. Faltinsen (2005) categorizes the methods for supporting a vessel's weight into four groups: *submerged hulls*, *hydrofoils*, *air-cushions*, and combination of these. The lift force induced by a hydrofoil vessel's fins and wings carry the vessel's weight at operational speed, much like an airplane. A pressurized air-cushion can also be used to lift the vessel from the free-surface. Faltinsen (2005) describes examples of such vessels. Most of the conventional displacement, semi-displacement, and planing crafts are categorized as submerged hulls.

Although the propulsion-resistance problem is the main focus for conventional displacement vessels, the seakeeping problem is more critical for high-speed vessels. The safety and operational limits for high-speed vessels are highly dependent on their seakeeping properties. The seakeeping problem can be viewed as a study of the dynamic behavior of a vessel advancing at sea in the presence of environmental

disturbances such as waves. The seakeeping problem can also be combined with the maneuvering problem in order to study the performance of a vessel following a desired path in a sea-way. Improving the seakeeping characteristics of high-speed vessels is subject of a continuous investigation. The Enlarged Ship Concept and Axe Bow Concept introduced by Keuning and Pinkster (1995) and Keuning et al. (2001) are two examples of such innovative studies.

The beam-to-draft ratio of monohull semi-displacement vessels can vary from 5 to more than 7, which makes these vessels quite different from displacement vessels. Consequently, the seakeeping properties of such vessels are expected to differ from those of displacement vessels. Monohull semi-displacement vessels are generally equipped with stern flaps, roll fins, and automatic control motion devices. On the other hand, planing vessels -which are typically smaller than semi-displacement vessels and operate at higher Froude numbers- suffer from issues such as cavitation and ventilation in addition to dynamic instability. Interested readers are referred to Faltinsen (2005) for a more detailed description of semi-displacement and planing crafts and their characteristic parameters.

As mentioned previously, as the vessel's speed increases, the importance of hydrodynamic pressure increases compared to hydrostatic pressure in carrying the vessel's weight. Due to this shift of importance, a vessel which is stable at rest can become unstable at high speeds. The stability of a vessel when advancing with forward speed is referred to as *dynamic stability* (analogous to *static stability*, which refers to the stability at rest). Dynamic stability can be viewed as a sub-set of the seakeeping problem. Although the static stability of a vessel is a well-studied problem, our understanding of dynamic stability is rather limited.

Different kinds of vessels may experience different types of dynamic instabilities, depending on their operational speed range. Figure 1.1 categorizes different types of possible dynamic instability scenarios for different types of vessels. As shown in Figure 1.1, the instabilities can be of oscillatory and non-oscillatory nature. For instance, a vessel in planing condition with Froude number higher than one may experience oscillatory instabilities in roll (chine walking), coupled heave and pitch (porpoising) and coupled roll, pitch, and yaw (cork-screwing). A detailed description of each instability can be found in Müller-Graf (1997) and Faltinsen (2005).

Here we shall focus our attention on a non-oscillatory type of instability known as *calm water broaching*, which is known to limit semi-displacement monohull vessels' operational Froude number to 1.2 (Lavis, 1980). Faltinsen (2005) defines calm water broaching as a non-oscillatory instability which generally starts by a sudden list due to loss of steady restoring moment in heel at high Froude numbers. This sudden change of list angle is followed by a violent yaw angle to one side, which may lead to capsizing.

Eda (1980) considered coupling of the roll motion with the sway and yaw motions as a contributing factor in dynamic behavior and stability of high speed vessels. Haarhoff and Sharma (2000) investigated the influence of speed and meta-centric height on dynamic instability in sway, roll and yaw. They showed that a stable vessel at rest may become unstable at higher speeds. For high-speed vessels, the increase in importance of hydrodynamic pressure contributes to the loss

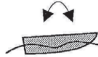


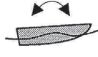

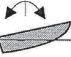



	HYDROSTATIC ←		→ HYDRODYNAMIC	
	DISPLACEMENT	SEMI-DISPLACEMENT		PLANING
	INCREASING FROUDE NUMBER →			
TRANSVERSE	TRANSVERSE HYDROSTATICS $\overline{GM} \leq 0$	LOSS OF \overline{GM}_T DUE TO WAVE EFFECT 	ROLL INSTABILITY NON ZERO HEEL NON OSCILLATORY 	"CHINE WALKING" DYNAMIC ROLL OSCILLATION 
LONGITUDINAL	LONGITUDINAL HYDROSTATICS $\overline{GM}_L \leq 0$	LOSS OF \overline{GM}_L DUE TO WAVE EFFECT 	TRIM INSTABILITY BOW DROP NON OSCILLATORY 	"PORPOISING" DYNAMIC PITCH-HEAVE OSCILLATION 
COMBINED	COMBINED $\overline{GM} \leq 0$ $\overline{GM}_L \leq 0$	COMBINED WAVE EFFECT 	BROACH NON OSCILLATORY 	"CORKSCREW" PITCH-YAW-ROLL OSCILLATION 

Figure 1.1: Different instability scenarios for a vessel at sea (Cohen and Blount, 1986)

of hydrostatic restoring moment in roll by reducing the vessel's metacentric height.

Baba et al. (1982) investigated the sway-roll-yaw instability in semi-displacement crafts by a series of simulations using the hydrodynamic coefficients obtained from captive model tests. They found that the metacentric height plays an important role in roll-induced dynamic instability. In Figure 1.2, the variation of steady list angle due to off-center weight on four different vessels is presented based on the experiments reported by Werenskiold (1993). The increase in the list angle due to loss of restoring moment by increasing the Froude number is interesting. Especially after Froude number of 0.8, where the vessels may start planing, a sudden change in the list angle's rate of increase is detectable.

Müller-Graf (1997) suggested an increase in the static metacentric height as a solution to this problem. Based on his guidelines for a semi-displacement round bilge monohull with 10 to 30 meters length, a metacentric height of 1 to 1.5 meters is suggested and below 0.8 meters must be avoided. Moreover, he suggested the application of spray rails as a way to reduce the loss of restoring moment in heel (Müller-Graf and Schmiechen, 1982). As Faltinsen (2005) pointed out, this can be explained by viewing the spray rail as a low-aspect-ratio lifting surface. Müller-Graf (1997) also referred to another closely related instability scenario as *yaw-roll* instability. This type of instability is initiated by a small change in the vessel's drift/yaw angle. This will induce a roll moment which may lead to a calm water broaching instability, as introduced above. The disturbance in the vessel's yaw angle can be induced by waves or inadvertent rudder actions. Moreover, propulsion units, steering units, faults in stabilization units, ventilation, and cavitation can

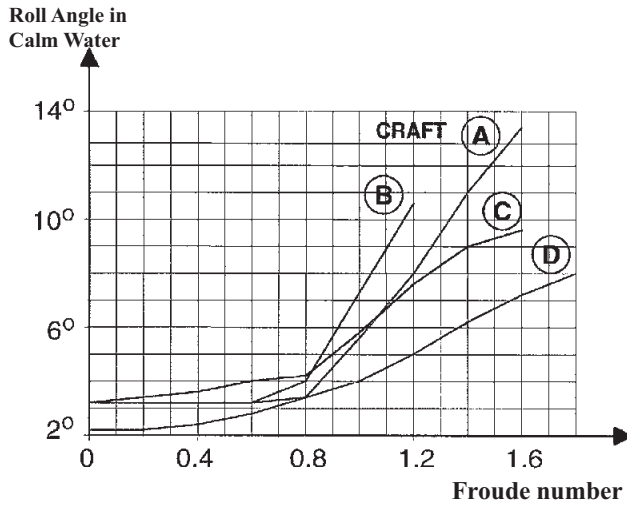


Figure 1.2: Variation of the heel angle with Froude number due to hydrodynamic loss of the metacentric height (Werenskiold, 1993).

be the source of such disturbances for high-speed vessels and therefore can lead to similar dynamic instability scenarios.

Lewandowski (2003) constructed a hard chine planing vessel's dynamic model in sway-roll-yaw using a series of hydrodynamic coefficients obtained from semi-empirical methods. Then he investigated the dynamic stability of the vessel with one (roll) and two (sway-yaw) degrees of freedom using a root locus analysis. Faltinsen (2005) presented sway-yaw and sway-roll-yaw analysis using analytically derived added mass and damping coefficients. The speed dependency of the coefficients is simplified in his analysis. Faltinsen (2005) mentions that a more detailed picture of the variation of hydrodynamic coefficients with respect to frequency and Fn , through numerical or experimental analysis, is required for more detailed dynamic stability investigations.

The prediction of dynamic instability in calm water is the main motivation for the present study. However, in order to study the dynamic stability of a system, the dynamic model of that system must be identified. This introduces, the hydrodynamics of semi-displacement vessels as the problem which must be dealt with first. The hydrodynamics of semi-displacement vessels is a complicated problem in itself. In particular, the presence of transom stern makes the problem difficult to handle with existing potential flow methods. The flow separates from the transom stern. This separation, at high enough speed, combines with ventilation and forms a dry stern. At lower speeds, the transom stern stays wet and a dead water zone forms behind the stern. Doctors and Day (2001) suggested that if a calm water transom stern Froude number, defined as $Fn_h = U/\sqrt{h_T g}$ where h_T is the stern draft, is more than approximately 2.5, a dry transom stern can be expected. Further investigations by Maki et al. (2005) led to similar findings. Maki et al.

(2005) suggested, however, that the difference between their findings and those by Saunders (1957) is related to the difference in Reynolds numbers in full and model scale.

Figure 1.3 shows how the free surface behind a dry transom stern evolves. The separated flow from the transom stern forms a hollow in the free surface. The water from the two sides of the vessel meet at a distance downstream which forms a large non-linear wave known as a *rooster-tail*. Capturing the free surface behind the transom stern using linear potential flow theories is troublesome due to non-linearities and the large variation of the free-surface elevation both at and after the hollow. Moreover, the atmospheric pressure on the transom stern is important for force prediction and must be included in the calculations.

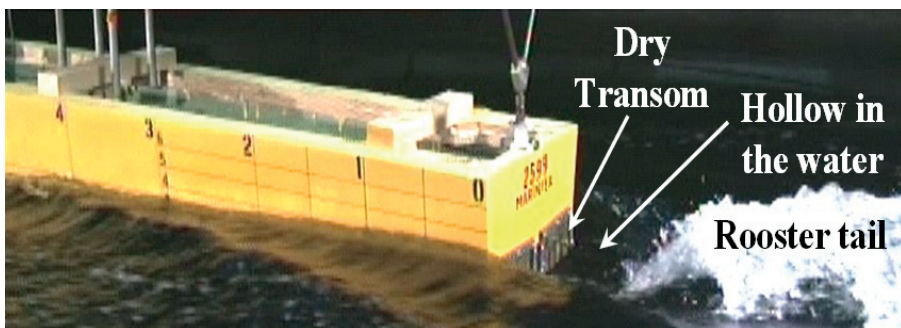


Figure 1.3: Waves behind a ventilated (dry) transom stern (Lugni et al., 2004).



Figure 1.4: Illustrations of non-linear flow around a semi-displacement vessel, Left: $Fn = 0.5$, Right: $Fn = 0.6$ with 10° drift angle, pictures from experiments at INSEAN by Fabbri et al. (2009).

The flow around semi-displacement vessels at high speed can be quite non-linear. Figure 1.4 shows snapshots of experiments realized at INSEAN by Fabbri et al. (2009) where a semi-displacement vessel towed with and without drift angle. The large bow wave and consequent overturning of the generated waves exemplify the complicated flow that can be expected. It would, however, be interesting to see to what degree the linear theory can be used to predict these nonlinear effects, especially when the goal is linear dynamic stability analysis.

1.2 Scope and objectives of the present study

In order to investigate the dynamic stability of a semi-displacement vessel, a linear dynamic stability analysis was chosen as the first step. A dynamic model of the system was needed, including the linearized hydrodynamic coefficients. These coefficients must be obtained from the forces acting on the vessel advancing and oscillating in calm water, i.e. by solving the *radiation* problem. Semi-displacement monohull vessels with round bilge were chosen as the subject of study. Infinite water-depth was assumed in order to avoid the complications occurring in shallow or confined waters.

The flow was assumed to be potential and linearized about the vessel's forward speed. This type of linearization was chosen based on the fact that high speed flows are the main focus of the present study. The three-dimensional boundary element method using distribution of Rankine sources and dipoles was selected to solve the linearized potential-flow problem. Viscous effects were included in the calculations indirectly when their role was expected to be significant. These effects were included by introducing a vortex sheet for the trailing edge flow separation, a 2D+t cross-flow drag model for the cross-flow separation, and a hollow body model for the flow separation from a dry transom stern. Other viscous effects are neglected.

Many different numerical techniques exist for solving the discretized boundary integral equations based on the Rankine singularities. A rational and systematic investigation on the properties of these methods was needed. A computer program was developed in a way which allows fast and easy implementation of different numerical schemes. In this way, the performance of different schemes in solving different problems was studied. Moreover, a systematic investigation using semi-discrete Fourier analysis was realized for different numerical methods. The program was verified and validated by solving a series of bench-marking problems with and without forward speed using steady-state and time-domain solvers. The obtained results were verified and validated against available analytical, numerical, and experimental data.

A semi-displacement vessel undergoing lateral motions can be simplified to a surface-piercing flat plate from a hydrodynamical point of view. Then, the flow separation from the plate's trailing edge resembles the flow separation from the transom stern. The numerical program was used to investigate the hydrodynamics of the flow around a free-surface-piercing flat plate with trailing edge flow separation at high speeds in steady and oscillatory motion. The objective was to find out to what degree the present linear model can capture the hydrodynamic coefficients by comparing the results to previous numerical and experimental data.

The application of the method in solving the flow around actual semi-displacement vessels was investigated. The objective was to examine the performance and accuracy of the present linear approach in solving the flow around semi-displacement vessels. The flow separation from the transom stern imposes complications due to the non-linear nature of the flow, which is difficult to capture. The calculations here were based on the development of the two-dimensional analytical solution for the flow in the vicinity of a dry transom stern by Faltinsen (2005), for three-dimensional

symmetric and asymmetric flows.

Finally, dynamic stability analysis based on the obtained hydrodynamic coefficients was pursued, in keeping with the main objective of the study. The simplified model of the plate was studied as an alternative to the complicated flow around an oscillating semi-displacement vessel. The dynamic stability in sway-yaw and sway-roll-yaw using this simplified model was investigated. The goal was to gain insight into the important parameters involved in these types of instabilities. Moreover, it is of interest to assess linear theory's ability to predict these types of instabilities.

1.3 Overview of the previous related studies

The nature of the present study combines many different areas. The related previous studies can be quite extensive for some of the areas addressed here. The intention, however, is not to give a complete overview of each area, but to present a short summary of the studies which were particularly influential during the completion of the present work.

These studies are addressed as follows: First, a review of the numerical methods for calculating hydrodynamic coefficients of advancing vessels, focusing on three-dimensional Rankine panel method, is presented. Then, a series of experimental investigations related to this problem are addressed, followed by the related numerical studies. The studies are organized based on the subject of study.

Rankine panel method

Strip theory is conventionally used to calculate ships' seakeeping characteristics. In particular, the so-called STF method (Salvesen et al., 1970) is very popular for calculating vessels' hydrodynamic coefficients with forward speed. In this method, the two-dimensional added mass and damping of the ship sections are combined by considering the forward speed and frequency of encounter in order to estimate the hydrodynamic properties of the vessel. This method, however, is more suitable for low Froude numbers and high oscillation frequencies (Faltinsen, 1990). Therefore, other methods must be adopted for the current study.

Hess and Smith (1967) introduced a numerical method for solving the potential flow around blunt bodies using boundary integral formulation. The method was based on discretization of the body-surface to flat panels and distribution of constant singularities on each panel. The source strength is obtained by satisfying the boundary conditions. Dawson (1977), among others, extended the method for solution of potential flow around bodies in or under the free surface by explicitly satisfying the linearized free-surface boundary condition. He introduced singularities on the free surface and used an upstream finite difference scheme to satisfy the radiation boundary condition. Later, in June Bai and McCarthy (1979), applications of similar methods for predicting an advancing ship's wave-making resistance and free-surface elevation are tested. At the same time, Hess (1979) introduced the application of higher-order source distributions and surface representations.

Jensen et al. (1986) solved the steady wave resistance problem by introducing singularities outside the fluid domain. Their desingularized method reduced the

inaccuracies in calculation of velocities close to the body surface. Later, Zhao and Faltinsen (1989) documented and demonstrated these inaccuracies. The desingularized method is developed further, among others, by Beck et al. (1993) to solve for the non-linear free-surface boundary condition.

Nakos (1990) used a three-dimensional Rankine panel method to solve the linearized steady wave-making and seakeeping problem in the frequency domain. He used B-spline functions to represent the distribution of Rankine sources and dipoles, while the surfaces were discretized using flat quadratic panels. The integrals of higher-order source distributions were calculated by the expansion method proposed by Newman (1986). The free-surface boundary condition was linearized around double-body flow in order to take the steady and unsteady flow interactions into account. The method was later developed to include time-domain problems in Vada and Nakos (1993), Nakos et al. (1993) and Kring (1994).

Raven (1993) and Raven (1996) introduced the raised panel method to solve the non-linear wave-making problem of a vessel advancing in calm water. Bunnik (1999) linearized the unsteady problem of an advancing ship undergoing oscillations about the nonlinear potential and free-surface elevation obtained from Raven (1996). He showed that upstream differentiation is important for satisfying the radiation boundary condition at higher forward speeds.

Liu et al. (1991) compared the application of Lagrangian shape functions in the boundary element method (for representing the surface geometry and singularity distribution) to a constant panel method. Xü (1992) used Lagrangian shape functions for calculating nonlinear water waves in three dimensions. Shao (2010) introduced the application of a body-fixed coordinate system in addition to Lagrangian shape functions to solve the problem of inaccurate m_j -terms in the calculating weakly-nonlinear wave body interactions. Interested readers are referred to Shao (2010) for a review of the applications of aforementioned methods for solving higher-order problems.

An important issue in the application of the boundary element method for water waves is the existence of numerical instabilities, damping, and dispersion errors. Longuet-Higgins and Cokelet (1978) first reported the existence of saw-tooth instabilities in the discrete solution of propagating free-surface waves. Sclavounos and Nakos (1988) used Fourier analysis to study the dispersion and damping properties of the waves generated by a disturbance moving under the free surface with constant velocity in two-dimensions. Moreover, they linked the numerical instabilities to the presence of spurious roots in the discrete dispersion relation. Romate (1989) also studied this problem by combining finite difference operators and higher-order polynomials as shape functions. Later, Nakos (1990) extended the two-dimensional analysis to three dimensions. He showed that the accuracy of the numerical method also depends on the elements' aspect ratio and $\tau = U\omega/g$, where U is the forward speed, ω is the frequency of oscillations, and g is the gravitational acceleration. Moreover, he argued that aliasing of the wave energy can explain the energy build-up in spurious roots and lead to the saw-tooth instability. Kim et al. (1997) used the numerical method by Nakos (1990) and looked at the accuracy of the method in capturing the waves traveling on the free surface in the absence of current. They investigated the *temporal* stability and showed that it results in a Courant-type

stability condition.

Raven (1996) considered the de-singularization effects on the constant element method's properties for the waves generated by a moving disturbance. The analysis was extended by Sierevogel (1998). She studied the accuracy of both upstream and downstream waves using constant elements and a finite difference method in two dimensions. Bunnik (1999) expanded the calculations by Sierevogel (1998) to three dimensions. He also investigated the temporal stability using Z-transformation and showed that although central difference schemes have good dispersion and damping properties, they may lead to an unstable solution.

Büchmann (2000) studied the spatial and temporal convergence and stability of the B-spline method with shape function differentiation. He also presented a Courant-type condition for stability which depends on the discretization properties. Recently, Kim et al. (2005) expanded the calculations for constant elements with de-singularization and a collocation point shift to include finite water depth effects as well.

It must be mentioned that the numerical method presented here, i.e. Rankine panel method, is not the only option for potential-flow computations around an advancing vessel at sea. Several other relevant numerical methods are listed below. Interested readers are referred to the original publications for more details.

- **The time-domain Green function** method is based on the work by Liapis and Beck (1985), King et al. (1988), and Lin and Yue (1990) among others. In this method, a linearized free surface boundary condition is satisfied by the time-domain Green function. Then, the solution is obtained by satisfying the body boundary condition on the discretized body surface.
- **The Mixed Eulerian-Lagrangian** method is a nonlinear method which captures the evolving free-surface elevation and its velocity potential. In this method, a boundary value problem is solved at each time step. Then, the fully nonlinear free-surface conditions are applied in a Lagrangian frame to step forward the free-surface properties in time. Early application of this method can be found in Longuet-Higgins and Cokelet (1976), Faltinsen (1977), and Dommermuth and Yue (1987).
- **The 2D+t** method is based on decomposing steady and unsteady 3D flows into a series of 2D problems in the time domain by means of coordinate transformation. This reduces the required computational effort. Then the 2D solutions are combined in order to obtain the solution to the original 3D problem. This method is most suitable for high-speed slender bodies. Early applications of the method for simple geometries can be found in Chapman (1976). The method was later applied to realistic high-speed ships (by Faltinsen and Zhao (1991)). The fully nonlinear free-surface condition and non-viscous flow separation were added to the method in studies by Sun and Faltinsen (2010), and Sun and Faltinsen (2011).

Hydrodynamic coefficients at low to moderate Froude numbers

Gerritsma and Beukelman (1965) measured distribution of vertical forces on a seg-

mented Series-60 vessel in heave and pitch and compared the results with the strip theory calculations including the forward speed effect. Later, Vugts (1970) extended their work by including the sway, yaw, and roll motions. He presented both experimental and numerical data for the distribution of hydrodynamic coefficients along the vessel. Two conditions, zero forward speed and $Fn = 0.2$, were investigated. Shao and Faltinsen (2012) presented comparisons between the body-fixed coordinate system method's results and the experimental data by Gerritsma and Beukelman (1965).

Journée (1992) investigated the hydrodynamic coefficients and ship responses in heave and pitch for a Wigley hull up to $Fn = 0.4$. He addressed the frequency and forward speed dependency of the hydrodynamic coefficients and compared with strip theory results. Nakos (1990) compared the results from his numerical method with the experimental data reported by Journée (1992).

Free-surface-piercing flat plate

The hydrodynamics of a surface-piercing flat plate at high and moderate Froude numbers, including lateral motions, have been studied numerically and experimentally. This problem can be a simplified alternative to the hydrodynamics of a thin or slender semi-displacement vessel. van den Brug et al. (1971) reported an extensive study on the hydrodynamic forces on a surface-piercing flat plate with both steady drift and oscillatory motion in sway and yaw at Froude numbers up to 1.35. These experiments have been the source of validation studies in many numerical calculations. Chapman (1976) introduced the 2D+t method based on a slender body and potential-flow assumption to calculate the transverse force and yaw moment. He investigated the influence of linear, second order, and nonlinear free-surface boundary conditions. He concluded that, while the nonlinear free-surface boundary condition can influence the free-surface elevation, it does not change the side force and yaw moment significantly. Kashiwagi (1983) also studied the added mass and damping coefficients of a surface-piercing flat plate in sway and yaw, numerically and experimentally, for Froude numbers up to 0.4. The method from Chapman (1976) was used for comparison. Moreover, Kashiwagi (1984) presented numerical values based on a modified lifting line theory for the roll motion of a flat plate.

Maniar et al. (1990) and Xü (1991) solved the potential flow problem in three dimensions using the thin-ship assumption and Kelvin-Havelock Green function. They pointed out the incompatibility between the pressure Kutta condition and the linearized free-surface boundary condition at the meeting point of the trailing edge and the free surface. They showed that the effects of this incompatibility are local and do not change the global solution. Landrini and Campana (1996) used double body linearization to formulate the problem. They investigated the influence of the bottom tip vortex on the side force and yaw moment. They showed that the bottom tip separation (keel vortex shedding) plays an important role in the transverse force and yaw moment, especially for lower draft-to-length ratios. They also demonstrated that, for their studied case, a linearized vortex sheet is sufficient to model the forces, and there is no need for nonlinear wake geometry.

Zhu and Faltinsen (2007) used a linear 3D Rankine panel method to solve the potential-flow problem. They took the plate's thickness into account and neglected the tip-vortex's effects.

Hydrodynamics of semi-displacement vessels

Molland et al. (1994) presented systematic investigations of the resistance properties of semi-displacement models through a series of model test experiments. He gave estimations of the so-called form-factor, which is important for estimating such vessels' resistance. Doctors and Day (2001), Maki et al. (2005), and Doctors (2007) presented a detailed experimental study of the formation of the transom stern hollow. Moreover, the influence of the transom stern on the vessel's resistance was discussed and numerical calculations were presented.

Keuning (1988) investigated, numerically and experimentally, the distribution of the steady vertical force along a semi-displacement vessel at high forward speed. Moreover, the distribution of added mass and damping coefficients in heave and pitch along the vessel were studied through forced-oscillation experiments on a segmented model. Faltinsen and Zhao (1991) presented linear and non-linear 2D+t calculations for the vertical hydrodynamic coefficients of a semi-displacement vessel at high speed. They compared the distribution of the vertical added mass and damping along the vessel with the experimental data reported by Keuning (1988). They pointed out the importance of non-linearities. Moreover, they discussed the sharp drop in the values of hydrodynamic coefficients at the vicinity of a dry transom stern and the deficiency of a 2D+t method for capturing this behavior. Sun and Faltinsen (2010) solved a similar problem by adding the non-viscous flow separation to a fully nonlinear 2D+t solution, thus obtaining a better agreement with the experimental data reported by Keuning (1988) for the distribution of the steady vertical forces along the vessel. Sun and Faltinsen (2011) extended the problem to oscillatory motions and showed that, except at the vicinity of the transom stern, their method can give good predictions of the vertical hydrodynamic coefficients distribution. Garne (2005) numerically and experimentally investigated the behavior of planing crafts in wave. He proposed a correction function based on the experimental measurements to capture the pressure drop close to the transom stern of planing hulls.

Reed et al. (1991) proposed a method to satisfy the Kutta-type condition at the transom stern using the lifting potential flow. They used two numerical methods, based on the distribution of Havelock and Rankine singularities, to investigate the flow around a high-speed vessel with transom stern. de Jong (2011) investigated the seakeeping characteristics of three different high speed vessels, both numerically and experimentally, by focusing on the seakeeping behavior in head seas. He adopted a numerical method using the time-domain Green function (based on the previous developments by Lin and Yue (1990) and van Walree (2002)) which satisfies the linearized free-surface boundary condition and consequently requires only the discretization of the body surface. He adopted a wake model similar to what is proposed by Reed et al. (1991) to enforce a smooth flow separation from the transom stern.

Lugni et al. (2004) reported a series of experiments measuring the free-surface elevation around a semi-displacement vessel with forward speed. In their study, special attention was paid to the formation of the transom stern hollow and rooster-tail. Moreover, they presented numerical calculations using a linear 2D+t and a 3D linear Rankine panel method and compared the results with the experimental data. In their 3D Rankine panel method, they used a hollow-body (also called false-body) model to take the transom stern flow separation into account. They extended the vessel's body by the hollow body where the shape of the hollow was obtained from a 2D+t calculation. Zhu and Faltinsen (2007) used a similar approach to calculate the free-surface elevation around a semi-displacement vessel with constant forward speed. They adopted the 2D potential-flow solution proposed by Faltinsen (2005) in the vicinity of a fully ventilated transom stern in addition to an iterative procedure to form the 3D hollow. Fabbri et al. (2009) investigated the hydrodynamic forces on an advancing semi-displacement vessel with constant drift angle. The vessel was towed in the tank with fixed drift angle while being free to sink, trim, and heel. The forces in horizontal plane, as well as yaw moment, were reported for a series of drift angles and Froude numbers up to 0.6. The vessel's trim, sinkage, and heel, induced by the forward speed and constant drift, are also documented, making the report a good source for validation of numerical computations.

In the recent years CFD methods are applied in capturing the flow behind a fully or partly ventilated transom stern. Examples of these investigations can be found in Starke et al. (2007) for 2D and Drazen et al. (2010) for 3D flows. As reported in these studies, this type of numerical method, although capable of capturing all the nonlinearities, is extremely expensive in terms of computational cost.

1.4 Outline of the present study

Chapter 2: Mathematical Formulation

The mathematical representation of the problem is described in this chapter. Coordinate systems are defined, and governing equations and boundary conditions are presented. The body and free-surface boundary conditions are linearized. Equations of motion for a six degree-of-freedom vessel are presented. Methods for calculating forces and moments, as well as their linearized decompositions, are addressed. A selection of techniques for indirect calculation of viscous effects in the present potential-flow method are presented. Finally, the theoretical formulation and application of the boundary integral method for the solution of potential-flow problems are introduced.

Chapter 3: Numerical Implementation

The numerical tools and techniques for solving the boundary integral equations are presented in this chapter. Different discretization methods using constant panels (CPM), higher-order Lagrangian shape functions (HOBEM), and B-splines are addressed. The numerical considerations involved in calculation of the integrals' kernels for each method are discussed. The discretized form of boundary integral

formulation, i.e. boundary element formulation, is presented for each method of discretization. Different time-marching methods for solving the initial-value problem in the time domain are touched upon. Considerations regarding free-surface truncation and the methods for satisfying the radiation boundary condition, such as upstream differentiation and damping zones, are discussed. Numerical grid generation methods for controlling the grid point distribution and discretizing boundary surfaces are presented. The application of advanced programming techniques for embedding the boundary element mathematics into the existing C++ compiler is touched upon. The benefits of using such methods in terms of efficiency and programming abstraction are discussed.

Chapter 4: Evaluation of Discretization Methods

The numerical properties of different discretization methods are systematically investigated in this chapter using semi-discrete Fourier analysis. The numerical dispersion and damping of constant elements, higher-order elements using Lagrangian shape functions, and B-spline methods are compared. The continuous and discrete forms of the dispersion relation are used for this purpose. Problems both with and without forward speed are considered. The findings from previous studies on similar topics are summarized.

Chapter 5: Non-separated Flows

In this chapter, a series of potential-flow problems, with and without forward speed, in steady-state and time-varying conditions, are solved using the presented numerical method. The results from the time-domain solver without forward speed are benchmarked against analytical results for waves radiated by a heaving semi-sphere and for diffraction of waves around a vertical circular cylinder. Then, the steady-state solver with forward speed is tested by solving the classical problem of a traveling Kelvin source under the free surface and the wave-making problem of an advancing Wigley hull. The time-domain solver is used to calculate hydrodynamic coefficients for an advancing Wigley hull and Series-60 vessel undergoing forced heave oscillations. The results are compared to existing numerical and experimental data.

Chapter 6: Tail-separated Flows

The steady and unsteady problems of a surface-piercing flat plate are considered in this chapter as examples of potential-flows with important flow separation effects. The classical problem of an advancing foil in infinite water is considered first. The flow separation from the foil's trailing edge is modeled by introducing a vortex sheet. Then the forces on a surface piercing flat plate with an angle of attack in steady forward motion are considered. The tail flow separation is modeled by introducing a linearized vortex sheet. The bottom-flow separation is shown to be important, and it is included by means of a 2D+t cross-flow drag model. The unsteady problem of a swaying and yawing surface piercing flat plate in forward motion is considered next. The time-varying vortices generated at the plate's tail

are propagated along a linearized vortex sheet. The hydrodynamic forces and coefficients are calculated and compared with existing numerical and experimental data.

Chapter 7: Hydrodynamics of Semi-displacement Vessels

A series of problems considering the flow around monohull semi-displacement vessels in motion are presented in this chapter. The steady problem of an advancing semi-displacement vessel on a straight course is considered first. The hollow body model is used to capture the dry transom stern effects. The free-surface elevation and the distribution of the steady vertical forces along the vessel are calculated and validated against existing numerical and experimental data. Then, the forces on a semi-displacement vessel with fixed drift angle on a straight course are considered. The results are compared against experimental data. A simplified 2D+t cross-flow drag model is used to explain the differences between numerical and experimental results for the transverse force. Heave oscillations of a semi-displacement vessel with high forward speed are solved in the time domain. The distribution of heave added mass and damping is calculated and compared to existing experimental and numerical data. It is shown that, the present 3D model is able to capture the sharp change in the values of these quantities close to the transom stern.

Chapter 8: Dynamic Stability Analysis

A simplified and preliminary dynamic stability analysis of a monohull semi-displacement vessel in sway-yaw and sway-roll-yaw is presented in this chapter. The hydrodynamic properties of the chosen semi-displacement vessel are simplified to be similar to a flat plate. The hydrodynamic coefficients in sway, roll, and yaw for an advancing, surface-piercing flat plate are presented for a series of Froude numbers and oscillation frequencies. The influence of different hydrodynamic coefficients on the solution to the equations of motion are investigated independently. The influence of the longitudinal (x_G) and vertical position of the center of gravity (\overline{KG}), as well as the vertical position of the metacenter (\overline{KM}) on the system's dynamic stability are also touched upon. It is shown that the sway-roll-yaw dynamic stability analysis predicts an instability for the system at a Froude number close to what has been observed in experiments.

Chapter 9: Summary and Future Work

A summary of the findings of the present study and suggestions for future work are presented in this chapter.

1.5 Main contributions

A three-dimensional Rankine panel method was developed for solving the potential flow around advancing and oscillating floating bodies. Advanced programming techniques were used to enhance the C++ compiler with the abstract formulation of

the boundary element method. In this way, many different discretization methods—such as constant, higher order with Lagrangian shape functions, and B-splines—were implemented in a modular way. This technique provided the possibility of comparing different discretization methods. Moreover, different problems with different boundary integral formulations could be implemented with mathematical abstraction, independent of the discretization method.

The numerical dispersion and damping of the discretized formulations were evaluated for different discretization methods. It was shown that different discretization methods and differentiation techniques were suitable for different kind of problems. The presented comparisons were beneficial in choosing the correct numerical scheme to achieve a stable solution and judging the validity of the results. Moreover, it was shown that forward speed played an important role in determining the best numerical scheme.

The two-dimensional semi-analytical solution by Faltinsen (2005) for the flow in the vicinity of a dry transom stern was combined with numerical grid generation methods and developed for three-dimensional flows. The free-surface behind the dry transom sterns of monohull semi-displacement vessels was captured by iterating the hollow surface. The model was validated by solving for the steady forward motion of a monohull semi-displacement vessel and comparing the free-surface elevation and the distribution of the vertical force along the vessel. It was shown that the present model could capture the drop in the steady vertical force at the transom stern due to atmospheric pressure. A 2D+t method does not capture this effect (e.g. Sun and Faltinsen (2010)).

The hollow body model was further developed to capture the asymmetric free surface shape behind the dry transom stern of a monohull semi-displacement vessel with fixed drift angle. Corrections due to viscous effects were added to the transverse force using a simplified 2D+t cross-flow drag model. The cross-flow separation was shown to explain the difference between experimental and numerical data.

The Application of the hollow body model was extended to solve the unsteady oscillatory flow in heave motion of a monohull semi-displacement vessel with high forward speed. The sharp drop in the distribution of vertical added mass and damping coefficients close to the ventilated transom stern due to atmospheric pressure was captured by the present 3D method. The previous 2D+t solutions, despite better estimations along the vessel, can not capture this effect due to the nature of the numerical solution (e.g. Sun and Faltinsen (2011)).

The importance of cross-flow drag on a plate with drift angle was discussed. The wave-making and viscous force in the transverse plane were separated in analogy to the Froude hypothesis. The force due to cross-flow separation was then considered by a 2D+t cross-flow drag with a rigid free-surface boundary condition. Comparisons with experimental data suggested that the free-surface and bottom-tip vortex interactions could be neglected up to a relatively high Froude number ($Fn = 1$). Moreover, the cross-flow separation resulted in a considerable increase in the non-dimensional transverse force which did not vary with Froude number. The influence of the draft and taper angles were calculated and discussed.

The hydrodynamic coefficients of an advancing surface-piercing flat plate in

sway, roll, and yaw were calculated. The generated vorticity from the trailing edge due to flow-separation was convected into the flow on a linearized vortex sheet. The influence of this vortex field was found to be important. The dependency of the coefficients on Froude number and oscillation frequency was investigated. It was confirmed that, while the coefficients were frequency dependent at lower Froude numbers, they were independent of frequency at higher speeds. The cross-flow drag seemed to be important especially at lower oscillations frequencies and Froude numbers, while its relative importance was reduced at higher frequencies and Froude numbers.

A dynamic stability analysis for a selected semi-displacement vessel in sway-yaw and sway-roll-yaw was presented. The hydrodynamics of a monohull semi-displacement vessel were simplified to a flat plate. The analysis for sway-roll-yaw suggested a possible dynamic instability about a Froude number which was close to the observed instability in experiments, and could not be captured by sway-yaw analysis. Based on an independent sensitivity study of the relevant parameters, the free-system's response frequencies and instability were sensitive to the added mass and damping coefficients (especially the cross coupling terms between sway-roll and yaw-roll in sway-roll-yaw analysis). Variation of the longitudinal position of center of gravity confirmed that moving the center of gravity forward improves the system's dynamic stability. The sensitivity study on \overline{KM} in sway-roll-yaw analysis did not show that the dynamic instability in sway-yaw is sensitive to the value of \overline{GM} , as long as it is positive. This maybe due to the simplification in the hydrodynamics from a semi-displacement vessel to a flat plate. On the other hand, increasing \overline{GM} by decreasing \overline{KG} introduced a dynamic instability region where the unstable roots belonged to a system with low frequency. The root's imaginary parts are, however, close to the free-system's roll frequencies, which are much higher. This suggested a possible low-frequency or non-oscillatory instability in sway-yaw, which is induced by the roll motion of a stiff system. This instability was sensitive to the cross coupling hydrodynamic coefficients in yaw-roll and sway-roll. The dependency of the hydrodynamic coefficients in sway and yaw on the quasi-steady heel angle should be considered and investigated as well.

Chapter 2

Mathematical Formulation

The problem of a rigid body moving in water and piercing the free-surface is formulated in this chapter. The chapter starts by defining the problem's coordinate systems in Section 2.1. The potential-flow theory is used to form the governing equations in Section 2.2. Then the boundary value problem is constructed by presenting the fully non-linear boundary conditions in Section 2.3. The problem is linearized about a base steady velocity potential, assuming steady forward motion and small oscillations. Two types of the base velocity potentials, Double Body (DB) and Neumann-Kelvin (NK), are presented in Section 2.5 and Section 2.6, respectively. The initial value problem for the time dependent and the steady-state formulation are presented in Section 2.7.

The influence of flow separation is discussed in Section 2.10, followed by modifications and extensions to account for flow separation in the present potential-flow formulation. Equations of motion for a rigid six-degrees of freedom vessel is presented in Section 2.8. The calculation of the first and second order forces and moments from the first order velocity-potential is discussed in Section 2.9. Further, the representation of the time dependent forces and moments in terms of the linear added mass and damping terms is discussed. The boundary value problem is reformed by means of Green's second identity into boundary integral formulation in Section 2.11.

2.1 Coordinate systems

A vessel advancing with mean forward speed U in negative X direction is considered (Figure 2.1). The vessel's body is assumed to be rigid. It is possible to decompose the motions of this rigid body into two parts. One is the mean forward translation by velocity $-U$, and the other is the oscillatory motions in six degrees of freedom about the vessel's mean position.

It is convenient to define different coordinate systems to handle different aspects of the problem. Two Cartesian coordinate systems $OXYZ$ and $Oxyz$ are defined. The XY plane of the Earth-fixed global coordinate system $OXYZ$ corresponds to the undisturbed free surface. The local inertial coordinate system $Oxyz$ is parallel

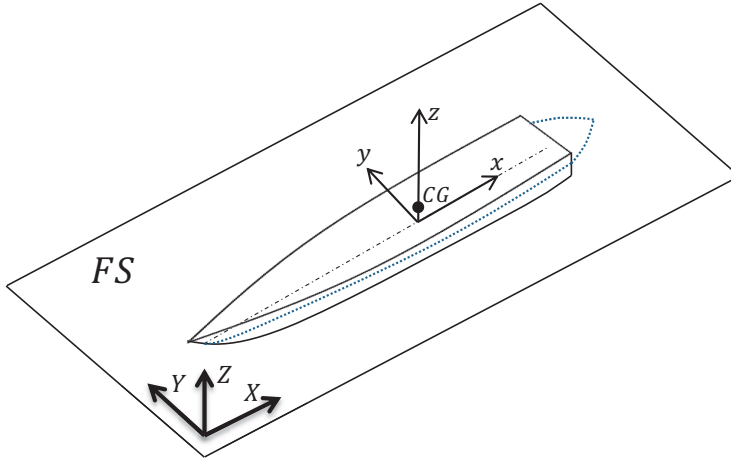


Figure 2.1: Coordinate systems for a semi-displacement vessel with forward speed, FS: free-surface, CG: center of gravity, Dotted line: waterline

to the $OXYZ$ coordinate system and moves with the vessel's forward speed. The z -axis of the $Oxyz$ system is going through the vessel's center of gravity while the vessel is in equilibrium condition with steady forward velocity. This coordinate system is the so-called *seakeeping* coordinate system. The motions of the vessel in this coordinate system are assumed to be periodic with small amplitude. The time dependent problem of a vessel advancing with forward speed changes into a steady-state problem in the seakeeping coordinate system. Therefore, the boundary value problem is formulated in this coordinate system.

Conventionally, the components of the translational motions along x , y and z -axis are called *surge*, *sway* and *heave*. The rotational motions about the same axes are called *roll*, *pitch* and *yaw*. To show the differences between oscillatory rotational motions and constant mean angles different names are usually used for the latter. The constant angles about x , y and z -axis are called *heel*, *trim* and *drift* respectively. Loading conditions and hydrodynamic forces during maneuvering may give a vessel heel, trim or drift angle. The draft of the vessel may also change in different operating conditions due to hydrodynamic forces. This type of constant translation along z -axis is called *sinkage*, in order to distinguish it from the oscillatory heave motion.

A third body-fixed coordinate system $Ox'y'z'$ is defined. This coordinate system is identical to the seakeeping coordinate system ($Oxyz$) in an steady forward equilibrium condition, however it moves with the vessel's oscillatory motions. It is convenient to express the body boundary condition in this coordinate system. As it will be shown later in Section 2.4, linearization may eliminate the need for this coordinate system. For a vessel at rest, the boundary value problem formulated in $Oxyz$ coordinate system is valid just by setting the body's forward speed equal to zero ($U=0$).

2.2 Governing equations

The motion of the fluid particles in the real water is primarily governed by two main forces, inertial and viscous. The Reynolds number is defined as the ratio between these two components.

$$Rn = \frac{\rho UL}{\mu} \quad (2.1)$$

Here, ρ is the fluid density, U is the fluid velocity, L is the characteristic length, and μ is the fluid's dynamic viscosity. For higher Reynolds numbers the importance of viscous forces reduces comparing to inertial forces in a non-separated boundary layer. As a consequence the viscous boundary layer becomes thinner by increasing the Froude number (e.g. Faltinsen (2005)). Therefore, for high Reynolds numbers irrotational-flow can be assumed outside the thin boundary layer.

A separated flow can carry the vorticity, generated in the boundary layer, into the fluid. The flow always separates from sharp corners. In presence of negative pressure gradient flow separation may also occur on smooth surfaces. The Reynolds number determine the flow regime, which plays an important role on where and when the flow separates from smooth surfaces. The separated flow carries a free shear layer, which contains vorticity, inside the fluid. The structure and thickness of the free shear layer depend on Reynolds number as well. The irrotational-flow is the basic assumption in the potential-flow theory. However, presence of vorticity in the fluid contradicts with this assumption. If a thin free shear layer is assumed, it is possible to say that the flow-irrotationality is still valid outside this thin layer.

For the present studies, the water can be assumed incompressible. This is not true for problems such as slamming, which involves high impact pressures (e.g. Faltinsen (1990)). Let us define the velocities of the fluid particles by $\mathbf{u}(\mathbf{x}, t) = (u, v, w)$, which is a function of location $\mathbf{x} = (x, y, z)$ and time (t). Assuming the fluid to be inviscid, and the flow to be irrotational ($\nabla \times \mathbf{u} = 0$), the fluid velocities can be defined as a gradient of a total velocity potential $\Phi(\mathbf{x}, t)$ (Eq. 2.2).

$$\mathbf{u} = \nabla\Phi = \mathbf{i}\frac{\partial\Phi}{\partial x} + \mathbf{j}\frac{\partial\Phi}{\partial y} + \mathbf{k}\frac{\partial\Phi}{\partial z} \quad (2.2)$$

Assuming the fluid to be incompressible as well ($\nabla \cdot \mathbf{u} = 0$), Φ must also satisfy the Laplace equation Eq. 2.3 in the water domain.

$$\nabla^2\Phi = \frac{\partial^2\Phi}{\partial x^2} + \frac{\partial^2\Phi}{\partial y^2} + \frac{\partial^2\Phi}{\partial z^2} = 0 \quad (2.3)$$

The pressure in the fluid is expressed by the Bernoulli equation. By using the total velocity potential function Φ and Eq. (2.2), the total pressure in the water domain can be defined as,

$$P_{tot} = -\rho\frac{\partial\Phi}{\partial t} - \frac{1}{2}\rho(\nabla\Phi \cdot \nabla\Phi) - \rho gz + C \quad (2.4)$$

Here g is the gravitational acceleration and C is a constant calculated from the pressure on the free surface. Viewing the problem from the seakeeping coordinate

system, the forward speed of the vessel appears as a constant inflow from infinity. Therefore, the total velocity potential far away from the body is equal to Ux , when $-U$ is the vessel's constant forward velocity. Rewriting Eq. (2.4) for a point on the free surface far away from the body we obtain,

$$C = p_a + \frac{1}{2}\rho U^2 \quad (2.5)$$

Here p_a is the value of the pressure on the free surface, which is assumed to be a constant. By substituting Eq. (2.5) into Eq. (2.4) the relative pressure $p = P_{tot} - p_a$ is defined as,

$$p = -\rho \frac{\partial \Phi}{\partial t} - \frac{1}{2}\rho (\nabla \Phi \cdot \nabla \Phi) - \rho g z + \frac{1}{2}\rho U^2 \quad (2.6)$$

Hereafter the relative pressure in Eq. (2.6) is referred to as pressure for convenience.

2.3 Boundary conditions

In order to complete the boundary value problem, conditions must be established along the boundaries of the potential flow domain. The initial form of these boundary conditions are presented here. Then the linearization techniques are discussed in Section 2.4.

Free-surface boundary condition

The free-surface boundary condition consists of two parts, *kinematic* and *dynamic*. The kinematic condition states that, the fluid particles on the free surface must stay on the free surface. Therefore, the velocity of the fluid particles normal to the free surface is equal to the velocity of the boundary itself. Assuming the free-surface elevation to be a single-valued function of the horizontal coordinates (x, y) and time $\zeta(x, y, t)$, the free surface can be described as $\zeta(x, y, t) - z = 0$. Then, the kinematic boundary condition can be written using the material derivative $(\frac{\partial}{\partial t} + \mathbf{u} \cdot \nabla)(\zeta(x, y, t) - z) = 0$ or,

$$\frac{\partial \zeta}{\partial t} + \frac{\partial \Phi}{\partial x} \frac{\partial \zeta}{\partial x} + \frac{\partial \Phi}{\partial y} \frac{\partial \zeta}{\partial y} - \frac{\partial \Phi}{\partial z} = 0 \text{ on } z = \zeta(x, y, t) \quad (2.7)$$

It must be mentioned that assuming the free surface to be a single-valued function imposes some limitations on the method's applicability. For instance, it would not be possible to model over-turning waves.

The dynamic condition deals with the pressure on the free surface. On the free surface, the relative pressure in Eq. (2.6) is zero and therefore Eq. (2.6) transforms into Eq. (2.8), which is the dynamic free-surface boundary condition.

$$\zeta = -\frac{1}{g} \left(\frac{\partial \Phi}{\partial t} + \frac{1}{2} (\nabla \Phi \cdot \nabla \Phi) - \frac{1}{2} U^2 \right) = 0 \text{ on } z = \zeta(x, y, t) \quad (2.8)$$

The two free-surface boundary conditions can be combined to eliminate ζ . The resulting combined equation is shown in Eq. (2.9) below. Here the differentiations with respect to different variables are shown by subscripts for clarity.

$$\Phi_{tt} + 2\nabla\Phi \cdot \nabla\Phi_t + \frac{1}{2}\nabla\Phi \cdot \nabla(\nabla\Phi \cdot \nabla\Phi) + g\Phi_z = 0 \text{ on } z = \zeta(x, y, t) \quad (2.9)$$

Difficulties arise in satisfying Eq. (2.9) on the free surface due to nonlinearities. In addition, the position of the boundary is not known beforehand. Iterative methods shall be used to capture the position of the boundary. These methods usually apply the free surface boundary condition in two steps using Eqs. (2.7) and (2.8). Alternatively, mixed Eulerian-Lagrangian method (MEL) can be used (e.g. Mei et al. (2005)). Different linearization methods can be used to effectively simplify the problem. These are explained later in Section 2.4.

Body boundary condition

The body boundary condition states that the flow cannot penetrate the solid body surface. Let us define the surface of the body as $S_B(\mathbf{x}', t) = 0$ in the body fixed coordinate system. Therefore, similar to free-surface kinematic boundary condition, the condition on the body can be defined as the material derivative of the surface.

$$\frac{DS_B}{Dt} = \left(\frac{\partial}{\partial t} + \nabla\Phi \cdot \nabla \right) S_B = 0 \quad (2.10)$$

Here $\nabla = (\frac{\partial}{\partial x}, \frac{\partial}{\partial y}, \frac{\partial}{\partial z})$ is the gradient vector in the seakeeping coordinate system. Alternatively, the velocity of the fluid normal to the body surface is equal to the velocity of the body's surface in that direction (Eq. 2.11).

$$\frac{\partial\Phi(\mathbf{x}, t)}{\partial\mathbf{n}} = \mathbf{U}_B \cdot \mathbf{n} \quad \text{where } \mathbf{x} \text{ on } S_B \quad (2.11)$$

Here \mathbf{U}_B is the velocity of a point on the body surface and \mathbf{n} is the normal vector to the body surface which points inside the fluid domain. Eq. (2.11) can be obtained from Eq. (2.10) using $\mathbf{n} = \nabla S_B / |\nabla S_B|$ and $\mathbf{U}_B = \frac{\partial S_B}{\partial t}$.

Bottom boundary condition

Infinite water depth is assumed in the present work. Therefore, the bottom boundary condition is simplified as shown in Eq. (2.12). The infinite water depth condition states that the disturbances caused by a body approaches zero far away from the body.

$$|\nabla\Phi - U| \rightarrow 0 \quad \text{as } z \rightarrow -\infty \quad (2.12)$$

Initial and radiation conditions

If the time-domain solution is considered, *initial* conditions must be defined for the boundaries. The initial elevation and velocity potential must be defined on the free

surface. However, in a steady-state solution, the initial condition is replaced by a *radiation* condition, which ensures solution's uniqueness. This condition is discussed with more details in Section 2.7. The numerical considerations for imposing the radiation boundary condition are presented in Section 3.7.

2.4 Linearization around a steady base flow

The fully non-linear problem is difficult to handle. Therefore linearization methods are widely used to simplify the problem. Here, we start the linearization process using the method presented by (Newman, 1978). In this method, the total velocity potential (Φ) is divided into a base steady velocity potential ($\bar{\phi}$) and a perturbation velocity potential (ϕ),

$$\Phi(\mathbf{x}, t) = \bar{\phi}(\mathbf{x}) + \phi(\mathbf{x}, t) \quad (2.13)$$

By assuming the base velocity potential to be of $O(1)$ and the perturbation velocity potential of $O(\epsilon)$, it is possible to linearize the equations about the base potential.

2.4.1 Free surface

If the total velocity potential in the combined free-surface boundary condition (Eq. 2.9) is substituted from Eq. (2.13), the resulting boundary condition after linearization will be,

$$\begin{aligned} \phi_{tt} + 2\nabla\bar{\phi} \cdot \nabla\phi_t + \nabla\bar{\phi} \cdot \nabla(\nabla\bar{\phi} \cdot \nabla\phi) + \frac{1}{2}\nabla(\nabla\bar{\phi} \cdot \nabla\bar{\phi}) \cdot \nabla\phi + \\ g\phi_z + g\bar{\phi}_z + \frac{1}{2}\nabla(\nabla\bar{\phi} \cdot \nabla\bar{\phi}) \cdot \nabla\bar{\phi} = 0 \quad \text{on } z = \zeta \end{aligned} \quad (2.14)$$

which is valid on the exact free surface $z = \zeta$. From Eq. (2.8), the free-surface elevation function ζ is calculated using the same substitution and shown in Eq. (2.15).

$$\zeta = \bar{\zeta} - \frac{1}{g}(\phi_t + \nabla\bar{\phi} \cdot \nabla\phi) \quad \text{on } z = \zeta \quad (2.15)$$

Here $\bar{\zeta}$ is the base free-surface elevation, which is the free-surface elevation due to the base velocity potential $\bar{\phi}$ (Eq. 2.16), and hereafter is called *base free-surface elevation*.

$$\bar{\zeta} = -\frac{1}{2g}(\nabla\bar{\phi} - U^2) \quad \text{on } z = \zeta \quad (2.16)$$

Getting the Taylor expansion of Eq. (2.15) about $\bar{\zeta}$ gives,

$$\begin{aligned} \zeta = \bar{\zeta} - \frac{1}{g}(\phi_t + \nabla\bar{\phi} \cdot \nabla\phi)_{z=\bar{\zeta}} + \\ (\zeta - \bar{\zeta})\frac{\partial}{\partial z} \left(\bar{\zeta} - \frac{1}{g}(\phi_t + \nabla\bar{\phi} \cdot \nabla\phi) \right)_{z=\bar{\zeta}} + \dots \end{aligned} \quad (2.17)$$

Here, subscript $z = \bar{\zeta}$ means that the expression inside the parentheses must be calculated at $\bar{\zeta}$. Keeping the terms up to $O(\phi)$ gives,

$$\zeta = \bar{\zeta} - \frac{1}{g} (\phi_t + \nabla \bar{\phi} \cdot \nabla \phi)_{z=\bar{\zeta}} - \frac{1}{g} (\zeta - \bar{\zeta}) (\nabla \bar{\phi} \cdot \nabla \bar{\phi}_z)_{z=\bar{\zeta}} \quad (2.18)$$

Solving Eq. (2.18) for ζ , an expression for the free-surface elevation as a summation of the base free-surface elevation and a perturbation free-surface elevation is obtained, as shown in Eq. (2.19) below.

$$\zeta = \bar{\zeta} - \left[\frac{\phi_t + \nabla \bar{\phi} \cdot \nabla \phi}{g + \nabla \bar{\phi} \cdot \nabla \bar{\phi}_z} \right]_{z=\bar{\zeta}} \quad (2.19)$$

Eq. (2.19) can be substituted in the kinematic free-surface boundary condition Eq. (2.7) in order to obtain a new combined condition, which is valid on $z = \bar{\zeta}$.

$$\begin{aligned} & \phi_{tt} + 2\nabla \bar{\phi} \cdot \nabla \phi_t + \nabla \bar{\phi} \cdot \nabla (\nabla \bar{\phi} \cdot \nabla \phi) + \frac{1}{2} \nabla (\nabla \bar{\phi} \cdot \nabla \bar{\phi}) \cdot \nabla \phi + g\phi_z \\ & - \left[\frac{1}{2} \frac{\partial}{\partial z} (\nabla \bar{\phi} \cdot \nabla (\nabla \bar{\phi} \cdot \nabla \bar{\phi})) + g\bar{\phi}_{zz} \right] \frac{\phi_t + \nabla \bar{\phi} \cdot \nabla \phi}{g + \nabla \bar{\phi} \cdot \nabla \bar{\phi}_z} \\ & + \frac{1}{2} \nabla (\nabla \bar{\phi} \cdot \nabla \bar{\phi}) \cdot \nabla \bar{\phi} + g\bar{\phi}_z = 0 \quad \text{on } z = \bar{\zeta} \end{aligned} \quad (2.20)$$

Assuming $\bar{\phi}$ to satisfy the free-surface condition on $\bar{\zeta}$, the last two terms of Eq. (2.20) cancel each other. In order to solve the problem by applying Eq. (2.20) on the base free-surface elevation, the problem has to be divided into two subproblems. First, is the solution of the steady base potential, which can be a simple, or complicated problem by itself. Second, is the steady or unsteady perturbation, which is assumed to be of lower order than the steady base potential. In order words, the generated waves due to vessel's steady forward motion and vessel's amplitude of oscillations have to be small for this formulation to be correct.

Different assumptions can be made about the steady base potential. The fully nonlinear steady velocity potential gives the most complete form of solution. However, the fully nonlinear solution of a vessel with steady forward speed is a complicated problem. Bunnik (1999) applied Eq. (2.20) on the base free-surface elevation using the solution provided by Raven (1996). Two other relatively simple and widely used choices are the Double-Body and Neumann-Kelvin linearizations, which are discussed in Sections 2.5 and 2.6. Using these simple base potentials, Eq. (2.20) can be further simplified and written about the mean free surface $z = 0$.

2.4.2 Body

Let us define the velocity of a ship's surface, moving forward with small oscillatory motions as,

$$\mathbf{U}_B = -U\mathbf{i} + \frac{d\boldsymbol{\delta}}{dt} \quad (2.21)$$

Here $\bar{\boldsymbol{\delta}}$ is the local displacement vector of the ship's surface in the seakeeping coordinate system ($Oxyz$), and \mathbf{i} is the unit vector in the x -direction. Since the motions are assumed to be small oscillatory motions, they can be written as,

$$\bar{\boldsymbol{\delta}} = \boldsymbol{\eta} + \boldsymbol{\Theta} \times \mathbf{x}' \quad (2.22)$$

Here $\boldsymbol{\eta}$ and $\boldsymbol{\Theta}$ are the vectors for translational and rotational motions of the ship, relative to the origin of the seakeeping coordinate system, and $'\times'$ represents the cross-product of the two vectors. Substituting $\bar{\Phi}$ from Eq. (2.13) into the body boundary condition in Eq. (2.11) gives,

$$\frac{\partial \phi}{\partial \mathbf{n}} = \frac{d\bar{\boldsymbol{\delta}}}{dt} \cdot \mathbf{n} - \nabla \bar{\phi} \cdot \mathbf{n} \quad \text{on } S_B \quad (2.23)$$

The fluid velocity on the instantaneous body-surface can be expanded about the mean surface using Taylor expansion as shown in Eq. (2.24). It must be noted that using Taylor expansion implies that the surface is assumed to be representable through an analytical function. This is not true, for instance, at sharp corners. Methods such as the one presented by Shao (2010) can be used to avoid this problem.

$$\mathbf{u}_{S_B} = \mathbf{u}_{\bar{S}_B} + [(\bar{\boldsymbol{\delta}} \cdot \nabla) \mathbf{u}]_{\bar{S}_B} + O(\bar{\boldsymbol{\delta}}^2) \quad (2.24)$$

Let us assume that the steady base velocity potential satisfies the body boundary condition, i.e. $[\mathbf{u} \cdot \mathbf{n}]_{\bar{S}_B} = [\nabla \bar{\phi} \cdot \mathbf{n}]_{\bar{S}_B} = 0$. Then, by linearizing the boundary condition about the mean position of the body (\bar{S}_B) using Eq. (2.24) we have,

$$\frac{\partial \phi}{\partial \mathbf{n}} = \left[\frac{d\bar{\boldsymbol{\delta}}}{dt} + \boldsymbol{\Theta} \times \nabla \bar{\phi} - (\bar{\boldsymbol{\delta}} \cdot \nabla) \nabla \bar{\phi} \right] \cdot \mathbf{n} \quad \text{on } \bar{S}_B, S_B \quad (2.25)$$

Since all the terms in Eq. (2.25) are of $O(|\bar{\boldsymbol{\delta}}|)$, this boundary condition can be applied both on \bar{S}_B or S_B , with the errors being of $O(|\bar{\boldsymbol{\delta}}|^2)$. Based on this linearization, there is no need to distinguish between the seakeeping (\mathbf{x}) and body-fixed (\mathbf{x}') coordinate systems any more. Detailed steps of the linearization procedure can be found in Timman and Newman (1962). They also presented a more compact form of Eq. (2.25), which accounts for the interactions between the steady and oscillatory flow field in a consistent manner (Eq. 2.26).

$$\frac{\partial \phi}{\partial \mathbf{n}} = \left[\frac{d\bar{\boldsymbol{\delta}}}{dt} + \nabla \times (\bar{\boldsymbol{\delta}} \times \nabla \bar{\phi}) \right] \cdot \mathbf{n} \quad \text{on } \bar{S}_B, S_B \quad (2.26)$$

Ogilvie and Tuck (1962) used the notations in Eq. (2.27) to rewire Eq. (2.25) in a more compact form of Eq. (2.28).

$$\begin{aligned} \boldsymbol{\eta} &= (\eta_1, \eta_2, \eta_3) \\ \boldsymbol{\Theta} &= (\eta_4, \eta_5, \eta_6) \\ \mathbf{n} &= (n_1, n_2, n_3) \\ \mathbf{x} \times \mathbf{n} &= (n_4, n_5, n_6) \\ -(\mathbf{n} \cdot \nabla) \nabla \bar{\phi} &= (m_1, m_2, m_3) \\ -(\mathbf{n} \cdot \nabla) (\mathbf{x} \times \nabla \bar{\phi}) &= (m_4, m_5, m_6) \end{aligned} \quad (2.27)$$

The interactions between the steady and unsteady flow fields are considered through the so-called m_j -terms in this notation.

$$\frac{\partial \phi}{\partial \mathbf{n}} = \sum_{j=1}^6 \left(\frac{\partial \eta_j}{\partial t} n_j + \eta_j m_j \right) \quad (2.28)$$

The importance of these terms are discussed in Nakos and Scлавounos (1990). In general, the calculations of m_j -terms are problematic from the numerical point of view. Moreover, as mentioned above, the calculation of these terms at sharp corners would be fundamentally wrong. Shao and Faltinsen (2010) proposed an alternative body-fixed calculation method to account for these terms indirectly.

2.4.3 Pressure

The fluid pressure on the body can also be linearized by substituting Eq. (2.13) into Eq. (2.6) and keeping the terms up to $O(\phi)$.

$$p^{(1)} = -\rho \frac{\partial \phi}{\partial t} - \rho (\nabla \bar{\phi} \cdot \nabla \phi) - \frac{1}{2} \rho (\nabla \bar{\phi} \cdot \nabla \bar{\phi}) - \rho g z + \frac{1}{2} \rho U^2 \quad (2.29)$$

The second-order terms in the pressure are,

$$p^{(2)} = -\frac{1}{2} \rho (\nabla \phi \cdot \nabla \phi) \quad (2.30)$$

It must be noted that since the velocity potential in Eq. (2.30) is the first-order linear potential, the second-order pressure mentioned here is the second-order pressure from the first-order potential. This is not the complete second-order pressure, which requires the boundary value problem to be formulated and solved up to the second order. Based on the linear assumptions made here, $p^{(2)}$ in Eq. (2.30) must be close to zero, otherwise the used free-surface boundary condition is not consistent. The second-order pressure calculated in this way can be used to indicate to what extent the linearization assumption is valid.

2.5 Double body linearization

One of the widely used base velocity potentials for linearization is the Double-Body velocity potential. In this method, the asymptotic solution for zero Froude number is used as the base solution, by assuming the free surface to be a symmetry plane, and $\bar{\phi}_n = 0$ on it. The term double body refers to having a mirror image of the body above the free surface. The boundary value problem for the double body velocity potential is stated in Eq. (2.31).

$$\begin{aligned} \nabla^2 \bar{\phi} &= 0 \\ \frac{\partial \bar{\phi}}{\partial n} &= 0 \quad \text{on } S_F \\ \frac{\partial \bar{\phi}}{\partial n} &= -(U\mathbf{i}) \cdot \mathbf{n} \quad \text{on } S_B \end{aligned} \quad (2.31)$$

Nakos (1990) used this type of linearization. The combined free-surface boundary condition stated in Eq. (2.20) is further linearized about the mean free surface, i.e. $z = 0$, to eliminate the need for capturing the exact steady free-surface elevation in order to solve the perturbation potential ϕ . Then, the known $\bar{\phi}$ from the solution of (2.31) is substituted into the boundary conditions in order to obtain ϕ .

This method accounts for the steady and unsteady flow interactions and it is more suitable for blunt bodies and low forward speeds (see for instance Shao and Faltinsen (2010)). At very high speeds $\bar{\phi} = 0$ is a more consistent free-surface boundary condition. Since the focus of the present work is on high-speed vessels the aforementioned method of linearization has not been implemented.

2.6 Neumann-Kelvin linearization

In this method the undisturbed inflow velocity potential is chosen as the base potential. This means that the perturbation due to presence of the body is of higher order than the inflow velocity potential. This is more suitable for slender or thin bodies at high speeds (see for instance Faltinsen (2005)). Therefore, the steady base velocity potential takes the form shown in Eq. (2.32) below.

$$\bar{\phi} = Ux \quad (2.32)$$

The mean free-surface elevation due to the steady base potential is then $\bar{\zeta} = 0$. Substituting this into Eq. (2.20), the free-surface boundary condition changes into the well-known Neumann-Kelvin condition presented below,

$$\phi_{tt} + 2U\phi_{xt} + U^2\phi_{xx} + g\phi_z = 0 \quad \text{on} \quad z = 0 \quad (2.33)$$

Both kinematic and dynamic free-surface boundary conditions after linearization are presented in Eq. (2.34) and Eq. (2.35).

$$\frac{\partial \zeta}{\partial t} + U \frac{\partial \zeta}{\partial x} - \frac{\partial \phi}{\partial z} = 0 \quad \text{on} \quad z = 0 \quad (2.34)$$

$$\zeta = -\frac{1}{g} \frac{\partial \phi}{\partial t} - \frac{U}{g} \frac{\partial \phi}{\partial x} \quad \text{on} \quad z = 0 \quad (2.35)$$

If the base velocity potential in Eq. (2.25) is substituted from Eq. (2.32), Eq. (2.36) is obtained for the body boundary condition. It must be noted that since $\bar{\phi} = Ux$ is chosen as the steady potential, $[\nabla \bar{\phi} \cdot \mathbf{n}]_{\bar{S}_B} = 0$ is no longer valid. In other words, the $\bar{\phi}$ does not satisfy the body boundary condition and can not be neglected.

$$\frac{\partial \phi}{\partial \mathbf{n}} = \left[\frac{d\delta}{dt} + (\boldsymbol{\Theta} \times \mathbf{i})U - U\mathbf{i} \right] \cdot \mathbf{n} \quad \text{on} \quad \bar{S}_B \quad (2.36)$$

This means that only $m_5 = Un_3$ and $m_6 = -Un_2$ are left from the m_j -terms, which account for the yaw and pitch angles. In other words, the interactions between the

steady and unsteady flow fields are not considered in this type of linearization. Substituting Eq. (2.32) into Eq. (2.29), the linearized form of Bernoulli's equation is obtained as follows,

$$p^{(1)} = -\rho \frac{\partial \phi}{\partial t} - \rho U \frac{\partial \phi}{\partial x} - \rho g z \quad (2.37)$$

while the second-order pressure stays the same as stated in Eq. (2.30).

2.7 Steady and unsteady problems

Until now the problem was formulated in Section 2.3 and linearized in Section 2.4. An initial or radiation condition must be specified in order to complete the boundary value problem. The perturbation velocity potential, ϕ , can be divided into steady and unsteady parts.

$$\phi(\mathbf{x}, t) = \bar{\phi}(\mathbf{x}) + \varphi(\mathbf{x}, t) \quad (2.38)$$

In Neumann-Kelvin linearization, both of these parts are of the same order. In the time-domain problem, the initial condition on the free surface is needed to solve the problem. The initial values for ϕ and free-surface elevation are usually needed to start up the solution. If the unsteady part is assumed to be harmonically oscillating, it can be rewritten as $\varphi(\mathbf{x}, t) = \bar{\varphi}(\mathbf{x})e^{i\omega t}$. Here $\bar{\varphi}$ and ω are the amplitude and oscillation frequency respectively. Substituting ϕ from Eq. (2.38) into the Neumann-Kelvin free-surface boundary condition (Eq. 2.33), the frequency-domain condition is obtained. Then, it can be separated for unsteady and steady velocity potentials, as showed in Eqs. (2.39) and (2.40) respectively.

$$-\omega^2 \bar{\varphi} + 2i\omega U \bar{\varphi}_x + U^2 \bar{\varphi}_{xx} + g \bar{\varphi}_z = 0 \quad \text{on } z = 0 \quad (2.39)$$

$$\bar{\phi}_z + \frac{U^2}{g} \bar{\phi}_{xx} = 0 \quad \text{on } z = 0 \quad (2.40)$$

The physical direction of travel for the generated waves must be enforced by means of a radiation condition. The radiation condition can be important both in time and frequency domain problems. This condition, for an oscillatory disturbance with zero forward speed, states that the generated waves must travel away from the source. For an advancing non-oscillatory disturbance in infinite water, this condition implies that there should be no upstream waves. Meaning, the waves generated by the body should only be present down-stream and not upstream. This is not the case for a body traveling in confined waters at the critical depth Froude number defined as $Fn_h = U/\sqrt{hg}$, where h is the water depth. Large upstream waves and *wash* may happen at small water depth to ship length ratios due to non-linearities of the solitary waves (e.g. Faltinsen (2005)).

For an advancing and oscillating disturbance in the free surface of an infinite water, the generated waves can appear upstream as well, if $\tau = \omega U/g < 1/4$. Here, $\tau_c = 1/4$ is the critical value. At this critical value, the generated waves due to disturbance's oscillations travel with the same speed as the disturbance itself. As a consequence, wave build-up occurs at this ratio.

2.8 Equations of motion

Equations of motion for a six degrees of freedom vessel at sea are briefly presented here. These equations are used to create the vessel's dynamic model, which is used later for dynamic stability analysis. A more detailed formulation can be found in Faltinsen (2005) and Fossen (1994), among others. Here, a simplified version of the equations, suitable for the application in the present work, is presented.

The forces which are acting on a vessel at sea are from different natures. For a ship at rest, and in its equilibrium condition, buoyancy and weight forces are canceling each other. If the center of gravity is not correctly aligned with the center of buoyancy, the vessel may have a trim or heel angle at its equilibrium condition.

The presence of forward speed introduces new forces into the equation. The ship *resistance force* is the most important force component, which determines vessel's speed for a certain thrust power. The ship speed is obtained by balancing the *thrust force* and the resistance force. The thrust force is produced by the ship's propulsion system, which can be propeller, water jet or even sails. Moreover, the forward speed induced trim and sinkage affect the vessel's resistance. This is especially important for high-speed vessels.

Ship resistance can be divided into two main parts, frictional and residual resistance. The frictional resistance is usually estimated by the flat plate's frictional coefficient from ITTC formula in Eq. (2.41).

$$C_{F0} = \frac{0.075}{(\log_{10}(Rn) - 2)^2} \quad (2.41)$$

This coefficient must be modified in order to take into account the differences between the shape of a ship's hull and a flat plate. A form factor ' \mathcal{K} ' is introduced to account for the *form resistance*. The viscous pressure resistance and flow separation can be mentioned as parts of the form resistance (e.g. Faltinsen (2005)). Experimental methods are usually used to evaluate the form factor. Although it is usually assumed that the form factor is not Froude number dependent, in reality this is not entirely true. For instance, the presence of a wet transom stern can enforce the form factor to be Froude number dependent. The effective frictional resistance coefficient defined as,

$$C_F = (1 + \mathcal{K})C_{F0} \quad (2.42)$$

while the resistance force is,

$$F^{(R)} = \frac{1}{2} \rho U^2 S_W C_F \quad (2.43)$$

Here, S_W is the total wetted area of the vessel's surface. S_W at zero speed is usually used in calculations. However, the actual wetted area is changing due to the generated waves and vessel's sinkage and trim. The residual resistance is assumed to be Froude number dependent. A main part of the residual resistance is the wave making resistance defined by the wave making coefficient C_w . This

coefficient must be obtained either by experiments or from numerical calculations. It must be noted that for high-speed vessels, the far-field picture of the waves does not represent the total residual resistance due to local effects and breaking waves (e.g. Faltinsen (2005)).

The forward speed can change the equilibrium condition of a ship, especially for semi-displacement monohull vessels. Meaning that due to the hydrodynamic forces, a ship will have different equilibrium conditions at different speeds. This implies changes in trim and sinkage. Moreover, an steady heel angle caused by an off-center weight can be increased at higher Froude numbers due to loss of metacentric height (e.g. Werenskiold (1993)). These changes may cause a vessel to become unstable at higher Froude numbers (see Section 1.1 and Chapter 8 for more details).

In the present work, the equilibrium between the thrust and resistance force is assumed. For semi-displacement monohull vessels, it is important to account for the sinkage, trim and heel when establishing the equilibrium condition at forward speed. These values must be obtained either from experiments or by an iterative numerical scheme.

Environmental waves can induce mean and oscillatory forces on an advancing vessel. The added resistance due to waves is an example of the wave-induced mean forces. While the mean forces must be canceled with the trust force, the oscillatory forces cause the vessel to oscillates around its mean position. By linearization, it is possible to separate the problem into the so called *radiation* and *diffraction*. The radiation problem focuses on the forces acting on an advancing vessel in calm water undergoing forced oscillatory motions. The diffraction problem, on the other hand, considers the forces acting on the vessel due to incoming waves, when the vessel is restrained from oscillating. For creating a dynamic model to be used in linear dynamic stability analysis, the radiation problem must be solved.

The forces acting on the vessel in the seakeeping coordinate system can be decomposed using linear theory as shown in Eq. (2.44) below.

$$\mathbf{F} = \mathbf{F}^{(rad)} + \mathbf{F}^{(dif)} + \mathbf{F}^{(R)} + \mathbf{F}^{(T)} + \mathbf{F}^{(C)} \quad (2.44)$$

Here $\mathbf{F}^{(rad)}$ and $\mathbf{F}^{(dif)}$ are the radiation and diffraction forces. $\mathbf{F}^{(R)}$ and $\mathbf{F}^{(T)}$ are the resistance and thrust forces respectively, and $\mathbf{F}^{(C)}$ is the control forces induced by the rudder or other control equipment. Based on linear theory, the forces in the radiation problem can be divided into *added mass* (A_{jk}), *damping* (B_{jk}) and *restoring* (C_{jk}) terms as showed in Eq. (2.45) below.

$$-A_{jk} \frac{d^2 \eta_k}{dt^2} - B_{jk} \frac{d \eta_k}{dt} - C_{jk} \eta_k = F_j^{(rad)} \quad (2.45)$$

The added mass and damping terms are defined as "*steady-state hydrodynamic forces and moments due to forced harmonic motion of a rigid body*" (Faltinsen, 1990). The restoring terms are associated with the forces and moments about the center of gravity due to hydrostatic pressure. This is in analogy with the spring stiffness in a mass-spring-damper system. It must be noted that restoring terms can be associated with the hydrodynamic pressure as well. However, added mass coefficients can also be used to represent these terms. Here, all the forces related to

hydrodynamic pressure are represented in terms of the added mass and damping coefficients, and restoring terms are only used to represent the hydrostatic restoring terms.

Let us assume an equilibrium between the resistance and thrust force and neglect the control forces. Then for a vessel moving with a constant forward speed we can write,

$$\sum_{k=1}^6 (M_{jk} + A_{jk}) \frac{d^2 \eta_k}{dt^2} + B_{jk} \frac{d\eta_k}{dt} + C_{jk} \eta_k = F_j^{(dif)} \quad (2.46)$$

Here M_{jk} is the generalized mass matrix (Eq. 2.47). Since the origin of the sea-keeping coordinate system is not at the center of gravity, the mass vector was generalized to include the moments due to the gravitational force at the center of gravity. By choosing the z -axis of the seakeeping coordinate system to go through the center of gravity at the equilibrium condition of the vessel with steady forward motion, the generalized mass matrix simplifies to,

$$M_{jk} = \begin{bmatrix} M & 0 & 0 & 0 & Mz_G & 0 \\ 0 & M & 0 & -Mz_G & 0 & 0 \\ 0 & 0 & M & 0 & 0 & 0 \\ 0 & -Mz_G & 0 & I_{44} & 0 & I_{46} \\ Mz_G & 0 & 0 & 0 & I_{55} & 0 \\ 0 & 0 & 0 & -I_{46} & 0 & I_{66} \end{bmatrix} \quad (2.47)$$

Here M is the vessel's mass, and z_G is the vertical position of the center of gravity in the $Oxyz$ coordinate system. I_{jj} and I_{kj} are the moment and product of inertia in the same coordinate system defined as,

$$\begin{aligned} I_{44} &= \iiint_{\Omega} (y^2 + z^2) dm & I_{55} &= \iiint_{\Omega} (x^2 + z^2) dm \\ I_{66} &= \iiint_{\Omega} (x^2 + y^2) dm & I_{46} &= \iiint_{\Omega} (xz) dm \end{aligned} \quad (2.48)$$

Here Ω refers to the complete volume of the vessel, and dm is the mass of an infinitesimal volume at (x, y, z) . The main part of the restoring force is associated with the change in the magnitude and center of the buoyancy force due to oscillations of the vessel. It is possible to relate this change to the vessel's water plane area (A_W) and the total displacement volume (∇) as shown in Eq. (2.49) below

(Faltinsen, 1990).

$$\begin{aligned}
 C_{33} &= \rho g A_W \\
 C_{35} = C_{53} &= -\rho g \iint_{A_W} x \, ds \\
 C_{44} &= \rho g \nabla (z_B - z_G) + \rho g \iint_{A_W} y^2 \, ds = \rho g \nabla \overline{GM} \\
 C_{55} &= \rho g \nabla (z_B - z_G) + \rho g \iint_{A_W} x^2 \, ds = \rho g \nabla \overline{GM}_L
 \end{aligned} \tag{2.49}$$

Here z_G and z_B are the vertical positions of the center of gravity and the center of buoyancy, respectively. \overline{GM} is the transverse and \overline{GM}_L is the longitudinal metacentric height. Other terms of C_{jk} are zero for a vessel with xz -plane of symmetry. The restoring terms in Eq. (2.49) were calculated for zero forward speed condition. As mentioned before, the speed dependent restoring terms, which are related to the hydrodynamic pressure, are taken into the added mass coefficients.

The calculation of added mass and damping coefficients for a vessel with forward speed are not straight forward. Numerical and experimental methods can be adopted to calculate these values. Based on Eq. (2.45), the solution for forced harmonic motions of a body can be used for this purpose. It is convenient to use complex notation for representing a harmonic motion. Assuming that the vessel is oscillating in j th mode, with frequency ω , and amplitude $\bar{\eta}_j$, we can write the vessel's motion in complex form as $\eta_j = \bar{\eta}_j e^{i\omega t}$. Substituting η_j into Eq. (2.46) gives,

$$\sum_{k=1}^6 (-\omega^2 M_{jk} - \omega^2 A_{jk} + C_{jk} + i\omega B_{jk}) \eta_k = F_j \tag{2.50}$$

Here F_j is the excitation load, which forces the vessel to harmonically oscillate. This force can be obtained, for instance, from numerical calculations or experiments. Separating Eq. (2.50) into real and imaginary parts, the added mass and damping terms are obtained as shown in Eq. (2.51) below.

$$\begin{aligned}
 A_{jk} &= -\frac{1}{\omega^2} \left(\mathbf{Re} \left(\frac{F_j}{\eta_k} \right) + \omega^2 M_{jk} - C_{jk} \right) \\
 B_{jk} &= \frac{1}{\omega} \left(\mathbf{Im} \left(\frac{F_j}{\eta_k} \right) \right)
 \end{aligned} \tag{2.51}$$

Here $\mathbf{Re}()$ and $\mathbf{Im}()$ refers to the real and imaginary parts of the function. Let us write the force as $F_j = \bar{F}_j e^{i(\omega t + \epsilon)}$, where ϵ is the phase difference between the force and vessel's motion. Then, Eq. (2.51) reduces to Eq. (2.52) below.

$$\begin{aligned}
 A_{jk} &= -\frac{\bar{F}_j \cos(\epsilon)}{\omega^2 \bar{\eta}_k} - M_{jk} + \frac{C_{jk}}{\omega^2} \\
 B_{jk} &= \frac{\bar{F}_j \sin(\epsilon)}{\omega \bar{\eta}_k}
 \end{aligned} \tag{2.52}$$

The added mass and damping coefficients in Eq. (2.52) can be obtained from analytical solutions for a few simple geometries. Numerical methods are usually needed for practical problems. The STF strip theory method (Salvesen et al., 1970) can be used to relate the added mass and damping of a vessel with forward speed, to the values of its 2D sections. It is well-known that these values are frequency dependent and in presence of forward speed they become Froude number dependent as well (e.g. Faltinsen (1990)). Another method for solving this problem is the 2D+t method. In this approach 2D time-domain solutions are combined to form a 3D steady-state solution to the problem (see for example Faltinsen and Zhao (1991)). Here a fully 3D method is used to calculate the forces in Eq. (2.52), in order to obtain the added mass and damping. The method for calculating forces are presented in the following section, while the numerical method is addressed in Chapter 3.

2.9 Calculating forces and moments

Direct pressure integration is used in the present work to calculate the forces and moments as shown in Eq. (2.53) below.

$$\mathbf{F} = \iint_{S_B} -\mathbf{n}p \, dS \quad j = 1 \dots 6 \quad (2.53)$$

Here \mathbf{n} is the generalized normal vector defined in Eq. (2.27) and p is the pressure on the body surface defined in Eq. (2.6). Since \mathbf{x} in Eq. (2.27) is the coordinate of points based on the seakeeping coordinate system, the moments calculated here can be used in Eq. (2.46). Occasionally, it is necessary to calculate the moments around a point besides the origin of the seakeeping coordinate system. Examples of such points can be the vessel's geometrical center, or the center of gravity. This can be done by defining $\mathbf{x} = \mathbf{r} - \mathbf{r}_c$, where \mathbf{r} is the position vector of the points on the body surface, and \mathbf{r}_c is the position vector of the center for calculating the moments.

In reality, the integration must be done on the instantaneous wetted surface of the body, which includes the changes of the body's wetted surface, both due to generated waves and oscillatory motions. However, based on the explanations given in Section 2.4.2, for the linear forces, the integration can be done on the mean wetted surface of the body. The mean wetted surface is the part of the ship's surface which is below the calm water plane in the equilibrium condition.

The linear and nonlinear parts of the pressure for Neumann-Kelvin linearization are shown in Eq. (2.37) and Eq. (2.30) respectively. By substituting the pressure into Eq. (2.53), and separating the integration boundaries to the integration below

the mean water plane and from there to the actual wave elevation we have,

$$\begin{aligned} \mathbf{F} = & \iint_{\bar{S}_B} \mathbf{n} \left(\rho \frac{\partial \phi}{\partial t} + \rho U \frac{\partial \phi}{\partial x} + \frac{1}{2} \rho (\nabla \phi \cdot \nabla \phi) + \rho g z \right) dS \\ & + \int_0^\zeta \int_{wl} \mathbf{n} \left(\rho \frac{\partial \phi}{\partial t} + \rho U \frac{\partial \phi}{\partial x} + \frac{1}{2} \rho (\nabla \phi \cdot \nabla \phi) + \rho g z \right) dl dz \end{aligned} \quad (2.54)$$

Here wl stands for the mean water line curve, and \mathbf{n} is the generalized normal vector defined in Eq. (2.27). By keeping the terms up to second-order, it is possible to separate the first and second order contribution to the force as,

$$\mathbf{F}^{(1)} = \iint_{\bar{S}_B} \mathbf{n} \left(\rho \frac{\partial \phi}{\partial t} + \rho U \frac{\partial \phi}{\partial x} + \rho g z \right) dS \quad (2.55)$$

$$\mathbf{F}^{(2)} = \iint_{\bar{S}_B} \mathbf{n} \left(\frac{1}{2} \rho (\nabla \phi \cdot \nabla \phi) \right) dS + \int_{wl} \mathbf{n} \left(\frac{1}{2} \rho g \zeta^2 \right) dl \quad (2.56)$$

The second term in Eq. (2.56) is calculated by assuming small variations in the normal vector in z -direction, close to the water line, i.e. the sides of the vessel are assumed to be vertical close to the water line. It must be noted that, similar to pressure, this is not the complete second-order force, since the complete second-order force requires solution to the second-order velocity potential. Eq. (2.56) is only the second-order force calculated from the first-order velocity potential. Similar to the second-order pressure, this second-order force indicates the validity of the linear assumptions and must be close to zero.

Here, we focus again on the radiation problem. The added mass and damping coefficients can be calculated from the hydrodynamic force and moment acting on the ship going through forced harmonic oscillations using Eq. (2.51). If only the hydrodynamic part of the force is calculated, then Eq. (2.51) simplifies to Eq. (2.57) below,

$$\begin{aligned} A_{jk} &= \frac{\rho}{\omega^2} \mathbf{Re} \iint_{\bar{S}_B} n_j \frac{\frac{\partial \phi}{\partial t} + U \frac{\partial \phi}{\partial x}}{\eta_k} dS \\ B_{jk} &= -\frac{\rho}{\omega} \mathbf{Im} \iint_{\bar{S}_B} n_j \frac{\frac{\partial \phi}{\partial t} + U \frac{\partial \phi}{\partial x}}{\eta_k} dS \end{aligned} \quad (2.57)$$

Here n_j is defined in Eq. (2.27). Assuming the form $F_j^{(rad)} = \bar{F}_j^{(rad)} e^{i(\omega t + \epsilon)}$ for the hydrodynamic radiation force, it is possible to rewrite Eq. (2.57) as,

$$A_{jk} = \frac{\bar{F}_j^{(rad)} \cos(\epsilon)}{\omega^2 \bar{\eta}_k} \quad B_{jk} = -\frac{\bar{F}_j^{(rad)} \sin(\epsilon)}{\omega \bar{\eta}_k} \quad (2.58)$$

The sign difference between the radiation forces $F_j^{(rad)}$ in Eq. (2.58), and excitation force F_j in Eq. (2.52) must be noted. Eq. (2.58) shows that, by assuming the force caused by a harmonic oscillation to be a harmonic oscillatory function, the values of the added mass and damping are determined by the *amplitude* ($\bar{F}^{(rad)}$) and *phase* (ϵ) of the force. The time series of force can be represented in the frequency-domain by means of Fast Fourier transformation. If the nature of the force is a single frequency harmonic function, then the transformation will only have one dominant frequency. In this way, the phase and amplitude of the force can be captured.

2.10 Flow separation

Flow separates from sharp corners. Moreover flow may also separate from smooth surfaces in presence of a negative pressure gradient, which introduces vorticity into the fluid. Flow separation may have important effects on the fluid flow and forces acting on a body. However, it is not possible to account for the flow separation effects directly in the potential-flow theory. Based on the type and nature of the separation, different additional steps must be taken in order to introduce flow separation effects into the present potential-flow model. Three types of flow separations were considered in the present work and treated accordingly. These are trailing edge separation, transom stern separation and cross-flow separation presented in the following sections.

2.10.1 Trailing edge flow separation

The trailing edge flow separation is a well known phenomenon for hydrofoils. The flow around the tail leaves the foil body tangential to the surface. This physical constrain is known as the *Kutta* condition. Without this condition, the velocity at the trailing edge, obtained from potential-flow theory, is infinite.

Vorticity is generated in the thin boundary layer on the foil. Due to the flow separation, this vorticity is shed from the tail of the foil into the fluid, and creates a free shear layer. The free shear layer can be defined as the path of the vortices in the fluid. Since the potential-flow formulation can not account for the circulation in the flow, the vortices must be excluded from the potential-flow domain. To do so the boundaries of the potential-flow domain are going around these singularities. The circulation effect of the vortices are included into the problem through the induced velocities of a singularity distribution. Here, the method proposed by Faltinsen and Pettersen (1987) and later used by Kristiansen (2009) was used to formulate the problem. A brief formulation of the method is presented for completeness.

Figure 2.2 shows a schematic view of a 2D foil with an angle of attack, and forward speed (U), in an infinite fluid. The shear layer due to the flow separation from its tail is shown with a dashed line. There is a discontinuity in the tangential flow across the free shear layer S_V , which implies a discontinuity in ϕ . Here, + and - refer to the two sides of the free shear layer. This jump in the tangential velocity is equal to the vorticity across the free shear layer (Faltinsen, 2005). Circulation,

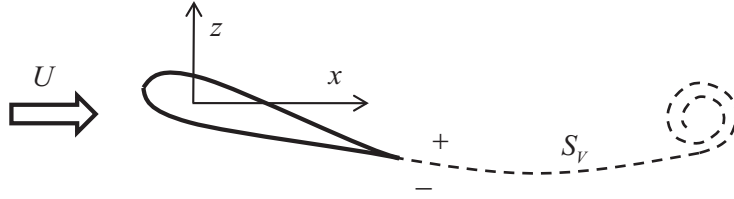


Figure 2.2: Transom stern separation coordinate system

for a mass of fluid bounded by the curve 'c', is defined as,

$$\Gamma = \oint_c \mathbf{u} \cdot d\mathbf{c} \quad (2.59)$$

Here \mathbf{u} is the fluid velocity vector, and $d\mathbf{c}$ is the tangent vector to curve 'c'. It is possible to relate circulation and vorticity, $\omega = \nabla \times \mathbf{u}$, using the Stocks theorem as shown in Eq. (2.60) below.

$$\oint_c \mathbf{u} \cdot d\mathbf{c} = \iint_{\Omega} (\nabla \times \mathbf{u}) \cdot \mathbf{n} d\mathbf{c} \quad (2.60)$$

Based on the Kelvin's theorem (Newman, 1977), in a potential-flow, the circulation is constant for a closed curve moving with the fluid. Therefore, it is possible to relate the circulation to the potential discontinuity at the trailing edge $\Gamma = \phi^+ - \phi^-$ (derivation details can be found in Faltinsen (2005)).

Let us assume the free shear layer to have an infinitesimal thickness. Therefore, the pressure on the two sides of the free shear layer must be equal $p^+ = p^-$. Using Eq. (2.6) to obtain the pressures at the two sides of the free shear layer gives,

$$\begin{aligned} \frac{\partial \phi^+}{\partial t} - \frac{\partial \phi^-}{\partial t} + \frac{1}{2} \left[\left(\frac{\partial \phi^+}{\partial x} \right)^2 - \left(\frac{\partial \phi^-}{\partial x} \right)^2 \right] + \\ \frac{1}{2} \left[\left(\frac{\partial \phi^+}{\partial y} \right)^2 - \left(\frac{\partial \phi^-}{\partial y} \right)^2 \right] + \\ \frac{1}{2} \left[\left(\frac{\partial \phi^+}{\partial z} \right)^2 - \left(\frac{\partial \phi^-}{\partial z} \right)^2 \right] = 0 \end{aligned} \quad (2.61)$$

The terms can be rearranged to obtain $\Gamma = \phi^+ - \phi^-$.

$$\begin{aligned} \frac{\partial}{\partial t} (\phi^+ - \phi^-) + \frac{1}{2} \left(\frac{\partial \phi^+}{\partial x} + \frac{\partial \phi^-}{\partial x} \right) \frac{\partial}{\partial x} (\phi^+ - \phi^-) + \\ \frac{1}{2} \left(\frac{\partial \phi^+}{\partial y} + \frac{\partial \phi^-}{\partial y} \right) \frac{\partial}{\partial y} (\phi^+ - \phi^-) + \\ \frac{1}{2} \left(\frac{\partial \phi^+}{\partial z} + \frac{\partial \phi^-}{\partial z} \right) \frac{\partial}{\partial z} (\phi^+ - \phi^-) = 0 \end{aligned} \quad (2.62)$$

which is the same as,

$$\frac{\partial \Gamma}{\partial t} + \mathbf{u}_s \cdot \nabla \Gamma = 0 \quad (2.63)$$

Here \mathbf{u}_s is the separation velocity, which is the average of the fluid velocity from the two sides of the body,

$$\begin{aligned} \mathbf{u}_s = \frac{1}{2} \left(\frac{\partial \phi^+}{\partial x} + \frac{\partial \phi^-}{\partial x} \right) \mathbf{i} + \frac{1}{2} \left(\frac{\partial \phi^+}{\partial y} + \frac{\partial \phi^-}{\partial y} \right) \mathbf{j} + \\ \frac{1}{2} \left(\frac{\partial \phi^+}{\partial z} + \frac{\partial \phi^-}{\partial z} \right) \mathbf{k} \end{aligned} \quad (2.64)$$

Eq. (2.63) states that the generated vortices leave the trailing edge by the separation velocity. As a consequence of assuming an inviscid flow, these vortices convect by the fluid flow, and do not dissipate. Conservation of vorticity in the fluid is stated mathematically using the material derivative in Eq. (2.65).

$$\frac{\partial \Gamma}{\partial t} + \mathbf{u} \cdot \nabla \Gamma = 0 \quad \text{on } S_V \quad (2.65)$$

Linearizing the shear layer can be done by assuming a flat layer, which extends only in the ambient inflow direction. It is assumed that the change in the shape of the free shear layer due to the velocities induced by the vortices are negligible. Therefore, the layer is only convected in the fluid by the ambient flow velocity U . In the seakeeping coordinate system, the ambient flow velocity is in x -direction. Therefore, Eq. (2.65) reduces to Eq. (2.66) on a linearized flat vortex sheet.

$$\frac{\partial \Gamma}{\partial t} + U \frac{\partial \Gamma}{\partial x} = 0 \quad \text{on } S_V \quad (2.66)$$

2.10.2 Transom stern flow separation

Semi-displacement monohull vessels are characterized by having a transom stern, and operating at high Froude numbers. The flow may separate from the transom stern at high Froude numbers. The separated flow may reattach to the stern. In this condition, a dead water zone is formed just behind the stern. If the transom stern Froude number is high enough, the separated flow does not reattach. This results in having a dry transom stern. The transom stern Froude number is defined

as $Fn_h = U/\sqrt{h_T g}$, where h_T is the transom stern draft shown in Figure 2.3. A transom stern is dry for $Fn_h > \sim 2.5$ (Doctors and Day, 2001). Separation from a transom stern forms a complicated problem. This is specially troublesome if the transom stern is fully or partly wet. Experimental methods are used to estimate the influence of the transom stern on the forces acting on the vessel. Solving the flow around a transom stern using numerical methods is computationally expensive (see for example Wyatt et al. (2008)).

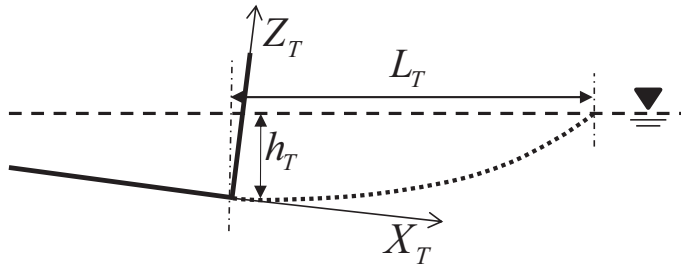


Figure 2.3: Transom stern separation coordinate system

The focus of the present work is on a dry transom stern. A widely used linearized approach to this problem is the so-called *false body* or *hollow body* method. Hollow body refers to the hollow in the free surface behind a dry transom stern. Different approaches exist in estimating the shape of the hollow body. Here the shape is constructed based on the analytical solution for a 2D potential flow in the vicinity of a dry transom stern, presented by Faltinsen (2005). In his method, the free-surface elevation behind the stern can be presented by Eq. (2.67).

$$Z_T = \frac{A_T}{U_S} X_T^{3/2} \quad (2.67)$$

Here, Z_T and X_T are the coordinates of the points in the transom stern coordinate system showed in Figure 2.3. A_T is a constant, which must be determined by numerical or empirical methods. For planning hulls, A_T can be obtained by matching the potential-flow solution in Eq. (2.67) to the empirical formulas by Savitsky (1988). For semi-displacement vessels in the present work, iterative method is used to determine this coefficient. U_S is the tangential velocity at the separation point. The linear dynamic free-surface boundary condition gives,

$$U_S = \sqrt{2gh_T + U^2} \quad (2.68)$$

A 3D shape can be constructed from this 2D line by assuming two second order polynomials as the water lines, leaving the sides of the body (Figure 2.4). The slopes of the curves at the body were determined by the slopes of the body surface. The closing point was assumed to be the point that the 2D separation line reaches the mean free surface. The surface was created by linear averaging of the three mentioned curves. Using Eq. (2.67) and Eq. (2.68), the length of the transom stern

hollow is,

$$L_T = \left(\frac{h_T}{A_T} \sqrt{2gh_T + U^2} \right)^{2/3} \quad (2.69)$$

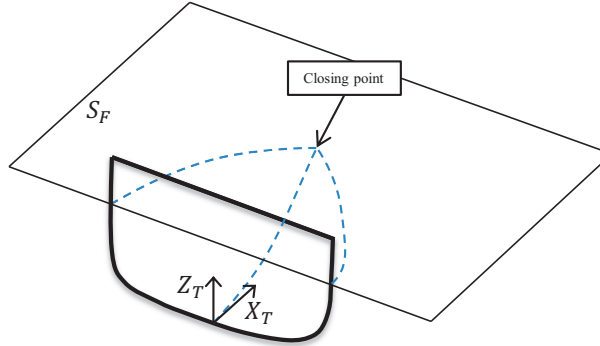


Figure 2.4: The 3D hollow behind the ship transom stern

Using this analytically made surface behind a dry transom stern, the separation from the transom stern can be treated indirectly. A false body is created and attached to the transom to represent the hollow in the free surface. The boundary condition on this *hollow body* is similar to the body boundary condition. The dynamic boundary condition is satisfied by iterative method to find the pressure as close as possible to zero. The kinematic boundary condition is satisfied by enforcing no flow through the surface. This is then similar to the body boundary condition in steady forward speed motion. Application of this boundary conditions are discussed in Section 7.2. For unsteady oscillations of the body, the hollow is not moving with the body and the boundary condition is different. Satisfying the boundary condition on this hollow surface will be discussed later with more details in Section 7.4.

2.10.3 Cross-flow separation

The viscous cross-flow separation may become important when a ship has transverse velocity or a drift angle. An oscillatory transverse velocity may also create a cross-flow separation. If the flow separation point is known, a similar method to the one described in Section 2.10.1 can be used. However, for a normal ship shaped body, it is not usually easy to determine the separation point. A full Navier-Stokes solver is needed to solve the problem completely.

Here an indirect method is used to account for the forces caused by the cross-flow separation. The method is based on a 2D+t scheme presented by Faltinsen (2005). Let us assume a ship with forward speed u , drifting with transverse velocity v . A Cartesian coordinate system $Ox_1y_1z_1$ is defined parallel to the seakeeping coordinate system (Figure 2.5). The origin of the coordinate system is at the

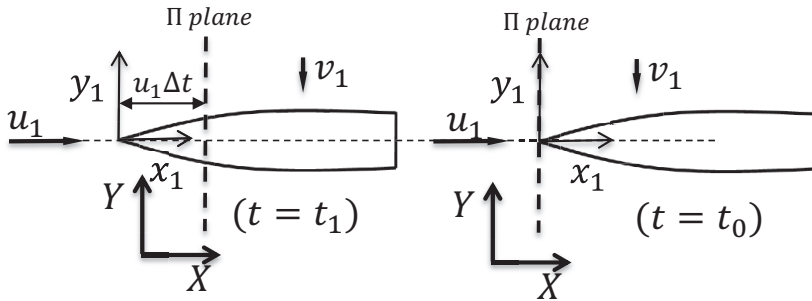


Figure 2.5: 2D+t coordinate system, $\Delta t = t_1 - t_0$

intersection of the mean free surface and the vessel's bow. From this coordinate system, the body's velocities are viewed as incoming flows, u_1 and v_1 . Flow may separate from the ship sections due to the cross flow v_1 . This generates vortices, which travel down stream due to the incoming velocity u_1 . The magnitude of the forces acting on the vessel is related to the strength of these vortices, which is higher for larger cross-flow velocities (v_1). In addition, the sections downstream of the flow feel the vortex generated by upper sections, depending on how far they are from the start point of the separation. Therefore, the force induced by vortices on a ship section also depends on the forward velocity (u_1), and the distance from the vessel's bow x_1 .

Viewing the problem from the Earth-fixed plane (Π), the steady 3D problem can be reformulated into a transient 2D problem of evolving ship sections, in a start-up transverse flow with velocity v_1 , as shown in Figure 2.6. This is the classical 2D+t formulation which is widely used in analysis of high-speed vessels (see for example Sun (2007)).

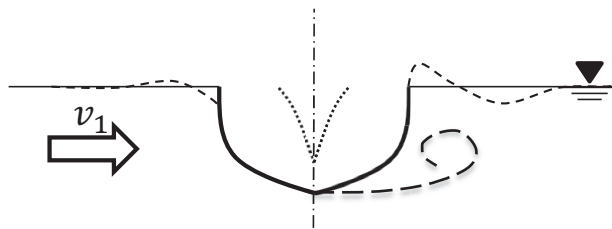


Figure 2.6: Schematic sectional view from Π -plane, solid line: ship section at $t = t_1$, dotted line: ship section at time t where $t_0 < t < t_1$, dashed line: free surface elevation and free shear layer in Π -plane

Let us simplify the problem by assuming a constant cross section, and ignore the free-surface interactions. By using a zero Froude number assumption, the free-surface boundary condition can be replaced by a zero vertical velocity condition, which is the wall boundary condition. Then, the free surface acts as a plane of

symmetry. Adding the image of the body above the free surface, the problem simplifies to a transient start up flow around a 2D section Figure 2.7. The transient drag force in start up flow on simple shapes, such as plate and circular cylinder, has been studied both experimentally and numerically.

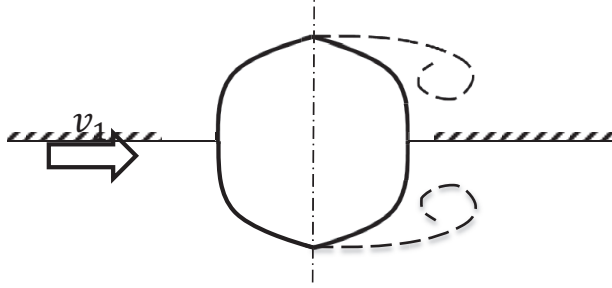


Figure 2.7: Schematic view of a ship section with its image above the free-surface in the Π -plane

Faltinsen (2005) presented a polynomial for the transient drag force on a circular cylinder based on the experimental data by Sarpkaya (1966). The transient drag force coefficient ($C_D(\mathcal{T})$) is presented against a non-dimensional time signature $\mathcal{T} = \frac{v_1 t}{L_C}$, where t is time, v_1 is the cross flow velocity, and L_C is the characteristic length of the 2D section. Using the coordinate system in Figure 2.5, we have $t = x_1/u_1$.

$$\mathcal{T} = \frac{v_1 x_1}{u_1 L_C} \quad (2.70)$$

Then, the transverse force on the vessel due to the cross-flow separation can be written as an integral of the drag forces on the sections.

$$F_{CF} = \frac{1}{2} \rho R v_1^2 \int_0^L C_D(\mathcal{T}) dx_1 \quad (2.71)$$

Here L is the water-line length of the body, ρ is the water density, and R is the section characteristic dimension. Similarly, for the yaw moment it gives,

$$M_{CF} = \frac{1}{2} \rho R v_1^2 \int_0^L C_D(\mathcal{T}) (x_c - x_1) dx_1 \quad (2.72)$$

Here x_c is the longitudinal position of the center for calculation of moment in the $x_1 y_1 z_1$ coordinate system. A similar method can be applied to other simple shapes, such as a flat plate. More details about this method is presented, together with its application, in the following chapters. A 2D Navier-Stokes solution is needed to determine the drag coefficient for other geometries. As will be discussed later, a start-up flow transient problem including the free surface and changes in the shape of the sections is required to capture the cross-flow force more accurately. However, the present simple approach gives a good estimation of the importance of the cross-flow separation.

2.11 Boundary integral formulation

The boundary value problem presented in Section 2.6 is reformulated using Green second identity into the boundary integral formulation. A brief description of the method and the theory behind it is presented here. More complete discussions on this matter can be found in many text books (for instance Newman (1977) and Faltinsen (1990)).

Let us assume two continuous functions, ϕ and G , defined in a volume Ω , bounded by a surface S . If the two functions have continuous first and second derivatives, the Green second identity states,

$$\iiint_{\Omega} (\phi \nabla^2 G - G \nabla^2 \phi) \, d\tau = \iint_S \left(G \frac{\partial \phi}{\partial n} - \phi \frac{\partial G}{\partial n} \right) \, dS \quad (2.73)$$

Assuming both functions to be harmonic, i.e. satisfy Laplace equation, Eq. (2.73) reduces to,

$$\iint_S \left(G \frac{\partial \phi}{\partial n} - \phi \frac{\partial G}{\partial n} \right) \, dS = 0 \quad (2.74)$$

Above formulation can be used to represent the boundary value problem. This representation, also known as *Boundary Integral* formulation, is helpful in reducing the solution domain from a volume to the boundary surfaces of the volume, which reduces the size of the problem. However, the computational effort needed to solve the problem is not always reduced, and sometimes it is faster to solve the problem in the volume. Different aspects of this issue are discussed in Chapter 3.

G , also known as *Green function*, can be chosen in a way to satisfy as many as boundary conditions as possible. In this way, fewer boundary conditions must be satisfied by ϕ . The simple basic choice for the Green function is the Rankine source shown in Eq. (2.75).

$$G(\mathbf{x}, \boldsymbol{\xi}) = \frac{1}{4\pi} \frac{1}{r(\mathbf{x}, \boldsymbol{\xi})} = \frac{1}{4\pi} \frac{1}{\sqrt{(\mathbf{x} - \boldsymbol{\xi}) \cdot (\mathbf{x} - \boldsymbol{\xi})}} \quad (2.75)$$

Here \mathbf{x} and $\boldsymbol{\xi}$ are the coordinates of two points, p and q , in space, and $r(\mathbf{x}, \boldsymbol{\xi})$ is the distance between the two points. Getting the derivative of the source function in Eq. (2.75) with respect to a vector \mathbf{n} , a dipole function is obtained as shown in Eq. (2.76)

$$\frac{\partial G(\mathbf{x}, \boldsymbol{\xi})}{\partial n} = \frac{1}{4\pi} \frac{\nabla(\mathbf{x} - \boldsymbol{\xi}) \cdot \mathbf{n}}{\sqrt{(\mathbf{x} - \boldsymbol{\xi}) \cdot (\mathbf{x} - \boldsymbol{\xi})}} \quad (2.76)$$

These functions satisfy Laplace equation and the faraway boundary condition. This means that all the other boundary conditions must be satisfied directly. Looking back at Eq. (2.74), the velocity potential function ϕ can be described with distribution of sources and dipoles on the boundaries.

Let us assume a single source at point \mathbf{x} inside the domain Ω as shown in Figure 2.8. The boundary of the domain must exclude this singular point from

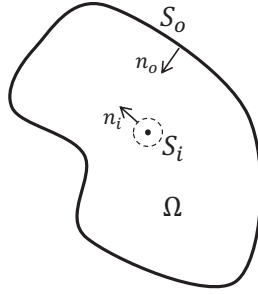


Figure 2.8: Boundary integration path and a single source in domain.

the volume. Therefore, the integration surface can be separated into two surfaces (Eq. (2.77)); S_o is the outer surface of the domain Ω and S_i is the surface of the sphere around the single source. The two normal vectors, n_o and n_i , point inside the domain.

$$\begin{aligned} & \iint_{S_o} \left(G(\mathbf{x}, \boldsymbol{\xi}) \frac{\partial \phi(\boldsymbol{\xi})}{\partial n(\boldsymbol{\xi})} - \phi(\boldsymbol{\xi}) \frac{\partial G(\mathbf{x}, \boldsymbol{\xi})}{\partial n(\boldsymbol{\xi})} \right) dS + \\ & \iint_{S_i} \left(G(\mathbf{x}, \boldsymbol{\xi}) \frac{\partial \phi(\boldsymbol{\xi})}{\partial n(\boldsymbol{\xi})} - \phi(\boldsymbol{\xi}) \frac{\partial G(\mathbf{x}, \boldsymbol{\xi})}{\partial n(\boldsymbol{\xi})} \right) dS = 0 \end{aligned} \quad (2.77)$$

Approaching the limit, by reducing the radius of the sphere around the source, the second integral in Eq. (2.77) reduces to $-4\pi\phi(\mathbf{x})$. The factor 4π , which is the area of a unit sphere, is also known as *solid angle*. Solid angle represents the area which the trajectories from the source enters the fluid domain (Mantic, 1993). Solid angle can also be defined for a point on the boundary. For a smooth boundary, the value for solid angle is always 2π . However, for sharp corners, the solid angle may varies between 4ϕ and 0. The method of calculation for solid angles on non-smooth boundaries are presented in Section 3.3.4. By replacing the second term in Eq. (2.77), the *direct boundary integral* formulation is obtained (Eq. (2.78)).

$$\mathcal{C}(\mathbf{x})\phi(\mathbf{x}) + \iint_S \left(G(\mathbf{x}, \boldsymbol{\xi}) \frac{\partial \phi(\boldsymbol{\xi})}{\partial n(\boldsymbol{\xi})} - \phi(\boldsymbol{\xi}) \frac{\partial G(\mathbf{x}, \boldsymbol{\xi})}{\partial n(\boldsymbol{\xi})} \right) dS = 0 \quad (2.78)$$

Here $\mathcal{C}(\mathbf{x})$ is solid angle at the point \mathbf{x} (Mantic, 1993).

The boundaries for two different problems are shown in Figure 2.9, which are a transverse section of a ship in free surface, and a hydrofoil advancing with angle of attack in infinite fluid. S_B and S_F refer to the surface of the body and free surface, respectively. S_V^+ and S_V^- are the two sides of the vortex sheet. S_∞ is the closing boundary at infinity, and the vectors represent the normal vectors on the boundaries. As discussed in Section 2.10.2, the hollow body behind the dry transom stern of a high speed semi-displacement vessel can also be treated as a

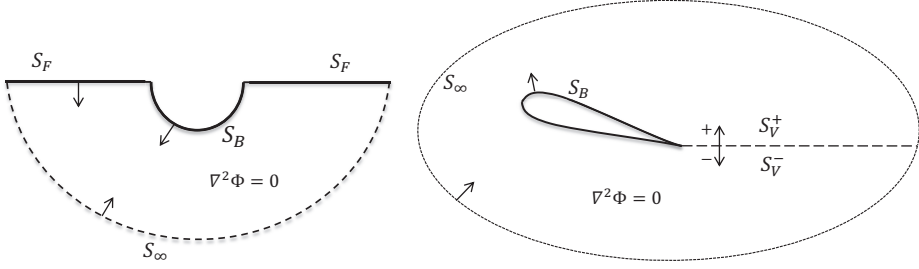


Figure 2.9: Boundaries of the domain

separate boundary (S_H). Separating Eq. (2.78) for the boundaries presented in Figure 2.9 gives,

$$\begin{aligned}
 \mathcal{C}(\mathbf{x})\phi(\mathbf{x}) &= \iint_{S_B} \phi(\boldsymbol{\xi}) \frac{\partial G(\mathbf{x}, \boldsymbol{\xi})}{\partial n(\boldsymbol{\xi})} dS - \iint_{S_B} G(\mathbf{x}, \boldsymbol{\xi}) \frac{\partial \phi(\boldsymbol{\xi})}{\partial n(\boldsymbol{\xi})} dS \\
 &+ \iint_{S_F} \phi(\boldsymbol{\xi}) \frac{\partial G(\mathbf{x}, \boldsymbol{\xi})}{\partial n(\boldsymbol{\xi})} dS - \iint_{S_F} G(\mathbf{x}, \boldsymbol{\xi}) \frac{\partial \phi(\boldsymbol{\xi})}{\partial n(\boldsymbol{\xi})} dS \\
 &+ \iint_{S_V^+} \phi^+(\boldsymbol{\xi}) \frac{\partial G(\mathbf{x}, \boldsymbol{\xi})}{\partial n(\boldsymbol{\xi})^+} dS - \iint_{S_V^+} G(\mathbf{x}, \boldsymbol{\xi}) \frac{\partial \phi^+(\boldsymbol{\xi})}{\partial n(\boldsymbol{\xi})^+} dS \\
 &+ \iint_{S_V^-} \phi^-(\boldsymbol{\xi}) \frac{\partial G(\mathbf{x}, \boldsymbol{\xi})}{\partial n(\boldsymbol{\xi})^-} dS - \iint_{S_V^-} G(\mathbf{x}, \boldsymbol{\xi}) \frac{\partial \phi^-(\boldsymbol{\xi})}{\partial n(\boldsymbol{\xi})^-} dS
 \end{aligned} \tag{2.79}$$

For a linearized vortex sheet, the integration terms in Eq. (2.79) can be simplified. As mentioned in Section 2.10.1, there is a jump in ϕ values on the two sides of the vortex sheet, while the normal velocity $\frac{\partial \phi}{\partial n}$ is continuous. Bearing in mind that $n^+ = -n^-$, it is possible to write,

$$\begin{aligned}
 &\iint_{S_V^+} \phi^+(\boldsymbol{\xi}) \frac{\partial G(\mathbf{x}, \boldsymbol{\xi})}{\partial n(\boldsymbol{\xi})^+} dS - \iint_{S_V^+} G(\mathbf{x}, \boldsymbol{\xi}) \frac{\partial \phi^+(\boldsymbol{\xi})}{\partial n(\boldsymbol{\xi})^+} dS \\
 &+ \iint_{S_V^-} \phi^-(\boldsymbol{\xi}) \frac{\partial G(\mathbf{x}, \boldsymbol{\xi})}{\partial n(\boldsymbol{\xi})^-} dS - \iint_{S_V^-} G(\mathbf{x}, \boldsymbol{\xi}) \frac{\partial \phi^-(\boldsymbol{\xi})}{\partial n(\boldsymbol{\xi})^-} dS = \\
 &\iint_{S_V^+} (\phi^+(\boldsymbol{\xi}) - \phi^-(\boldsymbol{\xi})) \frac{\partial G(\mathbf{x}, \boldsymbol{\xi})}{\partial n(\boldsymbol{\xi})^+} dS
 \end{aligned} \tag{2.80}$$

Based on Eq. (2.80), the integrals on the vortex sheet surfaces are simplified as a dipole distribution on the positive side of the vortex sheet. The dipole strength on the sheet is equal to $\Delta\phi = \phi^+ - \phi^-$ at the trailing edge, which is the circulation (Γ). Based on Eq. (2.66), the circulation propagates with the ambient flow downstream.

By substituting Eq. (2.80) into Eq. (2.79) we have,

$$\begin{aligned}
\mathcal{C}(\mathbf{x})\phi(\mathbf{x}) &= \iint_{S_B} \phi(\boldsymbol{\xi}) \frac{\partial G(\mathbf{x}, \boldsymbol{\xi})}{\partial n(\boldsymbol{\xi})} dS - \iint_{S_B} G(\mathbf{x}, \boldsymbol{\xi}) \frac{\partial \phi(\boldsymbol{\xi})}{\partial n(\boldsymbol{\xi})} dS \\
&+ \iint_{S_F} \phi(\boldsymbol{\xi}) \frac{\partial G(\mathbf{x}, \boldsymbol{\xi})}{\partial n(\boldsymbol{\xi})} dS - \iint_{S_F} G(\mathbf{x}, \boldsymbol{\xi}) \frac{\partial \phi(\boldsymbol{\xi})}{\partial n(\boldsymbol{\xi})} dS \\
&+ \iint_{S_V^+} (\phi^+(\boldsymbol{\xi}) - \phi^-(\boldsymbol{\xi})) \frac{\partial G(\mathbf{x}, \boldsymbol{\xi})}{\partial n(\boldsymbol{\xi})^+} dS
\end{aligned} \tag{2.81}$$

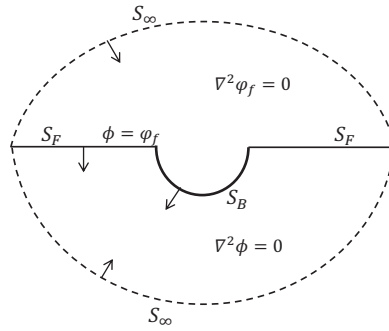


Figure 2.10: Boundaries of fictitious velocity potential φ

Another representation of the boundary integral formulation can be obtained by assuming a fictitious velocity potential φ_f , which is defined outside the water boundaries, and satisfies $\phi = \varphi_f$ on the shared boundaries, as shown in Figure 2.10. Writing Eq. (2.78) for φ_f and subtracting that from Eq. (2.78) gives,

$$\mathcal{C}(\mathbf{x})\phi(\mathbf{x}) = \iint_S \sigma(\boldsymbol{\xi}) G(\mathbf{x}, \boldsymbol{\xi}) dS \tag{2.82}$$

where $\sigma = \frac{\partial \phi}{\partial n} - \frac{\partial \varphi_f}{\partial n}$. In this formulation, known as *indirect boundary integral* or *source only* formulation, the velocity potential is described by a source distribution on the boundaries, instead of the combination of sources and dipoles. However, a dipole distribution is still needed on a vortex sheet to simulate the necessary circulation in order to capture the lifting effects. The boundary conditions can be substituted into Eq. (2.82) by getting its derivative with respect to the normal vector at the point \mathbf{x} on the boundaries, as shown in Eq. (2.83) below.

$$\mathcal{C}(\mathbf{x}) \frac{\partial \phi(\mathbf{x})}{\partial \mathbf{n}(\mathbf{x})} = \iint_S \sigma(\boldsymbol{\xi}) \frac{\partial G(\mathbf{x}, \boldsymbol{\xi})}{\partial \mathbf{n}(\mathbf{x})} dS \tag{2.83}$$

The dipole term in Eq. (2.83) is different from the dipole term in Eq. (2.78) due to the difference in their axes ($\mathbf{n}(\mathbf{x})$ and $\mathbf{n}(\boldsymbol{\xi})$). The direct boundary integral formulation is used in the present work.

Chapter 3

Numerical Implementation

The boundary value problem and its boundary conditions were presented in Chapter 2. Then, in Section 2.11, the boundary value problem was reformulated into a boundary integral formulation using the Green's second identity. Generally, an analytical solution does not exist for the boundary integral problem. Therefore, numerical methods must be adopted to solve the problem.

Boundary surfaces must be represented by elements. Moreover, on these elements, a distribution of sources and dipoles must be assumed. By doing so, the integration on the boundaries is transformed to summation of the integrals over elements. The new formulation is the so-called boundary element method (BEM). Different methods to represent the geometries and the distribution of values on surface-elements are discussed in Section 3.2, Section 3.3 and Section 3.4. For each discretization method, calculation of integrals on elements, boundary element formulation, and methods for calculating derivatives are presented. The number of elements representing the surfaces are finite. However, the free-surface boundary S_F , presented in Chapter 2, extends to infinity. Therefore, it must be truncated for numerical calculations. Consequences of truncating the free surface, and the methods to deal with them are presented in Section 3.7.

The time marching methods used for solving the initial value problem are presented in Section 3.6. Selection of a method to solve the linear equation system is discussed in Section 3.8. The grid generation process for the boundary element method is discussed in Section 3.9. Several notes regarding the programming techniques, used to develop a flexible, efficient, and reliable numerical program, are made in Section 3.10.

3.1 An overview on discretization methods

Different numerical tools could be used to solve the boundary integral equation. The collocation method was chosen for the present study. In this method the continuous equations are satisfied on a finite set of discrete points called *collocation points*. The distribution of continuous functions such as, the geometry of boundary surface (S), the velocity potential (ϕ), and the normal derivative of the velocity

potential ($\frac{\partial\phi}{\partial n}$) on the surfaces are estimated by the values of these functions at the collocation points.

The relation between an unknown function ($f(\mathbf{x})$) on a surface, and its discrete values ($f(\mathbf{x}_i)$), can be obtained using geometrical functions. These geometrical functions are often called *shape-functions*. These functions construct a continuous representation of data based on discrete values at a set of points' locations, by assuming a simple shape of a certain order. For this reason they are referred to as geometrical or shape functions.

The geometry of a boundary surface can also be represented using similar shape functions. The order and type of the shape functions, which represent a boundary surface, and the ones representing the unknown functions, are not necessarily the same. The relative importance of representation-order for surface curvature and the unknown distribution has been studied before (e.g. Hess (1979) and Hess (1990)). However, the surface curvature and the non-linearities of the problem make it difficult to draw a general conclusion on this matter. Usually, shape functions of the same order are used for representing surface geometry and unknown distribution, to keep uniformity of the equations, and reduce programming complexity. This may not be a good assumption, especially when the geometry is simple and the unknown distribution is complex. The distribution of velocity potential on a linearized flat free surface is an example.

The aforementioned numerical methods can be categorized into two main groups, low-order or constant panel method (CPM), and higher-order boundary element method (HOBEM). In the HOBEM the distribution of unknowns and the representation of surfaces are achieved by using shape functions of linear or higher order. Usually, the term HOBEM corresponds to the use of Lagrangian polynomials as the shape functions. On the other hand, B-splines and NURBS (non-uniform rational B-splines) are used to refer to higher-order methods which adopt these shape functions instead of Lagrangian polynomials. Both CPM and HOBEM methods were implemented and used in the present work. The B-spline methods were only used in numerical evaluation of the performance of the discretization scheme in Chapter 4. A brief description of the methods will be presented in the following sections.

Here the goal was not to design the most efficient and accurate solver for the boundary integral equations. The focus was more on having a flexible numerical tool which can be expanded to include newer and more complicated methods; in case the simpler ones can not provide enough accuracy to study our target problem. Therefore, simplicity of the method was the key here; and in most of the studies, the constant panel method and the linear panel method were used. However, as will be explained with more details in Section 3.10, the numerical tool was designed in a way that adopting higher order methods and faster equation solvers can be easily pursued. When ever reasonable results were obtained using simpler methods, more complicated methods were not implemented.

3.2 Constant panel method

The simplest way to discretize the boundary integral equations is constant panel method; first presented by Hess and Smith (1967) in their pioneering paper. In this method, the surface of the boundaries are approximated by plane quadrilateral panels. The properties of the surface, such as normal vector, and the unknown distribution, such as ϕ , are assumed to be constant on each panel and equal to the value at the center. For this reason, the name constant panel method (CPM) is usually used to refer to this method.

3.2.1 Representing surfaces

In order to represent the boundaries, points were distributed on the boundary surfaces. For each quadrilateral element (panel) a group of 4 points were selected. Then, the center of the four points were calculated by averaging the coordinates. The center is usually chosen to be the collocation point. Two vectors were created by connecting together two non-neighboring points. The cross product of these vectors was assumed to be parallel to the normal vector of the boundary surface. The approximate plane of the element was obtained using the center point and the calculated normal. The four original points are not necessarily in the obtained plane. Therefore the images of the points on the obtained plane were used as new coordinates for the element corners. A sample of such quadrilateral element is shown in Figure 3.1. The plus signs show the original points, which in this case are slightly different from the actual corners of the element.

A group of three points can be arranged into a triangular element. Calculating a plane from three points is straight forward. The normal vector and corners of a triangular element are identical to the original ones. The geometrical center of a triangular element is usually chosen as the collocation point. While paneling by triangular elements is easier, quadrilateral elements usually have better numerical properties. On the other hand, triangular elements could be of use in filling out spaces which otherwise result in a badly shaped quadrilateral element.

3.2.2 Boundary element formulation

Constant elements give an approximation of the boundary-surface and it's normals. Let us assume an arbitrary surface S , covered by N_E number of elements. Then, the integration on the surface can be replaced by a sum of the integrations on the surface of elements as shown in Eq. (3.1)

$$\iint_S f(\mathbf{x}) dS = \sum_{e=1}^{N_E} \iint_{\mathcal{E}_e} f(\mathbf{x}_e) dS \quad (3.1)$$

Here N_E is the total number of the elements, and $f(\mathbf{x})$ is an arbitrary function defined on the surface S . \mathcal{E}_e represents the surface of an element e . We can replace the surface integrals in Eq. (2.81) with Eq. (3.1). Since the velocity potential ϕ and the normal vector \mathbf{n} were assumed to be constant on each panel, they can be

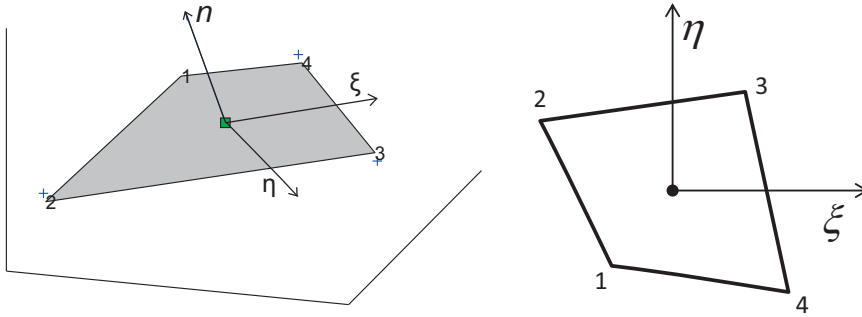


Figure 3.1: A schematic view of a 4-points quadrilateral constant element in space and its local coordinate system. Numbering of the corners are done in a way to show the correct direction for the normal vector using the right-hand-rule, +: Original points on the surface, square: Collocation points, n : Normal vector to the surface at the collocation point, (ξ, η) : Local coordinates of the element with n goes into the plane (not a right-handed coordinate system).

moved outside the integrals. The boundary element form of the equations are then obtained as follows.

$$\mathcal{C}(\mathbf{x})\phi(\mathbf{x}) = \sum_{e=1}^{N_E} \phi_e \iint_{\mathcal{E}_e} \frac{\partial G(\mathbf{x}, \boldsymbol{\xi})}{\partial n(\boldsymbol{\xi}_e)} dS - \sum_{e=1}^{N_E} \frac{\partial \phi}{\partial n} \Big|_e \iint_{\mathcal{E}_e} G(\mathbf{x}, \boldsymbol{\xi}) dS \quad (3.2)$$

Here N_E is the total number of the elements (panels), covering all the boundaries in the problem. $\mathcal{C}(\mathbf{x})$ is the solid angle at the point \mathbf{x} . The solid angle is defined as 4π times the ratio between the portion of sphere's area centered at the point \mathbf{x} , cut by the elements, and inside the fluid domain, to the whole sphere. Inside the fluid domain $\mathcal{C} = 4\pi$; while on the boundaries, for flat or smooth elements $\mathcal{C} = 2\pi$.

If we let the point \mathbf{x} approach the collocation points on the elements, a linear equation system will be obtained which can be solved for ϕ and $\frac{\partial \phi}{\partial n}$ on the boundaries. The boundary conditions are introduced into the equation system to balance the number of unknowns and equations. The collocation point is usually chosen to be at the geometrical center of the element. This point could be shifted in order to enforce certain properties on the solution, such as radiation condition (please see Section 3.2.5 and Section 3.7.1). Since the boundary conditions are explicitly satisfied at the collocation points, it is expected that the solution lose it's accuracy away from the collocation points.

Let us define the discrete set of collocation points $(\boldsymbol{\xi}_j)$ by \mathbf{q}_j and the discrete set of field points (\mathbf{x}_i) by \mathbf{p}_i . \mathbf{q}_e is also known as a *source* point. Here a *source* refers to both a source and/or a dipole. Since in this discretization method there is only one collocation point per each element the number of elements is equal to

the number of collocation points ($N_E = N_C$)

$$\sum_{j=1, j \neq i}^{N_C} \phi(\mathbf{q}_j) \mathcal{D}_{ij} - \sum_{j=1}^{N_C} \frac{\partial \phi(\mathbf{q}_j)}{\partial n(\mathbf{q}_j)} \mathcal{S}_{ij} - \mathcal{C}(\mathbf{p}_i) \phi(\mathbf{p}_i) = 0 \quad (3.3)$$

where,

$$\mathcal{D}_{ij} = \mathcal{D}_j^{(e)}(\mathbf{p}_i) = \iint_{\mathcal{E}_j} \frac{\partial G(\mathbf{p}_i, \boldsymbol{\xi})}{\partial n(\mathbf{q}_j)} dS \quad (3.4)$$

$$\mathcal{S}_{ij} = \mathcal{S}_j^{(e)}(\mathbf{p}_i) = \iint_{\mathcal{E}_j} G(\mathbf{p}_i, \boldsymbol{\xi}) dS \quad (3.5)$$

The superscript (e) was kept to emphasize that the term is related to the influence of one element. The linear equation system in Eq. (3.3) can be written in a matrix format as follows.

$$[A]_{N_C \times N_C} [\phi]_{N_C} = [B]_{N_C \times N_C} \left[\frac{\partial \phi}{\partial n} \right]_{N_C} \quad (3.6)$$

where,

$$\begin{aligned} [A]_{N_C \times N_C} &= [\mathcal{D}_{ij} - \delta_{ij} C_i]_{N_C \times N_C} \\ [B]_{N_C \times N_C} &= [\mathcal{S}_{ij}]_{N_C \times N_C} \end{aligned} \quad (3.7)$$

Here δ_{ij} is the Kronecker delta function. In other words, C_i only change the diagonal terms in the matrix of coefficients, $[A]$. Based on the type of the boundary condition, either ϕ or $\frac{\partial \phi}{\partial n}$ is known. Therefore, Eq. (3.6) can be rearranged and solved to obtain the unknown values on the boundaries.

3.2.3 Calculating integrals

The integrals in Eqs. (3.4) and (3.5) can be calculated numerically or analytically. They represent an integral of a constant distribution as a unit source or dipole on a flat element. Hess and Smith (1967) and Newman (1986) presented methods for calculating such integrals among others. The kernel of the integrals are singular close to the boundaries of an element. Therefore the collocation point must be placed away from the boundaries. The method presented in Newman (1986) was adopted in the present work to calculate the integrals. The local coordinate system of the element, which was shown in Figure 3.1, was used to formulate the integrals.

Let us assume p to be a field point with coordinate (x, y, z) , in the local coordinate system of an element. The corners of the element have the coordinates (ξ_n, η_n) where n is the corners indexes. θ_n is the polar angle of the vector from vertex n to $n + 1$ defined as, $\sin \theta_n = \frac{\eta_{n+1} - \eta_n}{s_n}$ and $\cos \theta_n = \frac{\xi_{n+1} - \xi_n}{s_n}$. s_n is the length of the side n defined as $s_n = \sqrt{(\xi_{n+1} - \xi_n)^2 + (\eta_{n+1} - \eta_n)^2}$. $\delta \eta_n = \eta_{n+1} - \eta_n$ using

a circular indexing. Similarly, $\delta\xi_n = \xi_{n+1} - \xi_n$. R_n is defined as the distance between vertex n and the point p as $R_n = \sqrt{(x - \xi_n)^2 + (y - \eta_n)^2 + z^2}$. Using above mentioned notations the integrals in Eqs. (3.4) and (3.5) can be expressed as shown in Eqs. (3.8) and (3.9) below.

$$\iint_{\mathcal{E}_j} \frac{\partial G(\mathbf{p}, \boldsymbol{\xi})}{\partial n(\mathbf{q}_j)} dS = \sum_{n=1}^4 \left[\tan^{-1} \frac{\delta\eta_n [(x - \xi_n)^2 + z^2] - \delta\xi_n (x - \xi_n)(y - \eta_n)}{R_n z \delta\xi_n} \right. \\ \left. - \tan^{-1} \frac{\delta\eta_n [(x - \xi_{n+1})^2 + z^2] - \delta\xi_n (x - \xi_{n+1})(y - \eta_{n+1})}{R_{n+1} z \delta\xi_n} \right] \quad (3.8)$$

$$\iint_{\mathcal{E}_j} G(\mathbf{p}, \boldsymbol{\xi}) dS = \sum_{n=1}^4 [(x - \xi_n) \sin \theta_n - (y - \eta_n) \cos \theta_n] \log \frac{R_n + R_{n+1} + s_n}{R_n + R_{n+1} - s_n} \\ - z \iint_{\mathcal{E}_j} \frac{\partial G(\mathbf{p}, \boldsymbol{\xi})}{\partial n(\mathbf{q}_j)} dS \quad (3.9)$$

3.2.4 Calculating derivatives

The derivatives can be calculated by differentiating the boundary element formulation in Eq. (3.10). However, as shown by Zhao and Faltinsen (1990), the accuracy of this method for calculating the velocities is decreasing by approaching the panel in direct boundary integral formulation. For indirect formulation or source-only distribution, this method is more accurate (see for instance Lee and Newman (1991)).

$$\mathcal{C}(\mathbf{x}) \frac{\partial \phi(\mathbf{x})}{\partial x} = \sum_{e=1}^{N_E} \phi_e \iint_{\mathcal{E}_e} \frac{\partial^2 G(\mathbf{x}, \boldsymbol{\xi})}{\partial x \partial n(\boldsymbol{\xi}_e)} dS - \sum_{e=1}^{N_E} \frac{\partial \phi}{\partial n} \Big|_e \iint_{\mathcal{E}_e} \frac{\partial G(\mathbf{x}, \boldsymbol{\xi})}{\partial x} dS \quad (3.10)$$

Derivatives can be obtained on the surface of the boundaries by finite difference method (FDM). This is based on the assumption that the obtained values at collocation points represent a differentiable function on the surface. Mapping technique can be used to relate an arbitrary surface in physical space to a flat surface in computational space, where the points are placed with equal spacing. Let (ξ, η, n) denotes the computational coordinate system. This system could also be seen as a curvilinear coordinate system attached to the boundary surface. Using the differentiation chain-rule we can write,

$$\begin{bmatrix} \phi_\xi \\ \phi_\eta \\ \phi_n \end{bmatrix} = \underbrace{\begin{bmatrix} x_\xi & y_\xi & z_\xi \\ x_\eta & y_\eta & z_\eta \\ n_1 & n_2 & n_3 \end{bmatrix}}_{C_M} \begin{bmatrix} \phi_x \\ \phi_y \\ \phi_z \end{bmatrix} \quad (3.11)$$

Here the subscripts show differentiation with respect to, except for n_i where they show the components of the normal vector on the surface. C_M is the mapping coefficient matrix from $(x, y, z) \mapsto (\xi, \eta, n)$. Differentiation with respect to ξ and η are

easily possible by a finite difference operator on a uniformly spaced computational plane. Since ϕ_n on the boundaries is defined using boundary conditions, the left hand side of Eq. (3.11) is known. Therefore, for calculating the right hand side we have,

$$\begin{bmatrix} \phi_x \\ \phi_y \\ \phi_z \end{bmatrix} = [C_M]^{-1} \begin{bmatrix} \phi_\xi \\ \phi_\eta \\ \phi_n \end{bmatrix} \quad (3.12)$$

A similar approach can be used to calculate the second order derivatives of ϕ on the boundaries. Using Clairaut's theorem of exchanging differentiation orders, and Laplace equation, the differentiation of velocities in three directions simplifies to the equation system shown in Eq. (3.13).

$$\begin{bmatrix} \phi_{x\xi} \\ \phi_{x\eta} \\ \phi_{y\xi} \\ \phi_{y\eta} \\ \phi_{z\xi} \end{bmatrix} = \underbrace{\begin{bmatrix} x_\xi & y_\xi & z_\xi & 0 & 0 \\ x_\eta & y_\eta & z_\eta & 0 & 0 \\ 0 & x_\xi & 0 & y_\xi & z_\xi \\ 0 & x_\eta & 0 & y_\eta & z_\eta \\ -z_\xi & 0 & x_\xi & -z_\xi & y_\xi \end{bmatrix}}_{C_M} \begin{bmatrix} \phi_{xx} \\ \phi_{xy} \\ \phi_{xz} \\ \phi_{yy} \\ \phi_{yz} \end{bmatrix} \quad (3.13)$$

Similarly the left hand side of Eq. (3.13) and the mapping coefficients can be calculated using finite difference operators. Then, the inverse of the mapping matrix is used to calculate second order derivatives. The mapping can become singular if the mapping matrix does not have an inverse. This can happen, for instance, if a line in the computational space is mapped to a point in the physical space. Singular mapping must be avoided in order to ensure an accurate calculation of the derivatives. Calculation of the higher order derivatives is problematic. Shao (2010) introduced a body-fixed coordinate system to avoid this problem. Continuation of the velocity potential outside the fluid domain is another way to increase the computational accuracy of the higher order derivatives (see Section 3.2.5).

The mapping function $((\xi, \eta, n) \mapsto (x, y, z))$ must be a one-to-one differentiable function. Then, the mapping coefficients can be obtained by a numerical grid generation method. More details on how to create such mapping functions and calculate mapping coefficients can be found in Section 3.9.

3.2.5 De-singularization and collocation shift

It is possible to separate the element (or point source) and the collocation point; and still form a linear equation system to solve. To do so, we must assume that the velocity potential function can be extended outside the fluid domain. Then the source singularity is placed outside the fluid domain, while the collocation points on the elements are kept on the boundaries, as shown in Figure 3.2. Since the singularity is removed from the boundary, this method is called *desingularized* method. Early application of this method on a linearized free surface can be found in Jensen (1987). Cao et al. (1991) showed how direct and indirect boundary integral formulations look like in a desingularized method. Without the singularity at the

boundaries it is easier to calculate the integrals in Eqs. (3.4) and (3.5). Moreover, since the velocity potential is presented as a smooth function at the collocation points, the velocities and higher order derivatives of the velocity potential can be obtained accurately using direct calculation of Eq. (3.10). Therefore, this method is widely used in the non-linear wave body interaction analysis (see for instance Beck et al. (1993)). The desingularization distance (the distance between source point and collocation point on an element) is highly important. Cao et al. (1991) studied the influence of desingularization distance and concluded that it must be linked to the mesh size in order to avoid problems with uniqueness and ill-conditioning of the equation system. Moreover, care must be taken at sharp corners and the connection of the body to the free surface. At these places, the analytical continuity of velocity potential assumption may become invalid.

Another version of this method can be obtained by placing the elements or panels outside the fluid boundaries, (for example inside the body), while keeping the collocation points on the actual boundary surface as shown in Figure 3.2. Since the panels are moved away from the boundaries, this method is called *raised panel* method. The boundary condition then can be satisfied at the collocation points, by balancing the induced velocities from a source distribution on a collocation point. Similar to the desingularized method, a continuous function is obtained for the velocity potential function at the collocation points in this way. Hughes and Bertram (1995) applied this method for the ship added resistance problem. Raven (1996) studied the influence of the distance between the panels and collocation points in a non-linear analysis of the ship's wave making resistance.

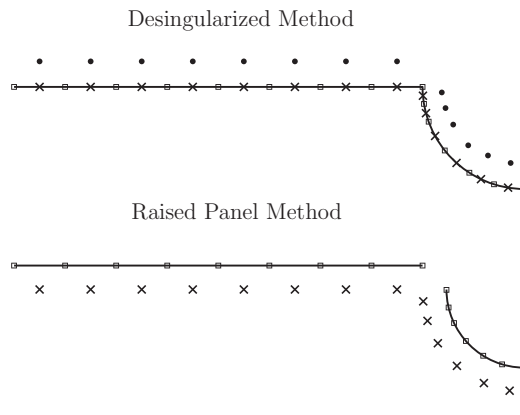


Figure 3.2: Schematic views of desingularized and raised panel methods. Half of the body section and free surface is shown. Boxes: element points, Dots: source points, Crosses: collocation points

In both desingularized and raised panel method, an additional horizontal shift may be applied to the collocation points. Jensen (1987) and Raven (1996) have used such horizontal shifts on the free surface collocation points to satisfy the radiation condition and introduce numerical damping. More details regarding the

collocation-shift is presented in Section 3.7 while the mathematical background is left for Chapter 4.

3.3 Higher-order boundary element method

Higher-order boundary element method or HOBEM is the term used when the boundary surface and the distribution of unknowns are assumed to vary over each element and not to be constant. Let us say, the constant panel method is of zero order. Then, the higher-order methods would have linear, quadratic, cubic, and possibly higher distributions. Even though using the B-splines for presenting the boundaries and the unknowns would be a higher order method, traditionally the term HOBEM is used when isoparametric interpolation functions, such as Lagrangian polynomials, are adopted. Here we will follow the same convention and leave the B-spline methods for the next section.

3.3.1 Representing surfaces

The boundary surfaces are divided into elements just like in the CPM method. However, the distribution of unknowns and the shape of the boundary are no longer assumed to be constant and flat on each element. Isoparametric interpolation functions are used to map all variables of interest into a parametric space (ξ, η) . Linear and higher-order Lagrangian polynomials (Eq. (3.14)) are used as the interpolation functions. These interpolation functions are also called *shape* functions.

$$l_i^m(\xi) = \prod_{k=1, k \neq i}^{N_P=m+1} \frac{\xi - \xi_k}{\xi_i - \xi_k} \quad (3.14)$$

Here N_N is the number of nodes and m is the order of the polynomial. Index i indicates that to which node this polynomial belongs. l_i^m gives a unit value at the node i and zero at all other nodes. Different 2D shape functions (l_i^m), for a line between $[-1, 1]$ in a parametric space coordinate ξ , are plotted in Figure 3.3. These polynomials are very popular in numerical analysis, especially in finite element method (FEM). More details about their properties can be found in text books such as Zienkiewicz et al. (2005).

For a 2D case, the Lagrangian polynomials can be used directly, as presented in Eq. (3.14), as shape functions. However, for a 3D case, combination of these polynomials along two perpendicular axes can be used to represent surface elements as shown in Eq. (3.15) below.

$$\mathcal{N}_j(\xi, \eta) = \mathcal{N}_{J,K}(\xi, \eta) = l_J^m(\xi)l_K^n(\eta) \quad (3.15)$$

For instance, the shape functions for a four-point linear element are obtained as,

$$\mathcal{N}_j(\xi, \eta) = \frac{1}{4}(1 + \xi_j\xi)(1 + \eta_j\eta) \quad (3.16)$$

The element shape in the physical and parametric space is shown in Figure 3.4. Other shape functions and element geometries can be found in Appendix A. By

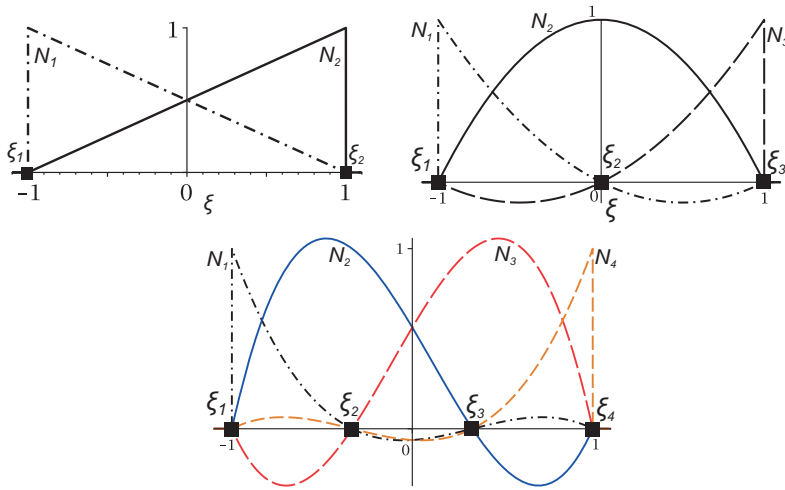


Figure 3.3: Linear, quadratic and cubic Lagrangian shape functions for a line in parametric space between $[-1,1]$. Black squares: nodes, ξ_j : node j 's coordinate, \mathcal{N}_j : node j 's shape function.

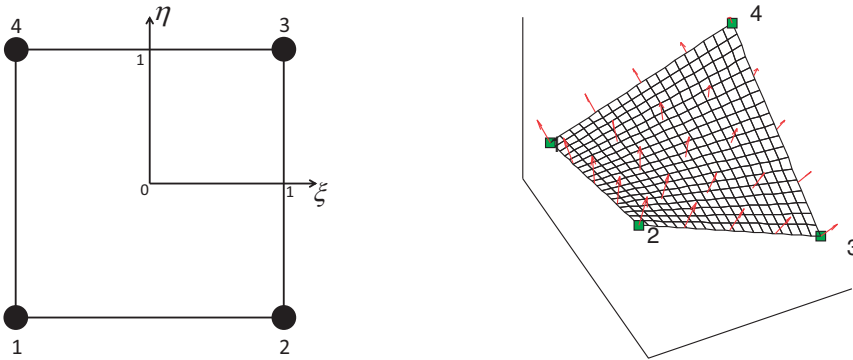


Figure 3.4: A linear element with 4 nodes in the parametric (ξ, η) and physical (x, y, z) space.

using the shape functions, the distribution of any variable on the element can be related to its values at the nodal points. The total number and position of the nodal points depend on the order of the shape function (see Appendix A). For instance, we can write the velocity potential ϕ on the surface of an element \mathcal{E} as,

$$\phi(\xi, \eta) = \sum_{j=1}^{j=N_N} \phi(\xi_j, \eta_j) \mathcal{N}_j^{(m)}(\xi, \eta) \quad (3.17)$$

Here $\mathcal{N}_j^{(m)}$ is the shape function for the node j , and m is the order of the poly-

nomial. N_N is the element's total number of nodes. Similarly, for the normal derivative of the velocity potential and the element's surface we can write,

$$\frac{\partial \phi}{\partial n}(\xi, \eta) = \sum_{j=1}^{j=N_N} \frac{\partial \phi}{\partial n}(\xi_j, \eta_j) \mathcal{N}_j^{(m)}(\xi, \eta) \quad (3.18)$$

$$\begin{aligned} x(\xi, \eta) &= \sum_{j=1}^{j=N_N} x(\xi_j, \eta_j) \mathcal{N}_j^{(m)}(\xi, \eta) \\ y(\xi, \eta) &= \sum_{j=1}^{j=N_N} y(\xi_j, \eta_j) \mathcal{N}_j^{(m)}(\xi, \eta) \\ z(\xi, \eta) &= \sum_{j=1}^{j=N_N} z(\xi_j, \eta_j) \mathcal{N}_j^{(m)}(\xi, \eta) \end{aligned} \quad (3.19)$$

By distributing a set of points on a surface (see Section 3.9) Eq. (3.19) can be used to reconstruct the surface by higher-order elements.

3.3.2 Boundary element formulation

Similar to CPM, the integrals on the surfaces can be decomposed into a summation of integrals on the elements. This means Eq. (3.1) is true in this method as well. Let us define $\mathbf{p} = (x_p, y_p, z_p)$ as field points, and $\mathbf{q} = (x, y, z)$ as source points. Since in this method, the surface normal vector and the unknown distribution are not constant on each element, we have

$$\mathcal{C}(\mathbf{p})\phi(\mathbf{p}) = \sum_{e=1}^{N_E} \iint_{\mathcal{E}_e} \phi(\mathbf{q}) \frac{\partial G(\mathbf{p}, \mathbf{q})}{\partial n(\mathbf{q})} dS - \sum_{e=1}^{N_E} \iint_{\mathcal{E}_e} \frac{\partial \phi(\mathbf{q})}{\partial n(\mathbf{q})} G(\mathbf{p}, \mathbf{q}) dS \quad (3.20)$$

The integrals on the elements can be simplified by rewriting the integral kernels in the parametric space (ξ, η) . We start by defining a vector \mathbf{r} , from the field point \mathbf{p} , to the source point \mathbf{q} on an element (\mathcal{E}) as,

$$\mathbf{r} = (x_p - x, y_p - y, z_p - z) \quad (3.21)$$

Since the source point \mathbf{q} is on the surface of the element, it can be described by the shape functions as,

$$\mathbf{r} = \left(x_p - \sum_{j=1}^{N_N} x_j \mathcal{N}_j, y_p - \sum_{j=1}^{N_N} y_j \mathcal{N}_j, z_p - \sum_{j=1}^{N_N} z_j \mathcal{N}_j \right) \quad (3.22)$$

where N_N is the total number of nodes, index j refers to the coordinate, and the shape function of the j th node of the element. The unit normal vector on the element surface is defined as,

$$\mathbf{n} = \frac{\mathbf{J}(\xi, \eta)}{|\mathbf{J}(\xi, \eta)|} \quad (3.23)$$

where, \mathbf{J} is the Jacobian vector presented below.

$$\mathbf{J}(\xi, \eta) = (J_1, J_2, J_3) = \mathbf{x}_\xi \times \mathbf{x}_\eta \quad (3.24)$$

The expressions of a source and a dipole are presented in terms of \mathbf{r} and \mathbf{n} , as a function of the parameters ξ and η in Eqs. (3.25) and (3.26), respectively.

$$G(\mathbf{p}, \mathbf{q}) = \frac{1}{|\mathbf{r}|} \quad (3.25)$$

$$\frac{\partial G(\mathbf{p}, \mathbf{q})}{\partial \mathbf{n}(\mathbf{q})} = \nabla G(\mathbf{p}, \mathbf{q}) \cdot \mathbf{n}(\mathbf{q}) = \frac{-\mathbf{r} \cdot \mathbf{n}}{|\mathbf{r}|^3} \quad (3.26)$$

By means of the Jacobian defined in Eq. (3.24), the integration domain is related to the parametric space as shown in Eq. (3.27) below.

$$dS(x, y, z) = |J(\xi, \eta)| d\xi d\eta \quad (3.27)$$

Using the aforementioned transformation, for a discrete set of field points (\mathbf{p}_i), we can write,

$$\mathcal{C}(\mathbf{p}_i)\phi(\mathbf{p}_i) = \sum_{e=1}^{N_E} \sum_{j=1}^{N_N} \phi(\mathbf{q}_j) \mathcal{D}_{ij}^{(e)} - \sum_{e=1}^{N_E} \sum_{j=1}^{N_N} \frac{\partial \phi(\mathbf{q}_j)}{\partial \mathbf{n}(\mathbf{q}_j)} \mathcal{S}_{ij}^{(e)} \quad (3.28)$$

Here, (\mathbf{q}_j) refers to the nodes of the element (e) and,

$$\mathcal{D}_{ij}^{(e)} = \mathcal{D}_j^{(e)}(\mathbf{p}_i) = \int_{-1}^1 \int_{-1}^1 \mathcal{N}_j(\xi, \eta) \frac{-\mathbf{r}(\xi, \eta; \mathbf{p}_i) \cdot \mathbf{n}(\xi, \eta)}{|\mathbf{r}(\xi, \eta; \mathbf{p}_i)|^3} |J(\xi, \eta)| d\xi d\eta \quad (3.29)$$

$$\mathcal{S}_{ij}^{(e)} = \mathcal{S}_j^{(e)}(\mathbf{p}_i) = \int_{-1}^1 \int_{-1}^1 \mathcal{N}_j(\xi, \eta) \frac{1}{|\mathbf{r}(\xi, \eta; \mathbf{p}_i)|} |J(\xi, \eta)| d\xi d\eta \quad (3.30)$$

To form an equation system, we assume that a total number of N_{TN} nodes are distributed on the boundary surfaces and grouped into N_E number of elements. If these nodes are used as collocation points then Eq. (3.28) is changed into an square system of linear equations as shown below,

$$[\mathcal{D}_{ik}]_{N_C \times N_C} [\phi_i]_{N_C \times 1} = [\mathcal{S}_{ik}]_{N_C \times N_C} \left[\left(\frac{\partial \phi}{\partial \mathbf{n}} \right)_i \right]_{N_C \times 1} \quad (3.31)$$

where,

$$\begin{aligned} \mathcal{D}_{ik} &= \sum_{e=1}^{N_E} \sum_{j=1}^{N_N} \delta_{kc} \mathcal{D}_{ij}^{(e)} - \delta_{ik} C_i \\ \mathcal{S}_{ik} &= \sum_{e=1}^{N_E} \sum_{j=1}^{N_N} \delta_{kc} \mathcal{S}_{ij}^{(e)} \end{aligned} \quad (3.32)$$

and δ_{kc} is the Kronecker function. Subscript $c(j, e; k)$ in the delta function is the *connectivity* index. When a collocation point is shared by two or more elements, the influence from these elements must be added up. To do so for a collocation point k , we need to know the elements which share this collocation point. Moreover, we need to know which element's node (j) corresponds to this collocation point. This can be achieved by matching the global index of the collocation points to the local index of the nodes on each element. Then, if node j of the element e corresponds to the collocation point k , the connectivity index is also k , and consequently the delta function calculates to 1. Otherwise it will be zero.

3.3.3 Calculating integrals

In order to form the equation system the integrals in Eqs. (3.29) and (3.30) must be calculated. These integrals are, however, singular, if the field point \mathbf{p}_i approaches the surface of the elements. The order of the integral's kernel singularity is the key in choosing the calculation method. The methods adopted here are summarized below.

Regular integrals

When the field point is away from the element, the integrals are well-behaved and can be calculated using a 2D Gauss-Legendre quadrature, as showed in Eq. (3.33) below.

$$\int_{-1}^1 \int_{-1}^1 f(\xi, \eta) d\xi d\eta = \sum_{i=1}^{N_{GP}} \sum_{j=1}^{N_{GP}} w_i w_j f(\xi_{i,j}, \eta_{i,j}) \quad (3.33)$$

Here, N_{GP} is the number of Gauss points in each direction. $(\xi_{i,j}, \eta_{i,j})$ are the control points, and w_i are the weights obtained from Legendre polynomials.

Singular integrals (self influence), direct method

In calculating the coefficients for the equation system Eq. (3.31), the integrals become singular if the field-point coincides with the source-point on an element. The integrals are in this case called *self influence* integrals. Different methods can be used to analytically reduce the order of the singularity and improve the accuracy of the numerical integration. Polar coordinate transformation from Liu and Lu (1988), and triangular mapping (also called triangle polar coordinate transformation) from Li et al. (1985) and Eatock Taylor and Chau (1992) are two widely used methods. Xü (1992) compared the two methods and concluded that they have similar accuracy. The triangular mapping technique was adopted in this study. In this method, the element in the (ξ, η) parametric space is divided into triangles, while keeping the singular node as one of the triangle's vertices. Then, the triangle in the (ξ, η) plane is mapped to a rectangle in the auxiliary parametric space (ρ_1, ρ_2) , as shown in Figure 3.5. The mapping is written mathematically in Eq. (3.34), where (ξ_i, η_i) are the coordinates of triangle vertices in $\xi\eta$ -plane.

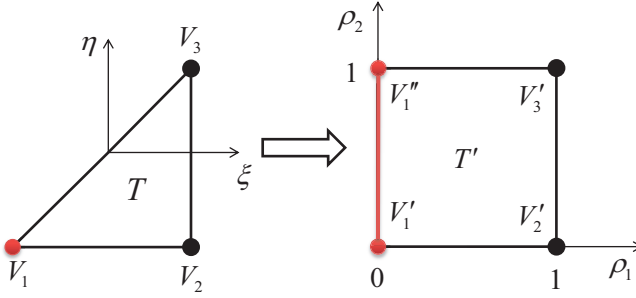


Figure 3.5: Mapping of a triangle in (ξ, η) plane to a square in (ρ_1, ρ_2) plane. $V_i = (\xi_i, \eta_i, 0)$ is a vertex of the triangle. V_1 (pole) a vertex of triangle which is mapped to a line in square. $V_i = (\xi_i, \eta_i, 0)$ are triangle vertices.

$$\begin{bmatrix} \xi \\ \eta \end{bmatrix} = \begin{bmatrix} \xi_1 & \xi_2 & \xi_3 \\ \eta_1 & \eta_2 & \eta_3 \end{bmatrix} \begin{bmatrix} 1 - \rho_1 \\ \rho_1(1 - \rho_2) \\ \rho_1\rho_2 \end{bmatrix} \quad \text{when } (\xi, \eta) \in T \quad (3.34)$$

In order to use the triangular mapping, to reduce the singularity order of a self-influence integral, the element must be divided into a set of triangles, while keeping the singular point as the triangles' pole (the point in the triangle, which maps to a line in the square). Examples of triangles arrangements for different elements are shown in Figure 3.6. Now using the triangular mapping in Eq. (3.34) the vector \mathbf{r} in Eq. (3.21) can be written as,

$$\mathbf{r}(\rho_1, \rho_2) = \rho_1 \mathbf{R}(\rho_1, \rho_2) \quad \text{where } \mathbf{R}(\rho_1, \rho_2) = (R_1, R_2, R_3) \quad (3.35)$$

and,

$$|\mathbf{R}(\rho_1, \rho_2)| = \sqrt{R_1^2(\rho_1, \rho_2) + R_2^2(\rho_1, \rho_2) + R_3^2(\rho_1, \rho_2)} \quad (3.36)$$

where,

$$\begin{aligned} x_p - x &= x_p - \sum_{j=1}^{N_N} \mathcal{N}_j x_j = -\rho_1 \sum_{j=1}^{N_N} H_j x_j = \rho_1 R_1(\rho_1, \rho_2) \\ y_p - y &= y_p - \sum_{j=1}^{N_N} \mathcal{N}_j y_j = -\rho_1 \sum_{j=1}^{N_N} H_j y_j = \rho_1 R_2(\rho_1, \rho_2) \\ z_p - z &= z_p - \sum_{j=1}^{N_N} \mathcal{N}_j z_j = -\rho_1 \sum_{j=1}^{N_N} H_j z_j = \rho_1 R_3(\rho_1, \rho_2) \end{aligned} \quad (3.37)$$

using the shape function relation,

$$\mathcal{N}_j(\xi, \eta) = \begin{cases} 1 + \rho_1 H_j(\rho_1, \rho_2) & \text{if } j \text{ is a singular node} \\ \rho_1 H_j(\rho_1, \rho_2) & \text{if } j \text{ is not a singular node} \end{cases} \quad (3.38)$$

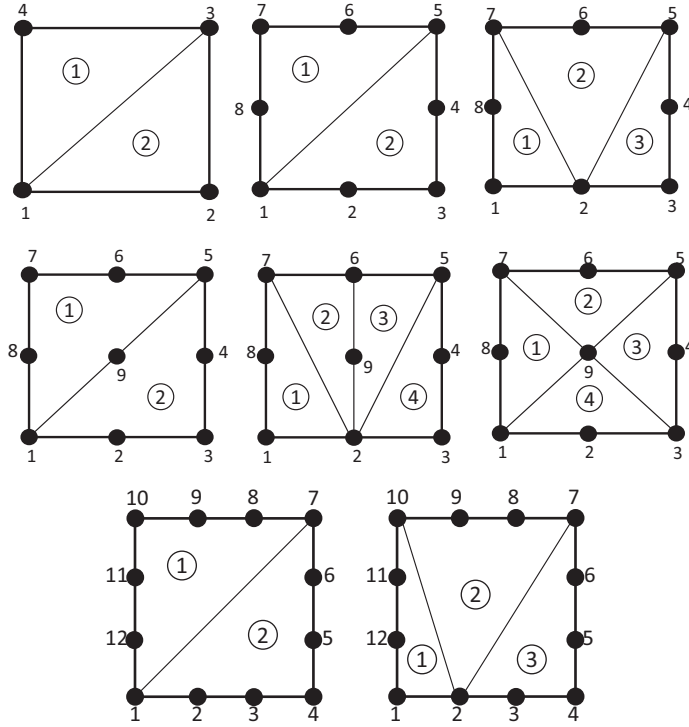


Figure 3.6: Dividing elements to triangles for different types of higher-order elements.

Here $H_j(\rho_1, \rho_2)$ is a desingularized shape function with non-zero value at $\rho_1 = 0$. Expressions for $H_j(\rho_1, \rho_2)$ in Eq. (3.38) are straight forward to calculate by replacing ξ, η in definition of \mathcal{N}_j from Eq. (3.34) based on ρ_1, ρ_2 . However, the calculations and expressions were lengthy, and therefore not presented here. A symbolic mathematical software package was used to calculate these expressions.

In order to transform the integrals into (ρ_1, ρ_2) -space the Jacobian of transformation must be calculated. The Jacobian for transformation from (ξ, η) - to (ρ_1, ρ_2) -space is,

$$J_T = 2\rho_1 A_T \tag{3.39}$$

where A_T is the area of a triangle in (ξ, η) -space. Now, let us see how we can use this transformation to remove the singularity of the integrals. By writing the integral in Eq. (3.30) in (ρ_1, ρ_2) -space we obtain,

$$\mathcal{S}_j^{(e)}(\mathbf{p}) = 2 \int_0^1 \int_0^1 \mathcal{N}_j(\xi, \eta) \frac{1}{|\mathbf{R}(\rho_1, \rho_2)|} |J(\rho_1, \rho_2)| A_T d\rho_1 d\rho_2 \tag{3.40}$$

which is no longer singular, and therefore can be integrated numerically. It must

be noted, for numerical integration using Gauss-Legendre method, the square must be further mapped to $[-1, 1] : [-1, 1]$, which requires a mapping coefficient of $1/4$. Performing similar transformation on Eq. (3.29) we obtain,

$$\mathcal{D}_j^{(e)}(\mathbf{p}) = 2 \int_0^1 \int_0^1 \mathcal{N}_j(\rho_1, \rho_2) \frac{-\mathbf{R}(\rho_1, \rho_2) \cdot \mathbf{J}(\rho_1, \rho_2)}{\rho_1 |\mathbf{R}(\rho_1, \rho_2)|^3} A_T d\rho_1 d\rho_2 \quad (3.41)$$

which still has $1/\rho_1$ type of singularity. Using Eq. (3.38), the singularity can be removed for the off-diagonal terms as shown in Eq. (3.42).

$$\mathcal{D}_j^{(e)}(\mathbf{p})_{(\mathbf{p} \neq \mathbf{q}_j)} = 2 \int_0^1 \int_0^1 H_j(\rho_1, \rho_2) \frac{-\mathbf{R}(\rho_1, \rho_2) \cdot \mathbf{J}(\rho_1, \rho_2)}{|\mathbf{R}(\rho_1, \rho_2)|^3} A_T d\rho_1 d\rho_2 \quad (3.42)$$

For the diagonal terms we have, $\mathcal{N}_j = 1 + \rho_1 H_j(\rho_1, \rho_2)$. Therefore the integral can be divided into a regular and a singular part. The remaining singular term for the diagonal integrals is,

$$2 \int_0^1 \int_0^1 \frac{-\mathbf{R}(\rho_1, \rho_2) \cdot \mathbf{J}(\rho_1, \rho_2)}{\rho_1 |\mathbf{R}(\rho_1, \rho_2)|^3} A_T d\rho_1 d\rho_2 \quad (3.43)$$

Calculating diagonal terms can be avoided, if the indirect method is adopted (e.g. Liu et al. (1991) and Xü (1992)). The indirect method is explained in Section 3.3.5. However, the indirect method is not always applicable. The direct method for calculating the singular integrals, presented by Teng et al. (2006) and Shao (2010), was adopted here. Let us define the non-singular part of the integral's kernel as,

$$f(\rho_1, \rho_2) = 2 \frac{-\mathbf{R}(\rho_1, \rho_2) \cdot \mathbf{J}(\rho_1, \rho_2)}{|\mathbf{R}(\rho_1, \rho_2)|^3} A_T \quad (3.44)$$

Then Eq. (3.43) can be written as,

$$\underbrace{\int_0^1 \int_0^1 \frac{f(\rho_1, \rho_2) - f(0, \rho_2)}{\rho_1} d\rho_1 d\rho_2}_{I_1} + \lim_{\epsilon \rightarrow 0} \underbrace{\int_{\rho_1(\epsilon)}^1 \int_0^1 \frac{f(0, \rho_2)}{\rho_1} d\rho_1 d\rho_2}_{I_2} \quad (3.45)$$

The integral part, I_1 , is no-longer singular, and it is possible to use a numerical scheme to evaluate it. For the integral in I_2 we have,

$$I_2 = - \lim_{\epsilon \rightarrow 0} (\ln \epsilon) \int_0^1 f(0, \rho_2) d\rho_2 + \int_0^1 f(0, \rho_2) \ln [R(0, \rho_2)] d\rho_2 \quad (3.46)$$

As Shao (2010) explained in his thesis, although the limit in Eq. (3.46) does not exist, it does not contribute to the diagonal terms. The reason is that, for a node, the summation of the integrals on all adjusting elements are canceling each other. The remaining line integral can be calculated by a standard numerical integration procedure.

3.3.4 Solid angles

The last piece of the puzzle, for making a complete equation system, is the solid angles at the collocation points. The need for calculating the solid angles can be avoided if the diagonal terms are calculated by the indirect method, presented in Section 3.3.5. Although, the indirect method is generally simpler, its application is problem-dependent, and not always possible. The direct method for calculating the solid angles, on the hand, can be adopted in any case. The method presented by Mantic (1993) was adopted here. A solid angle at the point \mathbf{p} is mathematically defined as,

$$\mathcal{C}(\mathbf{p}) = \frac{S_\epsilon}{4\pi\epsilon^2} 4\pi \quad (3.47)$$

where S_ϵ is the surface of the sphere with radius ϵ , centered at the node \mathbf{p} , inside the fluid domain, cut by the elements sharing the node \mathbf{p} , while ϵ approaches zero. Figure 3.7 shows the arrangement of the elements and the notations required for calculating the solid angle. The contribution to the solid angle from each element

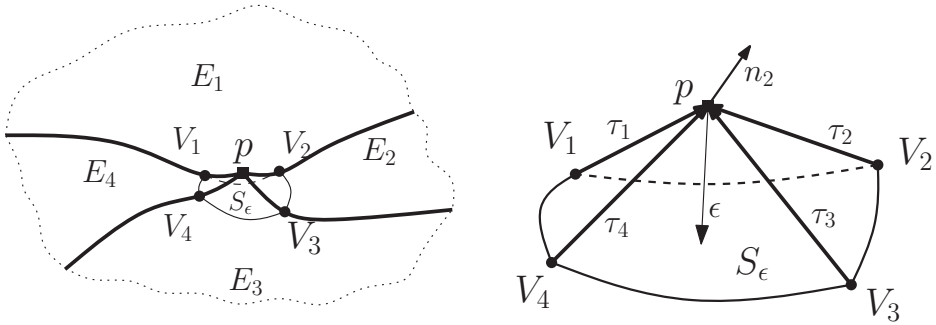


Figure 3.7: Arrangement of elements close to a node in calculating the solid angle. \mathbf{p} : node, ϵ : radius of the sphere S_ϵ centered at the node \mathbf{p} , E_i : elements sharing the node \mathbf{p} , V_i : intersection point of the sphere S_ϵ with the elements edges, $\boldsymbol{\tau}_i$: the vectors connecting vertices to the sphere center, \mathbf{n}_i : the normal vector on element E_i at the node \mathbf{p} .

can be calculated as ,

$$\gamma_i = \pi + \text{sgn}[(\mathbf{n}_{i-1} \times \mathbf{n}_i) \cdot \boldsymbol{\tau}_i] \arccos(\mathbf{n}_{i-1} \cdot \mathbf{n}_i) \quad (3.48)$$

where,

$$\text{sgn}(x) = \begin{cases} 1 & x > 0 \\ 0 & x = 0 \\ -1 & x < 0 \end{cases} \quad (3.49)$$

and \mathbf{n}_i and $\boldsymbol{\tau}_i$ are defined in the Figure 3.7, where cyclic convention applies. Then, the solid angle is defined as the summation of these contributions as shown in

Eq. (3.50).

$$\mathcal{C}(\mathbf{p}) = \sum_{i=1}^{N_E} \gamma_i - (N_E - 2)\pi \quad (3.50)$$

Here N_E is the number of elements which share the node \mathbf{p} .

3.3.5 Diagonal terms, indirect method

The diagonal terms, in the boundary element equation system (Eq. (3.31)), can be calculated using an indirect method. In this way, the difficulties in calculating the singular integrals in Eq. (3.43) and solid angles can be avoided. Following Liu et al. (1991), we can assume a known auxiliary velocity potential ϕ_1 , which is integrable on the boundaries. We write up Eq. (2.78) for ϕ_1 as shown in Eq. (3.51). The boundaries of the problem can be separated into, discretized-boundaries (S_d), non-discretized or remaining boundaries (S_r). Examples of the remaining boundaries can be S_∞ , which is excluded from the solution as explained in Section 2.11. Another example can be the free-surface (S_F) if the chosen Green function satisfies the free-surface condition. Then, the body surface must be discretized only.

$$\mathcal{C}\phi_1 = \iint_{S_d} \left(\phi_1 \frac{\partial G}{\partial n} - G \frac{\partial \phi_1}{\partial n} \right) dS + \iint_{S_r} \left(\phi_1 \frac{\partial G}{\partial n} - G \frac{\partial \phi_1}{\partial n} \right) dS \quad (3.51)$$

The integral on the discretized boundaries, S_d , can be calculated by the method described in this section. Let us call the integral on the remaining boundaries, I_r . Then, using one line of the equation system in Eq. (3.31), the Eq. (3.51) can be written as,

$$\mathcal{D}_{ii} = \frac{1}{(\phi_1)_i} \left[\sum_{k=1}^{N_C} \mathcal{S}_{ik} \left(\frac{\partial \phi_1}{\partial n} \right)_k - \sum_{k=1}^{N_C} \mathcal{D}_{ik} (\phi_1)_k + (I_r)_i \right] \quad (3.52)$$

where,

$$(I_r)_i = \iint_{S_r} \left((\phi_1)_i \frac{\partial G}{\partial n} - G \left(\frac{\partial \phi_1}{\partial n} \right)_i \right) dS \quad (3.53)$$

Therefore, for calculating the diagonal terms, the integral in Eq. (3.53) must be evaluated. This may be an easy, or difficult, task depending on the type of the problem and the choice of ϕ_1 . The simplest case would be a problem with closed domain, i.e. when all the boundaries are discretized. Then, there is no need for calculating I_r . Assuming a constant non-zero value for ϕ_1 , for instance $\phi_1 = 1$ in the whole water domain, Eq. (3.52) simplifies to Eq. (3.54).

$$\mathcal{D}_{ii} = - \sum_{k=1, k \neq i}^{N_C} \mathcal{D}_{ik} \quad (3.54)$$

The method can, as easily, work for the problem of a body in infinite fluid. In this case, $S_r = S_\infty$, can be assumed to be a sphere with a radius approaching infinity. Then, choosing $\phi_1 = 1$, the integral in Eq. (3.53) becomes 4π . When free surface exists, the domain is divided into a half sphere. $I_r = 2\pi$ is, however, not an accurate solution. Therefore, using this method requires either closing the domain, i.e. discretizing a semi-sphere around the body (computationally expensive), or choosing a velocity potential as ϕ_1 which makes calculating I_r analytically possible. Due to these difficulties the direct approach presented in Sections 3.3.3 and 3.3.4 was adopted in the present study.

3.3.6 Calculating derivatives

Unlike constant elements, higher order elements ensure surface and velocity potential continuity across elements. Moreover, depending on the order, the distribution of variables on the element surface is continuous and differentiable. Although, at the element edges discontinuities in surface slope and velocities may happen, away from the edges, the derivatives can be calculated using a direct differentiation of the shape functions.

As explained in Section 3.3.1, using the Lagrangian shape functions, the physical surface of an element is mapped to a parametric $\xi\eta$ -space. Therefore, similar to the finite difference method, Eqs. (3.11) and (3.13) can be used to calculate the first and second order derivatives on the element's surface. The mapping coefficients and the derivatives in the parametric space can be calculated using a shape-function differentiation. For instance,

$$\frac{\partial\phi(\xi, \eta)}{\partial\xi} = \sum_{j=1}^{N_N} \phi(\xi_j, \eta_j) \frac{\partial\mathcal{N}_j^{(m)}(\xi, \eta)}{\partial\xi} \quad (3.55)$$

The discontinuity in the surface's slope and derivatives is treated by getting the average of the values from neighbor elements. The error introduced due to this simplification can be reduced by decreasing the element sizes.

3.4 B-spline method

The B-spline method is shortly introduced in this chapter. The main intention is to compare this method to HOBEM, presented in the previous section, and put the two methods in a unified perspective. B-spline method is adopted later in Chapter 4 for investigating the numerical errors introduced by discretizing a free surface. The results from this numerical method are not presented here. However, as will be explained in the last section, the computer program was written in a way to cover this method as well. The intention was to provide a unified ground for comparing different numerical methods in the future.

3.4.1 Surface representation

In B-spline method the surfaces and the distribution of interest variables are mapped to a parametric space by using the B-spline base functions. B-spline base functions are first introduced by Schoenberg (1946) for data approximation. Nowadays this method is very popular in computer modeling and graphics (see for instance Rogers and Adams (1989)).

The mapping of a function $f(\xi)$ to a parametric space ξ by B-spline base functions is defined as follows.

$$f(\xi) = \sum_{j=1}^{N_V} a_j b_j^{(m)}(\xi) \quad (3.56)$$

The values a_j are the control weights of the function f . $b_j^{(m)}(\xi)$ is the B-spline base function of order m associated with the weight a_j . If $f(\xi)$ represents a curve in space, by an analogy to the geometrical shape of the curve, a_j will represent the vertices of a polygon, surrounding the curve (see Hsin et al. (1993)). Based on this analogy, we use the term *control vertices*, instead of weights, to refer to these values. N_V is the total number of these vertices. The m th order base function of a B-spline can be calculated using the recursive formula by Cox (1972) and de Boor (1972), presented in Eqs. (3.57) and (3.58) below.

$$b_j^{(1)}(\xi) = \begin{cases} 1 & \xi_j \leq \xi \leq \xi_{j+1} \\ 0 & \text{otherwise} \end{cases} \quad (3.57)$$

$$b_j^{(m)}(\xi) = \frac{\xi - \xi_j}{\xi_{j+m} - \xi_j} b_j^{(m-1)}(\xi) + \frac{\xi_{j+m+1} - \xi}{\xi_{j+m+1} - \xi_{j+1}} b_{j+1}^{(m-1)}(\xi) \quad (3.58)$$

Here ξ_j are the elements of a monotonically increasing vector in parametric space, called *knot vector*.

$$\xi_j = \xi_0 \leq \xi_1 \leq \dots \leq \xi_{N_K-1} \quad (3.59)$$

Based on above equations, the function $f(\xi)$ is a polynomial of degree $(m - 1)$, and continuously differentiable in the intervals between knots ($\xi_j < \xi < \xi_{j+1}$). At each knot, the function ($f(\xi_j)$) and its derivatives, up to and including $(m - 2)$, are continuous.

The B-spline base functions carry important characteristics, which are the reason behind their popularity. For instance, the sum of all base functions at any point in the parametric space ξ is equal to one.

$$\sum_{j=1}^{N_V} b_j^{(m)}(\xi) = 1 \quad (3.60)$$

Moreover, each base function of order m is a polynomial of degree $m - 1$, which is non-zero only on a finite interval in the parametric space ξ . This property of

the B-spline base function is called *compact support*, and the interval is called *base* or *support* of the function. Therefore the influence of each vertex is only felt in a finite space in the parametric domain, depending on the order of the base function. This means, unlike other curves such as Bézier curve, changing a vertex will only affect the B-spline in the vicinity of that vertex. For all the values of ξ , the base functions have positive or zero values, and except for $m = 1$, which corresponds to a flat line, all the other base functions have only one maximum.

As Eq. (3.58) suggests, the choice of knot vector has a significant influence on the B-spline base functions. In general, the knots can have any values as long as they increase monotonically. In practice, monotonically increasing integers, or normalized values in $[0, 1]$ interval, are usually used. Here, we preferred the normalized range between 0 and 1. In this way, the parameter can be linked to the non-dimensional arc length of the curve. The main types of the knot vectors generally in use are, *uniform*, *open* and *non-uniform*.

In a uniform knot vector, the elements are equally spaced with a distance $\Delta\xi$. In this way, a periodic uniform base function is obtained. The support of a uniform base function of order m is equal to m intervals. In other words, the influence of the base function is felt only on the $m\Delta\xi$ distance of the parametric space.

$$b_j^{(m)}(\xi) = b_{j-1}^{(m)}(\xi - \Delta\xi) = b_{j+1}^{(m)}(\xi + \Delta\xi) \quad (3.61)$$

An open knot vector has m repeated knots at the beginning and the end of the vector, where m equals to the B-spline's base function order. Therefore, the base function no longer has the periodic behavior close to the ends of the curve. In this way, higher degree of control is obtained on the value of the function at the end points by controlling only one vertex. This property is important, for instance, to ensure continuity between different domains. In the case of a non-uniform knot vector, the elements of the vector can be chosen as desired, which results in varying base functions. This is most useful in describing shapes with sharp corners. Repeating an element of the knot vector gives the ability to create a sharp corner in the curve. Each repetition of an element reduces the number of continuous derivatives at the knot by one.

The part of the curve between two knots is called an interval or element, and N_E is the number of elements. The relation between number of the elements (N_E), number of the vertices (N_V), and the order of the B-spline (m) is shown in Eq. (3.62).

$$N_V = N_E + m - 1 \quad (3.62)$$

Eq. (3.62) suggests that in order to have a valid element, $m \leq N_V$ must be satisfied. Similarity, the relation between number of knots and the order of the base function is,

$$N_K = N_V + m \quad (3.63)$$

Let us consider the following vector of knots in the parametric space. For clarity, integer values are used instead of normalized values between $[0, 1]$.

$$\xi_j = [0, 1, 2, 3, 4, 5, 6] \quad (3.64)$$

Combining Eqs. (3.63) and (3.64), it is possible to see that the number of knots is always larger than the number of elements, and not all intervals can be defined as elements. The reason is the fact that by increasing the order, additional knots are required to create a base large enough to support higher order base functions. Figure 3.8 shows the base functions for different orders and the knot vector in Eq. (3.64). The constrains in Eqs. (3.62) and (3.63) are shown graphically in this figure.

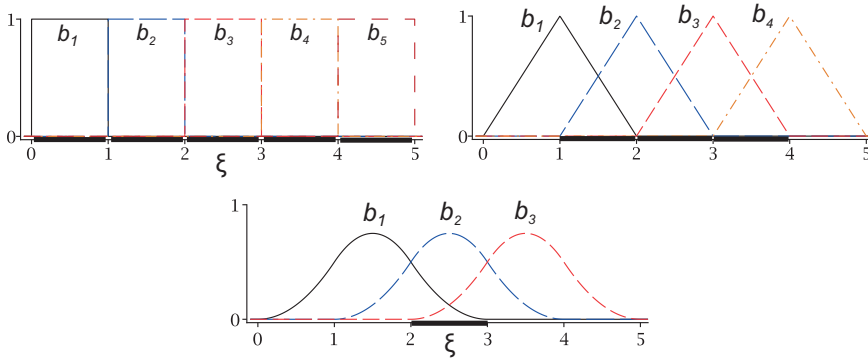


Figure 3.8: B-spline base functions of different orders. b_i : base functions.

A more generalized version of B-splines is the non-uniform rational B-splines or NURBS. NURBS are widely used in the field of computer graphics. Kim and Shin (2003) have used NURBS for more accurate representation of the geometry in potential flow calculations by panel methods. In this method, a rational base function is defined for the non-uniform B-spline, using a blending weight (w_j) as follows,

$$f(\xi) = \frac{\sum_{j=1}^{N_V} w_j a_j b_j^{(m)}(\xi)}{\sum_{j=1}^{N_V} w_j b_j^{(m)}(\xi)} = \sum_{j=1}^{N_V} a_j R_j^{(m)}(\xi) \quad (3.65)$$

where,

$$R_j^{(m)}(\xi) = \frac{w_j b_j^{(m)}(\xi)}{\sum_{j=1}^{N_V} w_j b_j^{(m)}(\xi)} \quad (3.66)$$

is the rational base function. It is clear that if all weights are chosen to be one, i.e. $w_j = 1$, we have $R_j^{(m)}(\xi) = b_j^{(m)}(\xi)$. In another words, the non-rational base function $b_j^{(m)}$ is a special case of the rational base function $R_j^{(m)}$.

Let us focus on the periodic uniform B-spline base function and assume the main base function ($b^{(1)}$) is defined in a symmetric interval $\xi \in [-h/2, h/2]$ as

shown in Eq. (3.67). Then, a recursive formulation using convolution integral for the base functions of higher orders can be obtained. This type of B-spline base function is the so-called *cardinal* or *centered* B-spline (Schoenberg, 1946).

$$b^{(1)}(\xi) = \begin{cases} 1 & |\xi| \leq \frac{h}{2} \\ 0 & \text{otherwise} \end{cases} \quad (3.67)$$

$$b^{(m)}(\xi) = b^{(m-1)}(\xi) \star b^{(0)}(\xi) = \frac{1}{h} \int_{-\infty}^{+\infty} b^{(m-1)}(\tau) b^{(0)}(\xi - \tau) d\tau \quad (3.68)$$

Two-dimensional surface base functions are made by multiplying the one-dimensional line base functions, as $B_j^{(m,n)}(\xi, \eta) = B_{IJ}^{(m,n)}(\xi, \eta) = b_I^{(m)}(\xi) b_J^{(n)}(\eta)$. The index j is related to a two-dimensional indexes (I, J) , by a global index counter. For instance, if $N_{V\xi}$ and $N_{V\eta}$ are the number of vertices in ξ and η directions, we can write $j = I + (J - 1)N_{V\xi}$, which gives $j = 1 \cdots N_V$. Here, $N_V = N_{V\xi} \times N_{V\eta}$ is the total number of vertices.

A two-dimensional base function carries the properties of the one-dimensional base function defined above. As showed, except for $m = 1$, generally a B-spline does not go through its vertices. The question is, how we can use a B-spline to represent a certain set of data points. From Eq. (3.62), it is possible to determine the number of vertices by fixing the number of elements and the order of B-spline. Therefore, in order to determine the B-spline, the values for weights must be calculated.

Let us assume a set of N_P number of known data points. There are two main methods for adopting a B-spline in representing the surface, and/or the variables defined by these data points. These are, interpolation, and approximation. In interpolation technique, the resulted B-spline goes exactly through the points defined in the data set. The number of vertices is bound to be equal to the number of data points. In this way, a linear square equation system will be obtained by introducing the values of the data points into Eq. (3.56). By solving the equation system, the values for vertices will be obtained. The parameter (ξ) must be determined at the data points in order to evaluate the base functions. The non-dimensional curve length is the natural choice for this purpose. Although the resulting B-spline curve is continuously differentiable up to $m - 1$, the resulted shape may not be smooth and may include unwanted wiggles. The relation between shape of the curve and the position of the vertices are not intuitive and care must be taken in applying this method.

An adjustment can be made to the method by introducing more data points than vertices. In this way a better and smoother curve can be obtained. However, the B-spline curve does not necessarily go through all of the data points. This is in fact an approximation method and results in an over-conditioned equation system, which must be solved by a least square method. In this way, the order of B-spline and the number of panels are independent of the number of data points.

3.4.2 Boundary element formulation

Using the B-spline representation, the boundary integral formulation presented in Chapter 2 is discretized into a boundary element formulation. For instance, let us consider a simple case of a body in infinite fluid. Then, the boundary integral formulation for the problem becomes,

$$\mathcal{C}(\mathbf{x})\phi(\mathbf{x}) = \iint_{S_B} \phi(\boldsymbol{\xi}) \frac{\partial G(\mathbf{x}, \boldsymbol{\xi})}{\partial n(\boldsymbol{\xi})} dS - \iint_{S_B} G(\mathbf{x}, \boldsymbol{\xi}) \frac{\partial \phi(\boldsymbol{\xi})}{\partial n(\boldsymbol{\xi})} dS \quad (3.69)$$

Let us represent the distribution of ϕ and $\frac{\partial \phi}{\partial n}$ by the B-spline base functions as follows.

$$\begin{aligned} \phi(\xi, \eta) &= \sum_{j=1}^{N_V} \phi_j B_j^{(m)(n)}(\xi, \eta) \\ \frac{\partial \phi(\xi, \eta)}{\partial n(\xi, \eta)} &= \sum_{j=1}^{N_V} \left(\frac{\partial \phi}{\partial n} \right)_j B_j^{(m)(n)}(\xi, \eta) \end{aligned} \quad (3.70)$$

It is important to remember that ϕ_j is not the value of ϕ at the node (ξ_j, η_j) . It is just a vertex, or weight, at the (ξ_j, η_j) -point of the B-spline, which represents ϕ distribution. Similarly, the surface of the boundary S_B is defined by B-spline as shown in Eq. (3.71).

$$\mathbf{x}(\xi, \eta) = \sum_{j=1}^{N_V} \mathbf{x}_j B_j^{(m)(n)}(\xi, \eta) \quad (3.71)$$

Doing so, the surface S_B is divided into $N_E = N_{E\xi} \times N_{E\eta}$ elements. Therefore, the integrals in Eq. (3.69) can be changed to summations.

$$\mathcal{C}(\mathbf{x})\phi(\mathbf{x}) = \sum_{j=1}^{N_V} \phi_j \mathcal{D}_j(\mathbf{x}) - \sum_{j=1}^{N_V} \left(\frac{\partial \phi}{\partial n} \right)_j \mathcal{S}_j(\mathbf{x}) \quad (3.72)$$

Here \mathcal{D}_{ij} and \mathcal{S}_{ij} are the integrated influence of a dipole and a source distribution, defined in Eqs. (3.73) and (3.74) respectively.

$$\mathcal{D}_j(\mathbf{x}) = \sum_{e=1}^{N_E} \iint_{\mathcal{E}_e} B_j^{(m)(n)}(\xi, \eta) \frac{\partial G(\xi, \eta; \mathbf{x})}{\partial n(\xi, \eta)} J(\xi, \eta) d\xi d\eta \quad (3.73)$$

$$\mathcal{S}_j(\mathbf{x}) = \sum_{e=1}^{N_E} \iint_{\mathcal{E}_e} B_j^{(m)(n)}(\xi, \eta) G(\xi, \eta; \mathbf{x}) J(\xi, \eta) d\xi d\eta \quad (3.74)$$

In reality, the base function $B_j^{(m)(n)}(\xi, \eta)$ is only non-zero on the support-elements. Therefore, the summations on different elements are only important on a few

number of elements surrendering the j th element. The number of elements depends on the order of the base function. For example, if $m = 1$ and $n = 1$ then $B_j^{(m)(n)}(\xi, \eta) = 1$ only on \mathcal{E}_j , and the formulation simplifies to the CPM formulation shown in Eq. (3.2), bearing in mind that the number of vertices and elements would be the same.

An equation system is formed based on the boundary element formulation in Eq. (3.72) using the collocation method. Unlike the previous methods, the number of collocation points in B-spline method can be different from the number of unknowns, i.e. $N_V \leq N_C$. If N_C number of collocation points (\mathbf{p}_i) is chosen to form the equation system, i.e. N_C/N_E number of points for each element, then a linear equation system is formed as shown in Eq. (3.75) below,

$$[\mathcal{D}_{ij}]_{N_C \times N_V} [\phi_j]_{N_V \times 1} = [\mathcal{S}_{ij}]_{N_C \times N_V} \left[\left(\frac{\partial \phi}{\partial n} \right)_j \right]_{N_V \times 1} \quad (3.75)$$

where,

$$\mathcal{D}_{ij} = \mathcal{D}_j(\mathbf{p}_i) - \mathcal{C}(\mathbf{p}_i) \sum_{j=1}^{N_V} B_j^{(m)(n)}(\xi_i, \eta_i) \quad (3.76)$$

$$\mathcal{S}_{ij} = \mathcal{S}_j(\mathbf{p}_i) \quad (3.77)$$

$\left(\frac{\partial \phi}{\partial n} \right)_j$ can be substituted from the boundary condition on each collocation point, taking into account Eq. (4.22). If one collocation point is chosen for each vertex, then the coefficient matrices become square. Otherwise, the number of equations will be more than the number of unknowns and the resulting over-determined system can be solved by a least square method. Galerkin method can also be used for setting up the equation system. The Galerkin method gives a slightly more efficient solution. More details on this matter can be found in Hsin et al. (1993).

3.4.3 Calculating integrals

For regular integrals, Gauss-Legendre quadrature is the natural choice. However, this method is inaccurate when the field point is close to the surface. Adaptive subdivision of the elements was adopted in previous studies such as Maniar (1995) in order to increase the accuracy of numerical integration in nearly-singular cases.

It is possible to analytically remove the singularity in the integrals' kernel as explained in Hsin et al. (1993). They introduced series expansion for 2D cases in order to calculate the integrals analytically. Later, Maniar (1995) adopted the method for 3D calculations. In this method, it is assumed that the B-spline shape functions are polynomials. If surfaces are represented with flat quadrilateral elements, the integration of variables can be done analytically. Nakos and Scлавounos (1994) used the *centered* B-splines to represent the variables on quadrilateral elements and calculated the integrals by a recursive formula presented in Newman (1987*b*) for higher order distributions.

For generalized B-splines, such as NURBS, a series of transformations are usually used to remove the singularity. The PART method by Hayami and Matsumoto (1994) is one of these methods, which reduces the order of singularity by a series of planar and polar transformations. Interested readers are addressed to the original publications.

3.4.4 Solid angles

The solid angle for a point on a surface defined by a B-spline can be calculated by the method described in Section 3.3.4. However, if the surface is defined by a uniform knot vector, and B-spline base functions with order higher than 3, the slope of the surface is continuous every where, which means the solid angle is 2π . This is not the case for low-order base functions or non-uniform knot vectors. As explained in Section 3.4.1, sharp corners can be introduced in a B-spline using a non-uniform knot vector created by repeating the knot vector elements.

3.4.5 Derivatives

As explained in Section 3.4.1, a B-spline of order m has continuous derivatives up to, and including, $m - 2$. Therefore, differentiation of the base functions can be used to calculate the derivatives of variables on the surface, as shown in Eq. (3.78) below.

$$\frac{\partial\phi(\xi,\eta)}{\partial\xi} = \sum_{j=1}^{N_V} \phi_j \frac{\partial}{\partial\xi} B_j^{(m)(n)}(\xi,\eta) \quad (3.78)$$

The method presented in Section 3.2.4, can be used to calculate the mapping coefficients between physical and parametric space. For higher order differentiations, fitting new B-spline to the derivatives or finite difference methods can be used.

3.5 Notes on discretization methods

Three different discretization methods were presented in the last three sections. The main question is, which one of these methods is the best for solving boundary integral equation. Unfortunately, it is not possible to find a simple answer to this question. Detailed comparisons between all different discretization methods are not easily available. Usually, the studies are pointed towards one type of discretization due to programming difficulties. As a general guideline, introducing a higher order distribution of unknowns helps in solving a problem with higher accuracy, using less number of elements (Liu et al., 1991). On the other hand, adopting a higher order surface representation can improve the accuracy of the solution by improving the accuracy of boundary and the boundary conditions (Kim and Shin, 2003). However, in practice, increasing the order of representation is not always helpful and may even be a source of complications. For instance, in constant panel method the coefficient matrix is diagonal-dominant. Increasing the order of distribution reduces the importance of diagonal elements and introduce stronger coupling between the

values on the boundaries. This may result in an unstable equation system. This can be the reason why in most of the previous studies the order of representation is limited to three and higher order methods are not pursued.

Presence of forward speed is another factor in choosing the appropriate discretization method. Cases with a higher forward speed have a higher tendency towards numerical instabilities. Generally, higher order methods improve the accuracy. In such cases, this includes the accuracy of capturing the numerical, as well as physical, waves. However, in lower order methods these errors are simply damped out. Meaning, for a certain problem, the higher order method can be unstable while the lower order gives physical and reasonable results. Therefore, choosing the best order of discretization, which results in an accurate, stable, and computationally efficient solution, is not an easy task. As will be discussed in the following chapters, different methods were found to be useful in solving different type of problems. However, pursuing all solution possibilities are out of the scope of the present study. Computations were done using a BEM library developed in C++ which provided a unified environment for all discretization schemes (see Section 3.10). A comparison between different methods from theoretical point of view can be found in Chapter 4.

3.6 Time marching methods

An initial-value-problem must be solved in order to find the time domain solution. A time marching scheme plays an important role in the stability and accuracy of the time domain solver. Three different time marching methods were discussed and implemented in the present work. However, the fourth order Runge-Kutta method was used in most of the present studies.

The time domain problem in the present studies consists of time evolution of the free surface potential and elevation. The forcing function, i.e. velocities on the body boundary, is assumed to be known in time for this type of analysis. The linear boundary conditions on free surface presented in Eqs. (2.34) and (2.35) are repeated here,

$$\frac{\partial \zeta}{\partial t} = -U \frac{\partial \zeta}{\partial x} + \frac{\partial \phi}{\partial z} \quad \text{on } z = 0 \quad (3.79)$$

$$\frac{\partial \phi}{\partial t} = -g\zeta - U \frac{\partial \phi}{\partial x} \quad \text{on } z = 0 \quad (3.80)$$

Above equations can be used for time stepping of the velocity potential and free surface elevation.

3.6.1 Explicit/Implicit Euler

Vada and Nakos (1993) showed that Euler backward method, in its purely explicit or implicit form, is unstable for the problems involve evolution of the free surface. However, a combination of the two can be used, as long as the forward speed is not

too high. The following form is assumed for the time marching of explicit/implicit Euler method.

$$\frac{\zeta^{(n+1)} - \zeta^{(n)}}{\Delta t} = -U \frac{\partial \zeta^{(n)}}{\partial x} + \frac{\partial \phi^{(n)}}{\partial z} \quad (3.81)$$

$$\frac{\phi^{(n+1)} - \phi^{(n)}}{\Delta t} = -g\zeta^{(n+1)} - U \frac{\partial \phi^{(n+1)}}{\partial x} \quad (3.82)$$

Here the superscript (n) is the current, $(n+1)$ is the next, and Δt is the duration of the time step. In this method, the treatment of the kinematic free-surface boundary condition is explicit. On the other hand, the dynamic condition is treated implicitly by substituting $\zeta^{(n+1)}$ from the kinematic condition. In this method, the BEM equation system is solved only once for each time-step.

3.6.2 ABM4

Fourth order Adams-Bashforth-Moulton method (ABM4) is a predictor-corrector type of time marching scheme. This method requires the past two time-steps in order to advance the solution one time-step. Here the method presented in Skourup et al. (2000) and Shao (2010) were adopted for analysis. In the first step, the velocity potential ϕ and the free-surface elevation ζ are updated using the explicit ABM4 predictor as follows,

$$\zeta^{(n+1)} = \zeta^{(n)} + \Delta t \sum_{k=1}^4 p_k \frac{\partial \zeta^{(n+1-k)}}{\partial t} \quad (3.83)$$

$$\phi^{(n+1)} = \phi^{(n)} + \Delta t \sum_{k=1}^4 p_k \frac{\partial \phi^{(n+1-k)}}{\partial t} \quad (3.84)$$

Here $p_k = [55/24, -59/24, 37/24, -9/24]$ are the predictor coefficients. $\frac{\partial \zeta}{\partial t}$ and $\frac{\partial \phi}{\partial t}$, for time step $(n+1-k)$, are obtained from Eqs. (3.79) and (3.80) respectively. By substituting $\phi^{(n+1)}$ and $\zeta^{(n+1)}$ into the dynamic free-surface condition (Eq. (3.80)) an estimation for $\frac{\partial \phi^{(n+1)}}{\partial t}$ is obtained. The value for $\phi^{(n+1)}$ can be updated using this value and the semi-implicit corrector of Adams-Moulton as follows,

$$\phi^{(n+1)} = \phi^{(n)} + \Delta t \sum_{k=1}^4 c_k \frac{\partial \phi^{(n+2-k)}}{\partial t} \quad (3.85)$$

where $c_k = [9/24, 19/24, -5/24, 1/24]$. Using Eq. (3.85) and the dynamic free-surface condition in Eq. (3.80), an iterative scheme can be adopted until convergence is achieved for $\phi^{(n+1)}$. As mentioned in Shao (2010), similar iterative scheme for $\zeta^{(n+1)}$ is computationally expensive due to the need for solving BEM equation at each step.

3.6.3 Runge-Kutta

An explicit fourth order Runge-Kutta method for time marching of the free-surface velocity potential and elevation were adopted here. This method consists of four intermediate steps. The steps must be performed in sequence in order to obtain the values for the next time-step. The steps are summarized below (Tanizawa, 2000).

First step:

$$\begin{aligned}\zeta^{(n+1/4)} &= \zeta^{(n)} + \frac{1}{2}\Delta t \zeta_t^{(n)} \\ \phi^{(n+1/4)} &= \phi^{(n)} + \frac{1}{2}\Delta t \phi_t^{(n)} \\ \phi_z^{(n+1/4)} &\Leftarrow \text{BEM solver} \Leftarrow \phi^{(n+1/4)}\end{aligned}\tag{3.86}$$

Second step:

$$\begin{aligned}\zeta^{(n+2/4)} &= \zeta^{(n)} + \Delta t \left(c_1 \zeta_t^{(n)} + c_2 \zeta_t^{(n+1/4)} \right) \\ \phi^{(n+2/4)} &= \phi^{(n)} + \Delta t \left(c_1 \phi_t^{(n)} + c_2 \phi_t^{(n+1/4)} \right) \\ \phi_z^{(n+2/4)} &\Leftarrow \text{BEM solver} \Leftarrow \phi^{(n+2/4)}\end{aligned}\tag{3.87}$$

Third step:

$$\begin{aligned}\zeta^{(n+3/4)} &= \zeta^{(n)} + \Delta t \left(c_3 \zeta_t^{(n+1/4)} + c_4 \zeta_t^{(n+2/4)} \right) \\ \phi^{(n+3/4)} &= \phi^{(n)} + \Delta t \left(c_3 \phi_t^{(n+1/4)} + c_4 \phi_t^{(n+2/4)} \right) \\ \phi_z^{(n+3/4)} &\Leftarrow \text{BEM solver} \Leftarrow \phi^{(n+3/4)}\end{aligned}\tag{3.88}$$

Fourth step:

$$\begin{aligned}\zeta^{(n+1)} &= \zeta^{(n)} + \dots \\ &\quad \frac{1}{6}\Delta t \left(\zeta_t^{(n)} + c_5 \zeta_t^{(n+1/4)} + c_6 \zeta_t^{(n+2/4)} + \zeta_t^{(n+3/4)} \right) \\ \phi^{(n+1)} &= \phi^{(n)} + \dots \\ &\quad \frac{1}{6}\Delta t \left(\phi_t^{(n)} + c_5 \phi_t^{(n+1/4)} + c_6 \phi_t^{(n+2/4)} + \phi_t^{(n+3/4)} \right) \\ \phi_z^{(n+1)} &\Leftarrow \text{BEM solver} \Leftarrow \phi^{(n+1)}\end{aligned}\tag{3.89}$$

Here the derivatives are shown by subscripts. The coefficients, (c_k) , for fourth order Runge-Kutta (RK4), and fifth order Runge-Kutta-Gil (RKG5), are presented in Table 3.1. As the calculation steps presented above are suggesting, for each time-step the boundary element equation must be solved four times. This makes the RK4 method one of the slowest methods. However, in a linear formulation, by using the LU-factorization method, the equation can be solved once. Then, at each time-step the solution is obtained by back substitution. Therefore, the time domain solution can be performed much faster.

Table 3.1: Coefficients for Runge-Kutta, RK4 and RKG5 time marching methods.

c_k	RK4	RKG5
c_1	0	$(\sqrt{2} - 1)/2$
c_2	1/2	$(2 - \sqrt{2})/2$
c_3	0	$-\sqrt{2}/2$
c_4	1	$(\sqrt{2} + 2)/2$
c_5	2	$2 - \sqrt{2}$
c_6	2	$2 + \sqrt{2}$

3.6.4 Choosing a time marching method

The order of accuracy for the explicit/implicit Euler method is low and, as suggested by Vada and Nakos (1993), it is not suitable for high forward speed problems. On the other hand, it requires only one solution per each time step, which makes it the fastest method. This method was used in the present studies for calculation of radiation problems without forward speed.

The ABM4 and RK4 methods both have the same order of accuracy ($O(\Delta t)^4$). The ABM4 method requires two solutions of BEM equation and three previous time steps. This means that at the start of the time-marching scheme, the solutions at previous time-steps must be assumed. The other, and more robust alternative, is to start the solution by another scheme such as RK4, which does not need previous time-steps, and then switch to ABM4.

The RK4 method needs four calls to BEM solver which makes it the most expensive time marching method among the ones presented here. However, here we are interested in the solution of a linear problem. Meaning, the boundary conditions are satisfied on the mean positions of the free surface and body, which do not change in time. Therefore, it is possible to significantly speed up the BEM solver using the LU-factorization method. In this case, for a reasonable size problem, the change in efficiency by adopting the ABM4 scheme was not significant relative to RK4.

3.7 Free surface truncation

In theory, the free surface defined in the boundary integral formulation is extended to infinity. In practice however, the surface must be discretized into a finite number of elements. Therefore, it must be truncated. The truncation of a free surface, both in steady and un-steady formulation, must be treated carefully in order to avoid numerical instabilities.

3.7.1 Steady problem, Radiation condition

In solving the steady problem numerically, the radiation boundary condition must be satisfied indirectly. It is known that the mathematical solution for the wave equation results in two wave systems (see for instance Lighthill (1960)). A physical wave system, which carries energy away from the source, and a non-physical

system, which travel towards the source. The physical solution can be ensured by introducing an infinitesimal shift to the frequency in complex plane. Another interpretation of this method is to think of the shift as an artificial viscosity known as Rayleigh viscosity (e.g. Wehausen and Laitone (1960)).

In the presence of a steady forward motion, for instance the waves generated by a vessel advancing in infinite water, the radiation condition translates to *no upstream waves*. This condition must be enforced numerically in order to ensure a physical solution.

Dawson (1977), in his revolutionary paper, used the upstream finite difference and argued that it satisfies the radiation condition by propagating the disturbances downstream. Another widely used approach is the collocation point shift (see Section 3.2.5). In this method, a small horizontal shift is applied on the collocation points in the opposite direction of the forward speed (same direction of incoming flow in seakeeping coordinate system). Jensen et al. (1986) showed that, in his desingularized method, the collocation shift in the opposite direction results in satisfying the opposite radiation direction.

Jensen (1987) and Scлавounos and Nakos (1988) showed that both upwind finite difference and collocation point shift introduce a Rayleigh viscosity and therefore satisfy the radiation condition. However, these methods also introduce a numerical damping, which is closely linked to their properties in satisfying the radiation condition.

Another closely related but different aspect of the steady-state solutions is the presence of destabilizing numerical waves. These are first described by Longuet-Higgins and Cokelet (1976) and named sawtooth oscillations. As discussed by Nakos (1990), the discretized free surface fails to capture the waves with wave lengths close to the size of few panels. The energy of these distorted waves are a source for numerical instability. More details on this matter can be found in Chapter 4.

Numerical waves must be taken out in order to stabilize the solution. This can be done, for instance, by introducing damping. The connection to radiation condition arises here. Raven (1988) introduced a new method to satisfy the radiation condition in his source only method, by imposing zero induced velocity due to all the sources, at the upstream boundary. However, he mentioned that due to numerical waves a better solution will be obtained using a collocation point shift applied on the upstream part of the free surface.

Scлавounos and Nakos (1988) derived a similar radiation condition by analyzing the *error velocity potential* for the source and dipole distribution method. They concluded that in order to satisfy the radiation condition in their method, the first- and second-derivative of the velocity potential in x direction must be set to zero at the up-stream boundary. They introduced a filtering technique to eliminate the waves with wave-lengths less than 5,6 panel-lengths in order to avoid numerical instabilities.

In the present method, we chosen the upwind finite difference to satisfy the radiation condition and filter out numerical waves simultaneously. The reason behind this choice can be linked to the physical interpretation. As mentioned by Romate (1992), from mathematical point of view, the equation system of a ship

advancing with forward speed can be viewed in two ways. First is to see the problem as an elliptic problem (Laplace equation) with time-dependent boundary conditions, and second to view the problem as a hyperbolic problem in propagation-space with an integral dependency due to the Laplace equation. As mentioned by Dawson (1977), the second view is in analogy to a disturbance being carried downstream by the momentum equation, while its presence is felt at the upstream through pressure changes. In the present work, solving the problem in a moving coordinate system, and presence of high forward speed, suggest the second view as a more suitable one.

The side boundaries have no significant influence, as long as they are placed outside the wave sector. Otherwise, the reflected waves from the side boundaries reach back, and destroy the solution. The Kelvin angle for the wave system can give an indication of the suitable distance (see, for instance Newman (1977) for definition of the Kelvin angle). The boundary at the end of the domain must be placed away from the ship to minimize the influence of the reflected waves. Using an upstream finite difference operator, this influence region was minimized. Nakos (1990) mentioned that for his method of differentiation, which has characteristics of a central method, the waves propagate upstream, typically a quarter of the transverse wave length.

3.7.2 Unsteady problem and damping zone

The waves generated due to a body with forward speed, or oscillatory motions in the time domain solutions, travel from the source and reach the boundaries. In absence of proper treatment, the waves reflect from the boundaries and travel back into the solution domain. The fact that the waves must leave the source and disappear in infinity can be considered as a radiation condition for this problem (Wehausen and Laitone, 1960). The radiation condition can be satisfied by absorbing the waves at, or letting them to pass through, the boundaries. Several different methods exist for this purpose. Example are,

- Periodic condition
- Wave absorbing, damping zone or numerical beach
- Matching to a simple far-field solution
- Satisfying a differential equation at the boundaries (Sommerfeld's boundary condition)

Romate (1992) presented a detailed review on these methods. In the present study, a wave absorbing condition, in the form of a damping zone, was adopted. This method is adaptable for different problems more than the other ones. The frequency range, and type of the waves inside the domain, have no significant influence on the implementation of this method. Therefore, it can be applied, with minimum changes, to a wide range of problems. The short-coming of this method is the need for relatively large damping area on the free surface, which increases the computational domain.

Different types of wave absorbing conditions are reviewed by Israeli and Orszag (1981). The damping zone adopted here is similar to the one presented by Nakos et al. (1993). In this method an artificial damping term is added to the free surface kinematic boundary condition. Therefore the free-surface conditions become,

$$\frac{\partial \zeta}{\partial t} = -U \frac{\partial \zeta}{\partial x} + \frac{\partial \phi}{\partial z} - 2\nu \zeta \quad \text{on } z = 0 \quad (3.90)$$

$$\frac{\partial \phi}{\partial t} = -g\zeta - U \frac{\partial \phi}{\partial x} \quad \text{on } z = 0 \quad (3.91)$$

Here ν is the strength of the Newtonian cooling factor, which has a zero value on the inner part of the free surface and positive value on the damping zone showed in Figure 3.9. The distribution of the damping strength is assumed to be quadratic with the distance from the start of the damping boundaries as shown in Eq. (3.92).

$$\nu = 3 \frac{D_S}{D_W^3} d^2 \quad \text{where, } 0 \leq d \leq D_W \quad (3.92)$$

Here D_W is the damping zone width and d is the distance from the start of the damping zone boundary. The over all damping strength is controlled by the D_S value. Eq. (3.92) provides a smooth distribution of the damping strength. This is important because a sudden change in the damping strength acts similar to a wall, and reflects the waves. The size of the damping zone and the strength were defined by numerical investigations. Bunnik (1999) studied the importance of Froude number, $\tau = \frac{\omega U}{g}$, and the waves entrance angle on the efficiency of the damping zone. He showed that for $\tau > 1$ the required damping strength based on 90% damping is almost independent of τ . However, for $\tau < 1$ the required damping strength is increasing rapidly with τ and Fn , and therefore must be defined carefully.

Let us look into the physical meaning of the damping term in Eq. (3.90). Following Nakos et al. (1993), we set the velocity to zero and assume the velocity potential to be in the form $\phi = \phi_0(z, y) e^{i\omega t} e^{\sqrt{u^2 + v^2} z}$. Here ω is the wave frequency and u, v are the components of the wave number \mathbf{k} in x and y directions respectively. Then, from the free-surface boundary conditions with a damping term in Eqs. (3.90) and (3.91), the wave frequency is obtained,

$$\omega = i\nu \pm \left[g\sqrt{u^2 + v^2} - \nu^2 \right]^{1/2} \quad (3.93)$$

Let us now compare Eq. (3.93) to the continuous version of the dispersion relation without damping $\omega^2 = g\sqrt{(u^2 + v^2)}$. This shows that the damping strength ν shifts the frequency in the complex plain, which translates to a damping error from the numerical point of view. Moreover, the real part of the frequency is changed, which results in a dispersion error on the damping zone. This error can be avoided by adding a counter part to Eq. (3.90) for zero speed as shown in Eq. (3.94). One can

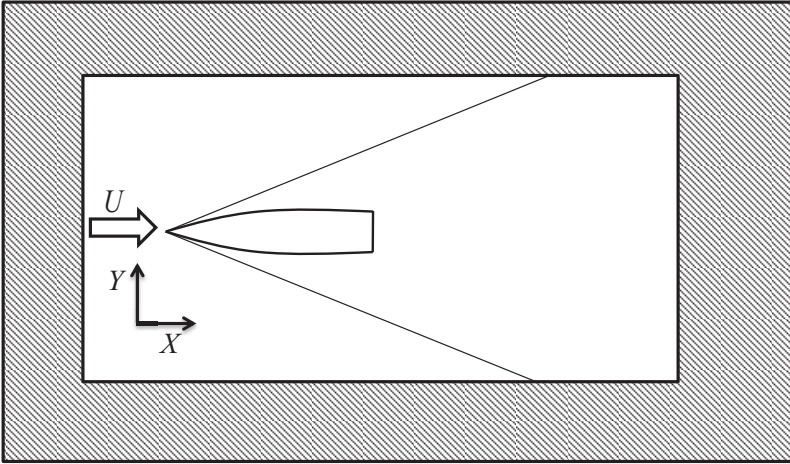


Figure 3.9: Schematic view of a damping zone. The shaded area represents the damping zone with a non-zero damping strength ν .

argue that since we are not interested in the solution on the damping zone, the error is not important.

$$\frac{\partial \zeta}{\partial t} = \frac{\partial \phi}{\partial z} - 2\nu\zeta + \frac{\nu^2}{g}\phi \quad \Rightarrow \quad \omega = i\nu \pm \left[g\sqrt{u^2 + v^2} \right]^{1/2} \quad (3.94)$$

The remaining question is, what kind of differentiation method must be used on the free surface in the time-domain problems. Kring (1994) used a shape function differentiation method. He applied smoothing filters on the free surface to eliminate the numerical waves. On the other hand, Bunnik (1999) argued that use of central difference is not stable, and used upwind difference to achieve a stable solution without smoothing. He linearized the unsteady velocity potential around the steady non-linear potential (Eq. (2.20)), and used the gradient of the steady potential to determine the upstream points. He also stated that for a small enough forward speed the central difference will be sufficient. This is again in agreement with the physical interpretation of the hyperbolic equations presented in Eq. (3.7.1). Bunnik (1999) also argued that this method can be used, even in presence of upstream waves, as long as a sufficient damping zone is introduced upstream. More details on the stability issues can be found in Chapter 4. Similar to the steady-state case, the upstream differencing is chosen for transient problems in the present study.

3.8 Solver scheme

Unlike most of the field methods, such as finite difference method (FDM) and finite element method (FEM), which give a narrow band equation system, the boundary element method (BEM) results in a fully populated matrix. The solution of an

equation system with fully populated matrix is more challenging in terms of the required memory and computation time. This is the reason why for larger problems the BEM method loses its advantages and becomes less efficient.

A BEM problem with N unknowns gives an equation system of $O(N^2)$, which requires $O(N^2)$ operations to form. Depending on the type of the matrix-solver, the computational time for solving the equation system varies. For instance, the LU-factorization method requires $O(N^3)$ operations. In the time-domain solutions of a linear problem (such as the ones studied here), only the right hand side of the equation system changes in each time step. Using LU-factorization, the coefficient matrix can be factorized once and used in all other time-steps. The solution using the factorized matrix need $O(N^2)$ operations. This method was adopted in the present study.

In order to reduce the time needed for solving the BEM equation system, the accelerated matrix solvers can be used. Predictor-FFT (p-FFT) and fast multipole method (FMM) are examples of such solvers. These methods can reduce the required memory and CPU operations as low as $O(N \log N)$. These methods were not implemented in the present study. Instead, as will be explained in Section 3.10, the program was written in a way to make changes in the matrix solver easily possible. Interested readers are referred to Shao (2010) for an interesting and rather complete review on the solution schemes. The choice of LU-decomposition is in agreement with the suggestions on the suitable application of different solvers in Shao (2010).

3.9 Grid generation

The solution procedure of a boundary element problem starts with discretizing the surfaces. Discretization plays an important role in the accuracy and stability of the solution (e.g. Chapter 4). The first step in discretization is the grid generation. Here we define the grid generation to be the process of distributing points on a surface and relating the properties of the points to a parametric space. Afterwards, the points are grouped into panels, elements, or patches which are the pieces of the surface. A grid can be structured or unstructured. The points on a structured grid can be mapped to a parametric space as shown in Figure 3.10. However, in an unstructured grid the points are distributed arbitrarily and it is not possible to form a mapping relation between the points on the surface and the parametric space.

It is well known that structured grids have better numerical properties, especially when it comes to calculation of the derivatives. Further, the use of higher order finite difference operators is easier on structured grids. However, the grid generation process for structured grids is complicated. This is a source of difficulty, especially when the surface geometry is complex.

The structured grid generation was adopted in the present study. Different methods can be used to generate structured grids. These methods can be simple, such as linear interpolation, or complicated, such as elliptic or hyperbolic grid generation. Let us start by assuming a surface bounded by four edges (for instance part

of the free surface), which can be defined by parametric curves. A differentiable and one-to-one mapping between the computational space and the parametric space, as well as the parametric space and the physical space, is assumed as shown in Figure 3.10 (see Section 3.9.1). The four corners of the surface are mapped to

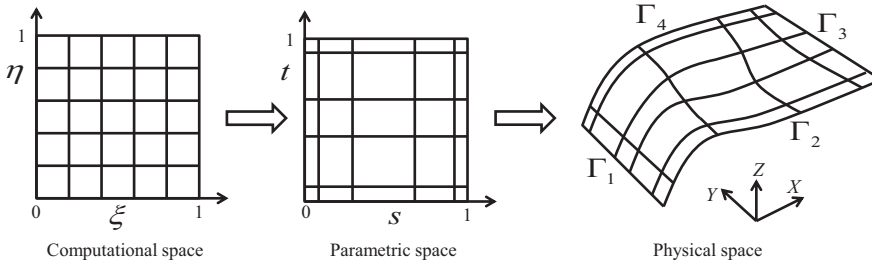


Figure 3.10: Surface grid generation and mapping in 3D space. (ξ, η) : computational space, (s, t) : parametric space, XYZ : physical space

the four corners of the parametric and computational domain with correct order. Moreover four edges of the surface are defined by $\xi = 0$, $\xi = 1$, $\eta = 0$ and $\eta = 1$ lines in the computational domain.

The lines $\xi = \text{const}$ or $\eta = \text{const}$ are called grid lines, while their intersections are called grid points. The quadrilaterals formed by the grid lines are called grid cells. Singularities must be avoided in the mapping. A singularity can arise, for instance, by mapping a line in the computational domain to a point in the physical domain. The boundaries of the physical surface must be defined in a way to avoid this type of singularity. The following points are important in generating a grid:

- Smooth grid lines, which give smoothly varying mapping coefficients.
- Concentration of grid points in to the areas with high variation of unknowns.
- A smooth variation in the area of the grid cells.
- Avoidance of distorted elements.

The goal is to find a suitable mapping between computational and physical space in order to acquire above properties as much as possible. The accuracy of the derivatives and numerical solution is dependent on the ability of a mapping function to meet these properties. Here, the details of the grid generation method will not be presented. Instead, a short summary of the methods used in the present study will be discussed. More details can be found in text books such as Thompson et al. (1999).

3.9.1 Distributing points on boundaries

Let us assume a boundary described by a parametric curve $\Gamma(s) = (x(s), y(s), z(s))$, where s is the curve parameter and between 0 and 1. It is not necessary for the parameter to have a physical meaning. However, the normalized curve length is

usually the first choice for s . The desirable vector of points on the curve Γ can be achieved by selecting a suitable vector of values for the curve parameter s . This brings the question of what are the suitable values and how we can control the point distribution on Γ by selecting them.

For this purpose, we define another parameter in $[0, 1]$ interval called ξ . A one-to-one relation between the points on Γ and the values in s and ξ is assumed. Let us assume that the points in ξ are always equally spaced. Since this is a suitable arrangement for numerical computations, we name the 1D space defined by the parameter ξ the *computational space*. Likewise, we name the 1D space defined by s *parametric* and 3D space *physical* space. Figure 3.11 shows these spaces for a sample curve. In this case, it is desired to have the points concentrated around the high curvature area. This is achieved by concentrating the points around the middle of the parameter s .

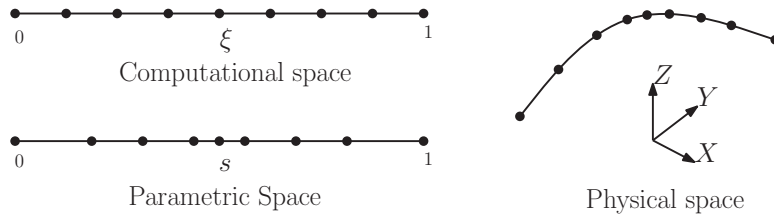


Figure 3.11: Distribution of points on a line in 3D space. ξ : computational space, s : parametric space, XYZ : physical space

$\rho(s) = \frac{\partial \xi}{\partial s}(s)$ can be viewed as a *grid point density* function. The larger value of ρ at a point s_0 means higher density of points at that point. By assuming a function for $\rho(s)$, the distribution for ξ is calculated as shown in Eq. (3.95).

$$\xi(s) = \int_0^s \rho(w)dw \quad (3.95)$$

Here w is the integration dummy variable. Some of the popular choices for the density function are,

- Equal arc length spacing, $\frac{\partial \xi}{\partial s} \propto \left| \frac{\partial \mathbf{x}}{\partial s} \right|$
- Curve-weighted spacing, points are concentrated on high curvatures $\frac{\partial \xi}{\partial s} \propto \kappa(s) \left| \frac{\partial \mathbf{x}}{\partial s} \right|$, when $\kappa(s)$ is the curvature.
- Grid attraction, points are concentrated around an attraction point u_j with strength k_j , $\frac{\partial \xi}{\partial s} \propto \frac{1}{\sqrt{(k_j(s-s_j))^2+1}}$

Using a combination of the above items is also a possibility. In the present study the main focus was on the third method. The grid attraction method makes it possible to increase the density of points around the areas with high variation of unknowns. This is important especially with a collocation method. Examples of

such cases will be discussed later in this study. A normalized form of the attraction function described above is chosen as shown in Eq. (3.96).

$$\frac{\partial \xi}{\partial s}(s) = \frac{\frac{1}{\sqrt{(k_j(s-s_j))^2+1}}}{\int_0^1 \frac{1}{\sqrt{(k_j(w-s_j))^2+1}} dw} \quad (3.96)$$

Substituting Eq. (3.96) into Eq. (3.95) and integrating, the mapping function between ξ and s is obtained as shown in Eq. (3.97).

$$\xi(s) = \frac{\operatorname{arcsinh}(k_j(s-s_j)) + \operatorname{arcsinh}(k_j s_j)}{\operatorname{arcsinh}(k_j(1-s_j)) + \operatorname{arcsinh}(k_j s_j)} \quad (3.97)$$

Assuming a distribution of values for s and an attraction point s_j with strength of k_j the corresponding distribution of ξ is obtained from Eq. (3.97). However, we are interested to obtain the s distribution by assuming a uniform ξ distribution, i.e. $s(\xi)$. This problem is solved by, first calculating $\xi(s)$ using a large number of points, and then using a linear interpolation to find the values of $s(\xi)$.

Let us demonstrate this by an example. Assume that it is desired to select m points on the curve Γ with concentration around the middle ($s = 0.5$). First, we define M to be the number of the intermediate points used for linear interpolation when $M > m$. More accurate results are obtained for larger values of M with the price of increased computational expenses. $M = 5m$ is suggested in Thompson et al. (1999) as a good approximation.

A uniform distribution of M points on s is assumed with $s_i = (i-1)\Delta s$, where $i = 1 \dots M$ and $\Delta s = 1/(M-1)$. Then, $\xi(s)$ is calculated for M points using Eq. (3.97). Figure 3.12 shows the distribution of points in computational and parametric space as well as the grid density function for $m = 11, M = 55, s_j = 0.5, k_j = 20$. Now, a uniform distribution of m points in the computational space is considered. The corresponding values for the same attraction point and strength in s can be found using the linear interpolation presented in Eq. (3.98).

$$s(\xi) = s(\xi_i) - \frac{\Delta s}{\xi_i - \xi_{i-1}}(\xi_i - \xi) \quad \xi_{i-1} < \xi \leq \xi_i \quad \text{and } i = 1 \dots M \quad (3.98)$$

Here Δs is from the intermediate level uniform distribution. Figure 3.13 shows the uniform distribution in ξ and the final concentrated distribution in s for $m = 11, s_j = 0.5$ and $k_j = 20$.

The choice of the attraction points is dictated by the problem requirement. For instance, in the wave making problem by a ship advancing in free surface, the velocity potential tends to be singular at the bow and stern area. Attraction points can be placed at these areas in order to ensure a higher density of collocation points. In this way, higher order variations of the unknowns can be captured even by methods with lower order elements.

Unlike attraction points, determination of the attraction strength is not straight forward. The equation system presented above has no closed-form solution for k_j . Eq. (3.99) gives an approximate relation between the point-density function and

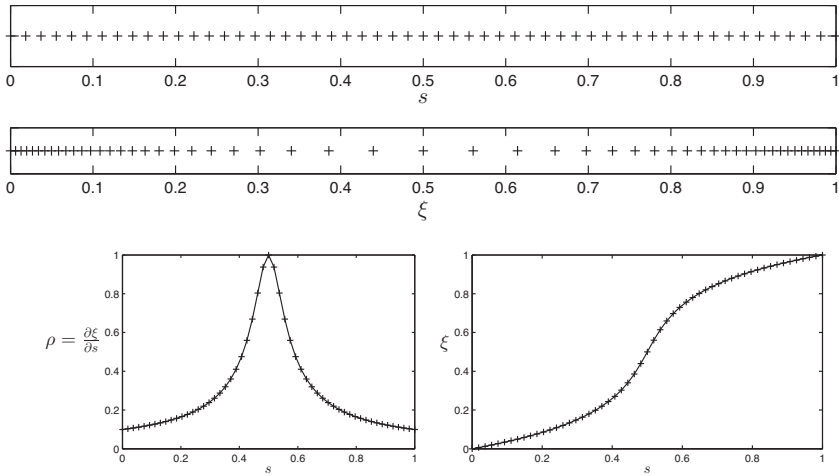


Figure 3.12: Influence of the grid density function in the grid attraction method (intermediate level). Number of points $M = 55$, Attraction point $s_j = 0.5$, Attraction strength $k_j = 20$, ξ : computational space, s : parametric space, $\rho = \frac{\partial \xi}{\partial s}$: grid density function. For a uniform distribution in s the point $s = 0.5$ is a repelling point in ξ .

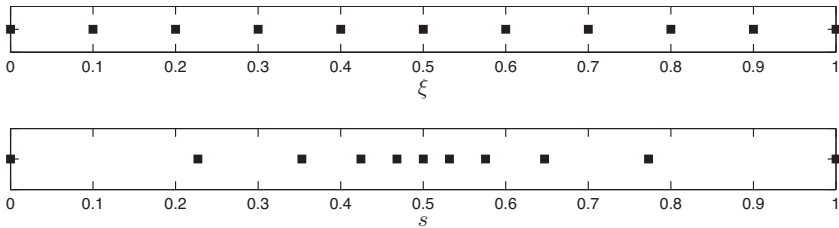


Figure 3.13: Influence of the grid density function in the grid attraction method (final level). Number of points $m = 11$, Attraction point $s_j = 0.5$, Attraction strength $k_j = 20$, ξ : computational space, s : parametric space, For a uniform distribution in ξ the point $s = 0.5$ is an attracting point in s .

the attraction factor. This value can be used as an initial guess and must be tuned until the desired distribution is achieved.

$$k_j \cong 15 \frac{\partial \xi}{\partial s}(s_j) \tag{3.99}$$

The attraction factor can be used to ensure a certain arc-length at the attraction point as well. This is particularly of importance in connecting boundaries of different surfaces together. A smooth transition between grids of different boundaries can be ensured by enforcing their elements to have equal sizes at the connecting points. Eq. (3.100) suggests an approximation for the attraction factor k_j if a

desired curve length $|\Delta \mathbf{x}|$ at the point s_j is prescribed.

$$k_j \approx 15 \frac{\Delta \xi}{|\Delta \mathbf{x}|} \frac{\partial \mathbf{x}}{\partial s}(s_j) \quad (3.100)$$

Here $\Delta \xi$ is the uniform distance in the computational space. $\frac{\partial \mathbf{x}}{\partial s}(s_j)$ term in Eq. (3.100) can be calculated using a simple finite difference method. Iterations on k_j value may be required in order to achieve the desired accuracy for the curve length at s_j . It is possible to define multiple attraction points on a single curve. The most popular case is two attraction points at the two ends, ($s_j = [0, 1]$). The method described above can be easily extended for such cases. The grid density function in Eq. (3.97) can be combined for K number of attraction points using a blending parameter λ_j with the condition $\sum_{j=1}^K \lambda_j = 1$ as shown in Eq. (3.101). The simplest choice would be $\lambda_j = 1/K$.

$$\xi(s) = \sum_{j=1}^K \lambda_j \frac{\operatorname{arcsinh}(k_j(s - s_j)) + \operatorname{arcsinh}(k_j s_j)}{\operatorname{arcsinh}(k_j(1 - s_j)) + \operatorname{arcsinh}(k_j s_j)} \quad (3.101)$$

More complicated types of grid density functions can be defined, for instance by taking the arc-length and curvature into account. For more details on this matter please see Thompson et al. (1999).

3.9.2 Algebraic surface grid generation

In the previous section, a method for distributing and controlling points on a curve in 3D space was introduced. The boundaries of a surface in 3D space can be treated as separate curves. A surface grid can be created by connecting the points distributed on the boundaries. One of the methods for this purpose is transfinite interpolation (TFI) technique. Different types of transfinite interpolations exist such as linear, Lagrangian and Hermite-cubic. In the present work, a linear TFI method was adopted which is summarized here.

Let us assume a surface bounded by four curves, Γ_1 to Γ_4 , as shown in Figure 3.10. The positions of the points, distributed on a surface, can be calculated based on the boundary points, using a linear TFI as shown in Eq. (3.102) below.

$$\mathbf{x}(\xi, \eta) = S(\xi, \eta) + T(\xi, \eta) + ST(\xi, \eta) \quad (3.102)$$

Here S , T and ST are defined in Eq. (3.103).

$$\begin{aligned} S(\xi, \eta) &= (1 - \xi)\Gamma_1(\eta) + \xi\Gamma_3(\eta) \\ T(\xi, \eta) &= (1 - \eta)\Gamma_2(\xi) + \eta\Gamma_4(\xi) \\ ST(\xi, \eta) &= (1 - \xi)(1 - \eta)\Gamma_1(0) + \xi\eta\Gamma_3(0) \\ &\quad + \eta(1 - \xi)\Gamma_1(1) + \xi(1 - \eta)\Gamma_3(1) \end{aligned} \quad (3.103)$$

3.9.3 Elliptic surface grid generation

A grid, generated by a transfinite interpolation, can be relaxed and refined using an elliptic grid generation method. Unlike TFI method, a better control over the grid quality inside the domain can be achieved by this method.

The method is based on assuming that the one-to-one mapping function, which relates the physical domain to the parametric domain ($(\mathbf{x} \mapsto (s, t))$), is a harmonic function on the surface inside the boundaries. Moreover, a *grid control map* is defined to be a differentiable one-to-one function, which relates the computational and parametric domain ($((\xi, \eta) \mapsto (s, t))$). The combination of the grid control map and inverse of the harmonic map, defines a map which transforms the computational domain to the physical domain ($((\xi, \eta) \mapsto \mathbf{x})$). This transformation obeys a quasi-linear system of elliptic partial differential equations shown in Eq. (3.104).

$$A\mathbf{x}_{\xi\xi} - 2B\mathbf{x}_{\xi\eta} + C\mathbf{x}_{\eta\eta} + D\mathbf{x}_{\xi} + E\mathbf{x}_{\eta} = 0 \quad (3.104)$$

where,

$$\begin{aligned} A &= \mathbf{x}_{\eta} \cdot \mathbf{x}_{\eta} & B &= \mathbf{x}_{\xi} \cdot \mathbf{x}_{\eta} & C &= \mathbf{x}_{\xi} \cdot \mathbf{x}_{\xi} \\ D &= AP_{11} - 2BP_{21} + CP_{31} \\ E &= AP_{12} - 2BP_{22} + CP_{32} \end{aligned} \quad (3.105)$$

Here P_{ij} are the grid control mapping operators, which are obtained from the control criteria required on the inner domain of the grid. The position of the boundary points are added to the equation system as Dirichlet boundary conditions. Other boundary conditions can be added to the equation system through the grid control maps. For instance, $\frac{\partial s}{\partial n} = 0$, where n is the local normal vector on a boundary Γ_1 , can be added to enforce the grid lines to be normal to the boundary. Similarly, $\frac{\partial s}{\partial \eta}$ can be selected to set a certain height for the cells close to the boundary. In general, grid control maps can be used to enforce desirable properties such as,

- Arc length control.
- Orthogonality at the boundaries.
- Internal grid orthogonality.
- Cell height at the boundaries.

The non-linear elliptic equation system in Eq. (3.104) can be solved by an iterative method (for instance Picard iteration method). Usually, the boundary conditions and control operators are kept constant during the iterations. The simplest control grid map is the identity map. In this case, all the control mapping operators are zero and Eq. (3.104) simplifies to,

$$A\mathbf{x}_{\xi\xi} - 2B\mathbf{x}_{\xi\eta} + C\mathbf{x}_{\eta\eta} = 0 \quad (3.106)$$

with the Dirichlet boundary condition at the boundaries. This type of grid is called *Laplace* or *harmonic* grid. The control mapping operators can also be calculated

from the grid attraction functions presented in Section 3.9.1. In this way, attraction functions can be used in combination with elliptic grid generation.

The computational effort, required for implementation of the other aforementioned grid control maps, can be high. We shall not discuss the details of these methods here. Interested readers are referred to Thompson et al. (1999) for further details and algorithms for imposing these conditions.

3.9.4 Paneling

Depending on the order and shape of the panels (elements), they require different number of points. For instance, quadrilateral constant panels need four points, while higher order quadratic elements need nine or eight points. The points must be arranged to follow the right-hand-rule and be consistent with the normal vector. In the present study, the normal vector on an element was assumed to point inside the fluid domain. Adaptive paneling scheme was used to group the grid points into elements, while ensuring the surface continuity. Distorted elements were avoided by breaking them into triangles, in order to avoid singular mapping points.

3.10 Programming

As mentioned in previous sections, a BEM problem is computationally expensive to form and solve. Therefore, developing an efficient program is important. Moreover, existence of many different choices for the surface and unknown representation, suggests many implementation scenarios. Therefore, an ideal program must be flexible. A flexible program provides the possibility to implement different scenarios with minimum modification and maximum usage of the existing code. Moreover, it is easier to understand and develop.

Flexibility in programs can be achieved by introducing concepts such as *modularity*, *abstraction* and *encapsulation*. Complicated programs can be simplified into bits and pieces by applying these concepts, which are studied extensively in the field of computer science and software engineering. *Object-oriented programming* (OOP) is a methodology which is developed to answer some of these needs. Applications of this programming methodology in scientific computing, can be found, for instance, in Yang (2000). More practical examples can be found, for instance, in Alnaes et al. (2009) for finite element and Qiao (2006) for boundary element programming.

Introducing these software engineering concepts into developing a computational program has lots of advantages. However, the short-coming of this idea is related to the program efficiency. The more a program is modular and flexible, it becomes less efficient. This can be easily seen when computational programs are written by object-oriented programming in a language such as C++ (see for instance Veldhuizen and Jernigan (1997) and Bassetti et al. (1998)). In general, a code runs faster, if it translates to machine language with minimum over-head. That is the reason why traditional scientific programming languages, such as FORTRAN, is used to write computational codes.

One possible solution to this problem is the so-called *compile-time* or *template* programming in C++ (e.g. Alexandrescu (2001)). This programming method makes it possible to enjoy the abstraction provided by the object-oriented programming, while achieve the efficiency required for a computational software. In fact, a program written in this method can be even faster than the codes written in languages such as FORTRAN (e.g. Veldhuizen and Jernigan (1997)). The idea of using the template programming in order to increase the computational efficiency was first introduced by Veldhuizen (1995) in the concept of *expression templates*. The idea behind this method is simple. The code is written in a way that the pre-compiler can translate the abstract-code to a detailed-code at the compile time, which is the source of the name compile-time programming. A sample of a matrix operation in abstract form, and after the pre-compilation is shown in Listings 3.1 and 3.2 respectively.

Using this method, almost any type of mathematical operator can be implemented and used in abstract form with high efficiency. In this way, complicated mathematical operations can be written simply in abstract forms and translated to a complicated, but efficient, code during the pre-compiling process, and then passed for compilation. This idea was successfully implemented in software packages such as Blitz++ (Veldhuizen, 2006) for matrix algebra and OpenFOAM (*OpenFOAM*, n.d.) for CFD calculations.

Listing 3.1: Code sample for a matrix summation in abstract form.

```
D = A + B + C
```

Listing 3.2: Code sample for a matrix summation in expanded form.

```
for (int j=1; j<=n; j++)
  for (int i=1; i<=m; i++)
    D(i, j) = A(i, j) + B(i, j) + C(i, j)
```

A C++ library for boundary element calculations was developed based on, aforementioned object-oriented programming and expression templates. Matrix algebra is implemented using Blitz++ (Veldhuizen, 2006) library. The library enjoys a great flexibility in introducing different types of discretization. Parallel computation (using OpenMP) during calculation of coefficient matrices was made possible, using the modular architecture of the program. It was possible to implement different hydrodynamic problems using the abstract mathematical formulation, without sacrificing the program's efficiency.

Let us demonstrate the use of abstract mathematical expressions by an example. Consider the steady-state problem of a ship advancing with forward speed in calm water. The mathematical formulation of the problem, presented in Eq. (3.107),

can be written in its discrete form using the BEM library as shown in Listing 3.3.

$$\begin{aligned} & \iint_{S_B} \phi(\mathbf{q}) \frac{\partial G(\mathbf{p}, \mathbf{q})}{\partial n(\mathbf{q})} dS + \iint_{S_F} \phi(\mathbf{q}) \frac{\partial G(\mathbf{p}, \mathbf{q})}{\partial n(\mathbf{q})} dS \\ & - \frac{U^2}{g} \iint_{S_F} \frac{\partial^2 \phi}{\partial x^2} G(\mathbf{p}, \mathbf{q}) dS - \mathcal{C}(\mathbf{p}) \phi(\mathbf{p}) = \iint_{S_B} \frac{\partial \phi(\mathbf{q})}{\partial n(\mathbf{q})} G(\mathbf{p}, \mathbf{q}) dS \end{aligned} \quad (3.107)$$

Listing 3.3: Code sample for a body advancing in free surface with forward speed U

```

/* comments:
B:          Body object.
FS:          Free surface object.
dphidn_B:   'dphidn' on body.
dn_FS:      'dn' operator on the free surface.
phi:        'phi' on the free surface and body.
C:          solid angles on the free surface and body.
Int<F,S>:    taking integral of function 'F'
              on surface 'S'.
dx<S>:      'dx' operator of surface 'S'.
zeta:       free surface elevation.
*/
dphidn_B = U*B.nx;
dn_FS    = U^2/g * dxx<FS>;

phi = solve (
    Int<dGdn,B> + Int<dGdn,FS> - Int<G,FS> * dn_FS - C
    ,
    Int<G,B> * dphidn_B
);

zeta    = - U/g * dx<FS>(phi);

```

In this way, different types of problems can be solved just by modifying the governing equations and the boundary conditions in their mathematical form. For instance, a more complicated type of the free-surface boundary condition, based on a double-body linearization, can be implemented just by modifying the '*dn_FS*' operator in its abstract form. It must be noted that the discretization part of the program which leads to creation of *B* and *FS* objects in Listing 3.3, is done as simply by other parts of the problem, and are not shown.

The goal here is not to present the details of the program and just to give an impression on the architecture of the code. Programming the most advanced and efficient boundary integral code was not the goal of the present study. However, the nature of the study required the possibility to implement different types of problems, with different boundary conditions. Therefore, the idea of having a flexible program with the possibility to write boundary integral mathematics in an abstract form was pursued. By taking advantage of the program's modularity, different aspects of the formulation, such as discretization type, unknown distribution order,

surface representation order, matrix solver, and even the dimension of the problem (2D or 3D) could be changed easily. Therefore, the program, potentially, gave the possibility to compare different discretization methods in one environment. Considering the limited time, however, different aspects of the program were developed only to meet with the requirements of the problems at hand.

Chapter 4

Evaluation of discretization methods

4.1 Introduction

The accuracy and stability of the numerical method presented in Chapter 3 are investigated in this chapter. The Fourier transformations of the continuous and discrete dispersion relations are compared to obtain an estimation of the method's accuracy. Furthermore, the temporal stability of the time-discretized problem is addressed using the growth-rate method.

Sclavounos and Nakos (1988) used Fourier analysis to study the dispersion and damping properties of the waves generated by a disturbance moving under the free surface with a constant velocity in two dimensions. They investigated the consistency and convergence of the discrete problem. The combination of finite difference schemes with constant panels were investigated in their paper. Moreover, they looked into the properties of a continuous differentiation using a third order B-spline method (equivalent to a second order polynomial). They concluded that their method have a better dispersion and damping properties than constant element method. Moreover, they linked the numerical instabilities to the presence of spurious roots in the discrete dispersion relation. Romate (1989) also studied this problem by combining finite difference operators and higher order polynomials as shape functions.

Later on, Nakos (1990) extended the two-dimensional analysis to three dimensions. He studied the waves generated by a moving disturbance under the free surface, which undergoes harmonic oscillations. He showed that the accuracy of the numerical method also depends on the elements' aspect ratio and $\tau = U\omega/g$. Moreover, he argued that the aliasing of wave energy can be the reason behind the energy build-up in spurious roots and lead to the saw-tooth instability. Kim et al. (1997) used the numerical method from Nakos (1990) and looked at the accuracy of the numerical method in capturing the waves traveling on the free surface in absence of current. They investigated *temporal* stability and showed that it results

in a Courant-type condition.

Raven (1996) considered the desingularization effects on the properties of a constant element method for the waves generated by a moving disturbance. Later Sieruevogel (1998) studied the accuracy of both upstream and downstream waves using constant elements and finite difference method in two dimensions. She also considered the time discretization schemes for numerical calculation of the time derivatives and investigated the temporal stability of her method. Bunnik (1999) expanded the calculations by Sieruevogel (1998) to three dimensions. He also investigated the temporal stability using Z-transformation. He showed that although a central difference scheme have good dispersion and damping properties they may lead to an unstable solution.

Büchmann (2000) studied the spatial and temporal convergence and stability of the B-spline method with shape function differentiation. He also presented a Courant-type condition for stability, which depends on discretization properties. Later in Büchmann (2001) he showed that the mentioned condition is not a *sufficient* but a *necessary* condition. He argued that forward speed (or current) can change the nature of instabilities from saw-tooth instability, and reduce the frequency of the numerical waves. Recently, Kim et al. (2005) expanded the calculations for constant elements, with desingularization and collocation point shift, to include finite water depth effects as well.

The present study is in some areas an extension to the previous studies mentioned above. Not all the aspects touched upon in the previous studies are covered here. In some parts, comparisons between the results presented here and the ones in the previous studies are presented. Different aspects of the discretized dispersion relation are investigated in the following sections. The intention is to find out the limitation of different models and assess the influence of different types of discretization step by step. The analysis presented here is not complete. For instance, the influence of grid non-uniformity and forcing function are not taken into account and left for future works. As argued by Büchmann (2001), these may have influence on the properties of the numerical method.

We start by focusing on the error in estimating the velocity potential on the free surface. For this purpose, it is assumed that the velocity potential on the body is known. In other words, all the effects due to presence of the body are considered as a known forcing function. In this way, the boundary integral formulation in Eq. (2.81) can be rewritten as Eq. (4.1) shown below.

$$\mathcal{C}(\mathbf{x})\phi(\mathbf{x}) + \iint_{S_F} G(\mathbf{x}, \boldsymbol{\xi}) \frac{\partial \phi(\boldsymbol{\xi})}{\partial n(\boldsymbol{\xi})} dS - \iint_{S_F} \phi(\boldsymbol{\xi}) \frac{\partial G(\mathbf{x}, \boldsymbol{\xi})}{\partial n(\boldsymbol{\xi})} dS = F \quad (4.1)$$

Here F is the forcing function. The forcing function represents the influence of all boundaries, except the free surface, as shown in Eq. (4.2).

$$F = \iint_{S_R} \phi(\boldsymbol{\xi}) \frac{\partial G(\mathbf{x}, \boldsymbol{\xi})}{\partial n(\boldsymbol{\xi})} dS - \iint_{S_R} G(\mathbf{x}, \boldsymbol{\xi}) \frac{\partial \phi(\boldsymbol{\xi})}{\partial n(\boldsymbol{\xi})} dS \quad (4.2)$$

Here S_R refers to all the remaining boundaries. Although the time parameter is omitted for clarity, ϕ is a function of both time and space ($\phi(\mathbf{x}, t)$). Assuming the

free surface to be flat on the $z = 0$ plane by linearization, the third term in Eq. (4.1) is equal to zero. Moreover, the solid angle is equal to 2π on the flat free surface. Let us assume that the free surface is extended to infinity. A uniform current U in positive x direction, or alternatively a vessel with forward speed U in negative x direction, is assumed. Then, the normal derivative of velocity potential on the free surface can be substituted from the linearized Neumann-Kelvin free surface boundary condition Eq. (2.33),

$$2\pi\phi(\mathbf{x}) + \frac{1}{g} \iint_{S_F} [\phi_{tt}(\boldsymbol{\xi}) + 2U\phi_{t\xi}(\boldsymbol{\xi}) + U^2\phi_{\xi\xi}(\boldsymbol{\xi})] G(\mathbf{x}, \boldsymbol{\xi}) dS = F \quad (4.3)$$

Let us separate the integrals for each term, and take the Fourier transform of the equation with respect to x, y and t . Using the convolution properties of the Green function and Fourier transform of the derivatives, we can write (see Appendix B.2),

$$2\pi\tilde{\phi} + \left(\frac{(-i\omega)^2}{g} + \frac{2U(-i\omega)(ik \cos \theta)}{g} + \frac{(ik \cos \theta)^2}{g} \right) \tilde{G}\tilde{\phi} = \tilde{F} \quad (4.4)$$

Here $\tilde{\phi}$ is the continuous Fourier transform of velocity potential and a function of (k, θ, ω) instead of (x, y, t) . Using inverse Fourier transform, the velocity potential is obtained as,

$$\phi(x, y, t) = \frac{1}{8\pi^3} \int_{-\infty}^{\infty} \int_{-\pi}^{\pi} \int_0^{\infty} \frac{\tilde{F}}{\tilde{\mathcal{W}}} e^{i(\omega t - kx \cos \theta - ky \sin \theta)} k dk d\theta d\omega \quad (4.5)$$

where

$$\tilde{\mathcal{W}} = 2\pi + \left(\frac{-\omega^2}{g} + \frac{2U\omega k \cos \theta}{g} + \frac{-k^2 \cos^2 \theta}{g} \right) \frac{2\pi}{|k|} \quad (4.6)$$

It is known that the poles of the integral's kernel ($\tilde{\mathcal{W}} = 0$) in Eq. (4.5) correspond to the wave-like solutions of the velocity potential. Setting $\tilde{\mathcal{W}} = 0$ and rearranging the equation, the familiar dispersion relation for a propagating wave is obtained (Eq. (4.7)).

$$\tilde{\mathcal{W}} = -\omega^2 + 2U\omega \cos(\theta)k - U^2 \cos(\theta)^2 k^2 + g|k| = 0 \quad (4.7)$$

Here k is the wave number, θ is the angle of propagation direction, and ω is the wave frequency. As expected, the representation of the problem using a continuous distribution of sources and dipoles, on a free surface extending to infinity, does not change the dispersion relation. However, in order to solve the problem numerically, we need to truncate and discretize the free surface. Truncation and discretization of the free surface introduce errors in our numerical model. These errors can be estimated by comparing the discretized version of the boundary integral formulation to the continuous form. Here, we neglect the truncation effects and focus on discretization. Both space and time discretization can introduce errors and therefore

are of importance. Since we are looking at the errors in the free-surface's velocity potential, it is convenient to measure it in terms of the errors in wave length (dispersion) and amplitude (damping or amplification).

Let us start by assuming the free surface to be discretized into infinite number of rectangular elements. The elements are assumed to be uniform in size with constant aspect ratio $\Lambda = \Delta y / \Delta x$, where Δx and Δy are the elements' spans in x and y directions respectively. As showed in detail in Chapter 3, the integral over the free surface changes into a summation over all elements. The summation over elements can be related to the summation over base functions. This is most natural for the B-spline method. As mentioned in Section 3.4, a first order B-spline corresponds to a constant panel, keeping in mind that the number of elements and shape functions are the same. For HOBEM, the linear shape functions can be related to the linear B-spline functions by changing the definition of the element's span. This is only true for uniform elements. The method presented here is not directly applicable for HOBEM of order more than linear. The elements of HOBEM represent the unknowns with a continuous slope inside the elements' boundaries, but a discontinuity exist at the boundaries. Therefore the shape functions no longer have the convolution properties required by the mathematical model (see Section B.3). The properties of the B-spline method of order higher than two can be studied to give an indication of the numerical properties of HOBEM.

Here, the two variable centered B-splines with the same order in both directions is adopted ($B_j^{(m)(m)} = B_j^{(m)}$). The B-spline base function is the same for all elements. Therefore, different elements base functions can be related to a single function at the origin by means of a simple translation (see Section B.3). Using this property the boundary integral formulation shows discrete convolution form as shown in Eq. (4.8).

$$\begin{aligned} 2\pi \sum_{j=-\infty}^{\infty} \phi_j B_{i-j}^{(m)} + \frac{1}{g} \sum_{j=-\infty}^{\infty} \left(\frac{\partial^2 \phi}{\partial t^2} \right)_j \mathcal{S}_{i-j} \\ + \frac{2U}{g} \sum_{j=-\infty}^{\infty} \left(\frac{\partial^2 \phi}{\partial x \partial t} \right)_j \mathcal{S}_{i-j} + \frac{U^2}{g} \sum_{j=-\infty}^{\infty} \left(\frac{\partial^2 \phi}{\partial x^2} \right)_j \mathcal{S}_{i-j} = F \end{aligned} \quad (4.8)$$

Here, $B_{i-j}^{(m)} = B_0^{(m)}(\mathbf{x}_i - \mathbf{x}_j)$ and,

$$\mathcal{S}_{i-j}^{(m)} = \mathcal{S}_j^{(m)}(\mathbf{x}_i - \mathbf{x}_j) = \iint_{-\infty}^{\infty} B_o^{(m)}(\boldsymbol{\xi}) G(\mathbf{x}_i - \mathbf{x}_j - \boldsymbol{\xi}) d\xi d\eta \quad (4.9)$$

where, \mathbf{x}_i and \mathbf{x}_j are the so-called field and source points respectively. Getting semi-discrete Fourier transform of Eq. (4.8) and using the discrete convolution properties, the *discrete dispersion relation* will be obtained, as shown in Eq. (4.10) below, where $(\hat{\cdot})$ represents the semi-discrete Fourier transformation.

$$\widehat{W} = 2\pi g + \widehat{D}^{(tt)} \frac{\widehat{\mathcal{S}}}{\widehat{B}^{(m)}} + 2U \widehat{D}^{(t)} \widehat{D}^{(x)} \frac{\widehat{\mathcal{S}}}{\widehat{B}^{(m)}} + U^2 \widehat{D}^{(xx)} \frac{\widehat{\mathcal{S}}}{\widehat{B}^{(m)}} = 0 \quad (4.10)$$

Here, \widehat{D} is the semi-discrete Fourier transform of the differentiation operator, which depends on the method of differentiation (see Section B.2.7). The expressions for $\widehat{B}^{(m)}$ and \widehat{S} are presented in Eqs. (B.54) and (B.56) respectively.

Similar to the continuous problem, the roots of the discrete dispersion relation represent the wave-like solutions of the discrete problem. Ideally these roots in Eq. (4.10) must be identical to the roots of the continuous dispersion relation in Eq. (4.7). However, in reality this is not the case. Assuming a frequency ω , a current speed U , and an angle θ the possible wave number k is obtained by solving Eq. (4.10). As mentioned before, the difference between the solution in the discrete and continuous problems can be evaluated in terms of the dispersion and damping errors. Following Sierrevogel (1998) and Bunnik (1999), let us assume the following relation between discrete (k_d) and continuous (k_c) wave numbers.

$$k_d = k_c(1 + C_r + iC_i) \quad (4.11)$$

In this way, C_r is an indication to dispersion error, while C_i represents the damping or amplification error. Looking at Eq. (4.5), we can conclude that $C_r > 0$ corresponds to shorter and $C_r < 0$ to longer numerical waves in comparison to the continuous waves, respectively. Moreover, $C_i < 0$ introduces damping, while $C_i > 0$ corresponds to amplification of the wave amplitude. It must be noted that the damping/amplification error due to discretization, i.e. C_i , must not be confused with a floating body damping coefficient introduced in Section 2.9. A step by step analysis of the discretization methods are presented in the following sections.

4.2 Zero forward speed (current)

To simplify the problem, the properties of the discrete dispersion relation can be compared to continuous one part by part. Let us start by focusing on a case without forward speed or current. Moreover, we assume the waves to travel only in positive x direction, which reduces our equations to two dimensional. Then, the continuous dispersion relation in Eq. (4.7) reduces to Eq. (4.12) below.

$$\widetilde{\mathcal{W}} = g|k| - \omega^2 = 0 \quad (4.12)$$

The discrete dispersion relation for this case can have different forms. By assuming continuous or discrete time and space three different sub-problems can be created as follows.

4.2.1 Continuous time and discrete space

As a first step, a problem continuous in time and discrete in space is assumed. This is the case, for instance, when a steady harmonic wave problem on a discrete free surface is studied. The discrete dispersion relation for this problem is shown in Eq. (4.13) below.

$$\widehat{\mathcal{W}} = 2\pi g\widehat{B}^{(m)} - \omega^2\widehat{S} = 0 \quad (4.13)$$

Here the time-derivative operator is substituted using continuous Fourier transformation (see Section B.2.7). The obtained wave numbers from the two dispersion relations, for different B-spline orders, and are compared in Figure 4.1 using the notation in Eq. (4.11). As Figure 4.1 shows, discretized waves are longer than

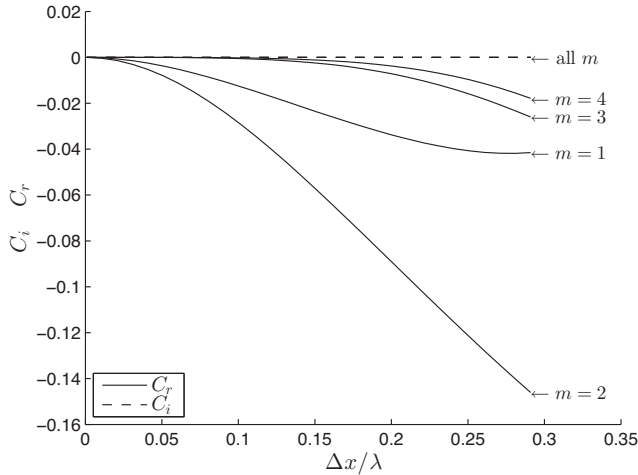


Figure 4.1: Dispersion and damping for waves without current, discretized space and continuous time, C_r : Dispersion, C_i : Damping, m : B-spline order, λ : Wave length., Δx : Element span in x

continuous waves. Meaning that the discretization introduces a *dispersion* in the problem. As expected, the error approaches zero by reducing the element-span to wave length ratio. The error also depends on the order of discretization. It is interesting to point out that the results for linear elements ($m = 2$) show higher dispersive solution than constant panels ($m = 1$). This has been reported before also by Romate (1989) for linear polynomials. Increasing the order to more than $m = 2$ improves the dispersive properties significantly. The damping introduced due to space discretization in this case is zero for all order of base functions. The dispersion error can be predicted, and controlled, by choosing a reasonable element-span to wave-length ratio for important waves in the problem. For instance, having 15 elements per wave length gives a dispersion error of order lower than one present for constant panel method (Sierevogel, 1998), which is in agreement with the practical guidelines for such problems. It is possible to conclude from Figure 4.1 that the number of elements can be reduced for higher order distributions, which consequently reduces the computational cost.

Figure 4.2 shows the relation between wave frequency and wave number from the discrete and continuous dispersion relations for different orders of space discretization. It is interesting to note that the wave group velocity (V_g), which is defined by the slope of $\omega - k$ curve, goes to zero when $\Delta x/\lambda$ approaches 0.5. As mentioned by Kim et al. (1997), these waves correspond to the so-called saw-tooth waves, with a wave length $\lambda = 2\Delta x$. Since the group velocity approaches zero for

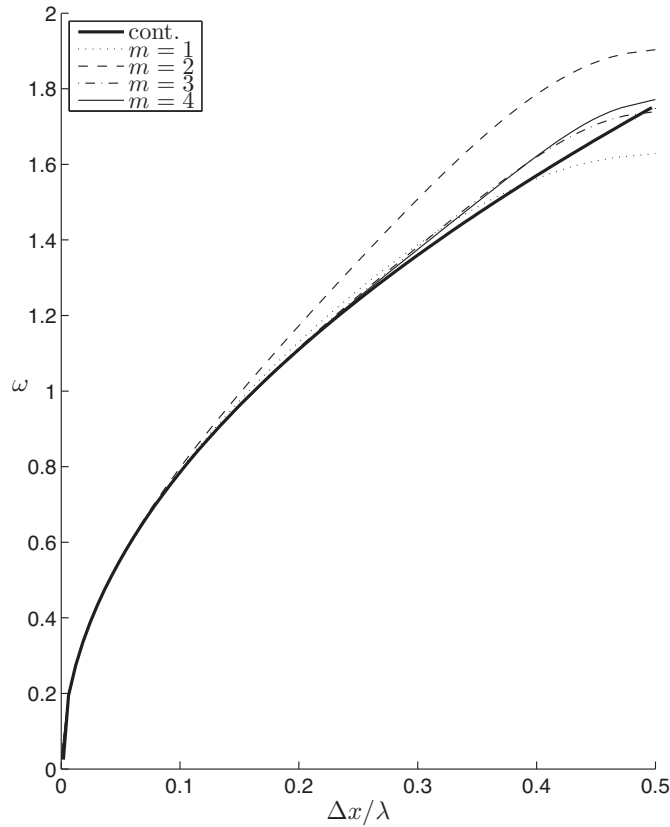


Figure 4.2: Frequency and wave number relation for discrete dispersion relation without current, discretized space and continuous time, ω : wave frequency, *Cont.*: Continuous solution, m : B-spline order, λ : Wave length, Δx : Element span in x

these wave-lengths, they can not carry the energy away from the source. Therefore, the energy introduced by a disturbance, such as an oscillating body, into these wave numbers amplifies in time. This can be one of the reasons behind the saw-tooth instability in the boundary integral solution of free surface waves, which was first mentioned by Longuet-Higgins and Cokelet (1978).

4.2.2 Continuous space and discrete time

Now let us assume a continuous space. This is usually not the case from a practical point of view. However, in this way, it is possible to study the influence of time discretization, independent of space. The discrete dispersion relation for continuous space and discrete time reduces to Eq. (4.14) shown below.

$$\widehat{\mathcal{W}} = g|k| + \widehat{D}^{(tt)} = 0 \quad (4.14)$$

Here, the backward differentiation was adopted for calculating the time derivatives. $\widehat{D}^{(tt)}$ is the Fourier transform of the finite difference operator for the double derivative in time, which depends on the finite difference operator order (see Section B.2.7). It is possible to implement more advanced time marching methods, such as ABM4 and RK4, in this case. However, including space discretization in an analysis, which is using a more advanced time-marching method, is not straight forward. Therefore, only the backward difference methods were considered in the present analysis, and latter combined with space discretization to give an indication of the importance of time marching methods on the overall solution.

The dispersion and damping of discrete waves for first, second, and third order backward finite difference operators are presented in Figure 4.3. The first order operator gives longer waves, while the second and third order operators result in shorter waves than the continuous problem. The best convergence rate by decreasing time-step belongs to the third order method. However, the damping error (C_i) of this method is positive, which corresponds to amplification in time and consequently an unbounded solution. The second order method shows better damping properties than the first order. Therefore, among backward difference methods, the second order method is more suitable for our problem.

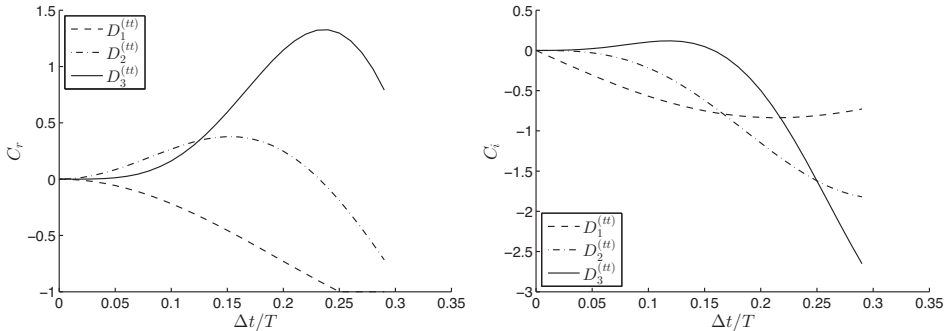


Figure 4.3: Dispersion and damping for waves without current, discretized time and continuous space. C_r : Dispersion, C_i : Damping, $D_k^{(tt)}$: k th order backward finite difference operator for double derivative in time, T : Wave period, Δt : Time step.

4.2.3 Discrete time and space

The combined time and space discretization is considered in this section. The discrete dispersion relation, with both time and space discretization, and without current is shown in Eq. (4.15) below.

$$\widehat{\mathcal{W}} = 2\pi g \widehat{B}^{(m)} + \widehat{D}^{(tt)} \widehat{\mathcal{S}} = 0 \quad (4.15)$$

The expression for $\widehat{B}^{(m)}$ and $\widehat{\mathcal{S}}$ can be found in Eqs. (B.54) and (B.56), respectively. Based on the results in the previous section, the second order backward

differentiation operator was chosen for double derivatives in time.

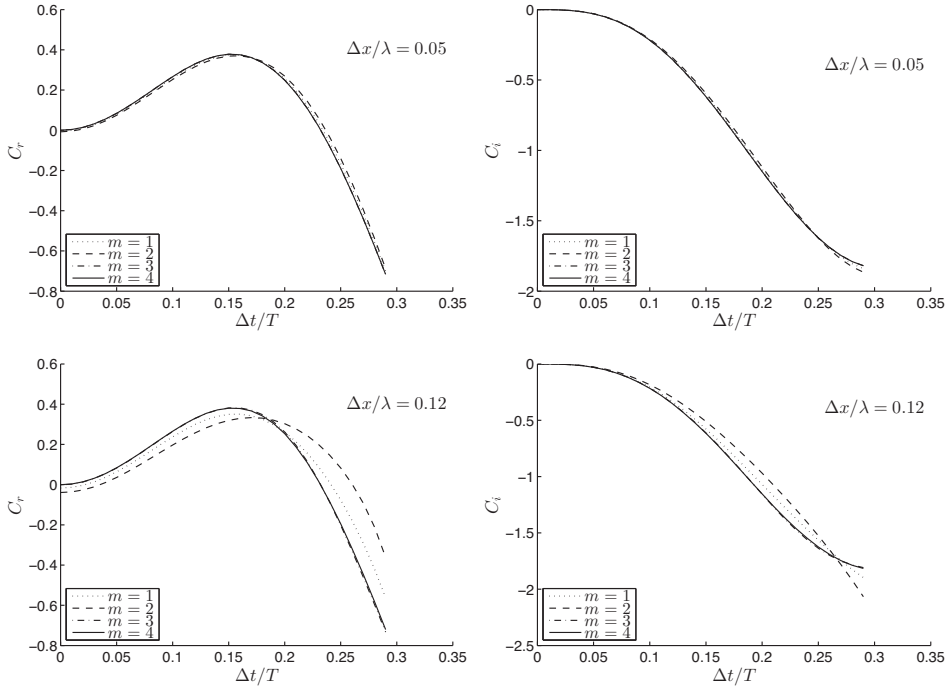


Figure 4.4: Dispersion and damping for waves without current, discretized time and space for different B-spline orders ($D_2^{(tt)}$). C_r : Dispersion, C_i : Damping, m : B-spline order, λ : Wave length., Δx : Element span in x , T : Wave period, Δt : Time step

Figure 4.4 shows the discrete wave dispersion and damping, with respect to $\Delta t/T$, for different values of B-spline order, and $\Delta x/\lambda$. As Figure 4.4 suggests, for $\Delta x/\lambda = 0.05$ the accuracy of the numerical method is dictated by the time derivative scheme, and the B-spline order plays no significant role. As $\Delta x/\lambda$ increases to 0.12, the influence of the spatial discretization appears. By decreasing the time-step, the discretized problem converges to a solution which is different than the continuous solution. As Figure 4.1 suggests, increasing the B-spline order decreases the dispersion error. It is interesting to note that the damping factor C_i shows dependency to the spatial discretization order, although the introduced damping by the spatial discretization was zero in the time-continuous case.

Figure 4.5 compares the continuous and discrete relation between the non-dimensional wave frequency and wave number, for two different spatial discretization orders. The second order backward difference operator was used for calculation of time double derivative. Different curves are plotted for different values of $\beta = \sqrt{\Delta x/(g\Delta t^2)}$, which indicates the relation between time-step and element-span. Comparing Figure 4.5 with Figure 4.2, we see that the group velocity no

longer approaches zero for the saw-tooth wave number, and instead, it goes to infinity. This was true for all orders of spatial discretization. This effect may be related to the damping introduced by the time discretization. Therefore, presence of saw-tooth instabilities are less expected in this case. However, as it will be discussed latter, it is not easy to make a general conclusion on the stability criteria for practical problems.

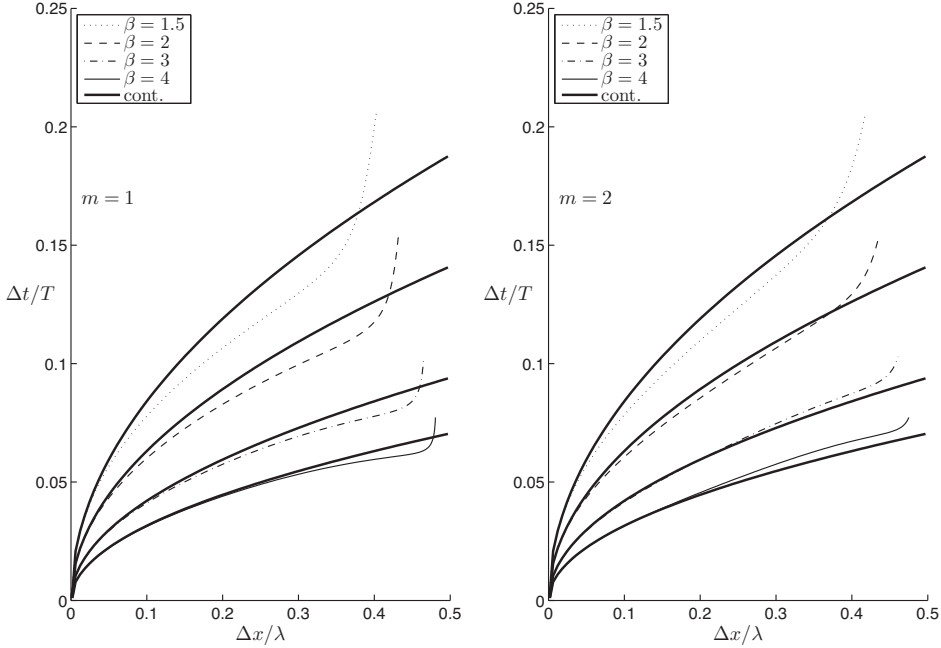


Figure 4.5: Frequency and wave number relation for discrete dispersion relation without current, discretized time and space, T : Wave period, Δt : Time step, *cont.*: Continuous solution, m : B-spline order, λ : Wave length., Δx : Element span in x , $\beta = \sqrt{\Delta x / (g \Delta t^2)}$

4.3 Steady forward speed

In this section, the steady wave pattern generated by a traveling disturbance, with velocity U in negative x direction, and infinite water depth is considered. This is equivalent to the problem of a ship advancing with a steady forward speed in absence of waves. In this case, the generated waves travel at different angles with respect to the axis of forward motion (x). Let us define the angle between x -axis and the wave propagation direction to be θ . Moreover, $k = 2\pi/\lambda$, where λ is the distance between two wave-peaks along the propagation axis. Then, the continuous dispersion relation in Eq. (4.7) reduces to Eq. (4.16) below.

$$\widetilde{\mathcal{W}} = g |k| - U^2 k^2 \cos^2 \theta = 0 \quad (4.16)$$

The discrete dispersion relation for the same problem is given in Eq. (4.17), where the expressions for discrete Fourier transformations are presented in Appendix B.

$$\widehat{\mathcal{W}} = 2\pi g \widehat{B}^{(m)} + U^2 \widehat{D}^{(xx)} \widehat{\mathcal{S}} = 0 \quad (4.17)$$

4.3.1 Two-dimensional waves

Let us assume long-crested waves which propagate in x direction only. Then, $\cos \theta = 1$ and the waves are simplified to two dimensional waves. The properties of the numerical method can be investigated by studying the dispersion operators defined in Eq. (4.18) below.

$$\begin{aligned} \widetilde{\mathcal{W}} &= 1 - \frac{U^2}{g} \bar{L}_c(k) = 0 \\ \widehat{\mathcal{W}} &= 1 - 2\pi F n_{\Delta x}^2 \bar{L}_d(k) = 0 \end{aligned} \quad (4.18)$$

Here, $\bar{L}_c(k) = |k|$, and $\bar{L}_d(k) = -\Delta x \widehat{D}^{(xx)} \widehat{\mathcal{S}} / \widehat{B}^{(m)}$. $F n_{\Delta x}$ is the element Froude number defined as $F n_{\Delta x} = U / \sqrt{g \Delta x}$. Following Sclavounos and Nakos (1988), the continuous and discrete dispersion operators were plotted against real non-dimensional wave number, from zero up to the principal wave number (0.5). Eq. (4.18) shows that k_c is a root of the continuous dispersion relation, when $\bar{L}_c(k_c) = g/U^2$. On the other hand, \bar{L}_d can result in a complex value. This means that k_d is a complex root for the discrete problem only if $\mathbf{Re} [\bar{L}_d(k_d)] = g/U^2$, while $\mathbf{Im} [\bar{L}_d(k_d)] = 0$.

Figure 4.6 shows the plots of the discrete and continuous operators for constant elements, with different differentiation orders. The intersection of a horizontal line at g/U^2 and \bar{L}_c , shows the root for the continuous dispersion relation. The discrete operator \bar{L}_d can have two intersections with this horizontal line, which means the possibility for having two different roots. However, the imaginary part of \bar{L}_d is non-zero, except at the limits. Therefore, the roots will not be real values. Since the operators are plotted against real values of wave number, estimating the complex root from these graphs is not straight forward. The difference between the real part of continuous and discrete operator can still be used as an estimation of the dispersion error. The imaginary part of the discrete operator can also be seen as an indication of the numerical damping.

Based on the aforementioned points, Figure 4.6 shows that the second order operator has the best dispersion properties among the operators considered here. Moreover, the imaginary part of the third order operator becomes negative by decreasing the element span, which means amplification. Therefore, the third order method is expected to be unstable. Figure 4.7 shows properties of the numerical method with second order difference operator and different B-spline orders. Interestingly, the discretization order has no significant influence on \bar{L}_d . However, the linear method seems to have slightly better properties.

A more direct way of assessing the properties of the numerical method is similar to what was presented in the previous section. Figure 4.8 shows the dispersion and damping of the numerical method in terms of C_r and C_i defined in Eq. (4.11). The

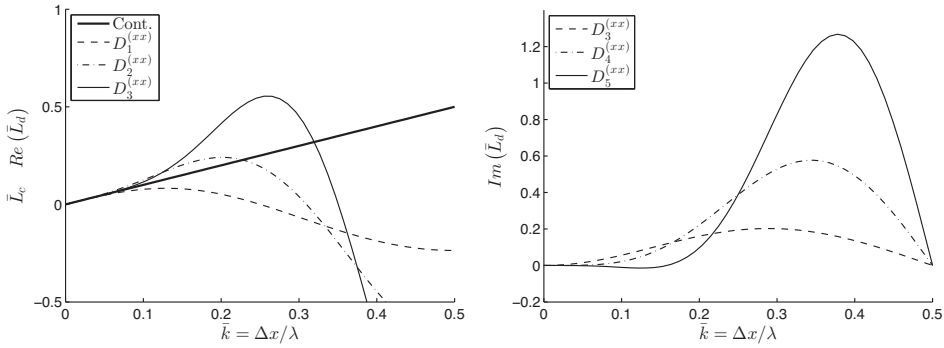


Figure 4.6: Comparison between discrete and continuous dispersion operators Eq. (4.18). Constant elements ($m = 1$). \bar{L}_c : Continuous dispersion operator, \bar{L}_d : Discrete dispersion operator, $D_k^{(xx)}$: Upstream finite difference operator for double derivative in x of order k , λ : Wave length, Cont.: Continuous operator.

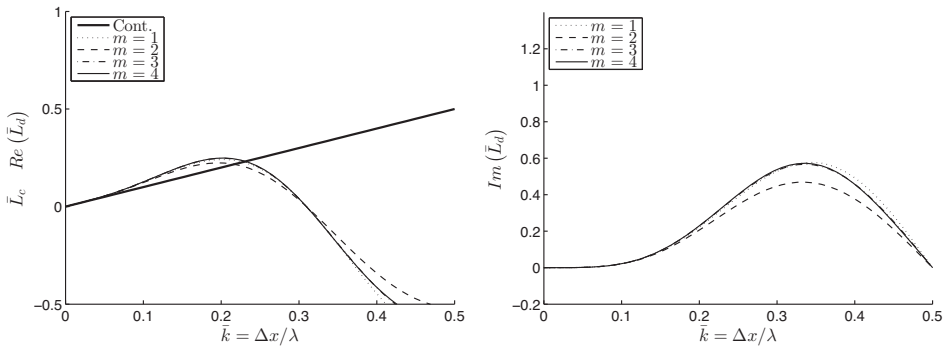


Figure 4.7: Comparison between discrete and continuous dispersion operators Eq. (4.18). Second order difference operator $D_2^{(xx)}$. \bar{L}_c : Continuous dispersion operator, \bar{L}_d : Discrete dispersion operator, m : B-spline order, λ : Wave length, Cont.: Continuous operator.

results are shown only for the root closest to the continuous solution. The $D_3^{(xx)}$ has positive C_i , which corresponds to amplification. The dispersion and damping properties mostly influenced by the differentiation operator, and the discretization order seems to have small influence. This is in agreement with the results from Figures 4.6 and 4.7.

The double derivative in x direction was calculated here using a double finite difference operator. Assuming a continuous and differentiable base function, the double derivative can be calculated analytically from the base function expression. In this case, the Fourier transform of the finite difference operator can be exchanged by the Fourier transform of a continuous differentiation (Eq. (B.59)). Moreover, a combination of a continuous and finite difference operator is also pos-

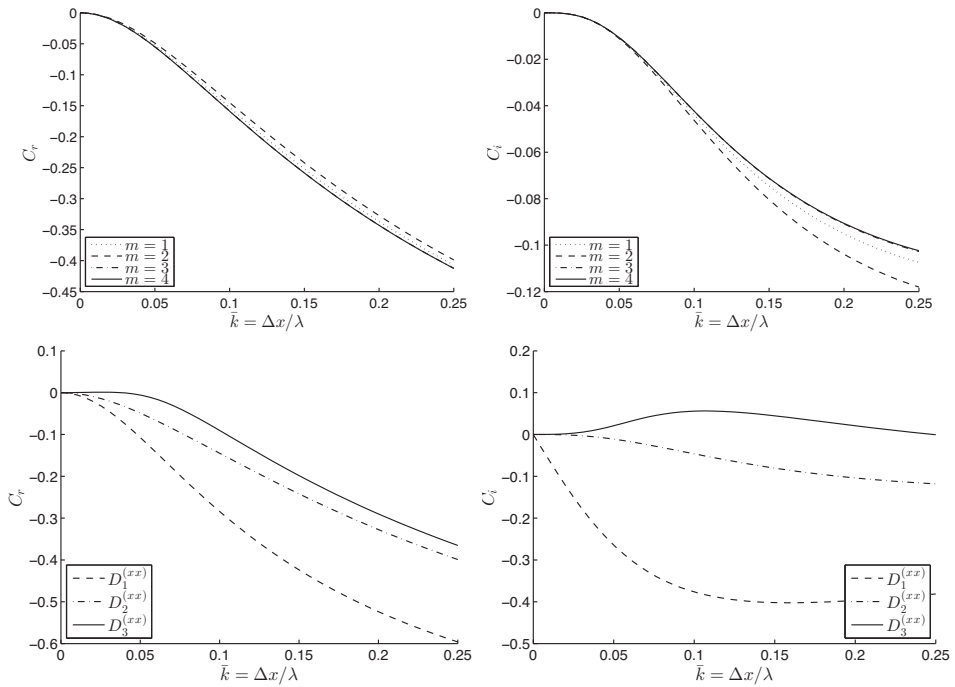


Figure 4.8: Comparison between discrete and continuous dispersion relation operator Eq. (4.18). \bar{L}_c : Continuous dispersion operator, \bar{L}_d : Discrete dispersion operator, $D_k^{(xx)}$: Upstream finite difference operator for double derivative in x of order k , m : B-spline order, λ : Wave length, Cont.: Continuous operator.

sible (Eq. (B.57)). As shown in Section B.3, the differentiation operator can be exchanged analytically between the base function and the source function (G). This is the case for indirect boundary integral formulation, when velocities are calculated by differentiating the source function (see for instance Dawson (1977)).

Sclavounos and Nakos (1988) studied different combinations for the differentiation operator, using the dispersion operators defined in Eq. (4.18). Figure 4.9 shows the continuous and discrete operators for combination of finite difference and continuous operators (Eq. (B.57)). This is similar to the method used by Dawson (1977). It is interesting to compare these results to the ones in Figures 4.6 and 4.7 for a double finite difference operator. The combined method shows much larger dependency on the B-spline order than the double finite difference method. Moreover, for the combined model, the imaginary and real part of \bar{L}_d go to zero at both limits of the non-dimensional wave number. In other words, the numerical solution converges to two solutions by decreasing element-span; one corresponding to the physical wave, while the other to the numerical saw-tooth wave. Therefore, filtering of the waves with a wave-length of order of few elements seems to be necessary in order to achieve convergence. Similar filtering methods were introduced by Nakos

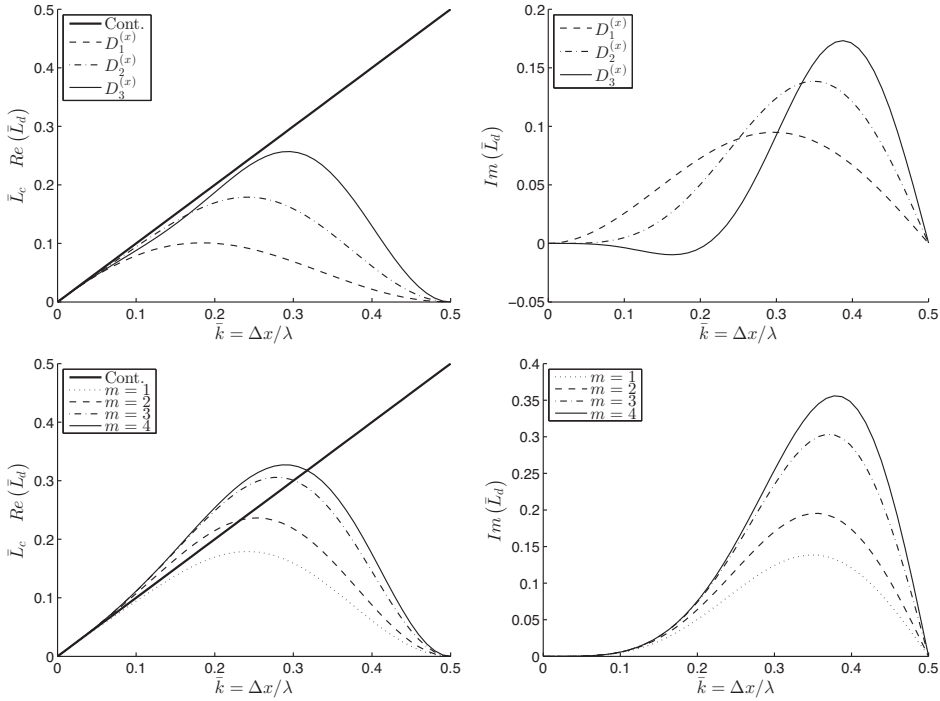


Figure 4.9: Comparison between discrete and continuous dispersion relation operator for combined continuous and finite difference operators. Constant elements ($m = 1$). \bar{L}_c : Continuous dispersion operator, \bar{L}_d : Discrete dispersion operator, $D_k^{(x)}$: Upstream finite difference operator for derivative in x of order k , λ : Wave length, Cont.: Continuous operator.

(1990) and Kring (1994) for steady-state and time-domain problems. However, at least based on this analysis, the double finite difference operator does not show a similar behavior.

4.3.2 Three-dimensional waves

If the three dimensional waves are considered, the discrete dispersion relation in Eq. (4.17) has two more parameters which influence the dispersion and damping properties of the numerical method. These are the wave propagation direction θ , and the elements' aspect ratio $\Lambda = \Delta y / \Delta x$. Let us start by assuming a continuous differentiation operator. In this way, the only source of numerical errors would be the surface discretization. The discrete dispersion relation for this case is presented in Eq. (4.19).

$$\widehat{\mathcal{W}} = 2\pi g \widehat{B}^{(m)} - U^2 k^2 \cos^2(\theta) \widehat{\mathcal{S}} = 0 \quad (4.19)$$

Figure 4.10 shows the dispersion error for different elements' aspect ratios and

propagation directions of waves. Since the derivatives were assumed to be calculated analytically, the damping is zero for all the cases in Figure 4.10. It is interesting to see that the dispersion error due to surface discretization is mostly positive. Meaning that the waves are shorter than they would be in the continuous solution. This is the opposite of the dispersion error due to the finite difference operator. As expected, the error generally increases by increasing Λ or θ .

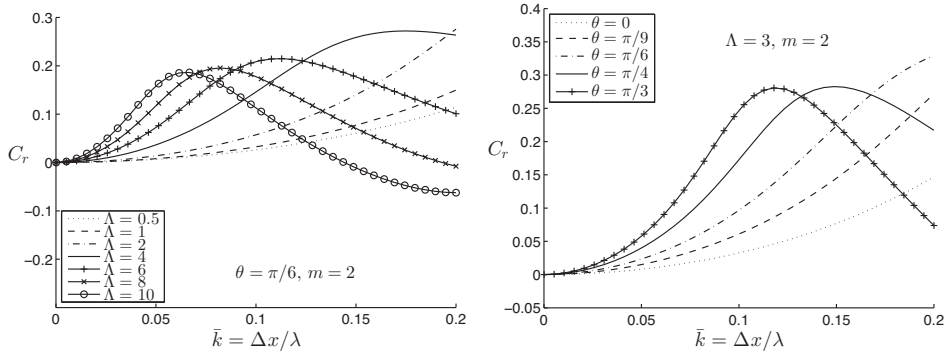


Figure 4.10: Dispersion and damping for surface discretization only, different wave propagation directions θ and element aspect ratio Λ . linear elements ($m = 2$), element aspect ratio $\Lambda = \Delta y / \Delta$. C_r : Dispersion, θ : wave propagation direction. λ : Wave length.

Figure 4.11 shows the dispersion and damping properties considering a second order double derivative in x for different propagation directions. Two aspect ratios, $\Lambda = 1$ and $\Lambda = 3$, are plotted for comparison. It is interesting to see that the dispersion errors, from surface discretization and the differentiation operator, cancel each other. For instance, the wave propagating in $\theta = \pi/4$ on elements with $\Lambda = 3$ has much better dispersion properties than $\theta = 0$. This cancellation is a function of the aspect ratio as well. Moreover, the waves propagating oblique to the current have better damping properties. This can be explained by considering the fact that the damping error is introduced by the double derivative operator. Therefore, the waves with smaller component in x -direction are less affected by the numerical differentiation.

The influence of the elements' aspect ratio, considering a second order double derivative in x , and linear elements, is studied in Figure 4.12. A wave traveling in the $\theta = \pi/6$ -direction was chosen to investigate the influence of aspect ratio. Similar to the propagation direction, the dispersion error introduced by a large aspect ratio is canceling the error due to numerical differentiation. However, the damping of the numerical method increases by increasing the aspect ratio.

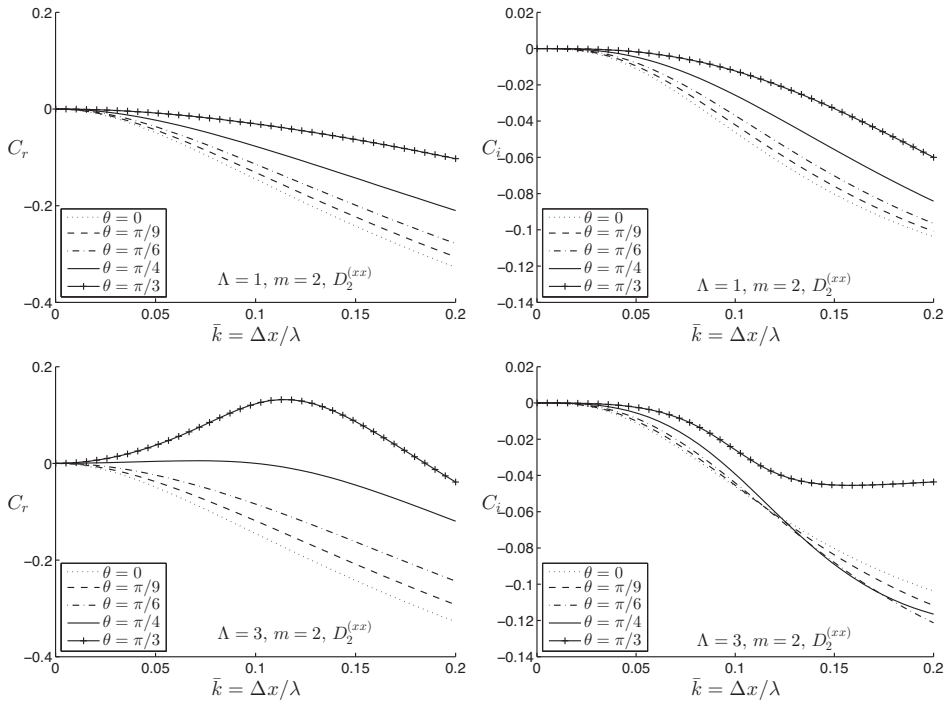


Figure 4.11: Dispersion and damping for different wave propagation directions $\theta, \Lambda = \Delta y / \Delta x$: element aspect ratio . C_r : Dispersion, C_i : Damping, θ : wave propagation direction. λ : Wave length.

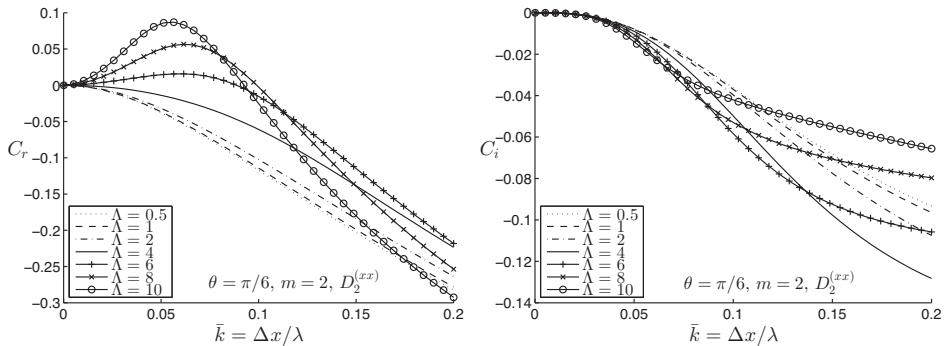


Figure 4.12: Dispersion and damping for different element's aspect ratio Λ . C_r : dispersion, C_i : damping, $\Lambda = \Delta y / \Delta x$: element aspect ratio. λ : Wave length.

4.4 Forward speed with oscillations

The complete form of the dispersion relation is considered here. This is of relevance for the waves generated by an oscillating disturbance with a constant forward speed. The full dispersion relation, assuming harmonic steady-state oscillations, is presented in Eq. (4.20). The temporal stability of the problem is addressed in Section 4.5. The main focus here is on the performance of the numerical methods for capturing the steady harmonic solution of the problem.

$$\widetilde{\mathcal{W}} = g|k| - \omega^2 + 2U\omega k \cos(\theta) - U^2 k^2 \cos^2(\theta) = 0 \quad (4.20)$$

As before, the problem is studied step by step. First, by assuming continuous differentiation, i.e. only the influence of a discrete source and dipole distribution. Second, by considering a harmonic solution in combination with discrete finite difference operators for spatial differentiation, and then the fully discretized version of the equation in time and space. The focus will be on linear elements with a second order finite difference operator for spatial derivatives. Bunnik (1999) performed similar analysis for his indirect boundary integral method with constant elements and desingularization. Interested readers are referred to his thesis for comparing the results presented in this section for direct boundary integral method with linear elements.

4.4.1 Continuous space and time derivatives

Here the space and time derivatives are assumed to be continuous. The intention is to study the influence of discrete source and dipole distribution in absence of the other numerical inaccuracies. The discrete dispersion relation for this case is shown in Eq. (4.21).

$$\widehat{\mathcal{W}} = 2\pi g \widehat{B}^{(m)} - \omega^2 \widehat{\mathcal{S}} + 2U\omega k \cos(\theta) \widehat{\mathcal{S}} - U^2 k^2 \cos^2(\theta) \widehat{\mathcal{S}} = 0 \quad (4.21)$$

The difference between Eq. (4.21) and Eq. (4.19) comes from the oscillatory motion of the source, which generate waves with frequency ω . This brings the so-called $\tau = U\omega/g$ parameter into the picture. Figure 4.13 shows the dispersion properties of waves with different values of τ , traveling at $\theta = 0$ on a discretized surface, with linear elements. Moreover, the dispersion properties of the waves with $\tau = 0.5$, traveling at different directions are also presented. Looking at the dispersion results for different values of τ , we see that the waves with larger τ have better dispersion properties. This may come as a surprise at first, since shorter waves must be more problematic to capture. However, τ and wave number are not independent parameters (see Eqs. (B.3) and (B.4)). For a constant Δx , increasing τ corresponds to shifting the dispersion curve to the right.

As shown in Section B.1 waves can travel upstream when $\tau < 1/4$. Figure 4.14 shows the dispersion properties of the numerical scheme for the waves traveling upstream. It is interesting to point out that unlike the downstream waves in Figure 4.13, the upstream waves have longer wave lengths. The dispersion properties of the upstream waves are acceptable. Moreover, similar to the downstream waves, deviating from x -axis increases the dispersion error.

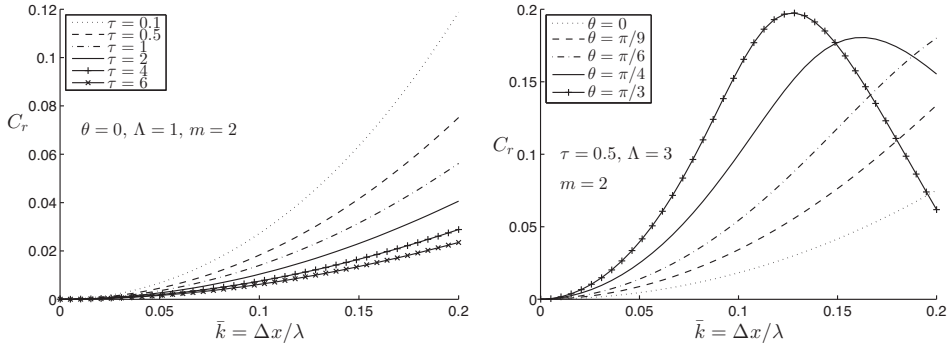


Figure 4.13: Dispersion properties of waves on a discrete surface. Linear elements ($m = 2$). $\tau = U\omega/g$, θ : wave propagation direction, C_r : Dispersion factor, $\Lambda = \Delta y/\Delta x$: element aspect ratio.

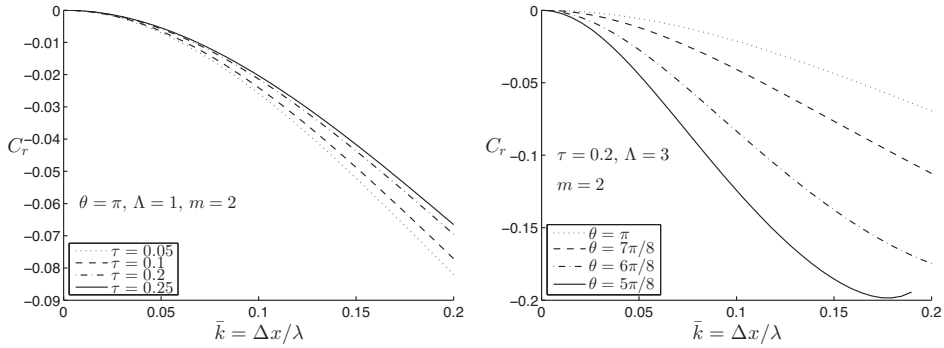


Figure 4.14: Dispersion properties of upstream waves on a discrete surface. Linear elements ($m = 2$). $\tau = U\omega/g$, θ : wave propagation direction, C_r : dispersion factor, $\Lambda = \Delta y/\Delta x$: element's aspect ratio.

4.4.2 Harmonic waves with discrete spatial derivative

The influence of numerically calculating the spatial derivatives, using a second order finite difference operator is studied in this section. Comparisons between different others of finite difference operators were presented in the previous sections. As mentioned in Section B.3, the spatial derivatives can also be calculated by an analytical differentiation of the shape functions. The properties of this type of differentiation can be found in studies by Nakos (1990) and Büchmann (2000). Assuming the waves to have a harmonic time dependency, the time derivatives in the discrete dispersion relation can be calculated analytically as shown in Eq. (4.22) below.

$$\widehat{\mathcal{W}} = 2\pi g \widehat{B}^{(m)} - \omega^2 \widehat{\mathcal{S}} - 2iU\omega \widehat{D}^{(x)} \widehat{\mathcal{S}} + U^2 \widehat{D}^{(xx)} \widehat{\mathcal{S}} = 0 \quad (4.22)$$

Figure 4.15 shows the dispersion and damping of downstream waves. Both of

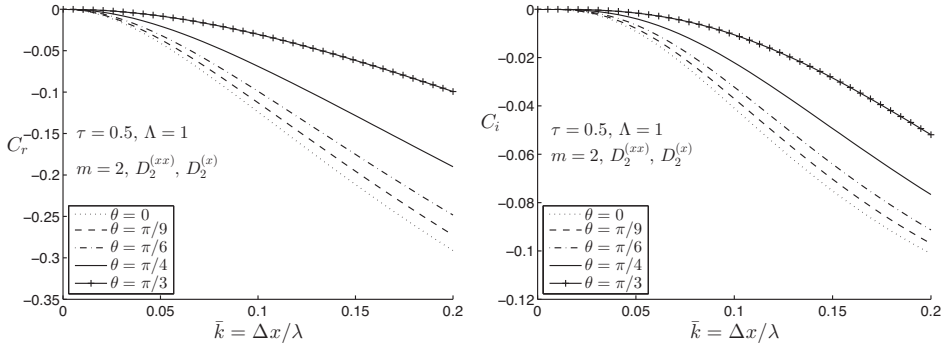


Figure 4.15: Wave dispersion and damping on a discrete surface with a second order finite difference operator for the spatial derivatives. $\tau = U\omega/g$, θ : wave propagation direction, C_r : Dispersion factor, C_i : Damping factor, $\Lambda = \Delta y/\Delta x$: element aspect ratio.

these aspects are governed by the finite difference operator used for differentiation in x -direction. Therefore, the waves which travel oblique to the current have better properties. Similar behaviors were discussed for steady forward speed case in Section 4.3.2. Figure 4.16 shows similar results for upstream waves. These waves travel against the dominant current flow. Therefore, an upstream finite difference operator, while the current defines the main direction of the stream, would not be a good choice, and large errors are expected. Interestingly, it seems that the error caused by the finite difference operator cancels the error due to discretization, and the obtained dispersion and damping properties are not unacceptable. In this case, the elliptic Laplace equation is the only source which governs the propagation of upstream waves.

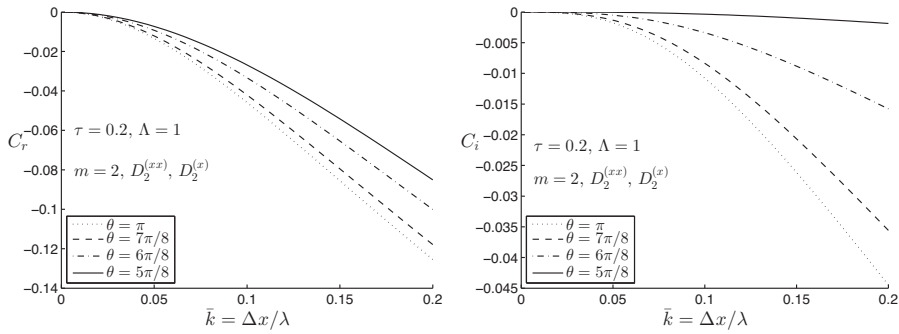


Figure 4.16: Upstream waves dispersion and damping on a discrete surface with a second order finite difference operator for the spatial derivatives. $\tau = U\omega/g$, θ : wave propagation direction, C_r : Dispersion factor, C_i : Damping factor, $\Lambda = \Delta y/\Delta x$: element aspect ratio.

4.4.3 Fully discretized dispersion relation

The fully discretized dispersion relation in space and time is studied in this section (Eq. (4.23)). Using the insight from the previous sections, the study is focused on linear elements (with B-spline base function of second order $m = 2$), together with a second order finite difference operator for the spatial derivatives. The first, second, and third order backward finite difference operators were used to calculate the single and double time derivatives in Eq. (4.23). The coefficients for these operators are presented in Section B.2.7.

$$\widehat{W} = 2\pi g \widehat{B}^{(m)} + \widehat{D}^{(tt)} \widehat{S} + 2U \widehat{D}^{(t)} \widehat{D}^{(x)} \widehat{S} + U^2 \widehat{D}^{(xx)} \widehat{S} = 0 \quad (4.23)$$

Figure 4.17 compares the dispersion and damping properties of different time derivative operators, with respect to the ratio between time-step and oscillations period. The $\Delta x/\lambda$ ratio was chosen to be 0.01 in order to minimize the spatial error at this stage. Similar to the results for the case without forward speed (see Section 4.2.2), the third order operator has the best dispersion properties. However, the positive C_i indicates amplification, which leads to an unstable scheme in time. The next best choice is the second order operator. This operator has a similar dispersion error to the first order, however, has much better damping properties.

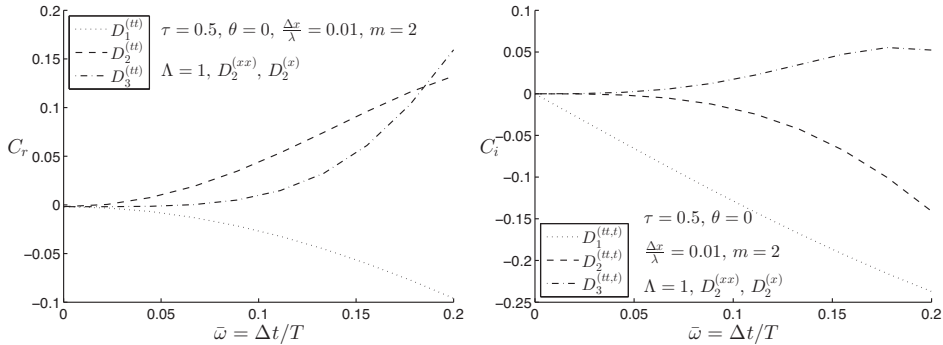


Figure 4.17: Downstream waves dispersion and damping for different time discretization orders with a second order finite difference operator for the spatial derivatives. $\tau = U\omega/g$, θ : wave propagation direction, C_r : dispersion, C_i : damping, $\Lambda = \Delta y/\Delta x$: element aspect ratio.

As mentioned before, more advanced time marching methods, such as AMB4 and RK4, most likely give better damping and dispersion properties. The current mathematical model needs modifications in order to be used for evaluating these schemes, which is left for future studies. The insight gained here can be used as guidelines in using higher order methods in practical problems.

Let us focus on the second order backward difference for the time derivatives. Figure 4.18 presents the dispersion and damping properties of different $\Delta x/\lambda$ ratios. As expected, the model converges to a constant dispersion and damping error by reducing the time step. The constant error, as expected, comes from the spatial discretization and the numerical calculation of derivatives, which reduces by

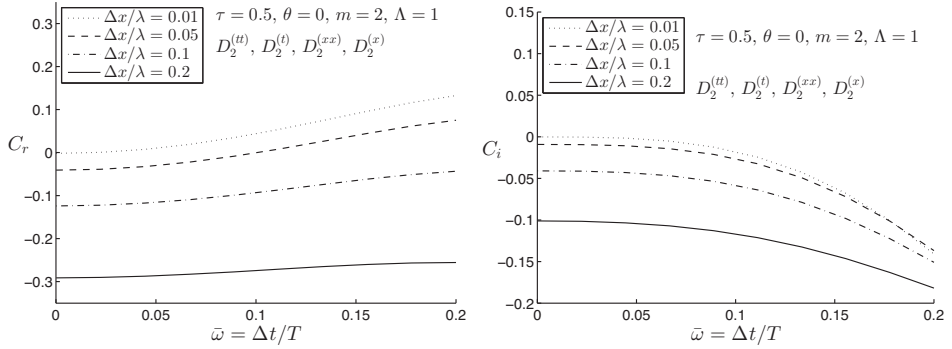


Figure 4.18: Downstream waves dispersion and damping for different $\Delta x/\lambda$ ratio with second order finite difference operator for spatial and time derivatives. $\tau = U\omega/g$, θ : wave propagation direction, C_r : dispersion, C_i : damping, $\Lambda = \Delta y/\Delta x$: element aspect ratio.

reducing $\Delta x/\lambda$. By comparing the damping in Figures 4.17 and 4.18, one can expect that C_i , for the third order time marching method, becomes negative for small enough time steps. In other words, the damping introduced by the spatial derivatives can stabilize the third order time marching scheme for small enough time steps.

4.5 Notes on temporal stability

In the previous sections, the stability of the numerical methods was considered for harmonic problems. However, instabilities can occur in a transient time-domain stage as well. This type of instability can be studied by considering the problem's growth factor in each time-step (Romate, 1989). Following Kim et al. (1997), we refer to this type of stability as *temporal stability*. For a simple time marching method, such as backward difference method, the temporal stability can be examined using the polynomial of the growth factor $Z = e^{i\omega\Delta t}$. As shown by Bunnik (1999), using a backward finite difference formula which involves $p_n + 1$ time instances, the discrete dispersion relation can be written in the form of a p_n -th order polynomial in Z as follows,

$$\begin{aligned} \widehat{W} = & \left(2\pi g \widehat{B}^{(m)} + U^2 \widehat{D}^{(xx)} \widehat{S} \right) Z^{p_n} \\ & + 2U \widehat{D}^{(x)} \widehat{S} \sum_{p=0}^{p_n} \frac{d_{p_n-p}^{(t)}}{\Delta t} \widehat{S} Z^p + \widehat{S} \sum_{p=0}^{p_n} \frac{d_{p_n-p}^{(tt)}}{(\Delta t)^2} Z^p \end{aligned} \quad (4.24)$$

The condition for a neutral stability is that all the complex roots of the polynomial in Eq. (4.24) must be in the unit circle. Since the value for Z corresponds to the growth rate of the transient solution, any root larger than one means an unbounded solution.

Using this methodology, Bunnik (1999) showed that for a second order time marching method, the central difference scheme for spatial derivatives results in an unstable system for almost any combination of element size and time step. Based on this analysis, he argued that, although the central difference operator gives the best dispersion and damping properties, its time-domain solution is unstable for a wide range of practical problems, and instead the second order upstream method is preferred. This supports the physical interpretation presented in Section 3.7.1 in favor of the upstream methods, despite their dispersion and damping errors.

The temporal stability results in a Courant-type criteria, and gives a relation between the maximum time step and element span. Dommermuth and Yue (1987) studied the linearized free-surface boundary condition using von-Neumann stability analysis, and suggested the criteria in Eq. (4.25) for a fourth order Runge-Kutta method.

$$\Delta t^2 \leq \frac{8}{\pi} \frac{\Delta x}{g} \quad (4.25)$$

Kim et al. (1997) used the growth factor method for assessment of their numerical method's temporal stability. They assumed a case without current (forward speed), and included the influence of the free-surface discretization using third order B-spline base functions. For a mixed implicit-explicit Euler time marching method, they arrived at the condition in Eq. (4.26).

$$\Delta t^2 \leq \frac{2}{g} \frac{\widehat{S}}{\widehat{B}} \quad (4.26)$$

Here \widehat{S} and \widehat{B} are defined in Eqs. (B.56) and (B.54), respectively. In presence of forward speed, the criteria will also depend on element Froude number and spatial differentiation operators. Due to presence of many different parameters, defining a general criteria is not an easy task. Bunnik (1999) studied the stability zones for different waves propagating on a discrete free surface, with different Froude numbers, numerically. The produced plots can be used to determine the stable zones for a specific set of parameters and numerical schemes.

A valid criteria must be defined by considering the roots of the fully discretized dispersion relation. Büchmann (2000) studied this criteria for a third order B-spline method. In his method the spatial derivatives are calculated using an analytical differentiation of the smooth B-spline base function. For a multi-step backward method, and element aspect ratio of one, he suggested the criteria in Eq. (4.27) to ensure an stable solution.

$$\Delta t^2 \leq \frac{1}{1.05^2} \frac{\Delta x}{g} \quad (4.27)$$

Later in Büchmann (2001), he showed that even by satisfying the criteria in Eq. (4.27) the solution may still become unstable. Using a fundamental study of the problem's eigen-solutions, he showed that the presence of forward speed changes the nature of the instability from saw-tooth instability, and reduces the frequency of the unstable numerical waves. He concluded that the criteria in Eq. (4.27) is a

necessary and not a *sufficient* condition. He related the instabilities to the inaccuracies of the mathematical model and considered the grid non-uniformity to be the source. However, no mathematical proof was provided in his paper that shows these instabilities are the result of the grid non-uniformity.

4.6 Conclusions

The dispersion, damping and stability of a group of different numerical methods were studied in this chapter. The insight provided by this type of analysis helps to estimate the accuracy of the results, and explain the presence of the non-physical numerical waves and instabilities.

The influence of different discretization aspects such as, order of the spatial and time derivatives, order of the discretization method, element's aspect ratio, the direction of propagation of waves, and the dispersion and damping properties are considered. It was shown that the presence of forward speed changes the performance of a numerical method dramatically. These changes can be in a way that a discretization method becomes suitable for a certain type of a problem, while not for the other. The influence of different discretization parameters on the spatial and temporal stability of the methods were also addressed.

The analysis provided here is not complete. There are several issues left which requires more study. Among them, the influence of the grid and base function non-uniformity, the influence of a force function, and the truncation boundaries can be named. Including these factors into the mathematical analysis is left for future works. However, the conclusions provided here were used as guidelines to choose and use suitable numerical methods, and interpret the results obtained in the following chapters.

Chapter 5

Non-separated Flows

5.1 Introduction

The numerical method, presented in the previous chapters, will be used here to solve a group of hydrodynamic problems, and the results are compared against existing analytical, numerical, and experimental data. The goal is to check the accuracy and functionality of the numerical method in practice for solving a range of hydrodynamic problems. The focus of this chapter is on non-separated flows. These are the cases where the flow separation is expected to dose not have a major contribution, and so can be neglected. The cases where flow separation plays an important role, are studied in the next chapter.

The problems have been chosen from well-studied hydrodynamic problems, which can act as a benchmark. The time-domain solver, in combination with the zero-speed formulation, is tested by solving the flow around a heaving semi-sphere in Section 5.2 and wave diffraction around a surface piercing vertical circular cylinder in Section 5.3. The steady forward speed formulation and the solver are examined by looking at a traveling source under the free surface in Section 5.4, and a Wigley hull in a steady forward motion in Section 5.5. The time-domain solver is combined with the forward speed formulation to solve forced heave motions of a Wigley hull and a Series-60 vessel with $C_B = 0.7$ in Sections 5.6 and 5.7, respectively.

5.2 A heaving semi-sphere on the free surface

The hydrodynamic forces on a heaving semi-sphere were studied and presented in this section. Direct boundary integral method, described in Chapter 2, was used to formulate the problem in terms of Rankine sources and dipoles distribution on the body surface and free surface. The problem was solved in the time-domain. At each time-step, ϕ on the free surface was assumed to be known. Since a radiation problem (forced heave oscillations) was considered, $\frac{\partial \phi}{\partial n}$ on the body surface could be obtained from the body boundary condition. Assuming the heave motion of the

semi-sphere to have the form $\eta_3 = \bar{\eta}_3 e^{-i\omega t}$, where $\bar{\eta}_3$ is the amplitude and ω is the frequency of the heave motion, the body boundary condition states,

$$\left. \frac{\partial \phi}{\partial n} \right|_{S_B} = -i\omega \bar{\eta}_3 e^{-i\omega t} n_3 \quad (5.1)$$

where, n_3 is the vertical component of the normal vector pointing inside the fluid domain, and positive upward. Numerical investigations showed that impulse start of the heave motion triggers high frequency waves, which cause longer transition time and probable instabilities. Therefore a cosine smoothing curve, as shown in Eq. (5.2) below, was used to start up the simulation.

$$\begin{aligned} \bar{\eta}_3 &= \bar{\eta}_3^{(0)} \frac{1}{2} \left[\cos \left(\frac{t}{T} \pi - \pi \right) + 1 \right] & 0 < t < T \\ \bar{\eta}_3 &= \bar{\eta}_3^{(0)} & t > T \end{aligned} \quad (5.2)$$

Here T is the ramp duration, and $\bar{\eta}_3^{(0)}$ is the final oscillation amplitude. Looking at Eq. (5.2), we see that $\bar{\eta}_3$ starts from zero at time $t = 0$ and increases to $\bar{\eta}_3^{(0)}$ at time $t = T$ following a smooth cosine function, and stays constant for $t > T$. In this way, the generation of high frequency waves could be avoided, the transition time reduced, and the numerical solution stabilized. This method was further used in the solution of all the time-domain problems in the present study to improve the numerical solution.

Let us rewrite the direct boundary integral formulation for this problem considering what has been mentioned until now. Eq. (5.3) shows the formulation of the problem at a time instance t_0 , after substituting the body boundary condition, and moving the known terms to the right-hand-side.

$$\begin{aligned} & \iint_{S_B} \phi(\boldsymbol{\xi}) \frac{\partial G(\mathbf{x}, \boldsymbol{\xi})}{\partial n(\boldsymbol{\xi})} dS - \iint_{S_F} \frac{\partial \phi(\boldsymbol{\xi})}{\partial n(\boldsymbol{\xi})} G(\mathbf{x}, \boldsymbol{\xi}) dS - \mathcal{C}(\mathbf{x}) \phi(\mathbf{x}) = \\ & + \iint_{S_B} \omega \bar{\eta}_3(t_0) \sin(\omega t_0) n_3 G(\mathbf{x}, \boldsymbol{\xi}) dS - \iint_{S_F} \phi(\boldsymbol{\xi}) \frac{\partial G(\mathbf{x}, \boldsymbol{\xi})}{\partial n(\boldsymbol{\xi})} dS \end{aligned} \quad (5.3)$$

Here the time dependency of the velocity potential function was omitted for clarity. The velocity potential on the free surface at start was assumed to be $\phi = 0$ as an initial condition. However, a time-marching method was required to obtain the free-surface velocity potential at future time-steps by satisfying the dynamic and kinematic free-surface boundary conditions. The Eulerian explicit-implicit time marching method, described in Section 3.6, was used for time stepping the potential and free-surface elevation. Eq. (5.4) shows how this method looks like for the present problem, where super-index n refers to the n th time step or time $t = n\Delta t$.

$$\begin{aligned} \zeta^{(n+1)}(\mathbf{x}) &= \zeta^{(n)}(\mathbf{x}) - 2\nu(\mathbf{x})\zeta^{(n)} - \Delta t \left[\frac{\partial \phi(\mathbf{x})}{\partial n(\mathbf{x})} \right]^{(n)} \\ \phi^{(n+1)}(\mathbf{x}) &= \phi^{(n)}(\mathbf{x}) - g\Delta t \zeta^{(n+1)}(\mathbf{x}) \end{aligned} \quad (5.4)$$

Here ν is the damping term introduced by the artificial damping boundary as discussed in Section 3.7.2. The time-step was chosen based on the oscillation period, $\Delta t = \omega/(2\pi N)$, where N is the number of steps per period. With current time-stepping method, 20 to 30 time-steps per period was chosen to obtain acceptable accuracy.

Knowing the ϕ on the free surface from Eq. (5.4) and $\frac{\partial\phi}{\partial n}$ on the body surface from Eq. (5.1), Eq. (5.3) can be solved to obtain $\frac{\partial\phi}{\partial n}$ on the free surface and ϕ on the body surface. The boundary integral formulation in Eq. (5.3), can be solved using the numerical methods presented in Chapter 3. Here, the free surface and body surface were discretized using 8-points quadratic elements (see Section A.2) and the boundary conditions were satisfied at the nodes of the elements. Figure 5.1 shows a view of a semi-sphere and half of the free-surface grid.

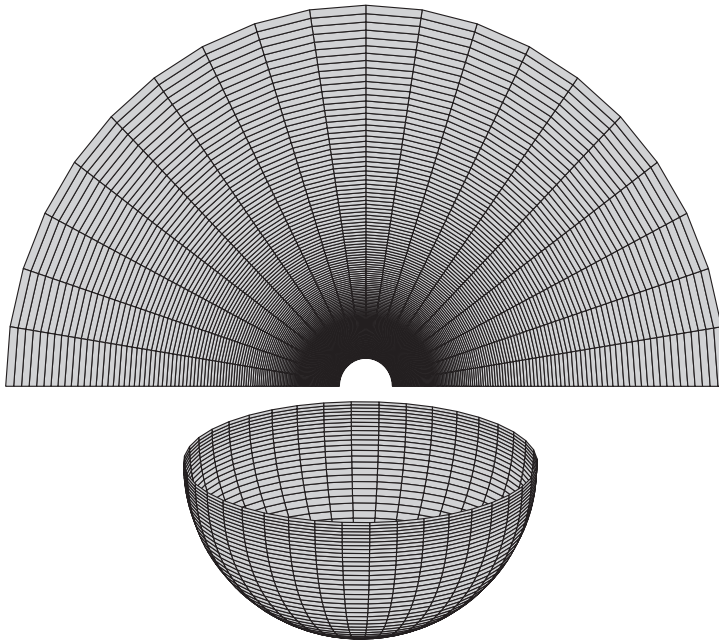


Figure 5.1: Grid for a heaving semi-sphere in free surface.

In order to ensure that the generated waves by the heaving semi-sphere are captured correctly, the size of the free-surface domain must be adapted to the generated wave-length. However, this requires generating different grids for each oscillation frequency. In the present study, the size of the domain was chosen to be four times the largest wave-length. The number of elements per wave, for 8-points quadratic panels, are 10 for the smallest wave-length of interest. Special attention was paid to the size of elements near the water line on the body and free surface in order to ensure high resolution, as well as smooth transition. The pole of the semi-sphere was closed by using a group of 6-point quadratic triangular elements.

The connecting nodes on the water-line were assumed as a part of the free surface, while contributions from the integration on the body was included separately.

The generated waves by the heaving semi-sphere were absorbed using a numerical damping layer, in order to avoid wave reflections from the boundaries of the truncated free surface. The span of the absorbing boundary is two times the largest wave length. The Newtonian-cooling factor presented in Eq. (3.92) was used to determine the distribution of the damping strength in the damping zone. The overall damping strength was adjusted individually for each wave length to achieve damping efficiency and avoid instabilities. The radial distance to the start-edge of the damping zone was used as the distance parameter in Eq. (3.92).

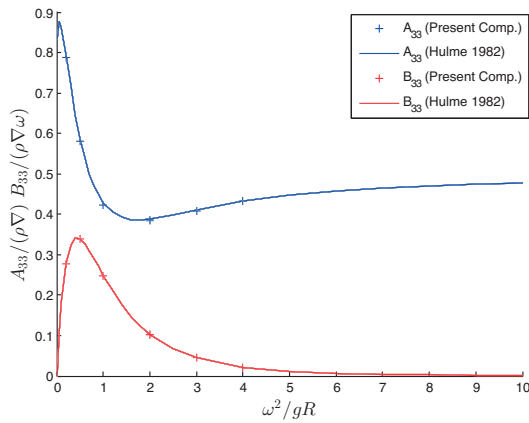


Figure 5.2: Added mass and damping of a heaving semi-sphere in free surface.

The pressure was calculated, and integrated in time, in order to obtain the forces acting on the body (see Section 2.9). The time-series of the vertical force were translated into added mass and damping coefficients in heave using Fourier transformation. The results were compared to a semi-analytical solution by Hulme (1982) in Figure 5.2 for a group of selected frequencies. The results from the present time-domain calculations agrees reasonably well with the semi-analytical results. It must be mentioned that due to practical difficulties the efficiency of the numerical method decreased extensively when frequency of oscillation approaches zero or infinity. For very low frequencies, which corresponds to large wave lengths, a large free surface domain is required while the elements' size are bounded by the size of elements on the sphere. This means large number of elements are required for calculation at such frequencies. For large frequencies, i.e. shorter wave lengths, the number of elements must be increased in order to provide enough resolution for the short wave lengths, which consequently increases the computational time. Although, semi-analytical calculations are free from these difficulties, they are not very useful in solving more general problems.

5.3 Wave diffraction by a vertical cylinder

The diffraction problem of an infinity long vertical circular cylinder in waves was chosen as the second case-study for this section. Many studies can be found for this hydrodynamic problem in the literature. Havelock (1940) presented an analytical solution to the diffraction velocity potential (ϕ_d) for the linear problem in the frequency domain and infinite water depth. MacCamy and Fuchs (1954) extended the solution to the finite water depths. In their solution, the diffraction velocity potential and free-surface elevation were presented using a summation series of Bessel and Hankel functions. The same problem was solved using our time-domain boundary integral code and the results were compared with the analytical solution. Since both methods were essentially solving the same mathematical problem, the results were expected to match with high accuracy.

Following Havelock (1940), the total velocity potential was divided into an incident and diffraction part, as shown in Eq. (5.5) below.

$$\Phi = \phi_i + \phi_d \quad (5.5)$$

The velocity potential for incident waves (ϕ_i) can be defined from linear theory as,

$$\phi_i = \frac{g\zeta_a}{\omega} e^{|k|z} e^{-i(\omega t - kx \cos \theta - ky \sin \theta)} \quad (5.6)$$

Here ω is the wave frequency, ζ_a is the wave amplitude, k is the wave number, and θ is the propagation direction. Assuming deep water, the wave frequency and wave length are related using the dispersion relation in Eq. (B.2). Since ϕ_i satisfies the Laplace equation and free-surface boundary condition we focus our attention to solving ϕ_d . The boundary integral equation can be written for the diffraction velocity potential as shown in Eq. (5.7).

$$\begin{aligned} & \iint_{S_B} \phi_d(\boldsymbol{\xi}) \frac{\partial G(\mathbf{x}, \boldsymbol{\xi})}{\partial n(\boldsymbol{\xi})} dS - \iint_{S_F} \frac{\partial \phi_d(\boldsymbol{\xi})}{\partial n(\boldsymbol{\xi})} G(\mathbf{x}, \boldsymbol{\xi}) dS - \mathcal{C}(\mathbf{x}) \phi_d(\mathbf{x}) = \\ & - \iint_{S_B} \frac{\partial \phi_d(\boldsymbol{\xi})}{\partial n(\boldsymbol{\xi})} G(\mathbf{x}, \boldsymbol{\xi}) dS - \iint_{S_F} \phi_d(\boldsymbol{\xi}) \frac{\partial G(\mathbf{x}, \boldsymbol{\xi})}{\partial n(\boldsymbol{\xi})} dS \end{aligned} \quad (5.7)$$

Similar to the problem in previous section, $\frac{\partial \phi_d}{\partial n}$ on the body surface was known from body boundary condition. Moreover, ϕ_d on the free surface was known at the initial stage and further obtained by time-marching method using the kinematic and dynamic free-surface boundary conditions. For a fixed vertical cylinder the body boundary condition can be defined using the normal fluid velocity on the body as shown in Eq. (5.8) below.

$$\frac{\partial \phi_d}{\partial \mathbf{n}} = -\nabla \phi_i \cdot \mathbf{n} \quad \text{on body-surface} \quad (5.8)$$

The problem was solved in the time-domain using the explicit-implicit Euler method. The time marching procedure is identical to the one described for a

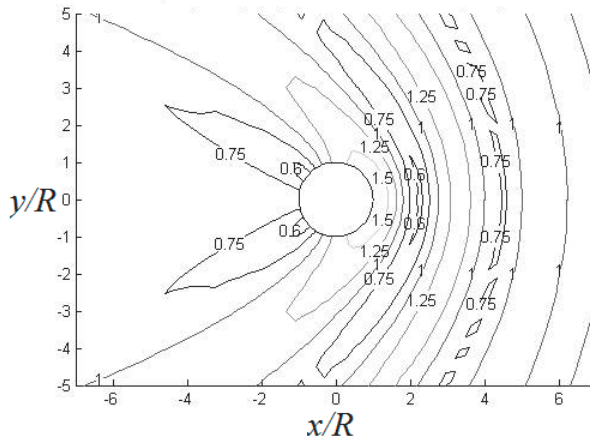


Figure 5.3: The amplitude of the diffraction potential relative to the amplitude of the incident potential on the free surface around a vertical fixed surface-piercing cylinder, Top half: numerical, Bottom half: analytical, R : cylinder radius.

heaving semi-sphere in Section 5.2. Moreover, a similar wave absorbing method was applied at the boundaries of the free surface domain. Both free surface and body surface were discretized using 8-nodes quadratic panels. The circular free surface domain, and radial discretization, adopted here, are also similar to the one used for the previous case of a heaving semi-sphere. The vertical cylinder was extended 10 times the wave length below the free surface in order to achieve infinite water depth condition. The elements on the column were chosen to be smaller close to the free surface in order to capture the exponential variation in diffraction velocity potential. The elements' size were gradually increased as the depth increases. Figure 5.3 compares the amplitude of the diffraction velocity potential from analytical method by Havelock (1940) and present time-domain numerical method. The results show good qualitative agreements. It must be mentioned that the waves in Figure 5.3 have not reached the damping zone yet.

As discussed in the previous section, the body boundary condition must be applied gradually in-order to avoid the high frequency waves which are excited by an impulse start. Similar approach was adopted here. The amplitude of the incident wave (ζ_i) was smoothly increased using a cosine smoothing function (see Eq. (5.2)). The time series for the diffraction wave elevation (ζ_d) can be calculated from ϕ_d , using the linearized free-surface dynamic boundary condition, as shown in Eq. (5.9) below.

$$\zeta_d(x, y, t) = -\frac{1}{g} \frac{\partial \phi_d(x, y, t)}{\partial t} \quad (5.9)$$

The transient solution for ζ_d , at three different locations on the water-line, are shown in Figure 5.4 and compared to the analytical steady-harmonic results. The locations are marked using a polar coordinate system (r, θ) with the origin at the

center of cylinder on the free surface. From Figure 5.4 one can conclude that after six periods of simulation, the numerically predicted amplitude and frequency are reasonably close to the analytical results for the present smoothing function.

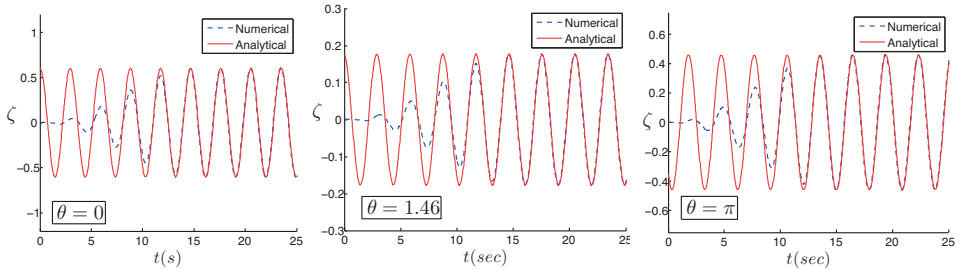


Figure 5.4: Time signal of the diffraction wave elevation around a vertical cylinder. $k = 0.47$: incident wave number non-dimensionalized by the cylinder radius R , ζ : diffraction wave elevation non-dimensionalized by the cylinder radius R , θ : polar position on cylinder in radians.

Figure 5.5 shows the diffraction wave elevation amplitude on the column surface at different polar positions. Three different wave numbers for the incident wave were studied. The agreement between the analytical and numerical results for the all three wave numbers were satisfactory. It must be mentioned that, similar to a heaving semi-sphere, the computational cost of the method increases for very short or very long incident waves.

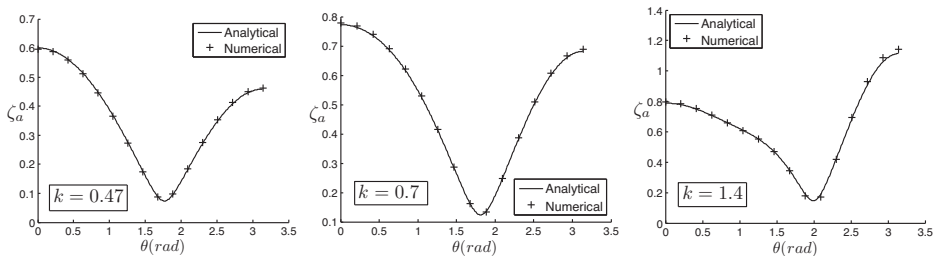


Figure 5.5: Diffraction wave elevation amplitude around a vertical cylinder. k : incident wave number non-dimensionalized by the cylinder radius R , ζ_a : amplitude of the diffraction wave elevation non-dimensionalized by the cylinder radius R

5.4 A traveling Kelvin source under the free surface

In this section, the linearized wave making problem of a single source traveling under the free-surface is considered. The main difference between the present problem and the previous examples are the presence of forward speed. Moreover,

by formulating the problem in the seakeeping coordinate system (see Section 2.1) there is no need for the time-domain solver and the solution can be obtained using the steady-state solver. In steady-state solver, the problem can be translated into one equation-system, and solved only once to obtain the steady solution. Therefore, it is computationally cheaper than the time-domain solution.

The problem was formulated based on the direct boundary integral formulation presented in Section 2.11, which simplified to Eq. (5.10) for the present case.

$$\mathcal{C}(\mathbf{x})\phi(\mathbf{x}) + \iint_{S_F} \frac{U^2}{g} \frac{\partial^2 \phi(\boldsymbol{\xi})}{\partial \xi^2} G(\mathbf{x}, \boldsymbol{\xi}) dS = \sigma G(\mathbf{x}, \mathbf{x}_s) \quad (5.10)$$

The boundaries consist only of the free-surface boundary in this problem. However, the singular source must be removed from the fluid domain which results in an additional forcing term in the right-hand-side of the boundary integral formulation. Here σ is the strength of the traveling source which is chosen to be one in the present study. Since S_F is flat, the influence of the dipole distribution on the free surface is zero and only the source distribution term remains. The normal derivative of the velocity potential on the free surface was replaced using the linearized Neumann-Kelvin free-surface boundary condition (see Section 2.6).

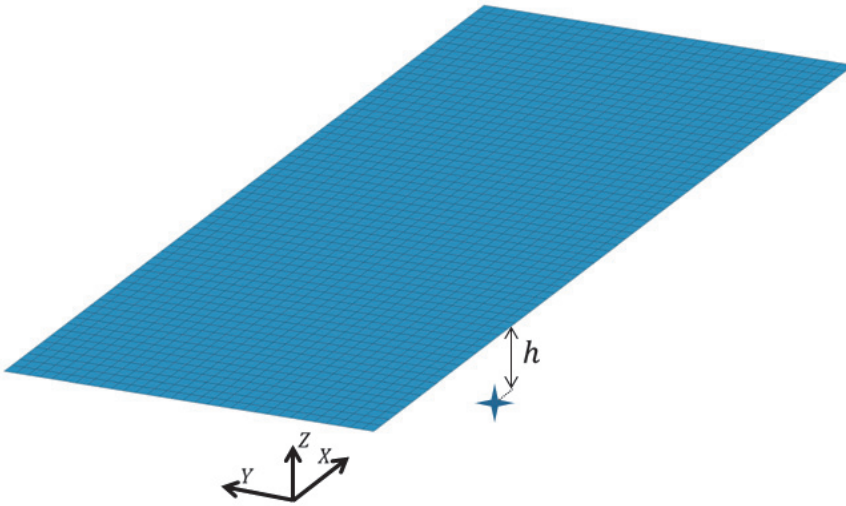


Figure 5.6: Kelvin source traveling under the free surface, arrangement.

Further, the problem was discretized using uniform linear quadrilateral elements. Figure 5.6 shows the problem arrangement and an example of the free-surface grid. The elements' aspect ratios, $\Lambda = \Delta x / \Delta y$, are equal to one where Δx and Δy are the elements' spans in x and y directions, respectively. $h = U^2/g$ is the source submergence depth. The guidelines provided in Sclavounos and Nakos (1988) were used to determine the free-surface domain boundaries based on the source's forward speed U .

A linear system of equations was formed using the right-hand-side of Eq. (5.10) as the matrix of coefficients, with the velocity potentials at the elements' nodes as the vector of unknowns. A second order upwind-finite difference formula was used to relate the derivatives to the velocity potentials on the free surface. This finite difference operator was subsequently combined to the matrix of coefficients to form one single system of equations. The known forcing function at each node was calculated from the equation's left-hand-side. Since the problem was assumed to be symmetrical about the xz -plane, the velocity potential was solved only on the upper-half of the free surface. The radiation boundary condition was satisfied implicitly by the use of upwind finite difference and no special treatment was applied on the free-surface truncation boundaries.

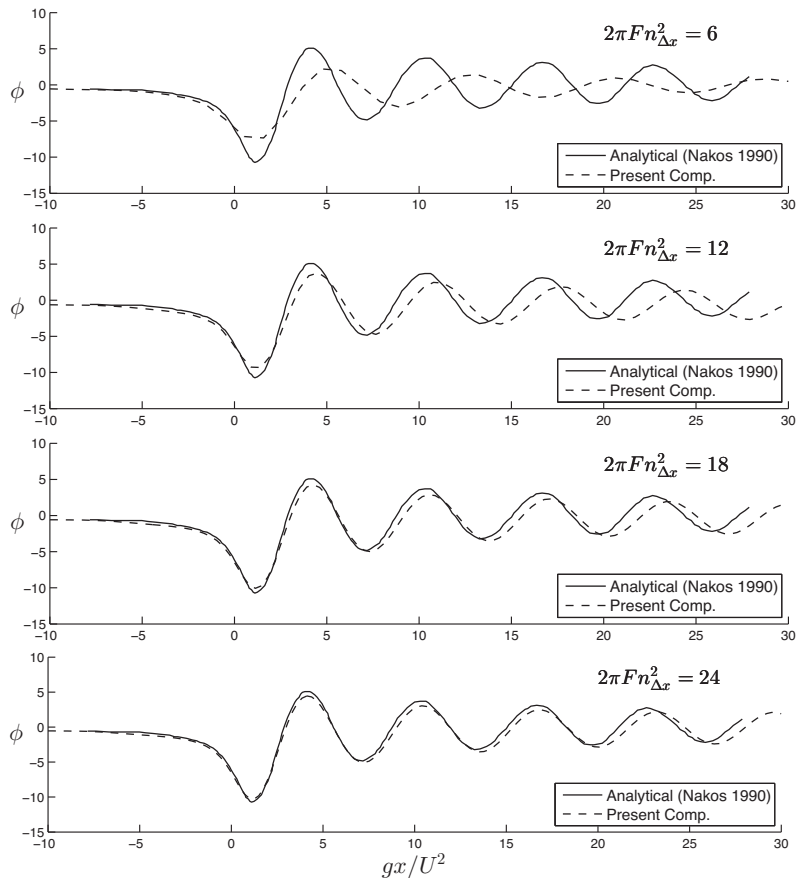


Figure 5.7: Kelvin source traveling under the free surface, convergence study using the velocity potential, source at $x = 0$ with submergence depth, $h = U^2/g$, Longitudinal cut at $y = 0.25U^2/g$.

Figure 5.7 compares analytical and numerical velocity potentials on a longi-

tudinal cut of the free surface. The cutting line is parallel to the x-axis, with a $0.25U^2/g$ transverse distance from the center line. The analytical results are from Sclavounos and Nakos (1988), where they have used the method presented in Newman (1987a). The numerical results are presented for four different grid resolutions. The resolutions are identified by the non-dimensional number $2\pi Fn_{\Delta x}^2$ where $Fn_{\Delta x} = U/\sqrt{\Delta x g}$. Considering that for the generated transverse waves by a moving source $k = g/U^2$, we have $2\pi Fn_{\Delta x}^2 = \lambda/\Delta x$ where λ is the wavelength. As shown by the analysis in Chapter 4, for linear elements, the numerical wave length is larger than the exact analytical solution. The influence of damping is clear for lower grid resolutions. The results show acceptable convergence pattern by increasing the number of elements per wave length.

5.5 A Wigley hull with forward speed

The wave making problem of a Wigley-hull body translating with constant forward speed is studied here. Due to the presence of body surface, the problem is more complicated in comparison to a single traveling source in the previous section. Moreover, the Wigley-hull is piercing the free surface, which means the elements on the free surface can no longer have uniform shapes. The geometry of the Wigley hull model was generated using the parabola presented in Eq. (5.11) below, where (x, y, z) are the coordinates of the points on the body surface.

$$y = \pm \frac{B}{2} \left[1 - \left(\frac{2x}{L} \right)^2 \right] \left[1 - \left(\frac{z}{L} \right)^2 \right] \quad (5.11)$$

Here B is the vessel's breadth, L is the length, and D is the draft at the still water level. The present model dimensions are $B/L = 0.1$ and $D/L = 0.0625$.

The boundary integral formulation of the problem is similar to the previous problem with addition of the integral over the body surface. xz -plane was assumed to be the plane of symmetry. In addition to the linearized free-surface boundary condition, the body boundary condition also substituted in the boundary integral formulation.

$$\begin{aligned} & \iint_{S_B} \phi(\boldsymbol{\xi}) \frac{\partial G(\mathbf{x}, \boldsymbol{\xi})}{\partial n(\boldsymbol{\xi})} dS + \iint_{S_F} \phi(\boldsymbol{\xi}) \frac{\partial G(\mathbf{x}, \boldsymbol{\xi})}{\partial n(\boldsymbol{\xi})} dS \\ & - \iint_{S_F} \frac{U^2}{g} \frac{\partial^2 \phi(\boldsymbol{\xi})}{\partial \xi^2} G(\mathbf{x}, \boldsymbol{\xi}) dS - \mathcal{C}(\mathbf{x}) \phi(\mathbf{x}) = - \iint_{S_B} U n_1 G(\mathbf{x}, \boldsymbol{\xi}) dS \end{aligned} \quad (5.12)$$

Here the no-flow trough the body-surface condition was applied by replacing the $\frac{\partial \phi}{\partial n}$ on the body with $-Un_1$, where U is the constant forward speed and n_1 is the x -component of the vector normal to the body surface.

The steady-state solver was used to solve the problem, just like the single source example in Section 5.4. The free surface and body surface were discretized using 9-points quadratic elements. Figure 5.8 shows a sample of the free surface and body surface grids. The elements on the free surface were generated using transfinite

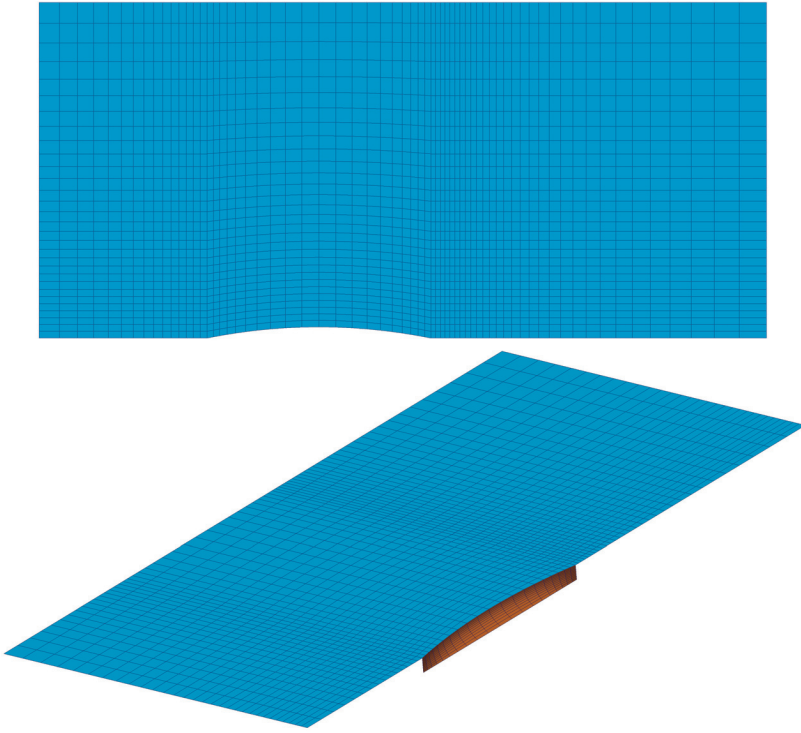


Figure 5.8: Grid for an advancing Wigley hull in free surface.

interpolation and elliptic grid generation methods to ensure higher grid resolutions at the critical areas, as well as smooth transition of the elements' sizes (see Section 3.9). A similar method was used to generate the body grid, to achieve higher grid resolution around the bow and stern, and close to the water-line.

The free surface was mapped to a uniform rectangular grid by using the numerical mapping coefficients (see Section 3.9). An upwind second order finite difference operator was used to calculate the derivatives in x direction (see Chapter 4). The radiation boundary condition was satisfied implicitly by the use of upwind finite difference. Therefore, no special treatment was necessary at the boundaries of the free-surface domain, as long as the boundaries were chosen at a proper distance (see Section 3.7.1). The free surface elevation at the Wigley hull water-line was calculated using the obtained velocity potential as shown in Eq. (5.13) below.

$$\zeta = -\frac{U}{g} \frac{\partial \phi}{\partial x} \quad (5.13)$$

The position of the body was assumed to be fixed, which means the induced shrinkage and trim due to forward speed was neglected. Figure 5.9 shows a comparison between the present calculations and the previous experiments and numerical calculations from June Bai and McCarthy (1979) for the free-surface elevation along

the body at two different Froude numbers. The results were in relatively good agreement with previous numerical results. However, as expected, the maximum surface elevation at the bow, which is related to the non-linearities of the flow in that area, was difficult to capture with linear theory. It must be noted that the forward speed induced sinkage and trim of the vessel were neglected in the present calculations.

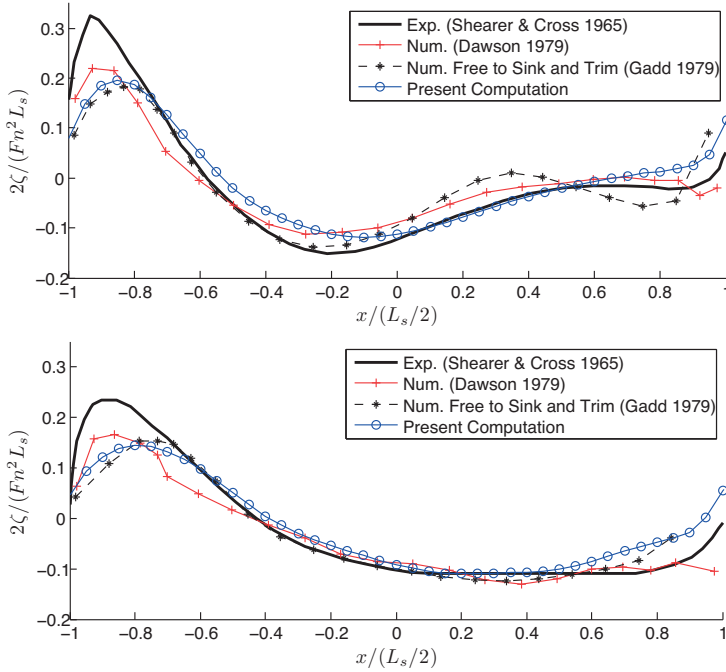


Figure 5.9: The free-surface elevation around an advancing Wigley hull. Top: $Fn = 0.348$, Bot: $Fn = 0.402$

5.6 A Wigley hull in forced heave oscillations

In this section the time-domain solver is tested for a modified Wigley hull translating with forward speed and undergoing forced heave oscillations.

The problem is formulated in the seakeeping coordinate system as presented in Chapter 2. The direct boundary integral formulation for this problem takes the form shown in Eq. (5.14) below.

$$\begin{aligned}
 & \iint_{S_B} \phi(\boldsymbol{\xi}) \frac{\partial G(\mathbf{x}, \boldsymbol{\xi})}{\partial n(\boldsymbol{\xi})} dS - \iint_{S_F} \frac{\partial \phi(\boldsymbol{\xi})}{\partial n(\boldsymbol{\xi})} G(\mathbf{x}, \boldsymbol{\xi}) dS - \mathcal{C}(\mathbf{x}) \phi(\mathbf{x}) = \\
 & - \iint_{S_B} \left(U n_1 - \frac{\partial \eta_3}{\partial t} n_3 \right) G(\mathbf{x}, \boldsymbol{\xi}) dS - \iint_{S_F} \phi(\boldsymbol{\xi}) \frac{\partial G(\mathbf{x}, \boldsymbol{\xi})}{\partial n(\boldsymbol{\xi})} dS
 \end{aligned} \tag{5.14}$$

Here, $\frac{\partial\phi}{\partial n}$ on the body surface was replaced by the linearized body boundary condition (Eq. (2.28)), where $\eta_3(t)$ is the time-dependent forced heave motion of the vessel. Similar to the previous time-domain problems, the value of ϕ on the free surface was assumed to be known at the start from the initial condition. Then, the 4th-order Runge-Kutta method was used for time-stepping the velocity potential and free-surface elevation, while the rest of the unknowns were obtained by solving the boundary integral equation in Eq. (5.14) at each time-step (see Section 3.6.3 for more details).

The surface of the body and the free surface were discretized using quadrilateral linear elements. An upwind second-order finite-difference method was used to calculate the derivatives in the kinematic and dynamic free-surface boundary conditions. The properties of this method in capturing the wave propagation on a discrete free surface were extensively discussed in Chapter 4. To avoid reflections from the free-surface boundaries, a numerical beach was adopted at the domain's sides to act as an absorbing boundary condition. The model presented in Section 3.7.2 was adopted. The size and strength of the numerical beach were chosen by numerical investigations, in order to achieve the best absorbing properties in the largest range of oscillation frequencies. The distribution of elements on the free surface and body surface are similar to the steady-state problem as presented in Section 5.5.

Table 5.1: Modified Wigley hull dimensions.

Property	unit	value
Length, L	m	3.0
Breadth, B	m	0.3
Draught, D	m	0.1875
Trim	deg	0.0
Displaced Volume, ∇	m^3	0.0946

The accuracy of the time-domain solver was tested first against the steady-state solver. In order to avoid the high-frequency waves due to impulsive start, the solution was started at rest, and then the forward speed was gradually increased until it reached the vessel's steady forward speed. The velocity was increased using a smooth cosine function as shown in Eq. (5.2) before. The time-domain solution was continued until the steady-state condition was achieved. The obtained velocity potentials on the body surface were compared to the results from the steady-state solver, from previous section. It has been found that after the time-domain solver reached the steady condition the values were almost identical. The obtained steady forward solution was used as an initial condition for the forced heave oscillations. The vessel's forced heave oscillations were also started with a gradually increasing amplitude as explained in Section 5.2.

The forces acting on the body was calculated using the direct pressure integration method as described in Section 2.9. The derivatives of the shape functions were used to calculate the water velocities on the body surface. The time series of the forces were translated into the added mass and damping coefficients, using

Eq. (2.58) and Fourier transformation.

The modified Wigley model used by Journée (1992) was chosen for comparison. The model dimensions and a view of the body plan is presented in Table 5.1 and Figure 5.10, respectively. Figure 5.11 shows the heave added mass and damping

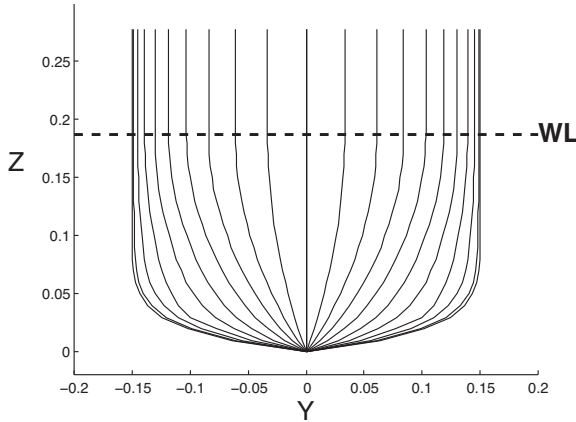


Figure 5.10: Modified Wigley hull body plan.

of the modified Wigley-hull with $Fn = 0.3$. The present values from Neumann-Kelvin linearization are compared to the numerical results by Nakos (1990) and experiments by Journée (1992). The experimental results are presented for two different oscillation amplitudes. The present results show the same trend and accuracy as the previous calculations.

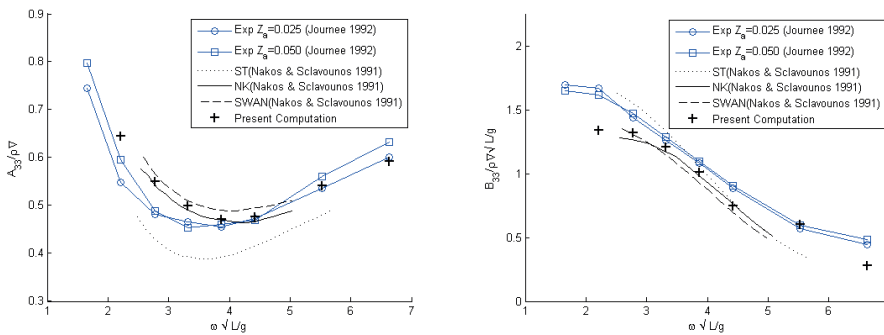


Figure 5.11: The added mass and damping coefficients in heave for a heaving Wigley hull with forward speed, $Fn = 0.3$, Z_a : forced heave motion amplitude in experiments, ST: Strip theory method. NK: Neumann-Kelvin method

5.7 A series-60 vessel in forced heave oscillations

The distribution of forces along a Series-60 vessel, translating with constant forward speed, and undergoing forced heave oscillation are studied here. The mathematical formulation of the problem and the numerical implementation are identical to the forced heave oscillations of a Wigley hull presented in Section 5.6. The experiments on a segmented series-60 model, with $Cb = 0.7$, by Gerritsma and Beukelman (1965) was chosen for comparison. The dimensions and properties of the model were summarized in Table 5.2 below.

Table 5.2: Series-60 model dimensions.

Property	unit	value
Length between perpendiculars, L	m	2.258
Length on the waterline, L_{wl}	m	2.296
Breadth, B	m	0.322
Draught, D	m	0.129
Displaced Volume, ∇	m^3	0.0657
Block coefficient, C_B	-	0.7

The model was divided into seven segments with equal lengths. In this way the force on each segment was measured separately and the added mass and damping for heave motion of each segment were calculated. Figure 5.12 shows a comparison between the heave added mass and damping of the vessel's segments, from experimental and numerical methods, for five different oscillation frequencies, at $Fn = 0.2$. The numerical values by Shao and Faltinsen (2012), using both Neumann-Kelvin and double-body linearization, are presented for comparison. They used a similar boundary integral formulation, with 12-points cubic elements, in their calculations. The agreement between present numerical results and previous values as well as experiments are acceptable.

From Figure 5.12 it is possible to see that the double-body formulation has a slightly better prediction of the forces along the body. This is expected since at this forward speed the change in the flow due to presence of the body plays an important role and must be included in the linearization. Moreover, the rigid free-surface boundary condition is more suitable at lower Froude numbers, which makes the double-body linearization a better choice.

5.8 Conclusions

A series of classical potential flow problem both with and without forward speed were studied using the steady-state and time-domain solvers. Different distribution orders, from constant to quadratic, were considered. Convergence and sensitivity study were carried out for the presented cases in order to gain insight on the performance and accuracy of the numerical models. A portion of the numerical results were presented in order to establish the performance and limitations of the present

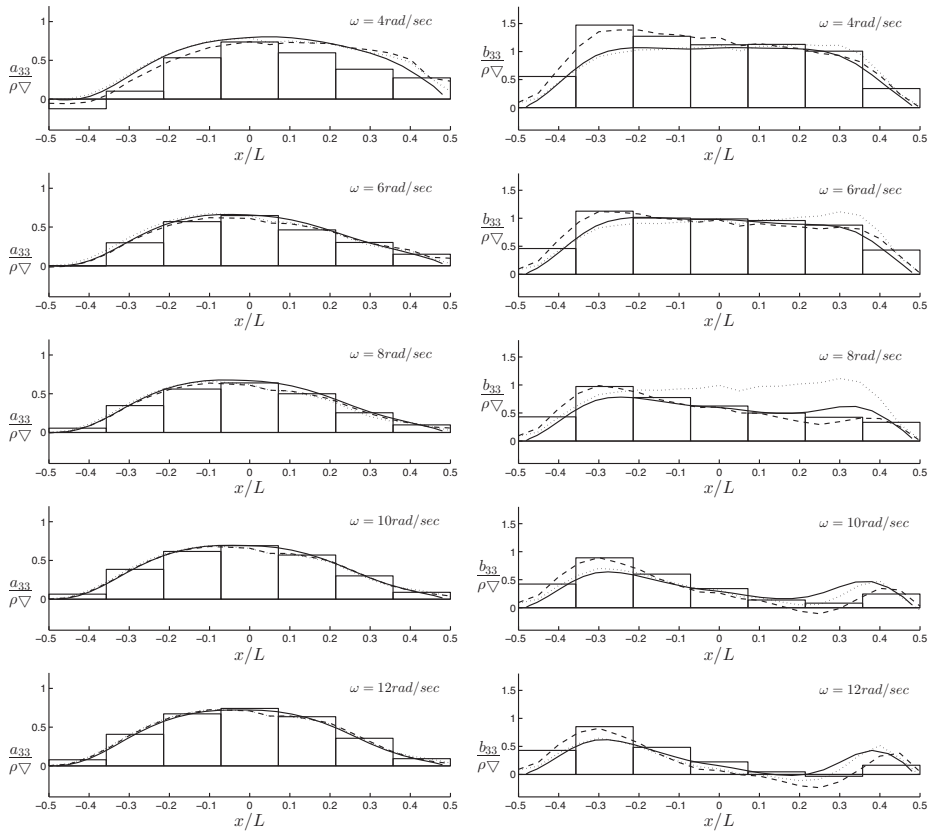


Figure 5.12: Added mass and damping in heave for a heaving series-60 vessel with forward speed, $Fn = 0.2$, Dashed lines: Double Body Shao and Faltinsen (2012), Dotted lines: Neumann-Kelvin Shao and Faltinsen (2012), Bars: Experiments Geritsma and Beukelman (1965), Solid lines: Neumann-Kelvin present computation.

numerical method. Obtained numerical results were compared against analytical, semi-analytical, numerical, and experimental data available in the literature for each case. The overall agreement of the numerical results were acceptable, considering the limitations due to discretization and linearization. These limitations were addressed and discussed to identify the domain of validity for the present numerical models.

Chapter 6

Tail-separated Flows

6.1 Introduction

The hydrodynamics of a low aspect ratio flat plate, which is advancing and oscillating in free surface, can be viewed, as a simplified version of a narrow semi-displacement vessel. This can be achieved mathematically, by transferring the body boundary conditions of a semi-displacement vessel to its center plane. Then, the flow separation from the vessel's transom stern, due to a drift angle or sway oscillations, can be simplified to the flow separation from the plate's trailing edge. Hence, the hydrodynamic model of an advancing and oscillating plate can represent a simplified version of a semi-displacement vessel's hydrodynamic model, which can be used, for instance, in dynamic stability analysis.

As mentioned in Chapter 2, due to fluid viscosity, the flow leaves the trailing edge of a lifting surface tangentially. In this condition, the flow separation plays an important role. The flow separation from a sharp trailing edge of an advancing foil with an angle of attack, is one example. Hence, this effect must be included in the solution. The so-called lift and drag forces on air/hydrofoils can be correctly calculated using potential-flow theory only if the flow separation from the trailing edge, and also sides of low aspect ratio foils, are included. As discussed in Section 2.10, there are several techniques to include flow separation effects in a potential-flow solver.

In this chapter, it is attempted to solve a series of problems with important tail and tip flow separations. A linearized vortex sheet method is used to include the trailing edge flow separation (see Section 2.10.1), while the tip flow-separation is included using a 2D+t cross-flow principle (see Section 2.10.3). Further, the application of these techniques in expanding the applicability of potential-flow methods are demonstrated.

First, we start by looking at the classical problem of a 2D section of a hydrofoil, advancing in un-bounded fluid, with an angle of attack. The accuracy and numerical implementation of the vortex-sheet method are discussed and comparisons are made with experimental results. Then, the free-surface effects are added to the problem by looking at a finite aspect ratio surface-piercing plate, advancing

in the free surface with a drift angle. Landrini and Campana (1996) showed that the bottom-tip flow separation effects are important. A 2D+t cross flow model, as described in Section 2.10.3, is adopted to include these effects. The results are compared against experimental and previous numerical data. Finally, the sway and yaw oscillations of an advancing surface-piercing plate are considered. The time-varying vortices generated from the tail are propagated on a linearized vortex sheet into the fluid. The added mass and damping coefficients of the plate are calculated and compared to the experimental and other numerical results.

6.2 Foil in infinite fluid

The classical problem of an advancing foil with constant speed U in unbounded fluid is studied in this section. A simple case of a 2D symmetrical NACA0012 foil with an angle of attack in unbounded fluid was investigated. A 3D NACA0012 model with length-to-cord ratio of 30 was modeled and the pressure distribution at the midsection was compared against the experimental results for a similar 2D foil from Gregory and O'Reilly (1973).

The flow separation from the trailing edge of the foil was considered by introducing a vortex sheet behind the foil. The linearized version of the vortex sheet was adopted, which means the sheet was assumed to be flat with zero thickness (see Section 2.10).

The flow must leave the trailing edge tangentially. This constraint, which is known as Kutta condition, can be ensured by enforcing the velocity potential to be continuous from the body into the fluid. As a result, the pressure is finite at the separation point. Since, in the presence of an attack angle, the velocity potentials on the two sides of the body are different, the jump in the velocity potential, in the longitudinal direction, is required to be continuous too. Morino and Kao (1974) achieved this by introducing a flat surface of singularities into the fluid and relating the strength of the singularities to the circulation around the body. Although, in reality, the wake surface is not flat, this type of linearization has been shown to be sufficiently accurate for small drift angles (e.g. Morino and Kao (1974)). From the linear part of the Bernoulli equation (Eq. (2.37)), the equality of the pressure at the trailing edge and along the vortex sheet can be described as follows,

$$p^+ = -\rho U \frac{\partial \phi^+}{\partial x} = -\rho U \frac{\partial \phi^-}{\partial x} = p^- \quad (6.1)$$

or simply,

$$\frac{\partial (\phi^+ - \phi^-)}{\partial x} = 0 \quad (6.2)$$

which means the potential jump, generated at the trailing edge, does not change along the vortex sheet in the x -direction. Therefore, the jump in the velocity potential created at the body, propagates with the flow downstream. A similar conclusion can be drawn by considering the conservation of vorticity defined in Eq. (2.66) for a problem reached the steady condition.

The direct boundary integral formulation presented in Eq. (2.81) was used to formulate the problem. As shown in Section 2.11 the integrals on the vortex sheet surfaces simplify to a dipole distribution on the positive side of the vortex sheet. The dipole strength on the sheet would be equal to $\Delta\phi = \phi^+ - \phi^-$ at the trailing edge, which is, based on Eq. (6.2), constant along the x -axis. By substituting the body boundary condition from Eq. (2.36) into Eq. (2.81) the following is driven,

$$\begin{aligned} \mathcal{C}(\mathbf{x})\phi(\mathbf{x}) &= \int_{S_B} \phi(\boldsymbol{\xi}) \frac{\partial G(\mathbf{x}, \boldsymbol{\xi})}{\partial n(\boldsymbol{\xi})} dS + \int_{S_B} G(\mathbf{x}, \boldsymbol{\xi}) \left(U_i \cdot \mathbf{n}(\boldsymbol{\xi}) \right) dS \\ &+ \int_{S_{V^+}} (\phi^+(\boldsymbol{\xi}) - \phi^-(\boldsymbol{\xi})) \frac{\partial G(\mathbf{x}, \boldsymbol{\xi})}{\partial n(\boldsymbol{\xi})^+} dS \end{aligned} \quad (6.3)$$

The body surface and the vortex sheet were discretized into a finite number of rectangular elements with linear distribution of unknowns. The extent of the vortex sheet was chosen by numerical investigations to minimize the influence of the domain truncation. Numerical grid generation methods presented in Section 3.9 were used to control the size of elements close to the important areas, such as the leading and trailing edges. Figure 6.1 shows a typical grid. The vortex sheet was modeled as a flat surface extended in the direction of the ambient flow except at the attachment point to the trailing edge. At the trailing edge, the vortex sheet was turned tangent to the foil mid-line.

It must be noted that the intention here is to solve the flow around a 2D foil. The reason for adopting a 3D high aspect ratio foil is to achieve a 2D flow at the mid-section. Moreover, it is known that the accuracy of the results highly depends on the grid resolution at the areas of high variation. Since the focus here is on the values around the mid-section, the elements were chosen to be finer at the mid-section and coarser close to the sides. Therefore, the results are not expected to be accurate away from the mid-section.

Satisfying the Kutta condition at the trailing edge is not straight forward. The goal is to enforce equality of the pressure, while allowing a jump in the values of ϕ (Eq. (6.1)). Unlike the method used by Morino and Kao (1974), by assuming linear instead of constant panels, a collocation point exactly at the trailing edge is obtained. Allowing for two different solutions of ϕ at the same point makes the equation system singular. Therefore, the condition must be enforced with extra care. Here the method proposed by Faltinsen and Pettersen (1983) and further used by Kristiansen (2009) was applied. To avoid the singularity, the values of ϕ were extrapolated linearly from the sides of the plate towards the trailing edge as follows,

$$\phi_j^+ = \frac{\phi_{j-1}^+ - \phi_{j-2}^+}{x_{j-1}^+ - x_{j-2}^+} (x_j^+ - x_{j-2}^+) + \phi_{j-2}^+ \quad (6.4)$$

$$\phi_j^- = \frac{\phi_{j-1}^- - \phi_{j-2}^-}{x_{j-1}^- - x_{j-2}^-} (x_j^- - x_{j-2}^-) + \phi_{j-2}^- \quad (6.5)$$

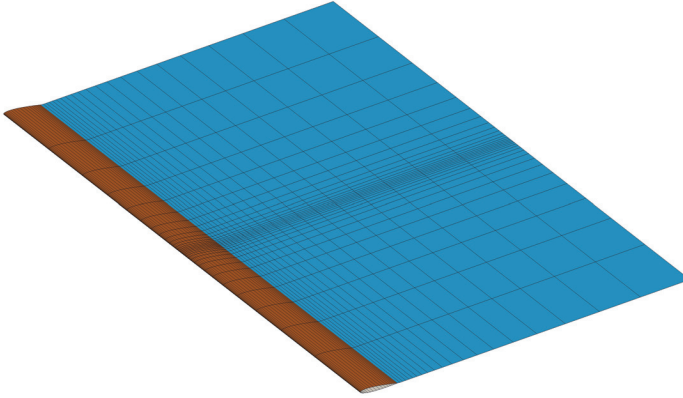


Figure 6.1: NACA0012 and vortex sheet grid. Length-to-cord ratio = 30, the elements are concentrated around the mid-section to obtain a better 2D-flow condition, suitable for comparing with the 2D experimental data.

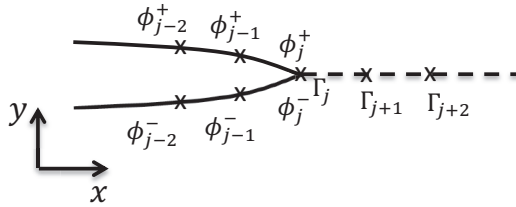


Figure 6.2: Extrapolation of velocity potential at trailing edge, $\Gamma_j = \phi_j^+ - \phi_j^-$.

Figure 6.2 shows a section of the plate, and the notations used in Eqs. (6.4) and (6.5). In addition, equality of the pressure in its linear form states,

$$\frac{\partial \phi_j^+}{\partial x} = \frac{\partial \phi_j^-}{\partial x} \quad (\text{i.e. at the trailing edge}) \quad (6.6)$$

By not satisfying the body boundary condition at the points j^+ and j^- , the equation system is two equations short. By adding the two extrapolations Eqs. (6.4) and (6.5), and the pressure equality Eq. (6.6), the number of equations exceeds the number of unknowns by one. In order to fix this, one more body boundary condition, for instance at $(j-1)^-$, must be taken out. To summarize, ϕ_j^+ was calculated from Eq. (6.4), ϕ_j^- from Eq. (6.6) and ϕ_{j-1}^- from Eq. (6.5). Therefore, due to linear extrapolation, it is important to have finer elements at the trailing edge. Γ_j is the strength of the dipole distribution on the vortex sheet, where $\Gamma_j = \phi_j^+ - \phi_j^-$. As Eq. (6.2) shows, this value does not change along the x -axis.

The method is validated by calculating the pressure coefficients and comparing the results for two attack angles of 6 and 10 degrees with experimental values in

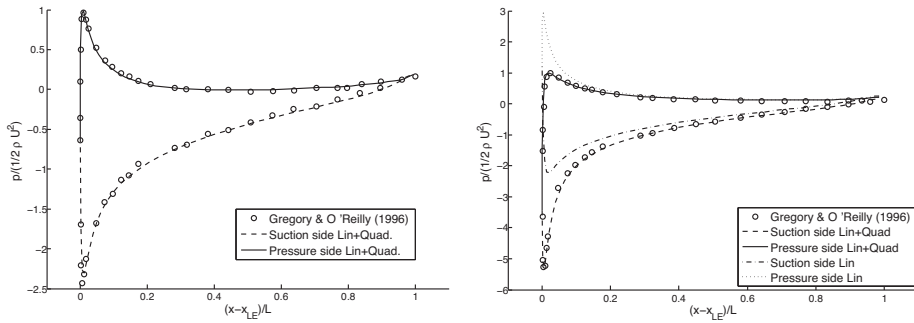


Figure 6.3: Two-dimensional NACA0012 pressure profiles, comparisons between experimental data by Gregory and O'Reilly (1973) and present numerical calculations, Left: $\alpha = 6^\circ$, Right: $\alpha = 10^\circ$, x_{LE} : longitudinal position of the leading edge, Lin: $p^{(L)} = -\rho U \frac{\partial \phi}{\partial x}$, Quad: $p^{(Q)} = -0.5\rho \nabla \phi \cdot \nabla \phi$.

Figure 6.3. For attack angle of 10 degrees, both linear and quadratic pressures are presented. It is interesting to note that, although the equality of pressures were enforced for the linear pressure at the trailing edge, due to thickness effects, the quadratic term in the pressure plays an important role, especially in the leading edge region. The overall agreement of the combined linear and quadratic pressure coefficients with the experimental data seems to be satisfactory.

6.3 Plate with a drift angle

The problem of a surface-piercing, finite aspect-ratio, flat plate, with forward speed and a small drift angle has been studied before experimentally and numerically. This problem resembles a simplified version of an advancing vessel with drift angle.

Chapman (1976) used the 2D+t method based on a slender body assumption within potential-flow theory to calculate the transverse force and yaw moment. He investigated the influence of linear, second-order and nonlinear free-surface boundary conditions and concluded that, while the nonlinear free-surface boundary condition can influence the free-surface elevation, it does not change the side force and yaw moment significantly.

Maniar et al. (1990) and Xü (1991) solved the potential-flow problem in three dimensions, using the thin ship assumption and Kelvin-Havelock Green function. They pointed out the incompatibility between the pressure Kutta condition and the linearized free-surface boundary condition at the meeting point of the trailing edge and the free surface. They showed that the effects of this incompatibility are local and do not change the global solution.

Landrini and Campana (1996) used a double-body linearization to formulate the problem. They investigated the influence of the bottom tip vortex on the side force and yaw moment. They showed that the bottom tip separation (keel vortex shedding) plays an important role in the transverse force and yaw moment

especially for lower draft-to-length ratios. They also demonstrated that, for their studied case, a linearized vortex sheet is sufficient to model the forces and there is no need for nonlinear vortex geometry. Zhu and Faltinsen (2007) used a linear 3D Rankine panel method to solve the potential-flow problem. They took the plate's thickness into account and neglected the tip-vortex's effects.

In the present work, the method by Zhu and Faltinsen (2007) is further developed. The transverse force and yaw moment acting on a surface piercing, finite aspect-ratio flat plate with forward speed and drift angle is studied. The potential flow formulation presented in Chapter 2 using the direct boundary integral method and Neumann-Kelvin linearization is adopted to solve the problem. The trailing edge flow separation is considered by enforcing the equality of pressure at the trailing edge. The separation wake is modeled using a dipole singularity distribution over a linearized vortex sheet as explained in Section 2.10.1, and with further details in this section. The viscous cross-flow separation transverse force and yaw moment are estimated by means of a 2D+t cross flow method (see Section 2.10.3). A fully 3D potential-flow problem, with both divergent and transverse wave systems, and without slenderness assumption for the body is solved.

6.3.1 Formulation

A plate with finite aspect ratio and small drift angle, which is advancing in negative X -direction, was considered. Two Cartesian coordinate systems $OXYZ$ (global) and $Oxyz$ (seakeeping) were defined as explained in Section 2.1. The geometrical center of the plate in the mean water level was chosen as the origin of the seakeeping coordinate system. Figure 6.4 shows the coordinate systems arrangement for the present problem. A third body fitted coordinate system $Ox'y'z'$ was obtained by rotating $Oxyz$ around the z -axis by the drift angle α . Therefore, the obtained x' and y' axes are along, and perpendicular to, the plate's plane, respectively. The forces are presented in this body fitted coordinate system. The plate's dimensions and configuration are presented in Figure 6.5. The plate's aspect ratio is $\Lambda = H/L$, where L is the plate's length and H is the mean draft.

Only the steady motion is studied in this section. Therefore the problem can be formulated independent of time. It is noted that, similar to the other cases presented before, the fully nonlinear problem is difficult to handle. Therefore, the Neumann-Kelvin linearization method presented in Section 2.6 was used to simplify the problem. As discussed in Section 2.6 this type of linearization is more suitable for high Froude numbers of slender bodies.

The first and second order pressure, as presented in Eqs. (2.37) and (2.30), can be calculated from the first order velocity potential. It is noted that based on the linearization adopted here, the second order pressure in Eq. (2.30), i.e. $p^{(2)}$, must be close to zero; Otherwise, the used free-surface boundary condition is not consistent. This second-order pressure, which is calculated based on the first-order potential, can indicate to what extent the linearization assumption is valid. The forces and moments acting on the body were calculated by pressure integration as showed in Section 2.9. The yaw moment was calculated with respect to z' -axis through the geometrical center of the plate in the free-surface plane (see Figure 6.4).

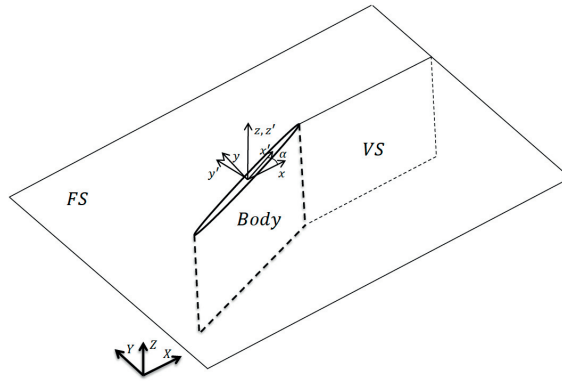


Figure 6.4: Schematic view of the problem and definition of the coordinate systems, a plate with drift angle advancing in the negative X -direction, FS : Free Surface, $Body$: Plate, VS : Vortex Sheet, α : drift angle

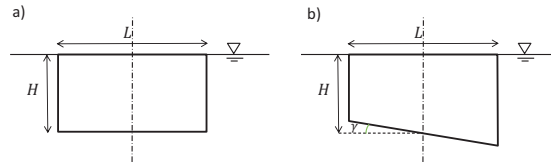


Figure 6.5: Definition of plate's dimensions, a) plate with constant draft, b) plate with variable draft, γ : plates taper angle

It is possible to separate the first-order and second-order contributions to the force as shown in Eqs. (2.55) and (2.56). As mentioned in Section 2.9, the second-order force presented in Eq. (2.56) is not complete, since the complete second-order force requires the solution for the second-order velocity potential. Eq. (2.56) is only the second-order force calculated from the first-order velocity potential. Similar to second-order pressure, this second-order force indicates the validity of the linear assumptions and must be close to zero. The transverse force and yaw moment are non-dimensionalized as follows:

$$\bar{F}_{y'} = \frac{F_{y'}}{\frac{1}{2}\rho U^2 L H} \quad (6.7)$$

$$\bar{M}_{z'} = \frac{M_{z'}}{\frac{1}{2}\rho U^2 L^2 H} \quad (6.8)$$

where the plate dimensions are shown in Figure 6.5.

Trailing edge separation

As discussed in the previous section, the Kutta condition must be enforced at the trailing edge. The drift angle of the plate creates a discontinuity in the velocity

potential at the trailing edge, similar to the attack angle in the previous problem. As pointed out by Maniar et al. (1990) and Xü (1991), there is an inconsistency between the pressure Kutta condition and the linearized free-surface boundary condition at the meeting point of the trailing edge and the free surface.

It was experimentally shown by van den Brug et al. (1971) and Maniar et al. (1990) among others, that the free-surface elevations at the two sides of the body are different due to the drift angle. This difference in the free-surface elevations continues along the body and into the fluid domain. In other words, while the pressure is continuous at the trailing edge below the free surface, there is a discontinuity in the free-surface elevation, and consequently the pressure, at the meeting point of the trailing edge and the free surface. This means that, immediately after the body, a sharp change in the free-surface elevation along the y -axis exists, which disappears a short distance downstream. On the other hand, the value for the free-surface elevation is assumed to be a single-valued function in linear theory, which cannot account for such a sharp change.

In order to properly capture this nonlinear phenomenon, a nonlinear formulation seems to be necessary. However, as mentioned also by Xü (1991), and showed later on in this study, the error due to this type of linearization is limited to a small area around the tail of the body, and has no significant influence on the overall results. In order to get around this inconsistency, it is important to ease the Kutta condition and allow for pressure inequality at the meeting point of the trailing edge and the free surface. In the present study, the Kutta condition was numerically applied as described in the previous section. However, at the connection point between the trailing edge and the free surface, the condition was relaxed to allow the free-surface elevations, i.e. pressures, to take two different values.

Bottom tip separation

The separation from the bottom tip of the plate contributes to the transverse force and yaw moment as pointed out by Chapman (1976) and investigated later by Landrini and Campana (1996). They introduced a vortex sheet, starting from the plate's tip, to take into account the cross-flow tip separation effects. To account for this influence in our model, a 2D+t approach described in Section 2.10.3 was used. The objective here is to make an estimation of the cross-flow separation importance in calculating the transverse force and yaw moment. In other words, we have used Froude hypothesis to separate the viscous and potential (wave making) parts of the force, and calculate them in an uncoupled way. The results comparisons with the experimental data will be presented to show the limits and validity of this uncoupling assumption.

Following the method presented in Section 2.10.3, an Earth-fixed plane (Π) was defined normal to the plate as shown in Figure 6.6(a). The motion of the body was viewed from this stationary plane. Due to plate's forward speed and drift angle, the plate's section appears to move through the stationary plane with velocity u_1 and slides side way with velocity v_1 (Figure 6.6(b)). A right-handed Cartesian body-fixed coordinate system $Ox_1y_1z_1$ was defined with x_1y_1 -plane corresponding to the mean free surface and x_1 along the plate center line, y_1z_1 -plane parallel to Π -plane

with z_1 pointing upward. The origin of this coordinate system is attached to the intersection of the plate's leading edge and the free surface. From this frame of reference, there is an incident cross-flow velocity v_1 . Looking at the problem from the Earth-fixed plane, it transforms into the transient problem of a uniform cross flow passing a 2D plate, in presence of free surface (Figure 6.7). By using a zero Froude number assumption, the free-surface boundary condition can be replaced by the zero vertical velocity condition, i.e. wall boundary condition.

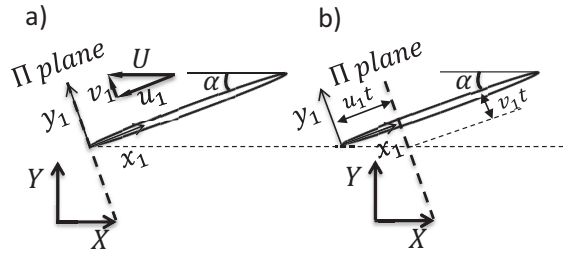


Figure 6.6: 2D+t coordinate system, a) plate reaches the Earth-fixed stationary plane, b) plate is passing through the Earth-fixed stationary plane.

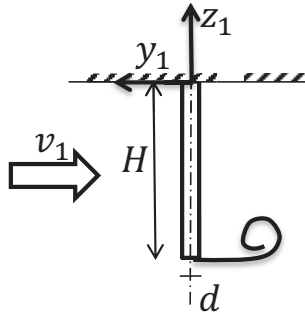


Figure 6.7: Section of a plate in a cross flow, 2D+t coordinate system, v_1 : Cross flow velocity, H : Plate's draft, d : Plate's thickness

The drag force due to a cross flow acting on a 2D plate in infinite fluid, or attached to a wall, is a well-studied fluid dynamic problem. However, most of the studies are dedicated to the mean and oscillatory drag coefficients after the initial transient period. Fink and Soh (1974) studied this problem numerically by a discrete vortex method and showed that the drag force coefficient starts from a large value (around 6) and then decreases rapidly during a short period in the beginning of the simulation and approaches its mean value. Due to numerical problems, it is, however, difficult to calculate the forces at the beginning of the simulation. Further studies by Faltinsen and Pettersen (1983) using a vortex sheet model, and Tønnessen (1999) using a finite element solution (FEM) of the laminar

Navier-Stokes equation, showed that due to these numerical problems the drag coefficient is unrealistically large at the few first time steps of the calculations. Similar studies were carried out by Koumoutsakos and Shiels (1996) using a 2D adaptive numerical method based on vortex methods. They also observed a similar behavior at the start-up of the simulation.

The transient cross-flow drag coefficient ($C_D(\mathcal{T})$) can be presented as a function of a non-dimensional time defined as \mathcal{T} in Eq. (6.9). In the present problem, the cross-flow velocity would be v_1 and the characteristic length was chosen to be the plate's draft (H). As demonstrated by Faltinsen (2005), the sections of the plate downstream the flow feel the vortex generated by the upper sections, depending on how far they are from the start point of the separation. The time (t) can be related to the position of a section relative to the leading edge in $Ox_1y_1z_1$ coordinate system as shown in Section 2.10.3. Using $x_1 = u_1t$ and $\tan \alpha = v_1/u_1$ we obtain,

$$\mathcal{T} = \frac{v_1}{u_1} \frac{x_1}{H} = \tan \alpha \frac{x_1}{H} \quad (6.9)$$

Then, the side force and yaw moment on the plate due to the cross flow drag (Eqs. (2.71) and (2.72)) become Eqs. (6.10) and (6.11) respectively,

$$F_{CF} = \frac{1}{2} \rho v_1 u_1 H^2 \int_0^{\tan \alpha L/H} C_D(\mathcal{T}) d\mathcal{T} \quad (6.10)$$

$$M_{CF} = \frac{L}{2} F_{CF} - \frac{1}{2} \rho u_1^2 H^3 \int_0^{\tan \alpha L/H} C_D(\mathcal{T}) \mathcal{T} d\mathcal{T} \quad (6.11)$$

where L is the plate's length, α is the drift angle and ρ is the water density. For the present case the side force and yaw moment are non-dimensionalized as shown in Eqs. (6.12) and (6.13).

$$\frac{F_{CF}}{\frac{1}{2} \rho U^2 L H} = \sin \alpha \cos \alpha \frac{H}{L} \int_0^{\tan \alpha L/H} C_D(\mathcal{T}) d\mathcal{T} \quad (6.12)$$

$$\frac{M_{CF}}{\frac{1}{2} \rho U^2 L^2 H} = \frac{1}{2} \bar{F}_{CF} - \cos^2 \alpha \frac{H^2}{L^2} \int_0^{\tan \alpha L/H} C_D(\mathcal{T}) \mathcal{T} d\mathcal{T} \quad (6.13)$$

Therefore, the cross-flow side force and yaw moment are proportional to the area and the moment of area under the curve ($C_D(\mathcal{T}), \mathcal{T}$). It is interesting to point out that, based on Eqs. (6.10) and (6.11), the length of integration is influenced by L , $\tan \alpha$, and H . Therefore, for a plate with constant H , the non-dimensional drag force and yaw moment (Eqs. (6.12) and (6.13)) are only a function of the drift angle and not the forward speed. It must be noted that this assumption approximates the flow three-dimensionality and does not account for the free-surface wave effects. It is expected that the non-dimensional cross-flow drag force becomes Froude number dependent for high Froude numbers, because of the free-surface interactions. This type of dependency is neglected here by applying the rigid free-surface condition.

A mean value of 5 was chosen for the drag coefficient at the beginning of the transition. A curve was fitted to the numerical values presented by Fink and Soh (1974) by fixing the start-up drag. A sensitivity study was carried out by changing the start-up value from 4 to 6, to investigate the dependency of the final results on the start-up value. Although the results are slightly varying, the changes were not significant. The final shape of the curve was adjusted by using one set of the experimental data for a plate with drift angle and forward speed from van den Brug et al. (1971), and used for all other cases.

Further studies using a complete Navier-Stokes solver, with proper free-surface condition, would be necessary to obtain, more accurately, the behavior of the drag coefficient at the beginning of the flow. It is noted that the present method is significantly different from a viscous cross-flow model used in engineering analysis of, for instance, ship maneuvering. The latter method is based on the 2D drag coefficients of the steady flow and will, for a flat plate with constant draft, predict a constant force per unit length along the plate. Moreover, the present method is not a complete 2D+t solution and was only used to calculate an estimation for the cross-flow separation force.

6.3.2 Discretization and numerical implementation

The direct boundary integral formulation presented in Eq. (2.81) was used to formulate the problem. As shown in Section 2.11, the integrals on the vortex sheet surfaces are simplified to a dipole distribution on the positive side of the vortex sheet. The dipole strength on the sheet would be equal to $\Delta\phi = \phi^+ - \phi^-$ at the trailing edge, which is, based on Eq. (6.2), constant along the x -axis.

Assuming constant forward speed and Neumann-Kelvin linearization, the body and the combined free-surface boundary condition in Eqs. (2.36) and (2.40) becomes,

$$\begin{aligned}\phi_n &= -U\vec{i} \cdot \mathbf{n} && \text{on plate's surface} \\ \phi_n &= \frac{U^2}{g}\phi_{xx} && \text{on free surface}\end{aligned}\tag{6.14}$$

Substituting the boundary conditions from Eq. (6.14) into Eq. (2.81) gives,

$$\begin{aligned}\mathcal{C}\phi(\mathbf{x}) &= \int_{S_B} \phi(\boldsymbol{\xi}) \frac{\partial G(\mathbf{x}, \boldsymbol{\xi})}{\partial \mathbf{n}(\boldsymbol{\xi})} dS + \int_{S_B} G(\mathbf{x}, \boldsymbol{\xi}) \left(U\vec{i} \cdot \mathbf{n}(\boldsymbol{\xi}) \right) dS \\ &+ \int_{S_F} \phi(\boldsymbol{\xi}) \frac{\partial G(\mathbf{x}, \boldsymbol{\xi})}{\partial \mathbf{n}(\boldsymbol{\xi})} dS - \int_{S_F} G(\mathbf{x}, \boldsymbol{\xi}) \left(\frac{U^2}{g} \frac{\partial^2 \phi(\boldsymbol{\xi})}{\partial \xi^2} \right) dS \\ &+ \int_{S_{V+}} (\phi^+(\boldsymbol{\xi}) - \phi^-(\boldsymbol{\xi})) \frac{\partial G(\mathbf{x}, \boldsymbol{\xi})}{\partial \mathbf{n}^+(\boldsymbol{\xi})} dS\end{aligned}\tag{6.15}$$

In order to solve Eq. (6.15), the boundaries were discretized into a finite number of rectangular panels. Linear distribution of unknowns on these panels was

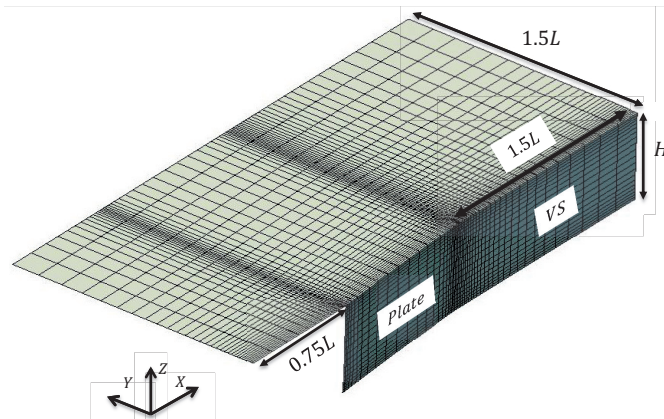


Figure 6.8: View of the numerical grid and free-surface dimensions, VS : Vortex sheet.

assumed. The boundaries of the computational domain were chosen based on the guidelines suggested by Zhu and Faltinsen (2007), in order to minimize the effects of domain truncation. The dimensions and an example of the computational grid are shown in Figure 6.8. The vortex sheet, which is bounded by the trailing edge and the free surface, is also limited to the extent of the free surface behind the plate. Although there were some local errors at the far downstream of the free surface, numerical studies showed that the effects of having a finite vortex sheet on the forces acting on the plate are negligible.

Points were distributed on the boundaries using the numerical grid generation methods described in Section 3.9 to control the point density on the grid. This proved to be important in adjusting the accuracy of the solution by increasing the density of the collocation points at the areas of high variation. The latter was done close to the sharp corners, such as the leading and trailing edge, as well as the bottom tip of the plate. In addition, a similar treatment was applied on the free surface close to the leading edge, where thin-ship 2D+t theory (Faltinsen, 2005) shows that the slope of the free surface has a singular behavior.

A second-order finite difference scheme was applied to calculate the derivatives on both the free surface and the body surface. In order to do so, structured grids were generated for the body and the free surface. Then, the surfaces were mapped to a computational domain for calculating the derivatives as described in Section 3.9. Since the problem has no symmetry plane, the velocity potential was solved everywhere on the boundaries, except on the vortex sheet.

Based on the discussions in Section 3.7.1, it is important to choose a correct direction of differentiation in order to ensure the solution's stability and satisfy the radiation condition, especially at higher Froude numbers. Therefore, upstream differentiation was used for the derivatives on the free surface. The problem of the saw-tooth instabilities, reported before in the literature (e.g. Nakos (1990)), was treated by adjusting the damping of the finite difference scheme based on the

Table 6.1: Number of panels and grid properties for Plate A (see Section 3.9.1 for definition of Grid Attraction Factor)

Grid	Plate	Free Surface	Grid Attraction Factor		Total
			Leading/Trailing Edge	Water/Tip line	
A	10x10	30x10	15	10	800
B	20x20	60x20	15	10	3200
C	30x20	90x20	15	10	6600
D	40x30	120x30	15	10	12000

conclusions derived in Chapter 4.

Since a 3D solver was used, the plate's geometrical properties, such as thickness and drift angle, were considered without linearization. In other words, the body boundary condition was satisfied on the actual position of the body. In order to avoid numerical difficulties, the shape of the plate section was assumed to be a parabola, with sharp corners at the leading and trailing edges. However, only flow separation from the trailing edge was included in the calculations.

6.3.3 Results and discussions

In this section, the results from a series of experimental and numerical cases are presented for comparison. Plate *A* from van den Brug et al. (1971) experiments is considered. The values for the transverse force and yaw moment are calculated and compared with experiments and previous numerical results. Aspect ratios of 0.5 and 0.2, with drift angles of 4.5 and 9 degrees are considered. From experiments by Kashiwagi (1983), a plate with aspect ratio $\Lambda = H/L = 0.1$, and drift angles of 4 and 8 degrees, are considered. The influence of a plate's taper angle on the forces are addressed at the end. The plate *E* from van den Brug et al. (1971) experiments, with aspect ratios of 0.2 and 0.5, and a taper angle of 4 degrees is studied for this purpose.

Grid sensitivity study

Convergence studies were carefully carried out for different test cases to assess the sensitivity of the transverse force and yaw moment to the grid density. The properties of the four selected grid arrangements, which were used in the calculations, are summarized in Table 6.1. Besides the number of elements for the free surface and the plate, the values for the attraction factors at the leading and trailing edges, as well as the water line and bottom-tip line, are presented. The arcsinh function, in combination with the attraction factors, were used as the control function in the Hybrid Curve Point Distribution Algorithm to generate the suitable point distributions along the boundaries (please see Section 3.9.1 for more details). The value of the attraction factors are an indication of the density of the grid points.

Figure 6.9 shows the convergence study for the transverse force and yaw moment on a plate with aspect ratio of 0.5 and drift angle of 4.5 degrees; using the grids

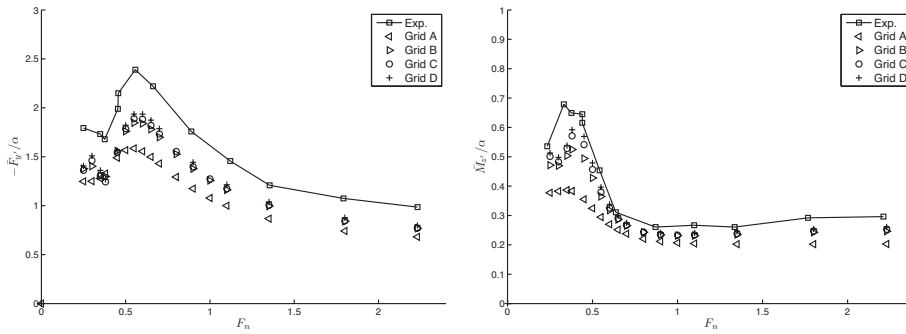


Figure 6.9: Convergence study for non-dimensional transverse force and yaw moment, Exp.: experimental results by van den Brug et al. (1971), drift angle $\alpha = 4.5^\circ$, aspect ratio $\Lambda = H/L = 0.5$, $\bar{F}_{y'} = \frac{F_{y'}}{\frac{1}{2}\rho U^2 LH}$, $\bar{M}_{z'} = \frac{M_{z'}}{\frac{1}{2}\rho U^2 L^2 H}$, Force and moment are normalized by the drift angle in radians, Grids are defined in Table 6.1.

described in Table 6.1. The values have an offset from the experiments but they show a convergence pattern. Besides the coarsest grid (Grid A), all the other three grids seem to follow the trend of the experimental values. The large variation in the transverse force between $F_n = 0.4$ and $F_n = 0.7$ is best captured by the finest grid (Grid D), while the results from the other two grids (Grid B and C) follow closely. Figures 6.10 and 6.11 show a similar convergence study for aspect ratios of 0.2 and 0.1, with drift angles of 4.5 and 4 degrees. A similar convergence pattern is visible, although, the relative differences between the numerical and experimental results are increasing by decreasing the aspect ratio.

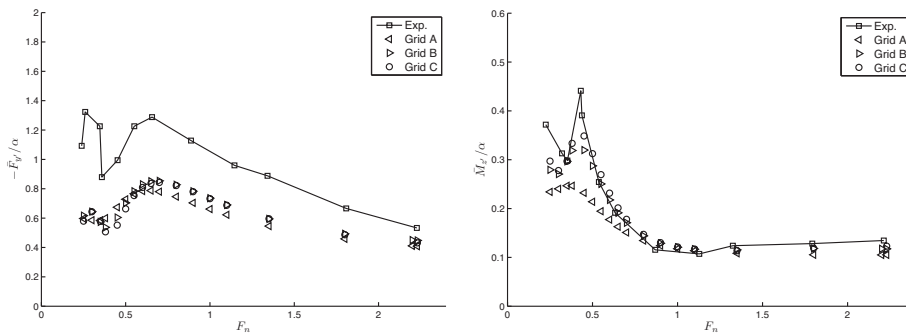


Figure 6.10: Convergence study for non-dimensional transverse force and drift moment, Exp.: experimental results by van den Brug et al. (1971), drift angle $\alpha = 4.5^\circ$, aspect ratio $\Lambda = H/L = 0.2$, further details as in Figure 6.9.

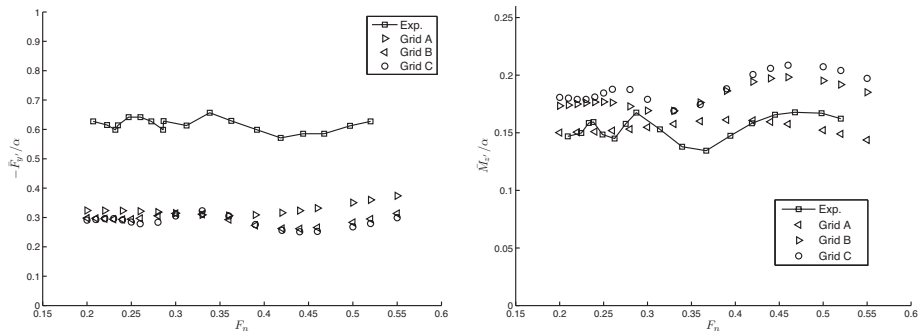


Figure 6.11: Convergence study for non-dimensional transverse force and drift moment, Exp.: experimental results by Kashiwagi (1983), drift angle $\alpha = 4.0^\circ$, aspect ratio $\Lambda = H/L = 0.1$, further details as in Figure 6.9.

Plate's thickness effects

Since a 3D solver was used in the present study, it is possible to investigate the effect of plate's thickness on the forces and moments acting on the plate. The thickness ratio was defined as the ratio between the maximum thickness of the parabola and the length of the plate $th = d_{max}/L$.

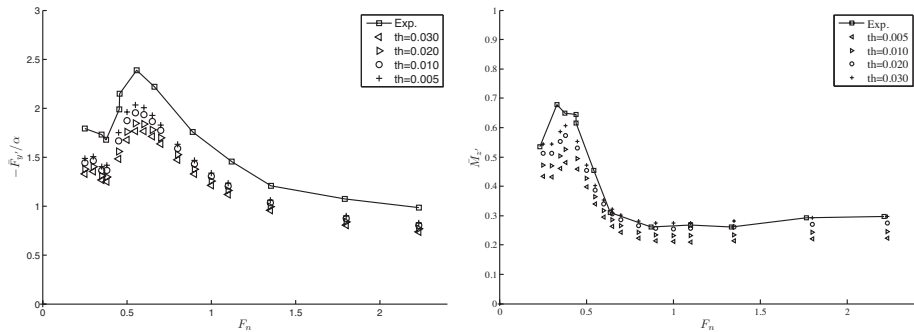


Figure 6.12: Effect of thickness on the non-dimensional transverse force and yaw moment, Exp.: experimental results by van den Brug et al. (1971), drift angle $\alpha = 4.5^\circ$, aspect ratio $\Lambda = H/L = 0.5$, $th = d_{max}/L$ where d_{max} is the maximum thickness of the plate and L is the plates length, Grid C from Table 6.1 is used, further details as in Figure 6.9.

Figure 6.12 shows the effect of the thickness ratio on the transverse force and yaw moment for a plate with aspect ratio 0.5 and drift angle 4.5 degrees. It can be concluded that by increasing the thickness ratio, the transverse force and yaw moment increase. In order to investigate a plate with zero thickness, the present boundary integral formulation needs modifications. Otherwise, a singularity occurs by approaching zero-thickness in the current formulation. From the two sets of

experiments considered here, the plate A from van den Brug et al. (1971) has the thickness ratio of 0.01 and the plate from Kashiwagi (1983) has a thickness ratio of 0.007. Therefore, the thickness ratio of 0.01 was used in the rest of this study in order to keep the compatibility with the experiments.

Importance of nonlinearities

The importance of nonlinearities was investigated by calculating the second order forces and moments from the first order velocity potential using Eq. (2.56). As discussed previously in Section 2.9, this is a part of the second order force and it does not represent the complete value; which requires the solution of the second order boundary value problem. However, it still can be of importance, in evaluating the validity of the linearization, and the estimation of the nonlinear contribution. Figures 6.13 to 6.15 show the values of the first and second order transverse force and yaw moment for different thicknesses and aspect ratios of, 0.5, 0.2, and 0.1 at the drift angles, 4.5 and 4 degrees.

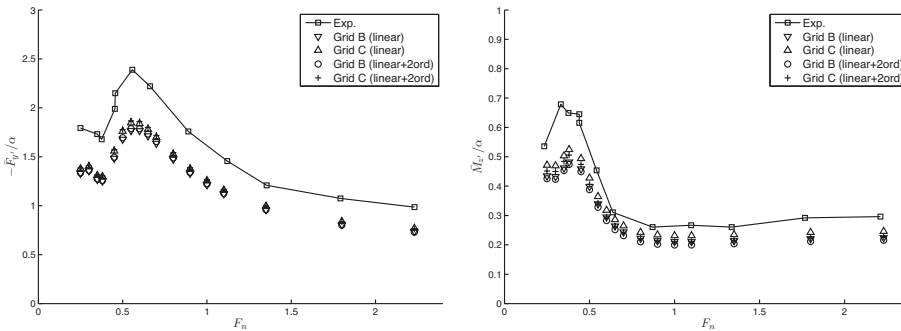


Figure 6.13: First and second order non-dimensional transverse force and yaw moment for two different grids, Exp.: experimental results by van den Brug et al. (1971), 2ord: second order force from first order velocity potential, drift angle $\alpha = 4.5^\circ$, aspect ratio $\Lambda = H/L = 0.5$, further details as in Figure 6.9.

Generally, the differences between the first and second order transverse forces are negligible, and the differences are more pronounced for the yaw moment, and increase for smaller aspect ratios. The second order yaw moment shows smaller values than the first order yaw moment. This is closer to the experiments for smaller aspect ratios, which is an indication of the importance of nonlinearities. The complete second order force is needed in these cases to judge the accuracy of the method. On the other hand, the linear results for aspect ratios of 0.2 and 0.5 are closer to the experiments, and the differences introduced by including the second order effects are small. Therefore, the linear assumption suits better the larger aspects ratios.

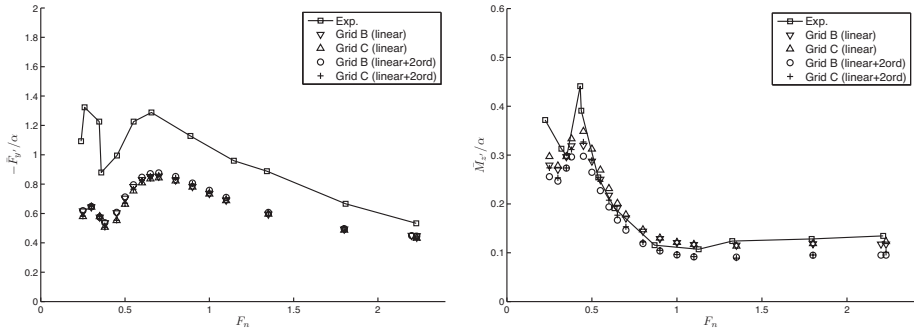


Figure 6.14: First and second order non-dimensional transverse force and yaw moment for two different grids, Exp.: experimental results by van den Brug et al. (1971), 2ord: second order force from first order velocity potential, drift angle $\alpha = 4.5^\circ$, aspect ratio $\Lambda = H/L = 0.2$, further details as in Figure 6.9.

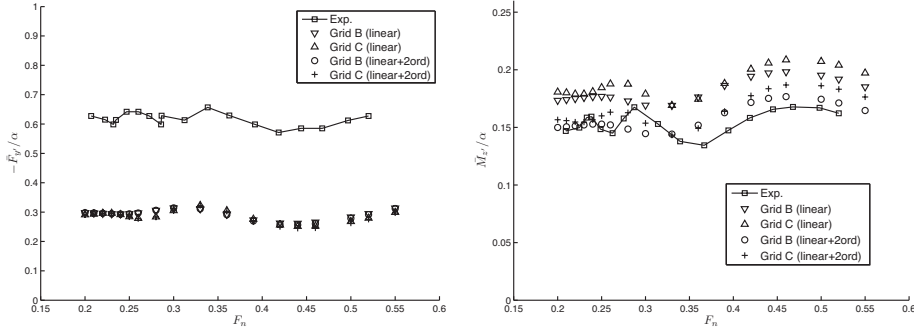


Figure 6.15: First and second order non-dimensional transverse force and yaw moment for two different grids, Exp.: experimental results by Kashiwagi (1983), 2ord: second order force from first order velocity potential, drift angle $\alpha = 4.0^\circ$, aspect ratio $\Lambda = H/L = 0.1$, further details as in Figure 6.9.

Viscous cross-flow (2D+t)

By looking at the results in Figures 6.13 to 6.15, it is clear that the values from the present potential flow calculation are lower than the experiments, while they follow the same trend. This difference is believed to be due to the cross-flow separation effects from the bottom tip of the plate. As explained in section Section 6.3.1, an attempt was made to consider these effects using a 2D+t viscous method with zero Froude number free-surface boundary condition. As shown in Eqs. (6.12) and (6.13), the cross-flow non-dimensional transverse force and yaw moment are only a function of the plate’s drift angle and draft. Therefore, for a constant draft and drift angle, the cross-flow force and moment are constant for all Froude numbers. This results in a constant shift in the potential flow results shown in Figures 6.13 to 6.15.

Table 6.2: Values for viscous cross-flow correction by the 2D+t method on transverse force and yaw moment, $\bar{F}_{y'} = F_{y'}/(0.5\rho U^2 LH)$, $\bar{M}_{z'} = M_{z'}/(0.5)\rho U^2 L^2 H)$, Force and moment are normalized by the drift angle in radians.

Aspect ratio ($\Lambda = H/L$)	0.5	0.2	0.1
$-\bar{F}_{y'CF}/\alpha$	0.39	0.37	0.34
$\bar{M}_{z'CF}/\alpha$	0.002	0.006	0.008
$\bar{F}_{y'CF}/\max(\bar{F}_{y'Exp.})$	0.16	0.29	0.51
$\bar{M}_{z'CF}/\max(\bar{M}_{z'Exp.})$	0.003	0.014	0.051

The values for the cross-flow transverse force and yaw moment, for different aspect ratios, are presented in Table 6.2. In addition, Table 6.2 shows the ratios between the cross-flow corrections and the maximum measured forces, which shows that the importance of the viscous corrections are increasing by decreasing the aspect ratio. It is noted that this ratio belongs to the peak force only, and is changing by varying Froude number. Figures 6.16 to 6.18 show the potential flow results for the first order transverse force and yaw moment with thickness ratio 0.01, plus the cross-flow corrections. Since the viscous cross-flow moments were very small, they are not shown in the yaw moment plots. The calculated viscous cross-flow transverse force shifts the potential results towards the experimental values. Due to the zero Froude number free-surface boundary condition, which was used for calculating the cross-flow effects, a difference between the experimental and computational results was expected at higher Froude numbers. However, this deviation starts at relatively higher Froude numbers than anticipated (around 1.0). This showed that the hypothesis of separating the viscous and potential flow effects in the transverse direction was valid even up to high forward Froude numbers.

For the yaw moment, the results are close to the experiments, without the viscous cross-flow corrections. The viscous cross-flow corrections to the yaw moment, as presented in Table 6.2, were negligible, except for aspect ratio 0.1. The non-dimensional yaw moment is much smaller in this case than for higher aspect ratios and the cross-flow correction, although small, is no longer negligible. This could be due to higher contributions of non-linear effects for smaller aspect ratios.

The present values for aspect-ratio 0.5 and the drift angle of 4.5 degrees are compared to other numerical results in Figure 6.19. A similar shift in the results were predicted by Landrini and Campana (1996). They solved the problem with and without a bottom tip vortex sheet, using double-body linearization. The difference between the two sets of their results was close to a constant value as well. The present results, without the cross-flow correction, are close to the Landrini and Campana (1996) results without the tip-vortex sheet, while the cross-flow correction shifts the present values towards their results with the tip-vortex. There is a small difference between the Froude number of the peak force in the present and the results from Landrini and Campana (1996). This might be due to their low Froude number free-surface boundary condition. They used the double body velocity potential as the base for linearization, while the undisturbed inflow velocity

potential was used here, which is believed to be more consistent at higher Froude numbers than the double-body potential.

Landrini and Campana (1996) have considered the vortex sheet and free surface interactions, but still, at higher Froude numbers, their deviations from the experimental results are larger than the present calculations; even though a simpler approach was used in the present calculations. This can be also a result of their free-surface boundary condition, which is not suitable for high Froude numbers.

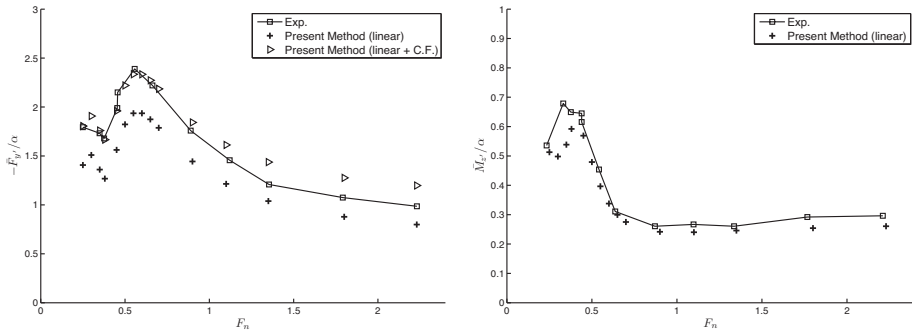


Figure 6.16: Comparison of non-dimensional transverse force and yaw moment, Exp.: experimental results by van den Brug et al. (1971), C.F.: Viscous Cross Flow (2D+t), drift angle $\alpha = 4.5^\circ$, aspect ratio $\Lambda = H/L = 0.5$, further details as in Figure 6.9.

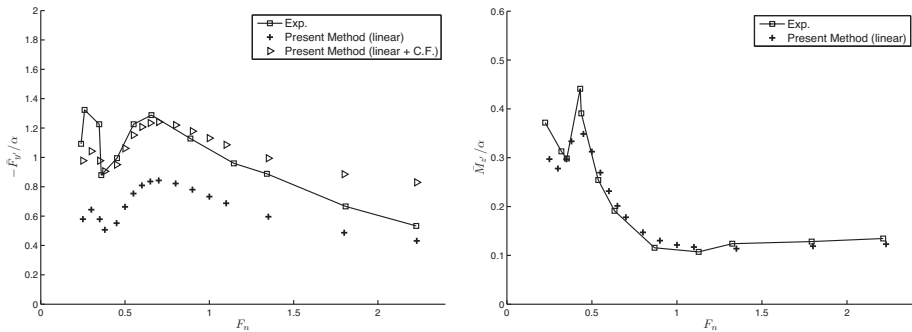


Figure 6.17: Comparison of non-dimensional transverse force and yaw moment, Exp.: experimental results by van den Brug et al. (1971), C.F.: Viscous Cross Flow (2D+t), drift angle $\alpha = 4.5^\circ$, aspect ratio $\Lambda = H/L = 0.2$, further details as in Figure 6.9.

Maniar et al. (1990) and Xü (1991) solved this problem using a thin-body assumption and distribution of Kelvin wave singularities. The present results, without the cross-flow correction, are very close to their values for the yaw moment. On the other hand, for the transverse force, the two curves are close to each other away from the region of the maximum force, while the position of the peak is

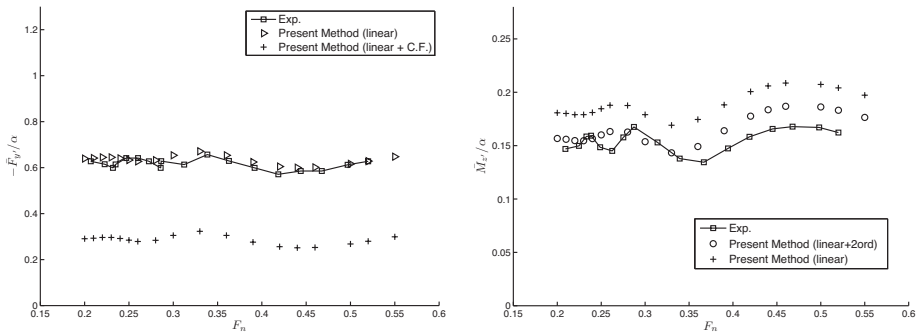


Figure 6.18: Comparison of non-dimensional transverse force and yaw moment, Exp.: experimental results by Kashiwagi (1983), C.F.: Viscous Cross Flow (2D+t), 2ord: second order force from first order velocity potential, drift angle $\alpha = 4.0^\circ$, aspect ratio $\Lambda = H/L = 0.1$, further details as in Figure 6.9.

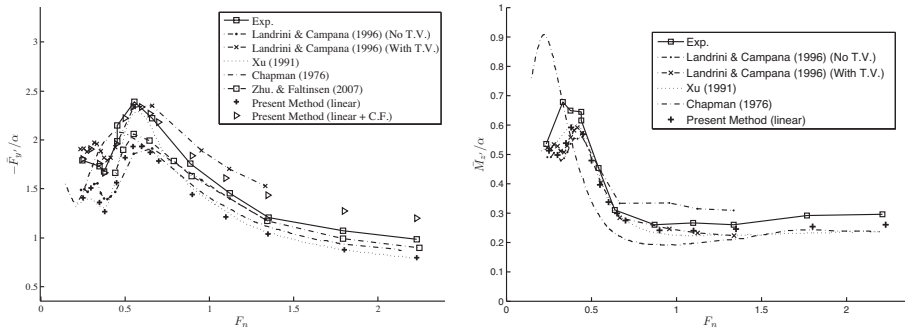


Figure 6.19: Comparison of non-dimensional transverse force and yaw moment, Exp.: Experimental results by van den Brug et al. (1971), C.F.: Viscous Cross Flow (2D+t), T.V.: Tip Vortex sheet, drift angle $\alpha = 4.5^\circ$, aspect ratio $\Lambda = H/L = 0.5$, further details as in Figure 6.9.

predicted similarly in both calculations. The results from Zhu and Faltinsen (2007), in which a similar method has been used for calculating the transverse force, are also presented for comparison.

Figure 6.20 shows similar comparisons for aspect-ratio 0.2 and drift-angle 4.5 degrees. Figure 6.21 also shows comparisons with the experimental results from Kashiwagi (1983) for a plate with aspect-ratio 0.1 . The importance of nonlinearities are more pronounced in the yaw moment; while the side force including the cross-flow correction follows the experimental results much better than the yaw moment. The results from the calculations by Landrini and Campana (1996) using the double-body linearization and a tip vortex sheet are closer to the measurements, which can be due to their linearization method. It also may indicate that the free-surface and tip-vortex interaction plays an important role for the transverse force,

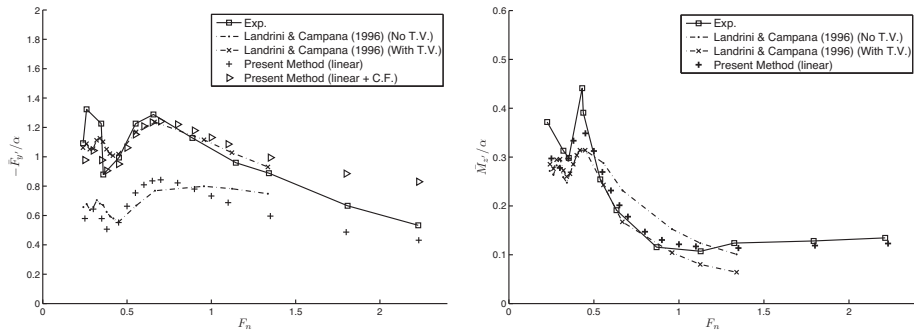


Figure 6.20: Comparison of non-dimensional transverse force and yaw moment, Exp.: Experimental results by van den Brug et al. (1971), C.F.: Viscous Cross Flow (2D+t), T.V.: Tip Vortex sheet, drift angle $\alpha = 4.5^\circ$, aspect ratio $\Lambda = H/L = 0.2$, further details as in Figure 6.9.

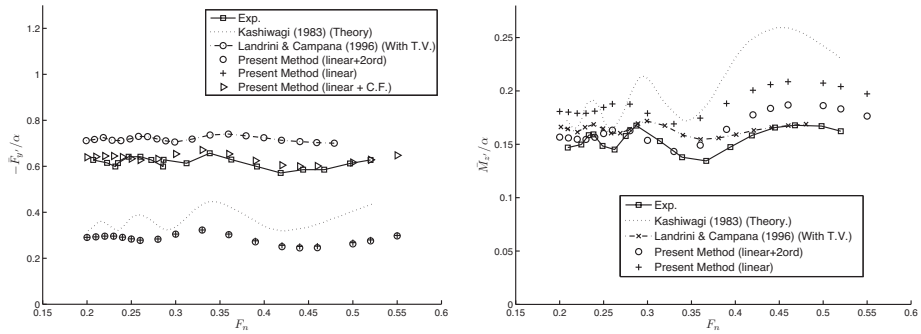


Figure 6.21: Comparison of non-dimensional transverse force and yaw moment, Exp.: Experimental results by Kashiwagi (1983), C.F.: Viscous Cross Flow (2D+t), T.V.: Tip Vortex sheet, 2ord: second order force from first order velocity potential, drift angle $\alpha = 4.0^\circ$, aspect ratio $\Lambda = H/L = 0.1$, further details as in Figure 6.9.

while it does not have much effect on the yaw moment.

Larger drift angles

Although the linear assumption in the present formulation requires the drift angle to be small, a set of higher drift angles were also studied. The results are presented in Figures 6.22 to 6.24 for the aspect ratios of 0.5 and 0.2, with a drift angle of 9 degrees from van den Brug et al. (1971) experiments, and an aspect-ratio of 0.1 and a drift-angle of 8 degrees from Kashiwagi (1983) experiments.

As shown in Figure 6.22, for the transverse force on the plate with $\Lambda = 0.5$, the deviation from the experimental results was larger and started from lower Froude numbers, but the influence of the second order forces was still negligible. However, for the aspect ratio of 0.2, Figure 6.23, the effect of the second order forces started

to be important, especially around the maximum side force. However, it was still negligible for the Froude numbers approximately lower than 0.5 and higher than 1.5. On the other hand, the deviation from the experimental results after the viscous cross-flow correction was much higher than for the aspect-ratio of 0.5. While, the corrected results for the aspect-ratio of 0.5 were closer to Landrini and Campana (1996) results with the tip-vortex, for aspect-ratio 0.2, it showed a clear difference, which did not exist at 4.5 degrees drift angle. This can be an indication that the vortex generated from the bottom-tip separation is stronger at higher drift angles, and at smaller drafts its interactions with the free surface matters.

Similar behavior is expected for $\Lambda = 0.1$ from Kashiwagi (1983)'s experiments. However, since these experiments were realized for relatively lower Froude numbers, our method still predicted the transverse force with reasonable accuracy.

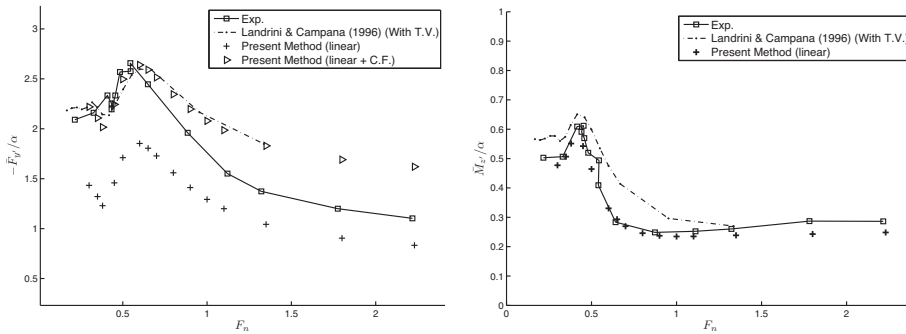


Figure 6.22: Comparison of non-dimensional transverse force and yaw moment, Exp.: Experimental results by van den Brug et al. (1971), C.F.: Viscous Cross Flow (2D+t), T.V.: Tip Vortex sheet, drift angle $\alpha = 9.0^\circ$, aspect ratio $\Lambda = H/L = 0.5$, further details as in Figure 6.9.

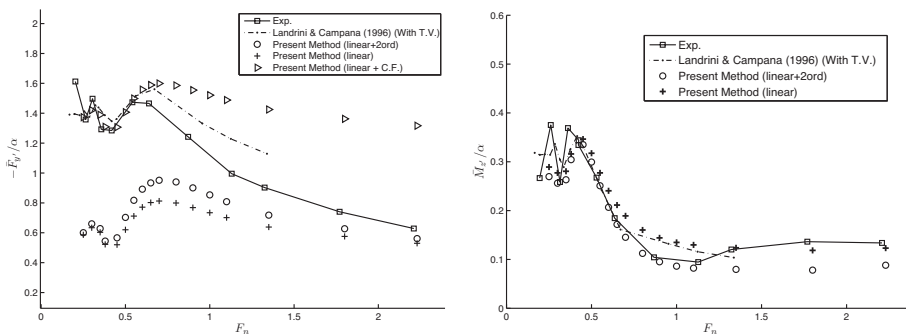


Figure 6.23: Comparison of non-dimensional transverse force and yaw moment, Exp.: Experimental results by van den Brug et al. (1971), C.F.: Viscous Cross Flow (2D+t), T.V.: Tip Vortex sheet, drift angle $\alpha = 9.0^\circ$, aspect ratio $\Lambda = H/L = 0.2$, further details as in Figure 6.9.

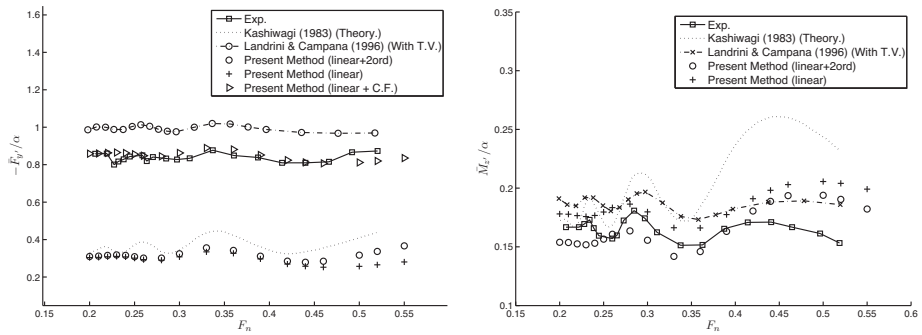


Figure 6.24: Comparison of non-dimensional transverse force and yaw moment, Exp.: Experimental results by Kashiwagi (1983), T.V.: Tip Vortex sheet, C.F.: Viscous Cross Flow (2D+t), 2ord: second order force from first order velocity potential, drift angle $\alpha = 8.0^\circ$, aspect ratio $\Lambda = H/L = 0.1$, further details as in Figure 6.9.

Looking at the yaw moment, we can see that these effects are not important for the aspect-ratios of 0.5 and 0.2, and the current method can predict the yaw moment with a reasonable accuracy, without any cross-flow correction. It is noted that the second-order yaw moment, for the case with aspect-ratio of 0.2, has clearly a larger influence at this drift angle, than in a similar case with 4.5 degrees. However, the results show larger deviations from the experimental results for the aspect-ratio 0.1.

Tapered Plate

A case of a tapered plate was also studied. The results were compared with the experimental values reported by van den Brug et al. (1971) for plate *E*, with taper angle of 4 degrees. The experiments were realized for a drift angle of 9 degrees only. The results for the two aspect ratios, 0.5 and 0.2, are shown in Figures 6.25 and 6.26.

The transverse side force, with viscous cross-flow correction, follows the experiments with reasonable accuracy for an aspect ratio of 0.5, while similar deviation from the experiments, as for a non-tapered plate, is identified. The yaw moment also agrees with the experiments. Due to the change in the draft along the plate, the cross-flow correction to the yaw moment is no longer negligible, however, it is small in this case.

The deviation of the cross-flow corrected side force, for the aspect-ratio 0.2, from the experimental results is much larger. As explained before, this can be due to the interaction between the bottom-tip vortex and the free surface, which in this case is increased by the smaller draft at the leading edge. The yaw moment on the tapered plate is over predicted by the potential-flow theory for this combination of aspect ratio and drift angle. Moreover, the stabilizing effect of the cross-flow yaw moment is interesting. It seems in order to get a better prediction of forces,

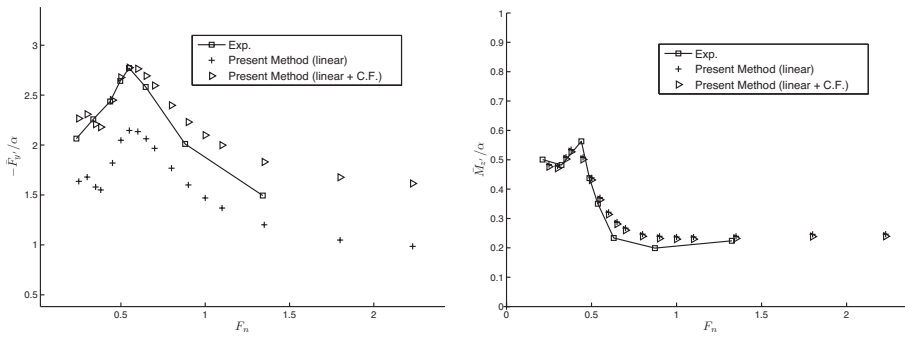


Figure 6.25: Comparison of non-dimensional transverse force and yaw moment, Exp.: Experimental results by van den Brug et al. (1971), C.F.: Viscous Cross Flow (2D+t), drift angle $\alpha = 9.0^\circ$, aspect ratio $\Lambda = H/L = 0.5$, taper angle $\gamma = 4^\circ$, further details as in Figure 6.9.

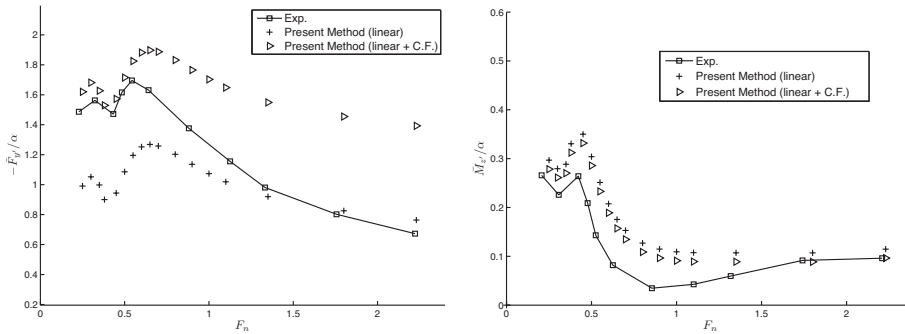


Figure 6.26: Comparison of non-dimensional transverse force and yaw moment, Exp.: Experimental results by van den Brug et al. (1971), C.F.: Viscous Cross Flow (2D+t), drift angle $\alpha = 9.0^\circ$, aspect ratio $\Lambda = H/L = 0.2$, taper angle $\gamma = 4^\circ$, further details as in Figure 6.9.

the interactions between waves and the cross-flow tip vortex must be taken into account.

6.4 Plate in oscillatory sway and yaw motions

The problem of a finite aspect ratio, surface-piercing plate, advancing with constant forward speed, presented in the previous section, is developed further by solving the harmonic oscillations in sway and yaw in the time-domain. The goal is to calculate the added-mass and damping coefficients for these modes of motion, which would be essential in linear dynamic stability analysis in the horizontal plane.

The experimental data by van den Brug et al. (1971) is used for validation of the model. Then, the model is used to investigate the influence of the plate's

draft and taper angle on the hydrodynamic coefficients. The calculated values are further used in Chapter 8 to investigate the dynamic stability of a vessel.

6.4.1 Formulation

A similar coordinate system to what has been presented in Figure 6.4 for an advancing plate with a drift angle was used in the present case. The difference is that in the present case, the drift angle is zero and the plate is in-line with the incoming flow. The oscillatory motion of the plate was taken into account using perturbation and linearization of the body boundary condition. Therefore, unlike the previous case in Section 6.3, the body boundary condition was linearized around the mean position of the body. Consequently, $Ox'y'z'$ coordinate system is always coincides with the $Oxyz$ coordinate system and, therefore, was omitted.

The problem was solved in the time-domain. Similar to the heaving Wigley hull in Section 5.6, the solution of this problem consists of two stages, also. The initial stage, in which the plate starts from the rest and gain speed smoothly until it reaches the steady forward velocity (using a cosine ramp function in Eq. (5.2)); and the oscillatory stage, in which the steadily translating plate starts to oscillate with a smoothly increasing amplitude until it reaches the desired value. The main difference between the present case and the heaving Wigley hull is the presence of a trailing edge flow separation. Due to the sway and yaw oscillations, the flow separates from the tail of the plate and propagates into the fluid in the form of vortices. This is similar to what happens in the steady forward motion of a plate with a drift angle as discussed in the previous section. However, due to the oscillations, the strength of the generated vortices and their signs are not constant and change with time.

The propagation of vortices was linearized as explained in Section 2.10.1 and similarly used in Section 6.3. Then, vorticity conservation in the fluid was satisfied by propagating the vortices generated at the trailing edge down-stream, with the ambient flow, on a flat vortex sheet extended in x -direction. The one-dimensional convection equation of vortices takes the form of a linearized parabolic equation; as shown before in Eq. 2.66 and repeated here in Eq. 6.16.

$$\frac{\partial \Gamma(\mathbf{x}, t)}{\partial t} + U \frac{\partial \Gamma(\mathbf{x}, t)}{\partial x} = 0 \quad \text{on } S_V \quad (6.16)$$

Here $\Gamma = \phi^+ - \phi^-$ is the strength of the vortices generated at the trailing edge, which propagates down-stream on the linearized vortex sheet S_V . The boundary integral formulation in Eq. (2.81) takes the following form in Eq. (6.17) for the present problem at each time-instance.

$$\begin{aligned} & \int_{S_B} \phi(\boldsymbol{\xi}) \frac{\partial G(\mathbf{x}, \boldsymbol{\xi})}{\partial \mathbf{n}(\boldsymbol{\xi})} dS + \int_{S_F} \frac{\partial \phi(\boldsymbol{\xi})}{\partial \mathbf{n}(\boldsymbol{\xi})} G(\mathbf{x}, \boldsymbol{\xi}) dS - \mathcal{C}(\mathbf{x}) \phi(\mathbf{x}) = \\ & \int_{S_B} \frac{\partial \phi(\boldsymbol{\xi})}{\partial \mathbf{n}(\boldsymbol{\xi})} G(\mathbf{x}, \boldsymbol{\xi}) dS - \int_{S_F} \phi(\boldsymbol{\xi}) \frac{\partial G(\mathbf{x}, \boldsymbol{\xi})}{\partial \mathbf{n}(\boldsymbol{\xi})} dS - \int_{S_{V+}} \Gamma(\boldsymbol{\xi}) \frac{\partial G(\mathbf{x}, \boldsymbol{\xi})}{\partial \mathbf{n}^+(\boldsymbol{\xi})} dS \end{aligned} \quad (6.17)$$

The known values at each time-instance were moved to the right-hand-side, while the unknown parts were collected on the left-hand-side. The linearized body boundary conditions for forced sway and yaw motions are obtained from Eq. (2.36) by assuming $\eta_j = \bar{\eta}_j \cos(\omega t)$ as shown in Eq. (6.18) below.

$$\begin{aligned} \frac{\partial \phi}{\partial n}(\mathbf{x}) &= -U\mathbf{i} \cdot \mathbf{n} - \omega \bar{\eta}_2 n_2 \sin(\omega t) && \text{(sway motion)} \\ \frac{\partial \phi}{\partial n}(\mathbf{x}) &= -U\mathbf{i} \cdot \mathbf{n} - \omega \bar{\eta}_6 n_6 \sin(\omega t) && \text{(yaw motion)} \end{aligned} \quad (6.18)$$

Therefore, $\frac{\partial \phi}{\partial n}$ on the body surface is known at all times from the prescribed motion of the body. On the other hand, ϕ on the free surface and Γ on the vortex sheet are known at start from the initial condition, and must be calculated using a time-marching method for the future time-instances. If the problem is started from rest, like the first stage of the calculation, these values can be assigned to zero. At each time-instance, $\frac{\partial \phi}{\partial n}$ on the free surface and ϕ on the body surface are obtained by solving the boundary integral equation. Then, the value for Γ at the trailing edge of the body is obtained from the distribution of ϕ on the body at each time-instance.

6.4.2 Discretization

To solve the boundary integral equation, the surfaces were discretized into rectangular elements with linear distribution of unknowns. The grid points were distributed with higher density at the areas of higher variations in order to increase the solution accuracy, using the methods described in Section 3.9 and used in Section 6.3. One of these important areas for this problem is around the trailing edge on the body and on the vortex sheet. The grid B from the previous section, described in Table 6.1, was used in the present calculations. The choice of the grid size was made based on a trade-off between the accuracy and the computational cost.

A 4th order Runge-Kutta method was used for time-stepping the solution in the present calculations. In this method, by means of the kinematic and dynamic boundary conditions as explained in Section 3.6.3, the velocity potential on the free surface for the next time-instance is obtained from $\frac{\partial \phi}{\partial n}$ of the current time-instance. The same time-marching method was adopted for solving the propagation of vortices on the vortex sheet. The plate thickness was taken into account explicitly and without any assumption on slenderness of the body. The shape of the plate was assumed to be a parabola, similar to the previous problem in Section 6.3.

The size of the free-surface domain and the method for generating grid are similar to what was used in Section 6.3. Close to the truncation boundaries of the free surface, a damping zone was adopted to absorb the waves generated by the oscillating plate (see Section 3.7.2). A second order up-stream finite difference scheme was used to calculate the derivatives on the free surface, using the same mapping technique used before in Section 6.3. The radiation boundary condition was satisfied by using this up-stream differentiation method in addition to the damping zone (see Section 3.7.1 and Chapter 4 for more details).

Truncating the vortex sheet inside the fluid domain has diverse effects on the solution close to the domain's down-stream boundary. These effects were partly

detectable by looking at the free-surface elevation around this area. The errors due to the vortex sheet truncation were minimized by extending the sheet further down-stream. The final size of the domain was chosen by numerical studies of the influence of the boundaries' positions on the hydrodynamic forces on the plate. The boundaries' distances presented in Figure 6.8, which were used for the steady-state case, tuned out to be sufficient for the present problem as well.

The convection of vortices is governed by a one-dimensional linearized parabolic equation (Eq. (6.16)). Therefore, choosing a correct direction for differentiation is essential. The correct direction must correspond to the propagation direction of the physical information in the fluid, which, by virtue of linearization, is the ambient flow direction. The second-order upstream finite difference scheme was used to calculate the derivatives on the vortex sheet and enforce the correct direction of propagation at the same time.

The time-step was chosen based on the number of steps per oscillation period. Usually 40 steps per-period gave satisfactory results. However, in order to avoid instabilities on the vortex sheet, the Courant-Friedrichs-Lewy (CFL) condition must be considered in choosing the time-step as well. In the simplest form, the grid velocity, defined by $\Delta x/\Delta t$, must not be higher than the physical velocity of traveling vortices as shown in Eq. (6.19) below.

$$\Delta t < \frac{\Delta x}{U} \tag{6.19}$$

This imposes a limit on the time scale, based on the minimum size of the elements in the x-direction on the vortex sheet. The elements were chosen to be smaller closer to the trailing edge. This owes to the interpolation of values at the trailing edge, to form a closed solution as explained in Section 6.3.1. Due to this interpolation, the accuracy of the solution reduces rapidly by increasing the size of the elements at the trailing edge. The combination of smaller elements at the trailing edge and the limit on the time-step due to stability criteria, increases the computational cost.

The forces on the plate were calculated using the direct pressure integration method explained in Section 2.9. The added mass and damping coefficients of the plate were calculated by eliminating the mean forces and taking a Fourier transform of the oscillatory part.

6.4.3 Results

As a first step, the time-domain solution of a translating plate with a fixed drift angle was compared to the results from the steady-state formulation in Section 6.3. A plate, with a given drift angle, was started from rest and the speed increased smoothly until it reached the target Froude number. As the forward speed increased, the generated vortices at the trailing edge got stronger and propagated down the vortex sheet. After the transient period, the vortex strength on the vortex sheet became constant and the solution reached the steady-state condition. The transient time was approximately three times the duration of the cosine ramp function (see Eq. (5.2)).

The transverse force and yaw moment acting on the plate after reaching the steady-state condition were compared to the results in Section 6.3 from the steady-solver. The values were almost identical, which indicated that the solver is ready to put to test for the oscillatory motions.

Comparisons with experiments

Plate D , from the experimental data by van den Brug et al. (1971), was chosen for comparison. The aspect ratio of the plate is $\Lambda = 0.2$. Moreover, the numerical calculations by Chapman (1975) using strip theory and 2D+t method with slender body assumption are presented for comparison. Attention must be paid on the differences between the coordinate systems and the definition of the hydrodynamic forces for comparing the results. Here, the results are presented in the form of non-dimensional added mass and damping coefficients, which previously introduced in Section 2.9.

Figures 6.27 to 6.30 show the non-dimensional added mass and damping coefficients for a series of non-dimensional frequencies at four different Froude number, from $Fn = 0.32$ to $Fn = 0.96$. It is apparent that the hydrodynamic coefficients are both frequency and Froude number dependent. However, as van den Brug et al. (1971) reported, the frequency dependency of the coefficients decreases by increasing the Froude number. For instance, for $Fn = 0.96$ in Figure 6.30 the hydrodynamic coefficients are almost constant for all oscillation frequencies. On the other hand, for $Fn = 0.32$, high dependency on the oscillation frequency is evident from Figure 6.27.

As pointed out by Chapman (1975), the strip theory method is not suitable for predicting the hydrodynamic coefficients in high forward speed. Neglecting the lifting effects due to flow separation from the trailing edge is believed to be the main reason. The results from the 2D+t method from Chapman (1975) follows the experiments much closer than the strip theory results. The present calculations agree reasonably well with the experimental and 2D+t results. However, the slenderness assumption is not essential to the present method of calculation, which uses 3D Rankine panels and a vortex sheet. Therefore, the solver can be used for calculating the hydrodynamic coefficients of non-slender bodies in the same manner.

The inaccuracy in the hydrodynamic force measurements for the oscillatory motions, reported by van den Brug et al. (1971), must be mentioned. The plate's deformations due to the hydrodynamic forces are in some cases contributed to the measured reaction forces. These effects are smaller for the plates which have more solid structures. Therefore, only the comparisons with the thickest plate (D) is presented here.

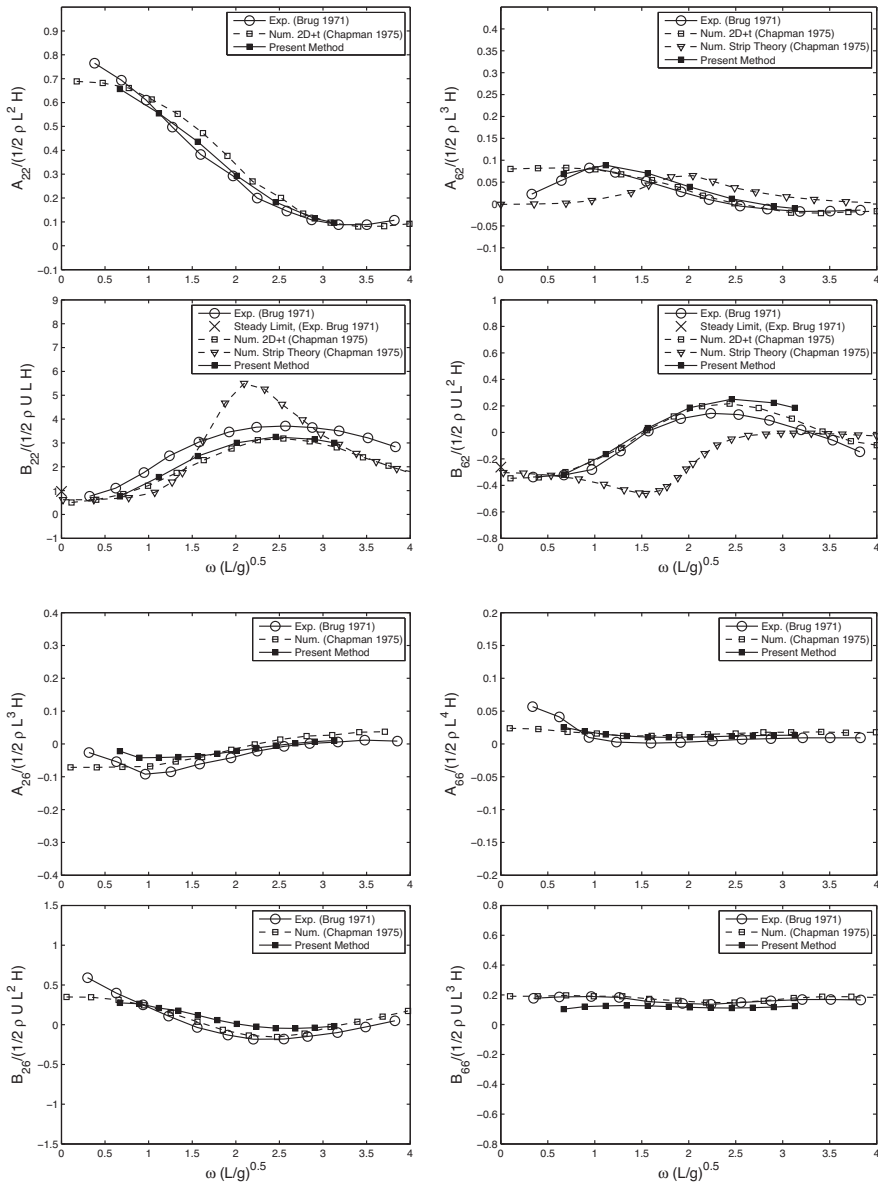


Figure 6.27: Comparison of the non-dimensional added-mass and damping in sway and yaw for a surface-piercing plate with forward speed, $F_n = 0.32$, Exp.: Experimental data, aspect ratio $\Lambda = H/L = 0.2$.

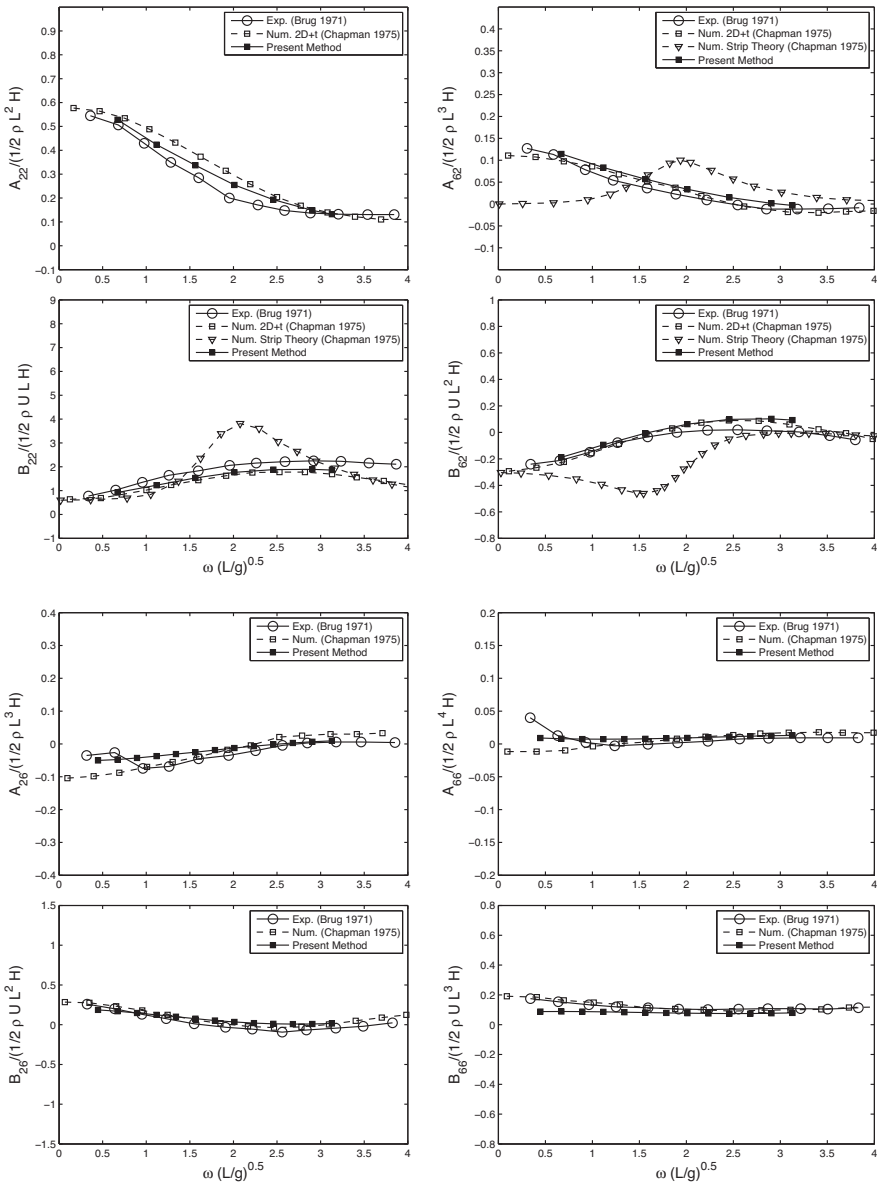


Figure 6.28: Comparison of the non-dimensional added-mass and damping in sway and yaw for a surface-piercing plate with forward speed, $F_n = 0.48$, Exp.: Experimental data, aspect ratio $\Lambda = H/L = 0.2$.

For the Froude numbers $F_n = 0.32$ and $F_n = 0.96$ in Figures 6.27 and 6.30, the steady-limit values, corresponding to the zero oscillation frequency, are also presented. By reducing the oscillation frequency to zero, the oscillatory problem approaches the steady-state problem of forward translation of a plate with a constant drift angle. These values are shown by crosses in B_{22} and B_{62} plots, which correspond to the steady transverse force and yaw moment, respectively. The differences between the calculations and the experimental data at the limit are equivalent to the linearized contribution of the flow separation from plate's tip as discussed in Section 6.3.3. The differences here are consistent with the values calculated for the contribution of the bottom-tip flow separation in the previous section. This difference is larger for $F_n = 0.32$ than $F_n = 0.90$. This agrees with the predictions in Figure 6.17, which shows a smaller difference between the potential-flow forces and the experimental values for higher Froude number. The 2D+t cross-flow method, neglecting the free-surface effects, were used for calculating the cross-flow forces in the previous section. As discussed in Section 6.3.3, the interaction between the bottom-tip vortex and the free-surface waves at high Froude numbers maybe the reason for this change.

The effects of the flow separation from the bottom-tip due to oscillatory motions were neglected. At higher Froude numbers the hydrodynamic coefficients are speed-independent. It means that the importance of flow separation, which is generally frequency dependent, reduces by forward speed. As a consequence, the bottom-tip flow separation, which proved to be important for a plate with a fixed drift angle, seems to rapidly lose its importance by increasing the forward speed. The bottom-tip flow separation can be included in the calculations by introducing a horizontal vortex sheet, or by using a 2D+t viscous solver to solve the viscous flow across a swaying plate's section by neglecting the free surface. Both of these methods require the problem to be solved for a series of initial conditions, at each oscillation frequency and Froude number. Moreover, the obtained forces must be linearized in order to be presented in terms of the added mass and damping coefficients. Continuation of this study is left for future works.

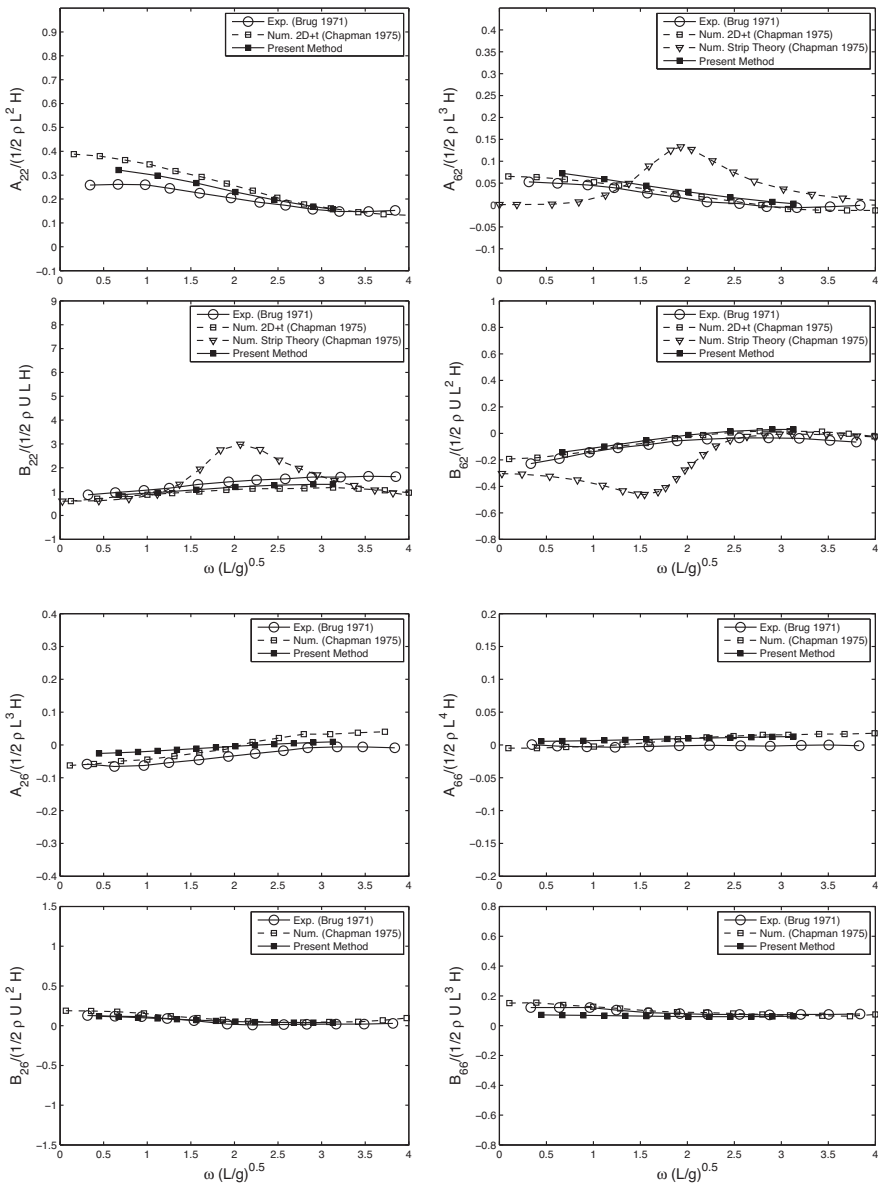


Figure 6.29: Comparison of the non-dimensional added-mass and damping in sway and yaw for a surface-piercing plate with forward speed, $Fn = 0.64$, Exp.: Experimental data, aspect ratio $\Lambda = H/L = 0.2$.

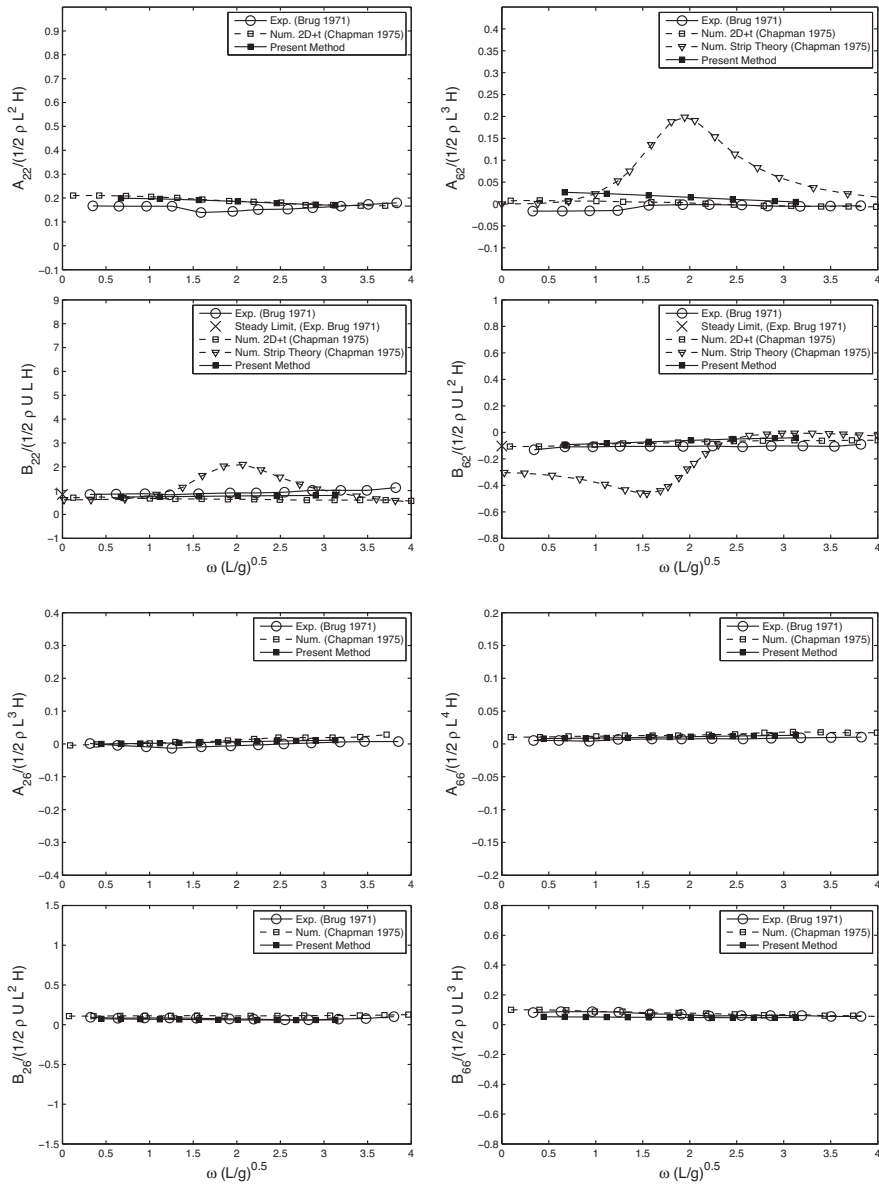


Figure 6.30: Comparison of the non-dimensional added-mass and damping in sway and yaw for a surface-piercing plate with forward speed, $F_n = 0.96$, Exp.: Experimental data, aspect ratio $\Lambda = H/L = 0.2$.

Notes on the importance of a vortex sheet

Figure 6.31 shows the added mass and damping coefficients in the sway motion of a plate. The experimental data from van den Brug et al. (1971) and the numerical calculations using a 2D+t method are presented. The calculations from the present method, with and without a vortex sheet, are also included. The influence of the vortex sheet on the hydrodynamic coefficients is clearly demonstrated.

In 2D+t method the problem is only solved up to the trailing edge. Consequently, the flow separation from the plate's trailing edge, and the traveling vortices in the fluid, are not explicitly included in the 2D+t method. However, neglecting the vortices in the present 3D method leads to unacceptable results. Since in the present method the problem is solved in the 3D domain the flow separation must be considered explicitly by introducing a vortex sheet. Otherwise, the 3D method will enforce the velocity potential to have one value at the trailing edge. However, the jump in the velocity potential at the trailing edge is the key to the necessary flow separation, which plays an important role. Removing this discontinuity results in an incomplete and inconsistent formulation, which changes the overall picture of the flow.

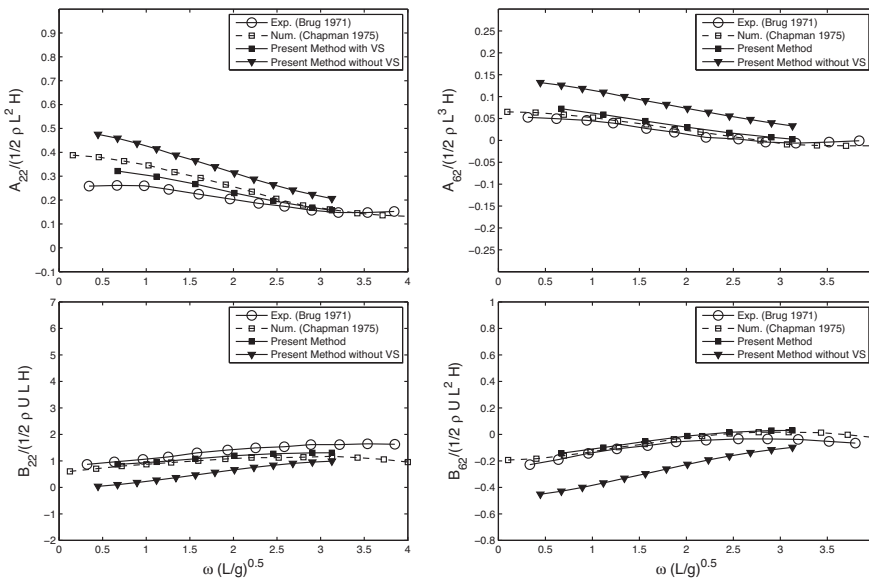


Figure 6.31: Importance of vortex sheet in calculating the added-mass and damping coefficients in sway of a surface-piercing plate with forward speed, $Fn = 0.64$, Exp.: Experimental data, aspect ratio $\Lambda = 0.2$.

In the 2D+t method, the discontinuity is implicitly allowed by solving the problem for separated transverse sections along the body. In other words, it is implicitly assumed that the discontinuity at the trailing edge travels down-stream to infinity. Since the 2D+t solution does not reach the meeting point of the flow from

the two sides, handling the discontinuity never becomes an issue. The importance of these discontinuities (vortices) after they leave the body is assumed to be small in the 2D+t method. This is true especially for higher Froude numbers. By looking at the comparisons presented in Section 6.4.3, it is possible to confirm the validity of this assumption.

Influence of draft and taper angle

The influence of draft and taper angle on the hydrodynamic coefficients in sway and yaw are briefly presented here. Figure 6.32 shows the results for three aspect ratios at $Fn = 0.45$. The aspect ratio of 0.2 is also presented with taper angle of 4 degrees. Changing the draft has stronger effects on sway coefficients than yaw. Similarly, changing the taper angle influences the coefficients on sway more than yaw. Figure 6.32 shows the results for $Fn = 0.68$. As the dependency of the values to the frequency decreases, the changes due to draft and taper angle also appear as constant shifts in the curves. The influence of the draft and taper angle on the hydrodynamic model of the plate is important, for instance, in dynamic stability predictions. Increasing the taper angle is known to improve the steady-state stability of an advancing plate by decreasing the destabilizing yaw moment (e.g. van den Brug et al. (1971)). However, further investigations are required to clarify the influence of these parameters on the dynamic stability of a plate.

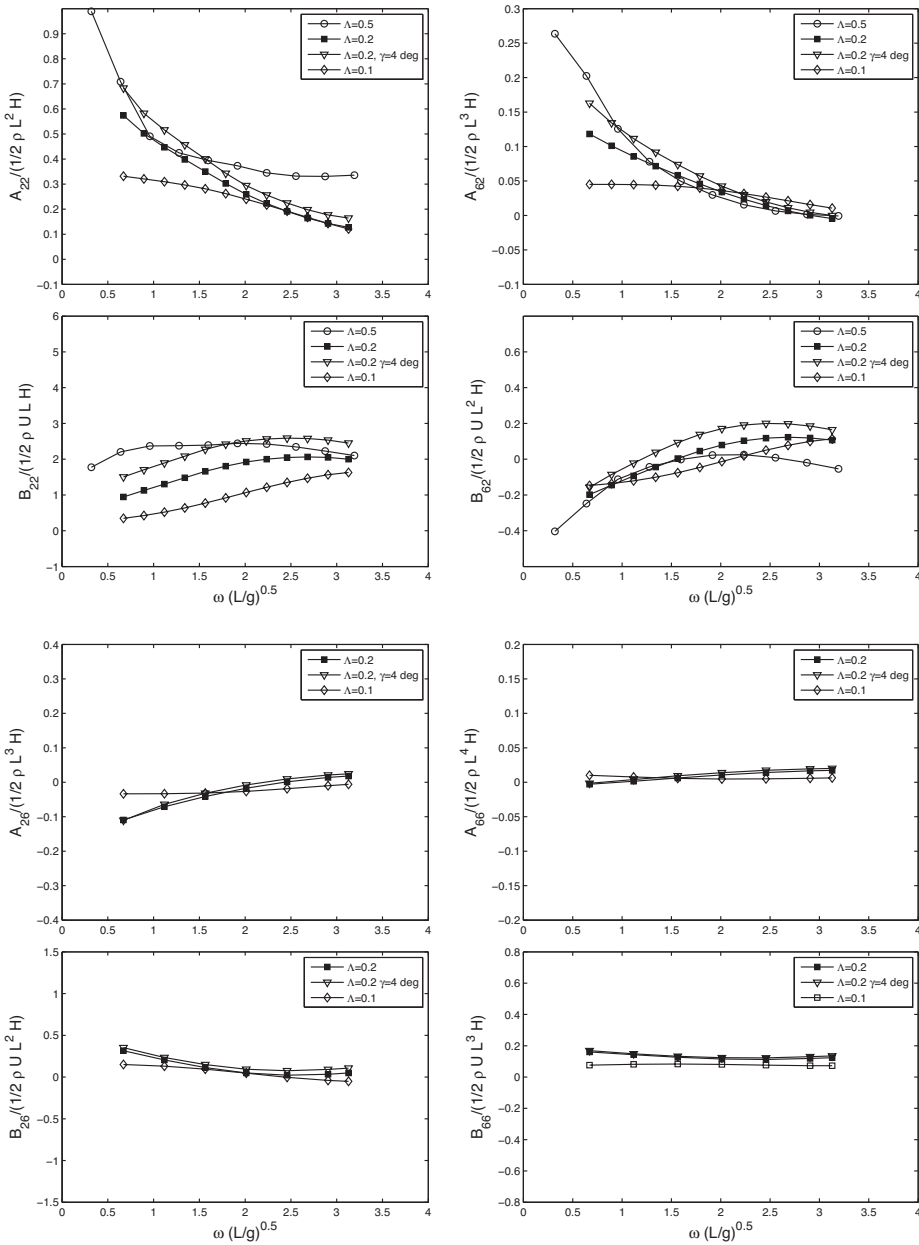


Figure 6.32: Influence of draft and taper angle on the added-mass and damping in sway and yaw of a surface-piercing plate with forward speed, $F_n = 0.45$, $\Lambda = H/L$: aspect ratio, γ : taper angle.

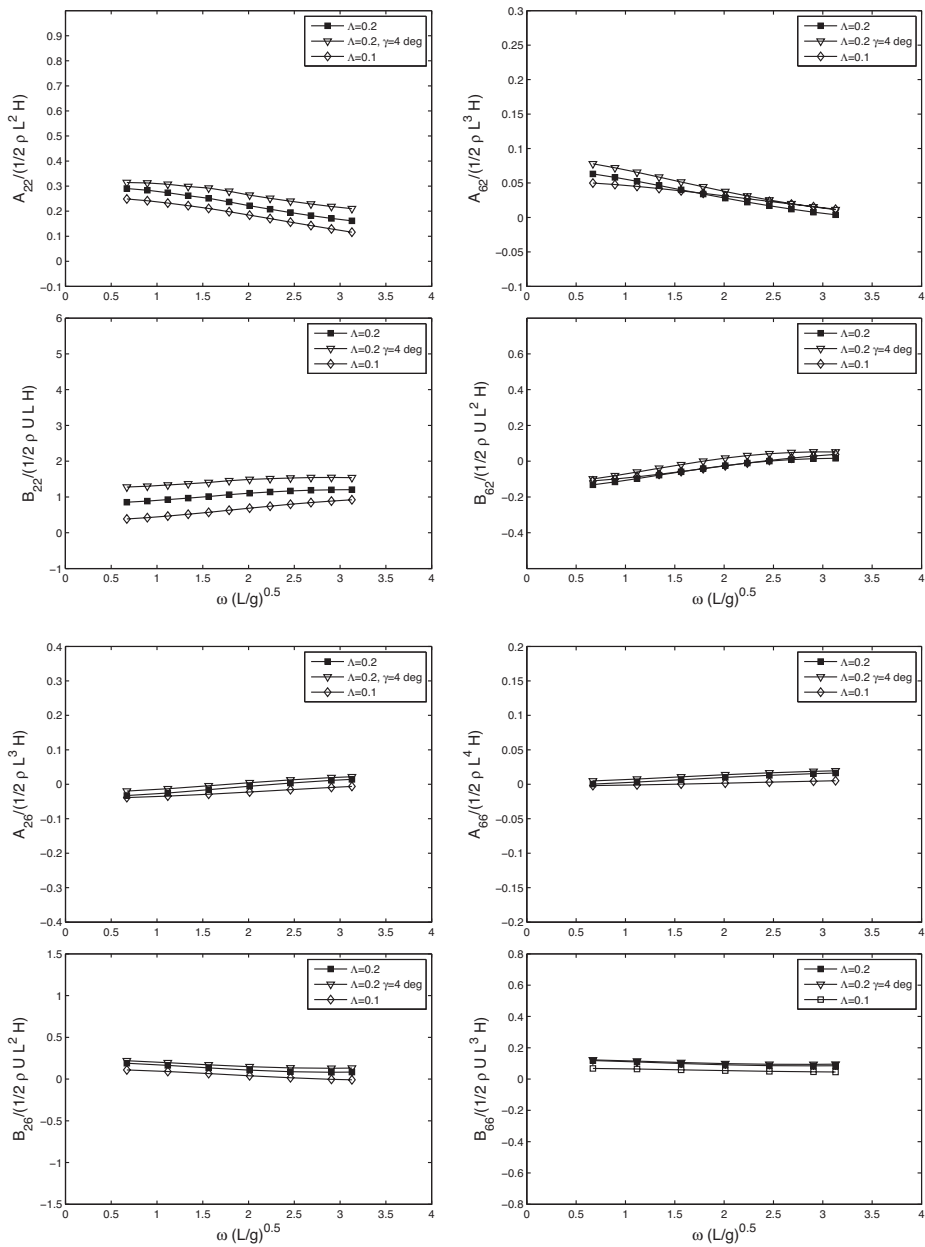


Figure 6.33: Influence of draft and taper angle on the added-mass and damping in sway and yaw of a surface-piercing plate with forward speed, $Fn = 0.68$, $\Lambda = H/L$: aspect ratio, γ .: taper angle.

6.5 Conclusions

A set of problems with flow separation were studied in this chapter. Dipole singularities were introduced on a wake sheet behind the trailing edge of the body, together with a Kutta condition at the trailing edge, to capture the flow separation. The Kutta condition was satisfied by enforcing the continuity on the velocity potential jump at the separation line. The shape of the sheet was linearized to a vertical flat surface. Both steady and unsteady problems were considered. In the unsteady case, the time varying dipole strength was propagated with the ambient flow along the x -axis.

For the steady case, it was shown that the cross-flow separation from the plate's tip contributes to the transverse force and yaw moment. A viscous 2D+t method, using a rigid free-surface boundary condition was used to account for this effect in the present work. It was shown that the non-dimensional forces acting on a plate due to the bottom-tip flow separation with a rigid free-surface boundary condition depend on the drift angle and not the Froude number. Therefore, it imposes only a constant shift on the curve of the non-dimensional transverse force against Froude number. This shift seems to fill the gap between the potential flow results and the experiments correctly, especially for Froude numbers approximately lower than 1.0. Deviation from the experimental values appeared by increasing the Froude number. Neglecting the interactions between the cross-flow tip-vortex and the free surface by imposing the rigid free-surface boundary condition is believed to be the reason. The influence of the tip separation on the yaw moment was shown to be negligible.

The potential-flow results for the hydrodynamic coefficients in sway and yaw were compared with experimental and 2D+t results. It was shown that for unsteady cases the cross-flow separation loses its importance by increasing the forward speed and oscillation frequency. The influence of draft and taper angle, as well as the vortex sheet on the hydrodynamic coefficients were presented and discussed. It has been shown that the results from the present numerical model agrees reasonably well with the experimental and numerical results using thin and slender body assumptions, while it can be used for non-slender bodies as well. This model can be further used to construct hydrodynamic models for investigation of dynamic stability.

Chapter 7

Hydrodynamics of Semi-displacement Vessels

7.1 Introduction

Hydrodynamics of semi-displacement monohull vessels are addressed in this chapter. This type of vessel is known for having an instability issue in calm water, known as calm water broaching. This type of instability was described in Chapter 1 and will be studied further in Chapter 8. To study this instability, a hydrodynamic model of a semi-displacement vessel is needed. A plate's hydrodynamic model was presented in Chapter 6 as a simplified alternative for a semi-displacement vessel's hydrodynamic model. This chapter is an attempt to understand, and model, the complicated hydrodynamics of semi-displacement vessels using a simple potential-flow formulation.

For semi-displacement vessels, the buoyancy and lift force are equally important for carrying the weight at operational speed. Flow separation from the transom stern complicates the flow around semi-displacement vessels. For a high enough transom stern Froude number, the separation combines with ventilation and forms a dry transom stern. Since the Froude number of interest in the present study is high, the dry transom stern condition is always assumed in the calculations. The applications of the hollow-body method, described in Section 2.10.2, is further demonstrated and developed in the following sections.

First the steady forward motion of semi-displacement monohull vessels are studied. The free surface elevation on the water line and the distribution of hydrodynamic vertical forces are compared with experiments. Two groups of experimental data for two different vessels are used for comparison. The hollow body method is used to model the dry transom stern effects and the hollow in the free surface. Then, the steady motion of a semi-displacement vessel with a fixed drift angle is considered. The hollow body model was developed with asymmetric shape in order to take the effects of drift angle into account. The importance of the cross-flow separation on the transverse force and yaw moment is discussed. Simple viscous

corrections to the longitudinal force and a 2D+t cross flow model for the transverse force and yaw moment are adopted.

The harmonic forced heave oscillation of a semi-displacement vessel is also considered. The boundary condition on the hollow body is further developed to take into account the oscillatory motion. The problem is solved in the time-domain. The distribution of the added mass and damping in heave along the vessel are validated against experimental and numerical data.

7.2 Steady forward speed

A semi-displacement vessel advancing with constant forward speed was considered. As previous examples the linearized Neumann-Kelvin free-surface boundary condition and the body boundary condition were adopted. As mentioned in Section 2.10.2, the flow separation from the transom stern of semi-displacement vessels must be considered in the calculation. Since it is not possible to include these effects directly in the potential flow solution, an indirect "hollow body" method for the dry transom stern condition was adopted in the present study. In this method, the hollow in the free surface behind the transom stern is captured using a semi-analytical formulation. The dynamic free-surface boundary condition was satisfied by minimizing the pressure on the surface, using iterations on the hollow shape. Both first and second order pressures were taken into account from Eqs. (2.29) and (2.30) (Note that the second-order pressure does not have the complete second-order effects, please see Section 2.4.3 for more details). Then, the kinematic boundary condition was satisfied by enforcing no flow through the surface. In this way, the non-linearity in the free surface was captured directly by the hollow surface, whilst on the other parts of the free surface, the linearized condition was applied. The boundary conditions on the hollow surface are presented in Eq. (7.1) below.

$$\begin{aligned} \frac{\partial \phi}{\partial n} &= -U \vec{i} \cdot \mathbf{n} && \text{on hollow surface} \\ p &\simeq 0 && \text{on hollow surface} \end{aligned} \quad (7.1)$$

By substituting the steady form of the boundary conditions from Eqs. (2.36) and (2.33) for body and free surface, and Eq. (7.1) for the hollow body, the boundary integral formulation in Eq. (2.81) takes the following form for the present problem.

$$\begin{aligned} \mathcal{C}(\mathbf{x})\phi(\mathbf{x}) &= \int_{S_B+S_H} \phi(\boldsymbol{\xi}) \frac{\partial G(\mathbf{x}, \boldsymbol{\xi})}{\partial \mathbf{n}(\boldsymbol{\xi})} dS + \int_{S_B+S_H} G(\mathbf{x}, \boldsymbol{\xi}) \left(U \vec{i} \cdot \mathbf{n}(\boldsymbol{\xi}) \right) dS \\ &+ \int_{S_F} \phi(\boldsymbol{\xi}) \frac{\partial G(\mathbf{x}, \boldsymbol{\xi})}{\partial \mathbf{n}(\boldsymbol{\xi})} dS - \int_{S_F} G(\mathbf{x}, \boldsymbol{\xi}) \left(\frac{U^2}{g} \frac{\partial^2 \phi(\boldsymbol{\xi})}{\partial \xi^2} \right) dS \end{aligned} \quad (7.2)$$

Here S_H represents the surface of the hollow body. Since the boundary condition on the hollow body is identical to the one on the body surface, the integration on the hollow surface was combined with the body surface. Using the hollow body

model, the Kutta condition at the transom stern was satisfied indirectly. Therefore, there was no longer a need for a vortex sheet.

Next, the surfaces in Eq. (7.2) were discretized, and collocation method was used, in order to form a linear equation system. Four points linear elements, with source and dipole distribution, were adopted for discretization. Numerical grid generation methods, presented in Section 3.9, were used for distribution of points and creating elements. The density of the grid points were controlled using hybrid point distribution method to allow a higher point resolution around areas with an extreme variation (see similar cases in the previous chapters). The details of the body surface and its discretization are discussed in the following sections.

Similar to the Wigley hull at forward speed in Section 5.5, a second order up-stream finite difference scheme was used to calculate the derivatives on the free surface. The radiation condition was enforced in this way on the waves generated by the vessel. The pressure on the hollow surface and body surface were calculated, using a second order central difference method and the shape functions. A linear equation system was created by combining the boundary integral equation and the boundary conditions; and later solved using a LQ-solver. This method of solution, as was presented before, was referred to as the steady-state solver. Several quantities of the obtained results are compared to experimental values in the following sections.

7.2.1 Free surface elevation

A semi-displacement vessel used in the experiments by Lugni et al. (2004) was chosen for comparison. The vessel properties and a schematic view of the body plan can be found in Table 7.1 and Figure 7.1.

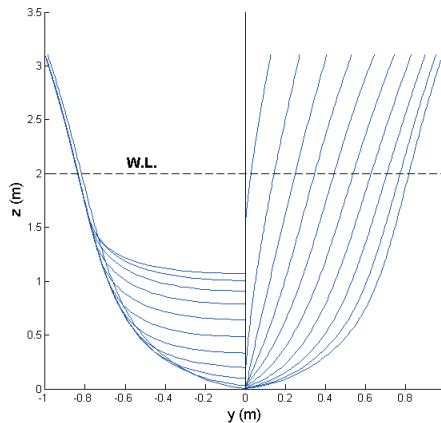


Figure 7.1: The body plan of the semi-displacement vessel used in Lugni et al. (2004).

The hollow body was constructed for this model using the procedure described

in Section 2.10.2. Figure 7.2 shows a view of the generated grids, for the body and half of the hollow surface. The central separation line was calculated from Eq. (2.67). (X_T, Y_T, Z_T) is the transom stern coordinate system. The closing point was defined as the intersection of the separation line and the mean free surface. The water-line was assumed to be a second order polynomial which connects the closing point and the transom stern. The slope of the water line at the stern was chosen equal to the slope of the body surface in the xy -plane.

Table 7.1: Parameters for the semi-displacement vessel used in Lugni et al. (2004).

Parameter		Value for vessel
L	(m)	25.0
Beam, B	(m)	1.75
Draft D	(m)	2.0
Displaced volume	(m^3)	40.48
LCG (positive towards aft)	(m)	1.7

It was important to avoid singular mappings in the discretization of the hollow surface (see Section 3.2.4). Having smooth and well shaped elements on the hollow surface facilitated the calculation of pressure and the iteration procedure. On the other hand, having squeezed or narrow elements decreased the accuracy in the calculation of pressure and consequently made the convergence procedure troublesome and in the worst case led to divergent. Therefore, proper use of numerical grid generation methods was important.

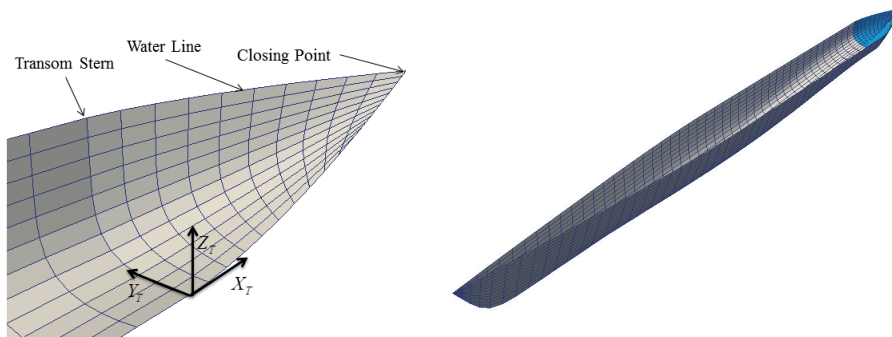


Figure 7.2: A sample of the grid for semi-displacement vessel from Lugni et al. (2004) (Right) and half of its hollow-body (Left). The hollow body is shown as a dark blue extension to the body in the right figure.

The trim and sinkage of a semi-displacement vessel at high Froude numbers must be considered in the calculations. Here, the experimental values were considered in the numerical simulation by shifting and rotating the body. Only the

resulted under water part of the body surface then discretized. An iterative procedure was required to calculate the induced sinkage and trim, which was left for future work.

A semi-displacement monohull, on a straight course, with constant speed, was tested at INSEAN towing tank by (Lugni et al., 2004). The free-surface elevation was calculated, for two Froude numbers, by the present method and were compared with the experimental and numerical values in Figure 7.3. The overall agreement of

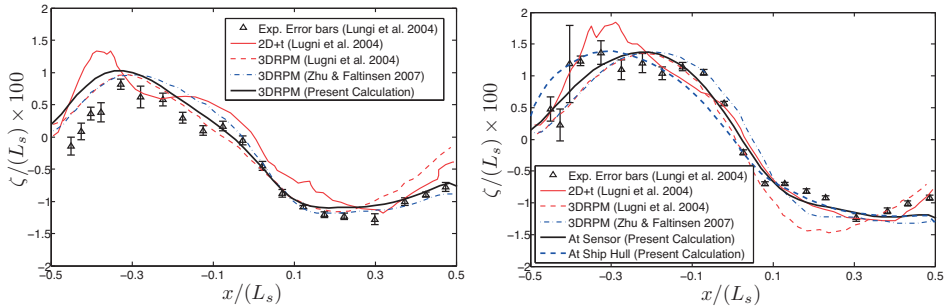


Figure 7.3: Free surface elevation around a semi-displacement. Left: $Fn = 0.5$, Right: $Fn = 0.7$, Bars: Experimental uncertainty, L_s : ship length.

the results was satisfactory. The experimental values for the free-surface elevation were obtained using sensors with 3 cm distance from the 4-meters long model hull. The bars in the plots represents the experimental uncertainty. As mentioned by (Lugni et al., 2004), the large error bars for the surface elevation are believed to be due to ventilation at the pressure sensors. The calculated free-surface elevation at the body is also presented for Froude number 0.7. We note a clear difference between the free-surface elevation at the hull and at the pressure sensors, which reflects the sharp change in the free-surface elevation in the transverse direction.

7.2.2 Sectional vertical force

Keuning (1988) conducted a series of experiments using a semi-displacement model with parameters presented in Table 7.2. Figure 7.4 shows the model's body plan. The model was divided into seven equally spaced segments and the vertical force was measured on each segment in order to capture the distribution of the force along the vessel.

Similar to the previous example, the hollow body model was used to capture the flow separation from the transom stern. The vessel's trim and sinkage were included in the calculation by rotating the body and discretizing the vessel body surface under the mean free surface. Figure 7.5 shows a view of the body and hollow surface grid.

The distribution of the vertical force along the vessel was calculated by integrating the pressure. The steady vertical force distribution along the ship for Froude number 1.14 is presented in Figure 7.5. The vessel's 1.62 degrees trim and 0.004 m sinkage, as suggested by Sun and Faltinsen (2010), was applied in the calculations.

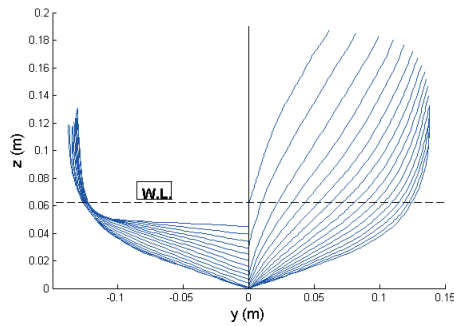


Figure 7.4: Body plan for the semi-displacement model used by Keuning (1988).

Table 7.2: Parameters for the semi-displacement model used in Keuning (1988).

Parameter		Value for vessel
Length of waterline L_{wl}	(m)	2.00
Beam of waterline B_{wl}	(m)	0.25
Draft D	(m)	0.0625
Displaced volume	(m^3)	0.01248
Block Coefficient C_B		0.396
LCB (positive towards aft)	(% of L_{wl})	5.11

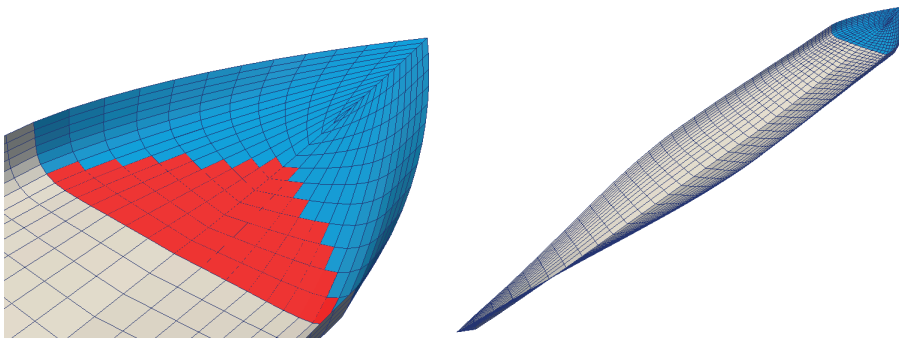


Figure 7.5: Grid for the semi-displacement model from Keuning (1988) and its hollow-body, Blue part: hollow-body behind the transom stern, Red part: part of the hollow-body which is almost a horizontal flat surface.

The overall agreement between the experiments and the linear theory was satisfactory. While the nonlinear 2D+t method by Sun and Faltinsen (2010) predicts the values more accurately along the body, the present method gave better predictions close and at the transom. This is due to the fact that the 2D+t theory neglects the effects of the downstream flow, while close to the transom stern these effects

are known to be important. In the present method, these effects are considered by imposing a tangential flow condition at the transom and solving a 3D problem.

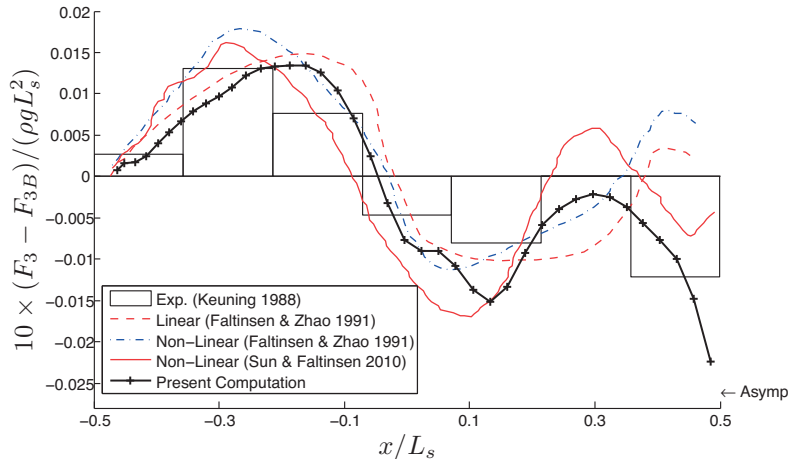


Figure 7.6: Sectional hydrodynamic vertical force on Keuning (1988) semi-displacement vessel, F_3 : total vertical force, F_{3B} : hydrostatic vertical force, $Fn = 1.14$, Trim = 1.62° , L_s : length of the ship's water line at rest, Asymp.: Asymptotic of the vertical hydrodynamic force which cancels the buoyancy at the transom stern. The non-dimensional vertical hydrodynamic force on the last section ($\times 100 F_{3D} / (\rho g L_s^3)$) from, experiments: -0.173, Sun and Faltinsen (2010): -0.028, present method: -0.171.

The total pressure on the body was subdivided into the hydrostatic pressure (p1), the linear hydrodynamic pressure (p2) and the nonlinear hydrodynamic pressure (p3) which has not been considered in the present work due to linearization. The distribution of these forces along the vessel is shown in Figure 7.7. The consistency of the values is checked at the transom by examining the total force distribution acting on the vessel, i.e. we must add the hydrostatic force to the predicted hydrodynamic force. The sum of all the forces must go to zero at the transom stern due to the atmospheric pressure. This condition was satisfied as shown in Figure 7.7.

The agreement of the total force with values presented by Sun and Faltinsen (2010) is fairly acceptable. However, as mentioned earlier, the present results are more consistent with the dry transom stern effects close to the transom. A similar variation in the pressure close to the transom stern was proposed by Garne (2005) for planing hulls based on a series of model test measurements. Hydrostatic forces were calculated by numerical integration of the pressure over the submerged body. Due to the complex shape of the model, accuracy of the values was highly dependent on the number of linear panels, which were used to represent the body surface. The hydrodynamic force is in good agreement with the results by Sun and Faltinsen (2010) around the mid-ship, while there are disagreements at the bow and

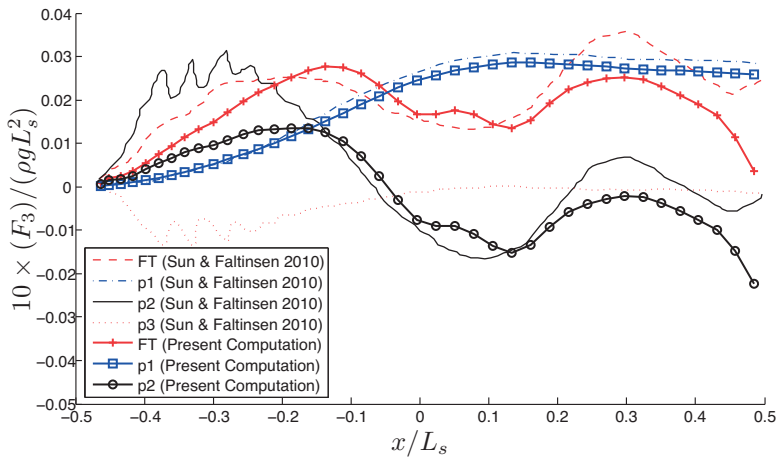


Figure 7.7: Components of the sectional vertical force on Keuning (1988) semi-displacement vessel, $F_n = 1.14$, Trim = 1.62° , L_s : length of the ship's water line at rest, FT: Total vertical force, p_1 : hydrostatic pressure, p_2 : linear hydrodynamic pressure, p_3 : nonlinear hydrodynamic pressure.

stern. The reason at the bow is believed to be due to the fact that nonlinearities are neglected in the present method. The nonlinear term in the pressure has the maximum effect at the bow, as shown in Figure 7.7. However, the difference at the stern is believed to be due to the effect of the atmospheric pressure at the transom stern, which is not considered in the 2D+t method.

7.3 Forward motion with a drift angle

The problem of a semi-displacement vessel with forward speed presented in Section 7.2 is extended in this section by including a fixed drift angle. An schematic view of the problem is shown in Figure 7.8. In addition to the coordinate systems defined in Section 2.1 a third body-fitted coordinate system $Ox'y'z'$ was defined. The origin of this coordinate system is at the vessel's center of gravity and it is rotated by the vessel's trim, heel and drift angle. As before, the boundary value problem was formulated in the $Oxyz$ coordinate system, while the forces and moments were calculated in the body-fixed $Ox'y'z'$ coordinate system.

A semi-displacement monohull vessel tested at INSEAN by Fabbri et al. (2009) was chosen for comparison. The main dimensions of the model are presented in Table 7.3. The body plan of the vessel is also presented in Figure 7.9. The vessel was free to trim, heel and sink. The vessel's drift angle in the xy -plane was fixed and the vessel was towed using a carriage with different Froude numbers. The resistance and transverse force as well as the yaw moment acting on the vessel were measured in the body-fixed coordinate system $Ox'y'z'$. The vessel's steady trim, heel and sinkage were also recorded during the experiments for each Froude

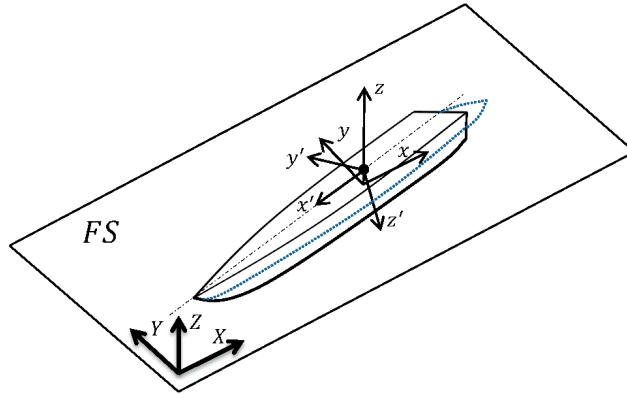


Figure 7.8: Coordinate system for a semi-displacement vessel with a drift angle.

number. These values were imposed in the present numerical calculations.

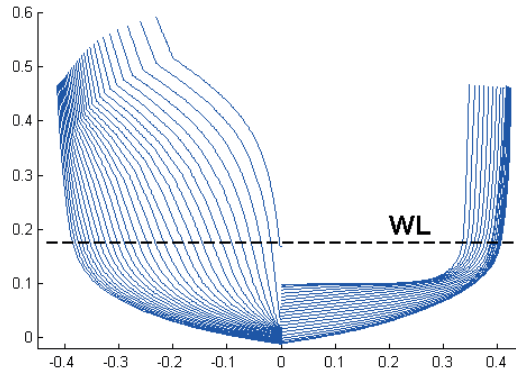


Figure 7.9: Athena semi-displacement body-plan.

Table 7.3: Parameters for Athena semi-displacement used in Fabbri et al. (2009).

Parameter		Value for model
L_{WL}	(m)	5.488
Beam, B	(m)	0.806
Draft T	(m)	0.175
Displacement	(ton)	0.334
LCG	(m)	2.390
KG	(m)	0.370

As explained in Section 2.10.2, due to the transom stern shape, flow separation

occurs at the vessel's stern. This may cause the stern to become partly or fully ventilated. As shown by Doctors and Day (2001), a dry transom stern is expected for the transom stern draft Froude number larger than 2.5 (see Section 2.10.2). This condition holds for all the cases studied here. A hollow body model, similar to what has been explained in Section 2.10.2, and used in Section 7.2, was adopted here. However, due to the ship's drift angle in the present case, the hollow shape can no longer be symmetric about the xz -plane. Section 7.10 shows a schematic view of the hollow and the vessel's transom stern. The asymmetric shape was constructed by assuming that the separated flow moves only in the x -direction at the mid ship and that it can be described by Faltinsen's formulation for 2D flow close to a transom stern (see Section 2.10.2). The separation lines, which from the sides of the vessel at the waterline, were assumed to be second order curves, while the end point and the slopes of the curves at the transom are known. The slopes of the separation lines were assumed to be equal to the slopes of the vessel's water-line at the transom stern. The connecting point of these curves was assumed to be the closing point of the hollow, which was determined by the meeting point of the free surface and the 2D separation line in the x -direction.

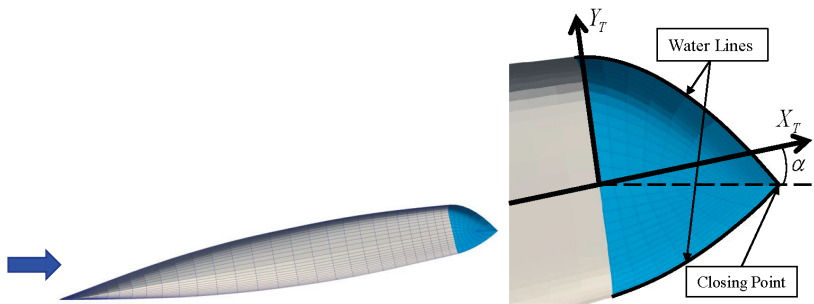


Figure 7.10: Hollow-body coordinate system for a semi-displacement vessel with drift angle, Blue part: hollow-body behind the transom stern.

The 3D hollow was constructed based on these three curves and the profile of the transom stern by using a linear transfinite interpolation method (see Section 3.9.2). This method of constructing the 3D hollow gives an asymmetric shape. Larger drift angles give larger deviation from a symmetric shape. Similar to the symmetrical hollow, the constant in the central 2D separation line was determined by an iterative procedure in an attempt to find the minimum pressure on the hollow surface, which is in fact a part of the free surface.

It is expected that the asymmetric hollow-body method becomes less accurate due to nonlinearities for larger drift angles or higher Froude numbers. The Neumann-Kelvin linearization and the assumed basic shape for the transom stern hollow are expected to cause inaccuracies. For example, larger differences in the distances of the two sides of the transom stern to the x -axis will cause the water from one side to reach the center-line sooner than the other side. This may form a connecting region instead of a point. Moreover, at high drift angles the flow at the suction side may separate from the vessel's body even before the transom stern.

Therefore, in the present study, the focus is on small drift angles.

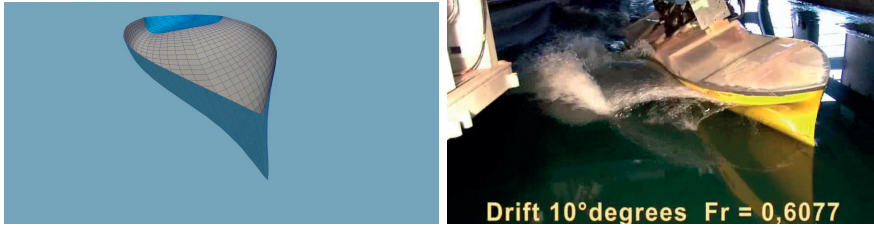


Figure 7.11: Athena semi-displacement vessel grid (left) and an snapshot of the experiments at INSEAN by Fabbri et al. (2009) (right). The experimental values for steady sinkage, trim and heel angles were adopted in creating the under water part of the vessel's surface, $Fr = 0.6077$, Drift angle (α) = 10° .

The drift angle will influence the heel and trim angles. These effects, as well as the vessel's sinkage, are important in calculating the correct hydrodynamic forces acting on the vessel and must be considered in the calculations. Fabbri et al. (2009) reported these values for different trim angles in steady condition. These values were directly adopted in the calculations by changing the under water surface of the ship. A sample picture from experiments and the numerical grid is presented in Figure 7.11 to show the similarity between the body-locations. The large overturning wave at the bow is indicating the presence of important non-linear effects. However, we focus on the linear theory and see to what degree it can be used to describe this complicated problem.

Similar as before, the numerical solution was started by discretizing the boundary surfaces into linear rectangular and triangular elements, with Rankine source and dipole distributions. The boundaries of the computational domain have been chosen based on the guide lines suggested by Zhu and Faltinsen (2007) for a flat plate with a drift angle. The dimensions and a sample of the computational grid are shown in Figure 7.12. The grid points distribution on the boundaries was chosen in a way to provide a better resolution and accuracy at the important areas using the methods described in Section 3.9.

No-upstream-waves condition was assumed in the present work. A second order upstream finite difference method was used for all the derivatives on the free surface in order to ensure stability and satisfy the radiation condition similar to the previous cases. Since the problem has no symmetry-plane, the potential was solved everywhere on the boundaries. As shown by Bunnik (1999), and further discussed here in Section 3.7 and Chapter 4, a correct direction of differentiation is important, especially for high Froude numbers.

Similar to the flat plate with a drift angle in Section 6.3, the cross-flow may cause flow separation from the vessel's keel. It is not possible to model the cross-flow separation directly by the present method. However, in analogy to the flat plate, an attempt was made using the 2D+t method with a rigid free-surface boundary condition to estimate the value for this type of phenomenon, and see if it can qualitatively explain the differences between the numerical and experimental results.

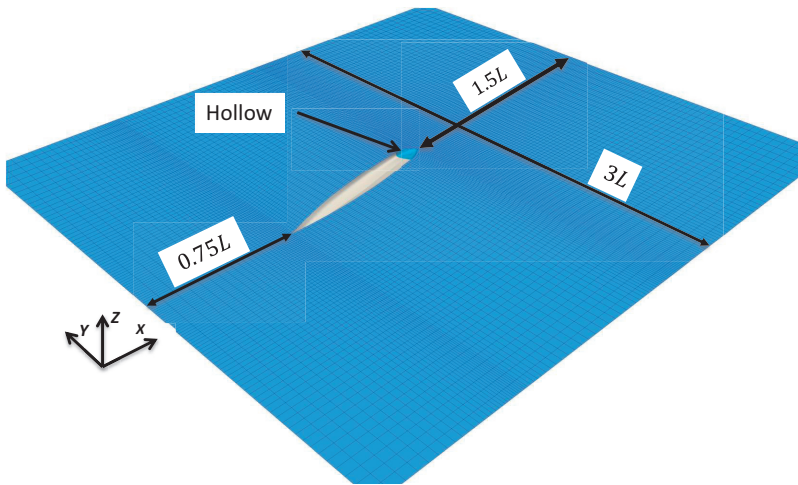


Figure 7.12: Computational domain for Athena semi-displacement vessel.

For this purpose the viscous cross-flow 2D+t approach, presented in Section 2.10.3

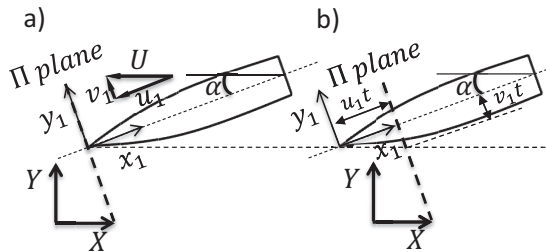


Figure 7.13: 2D+t coordinate system for a semi-displacement with drift angle.

and further used in Section 6.3, was applied. A similar method was applied for the cross-flow separation of a Wigley hull at low Froude numbers by Wong and Calisal (1996). A view of the 2D+t coordinate system is shown in Figure 7.13. Looking at the problem from the Earth-fixed plane (Π), it transforms into the transient problem of a uniform ambient cross-flow velocity (v_1) passing a 2D ship section, in presence of the free surface (see Section 2.10.3). Here, for simplicity, the ship cross-sections were simplified into half circles with the radius equal to the ship's local draft ($D(x_1)$). By taking advantage of the symmetry plane created by the rigid free-surface boundary condition, the problem can be replaced by the transient drag force acting on a 2D circle facing a start up flow in infinite fluid. The polynomial presented by Faltinsen (2005) -based on the experimental data from Sarpkaya (1966)- for 2D+t calculations of the drag force was used to describe the transient drag force. The transient cross-flow drag coefficient ($C_D(\mathcal{T})$) can be expressed as a function of the non-dimensional time \mathcal{T} defined in Eq. (2.70). The variation of

the transient drag coefficient for a cylinder in start-flow, based on non-dimensional time, is shown in Figure 7.14. Here, the characteristic length (L_C) is the vessel's

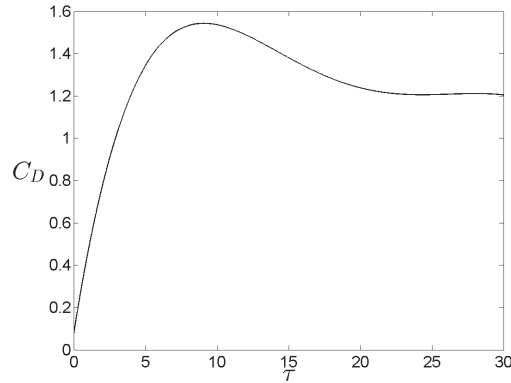


Figure 7.14: Non-dimensional cross-flow drag coefficient for a cylinder in start-flow, $\mathcal{T} = \frac{v_1}{u_1} \frac{x_1}{L_C}$: non-dimensional time signature.

local draft ($D(x_1)$). Using the relation $\tan \alpha = v_1/u_1$, the cross-flow transverse force and yaw moment in Eqs. (2.71) and (2.72) transforms into,

$$F_{CF} = \frac{1}{2} \rho U^2 \sin^2 \alpha \int_0^L D(x_1) C_D(\tan \alpha x_1 / D(x_1)) dx_1 \quad (7.3)$$

$$M_{CF} = \frac{1}{2} \rho U^2 \sin^2 \alpha \int_0^L D(x_1) C_D(\tan \alpha x_1 / D(x_1)) (x_c - x_1) dx_1 \quad (7.4)$$

Here, L is the vessel's water-line length, α is the drift angle, and ρ is the water density. The steady trim, heel, and sinkage were considered in calculating the draft for each vessel's section. Therefore, unlike the flat plate in Section 6.3, where the non-dimensional cross-flow transverse force and yaw moment were only functions of the drift angle, here, they are slightly Froude-number dependent. It must be noted that this method does not account for all 3D flow effects and, as mentioned, it neglects the wave effects.

The resistance and transverse force as well as the yaw moment were calculated in the body-fixed coordinate system, using the described numerical method, and compared with experiments from Fabbri et al. (2009). Convergence study was performed for the three grids listed in Table 7.4. As a sample, a plot for the convergence study of the transverse force and yaw moment for 10 degrees drift angle are shown in Figure 7.15. The convergence patterns of the results are satisfactory. It is clear that the converged results deviate from the experimental data. The possible reasons behind this deviation and the correction methods are discussed in the following.

Due to presence of uncertainty in the experimental values, a series of sensitivity tests were performed carefully for all the parameters involved in the calculations.

It was concluded that varying trim, heel, and sinkage of the vessel, in the order of magnitude of the measurements' accuracy, have no significant influence on the resulting force and yaw moment. The same conclusion is drawn for the hollow-body iteration parameter.

Table 7.4: Grid convergence study parameters for Athena semi-displacement used in Fabbri et al. (2009).

Grid	Ship + Hollow	Free Surface	Total
A	$13 \times 10 \times 2$	$43 \times 13 \times 2$	1118
B	$25 \times 15 \times 2$	$82 \times 25 \times 2$	4100
C	$38 \times 20 \times 2$	$124 \times 38 \times 2$	9424

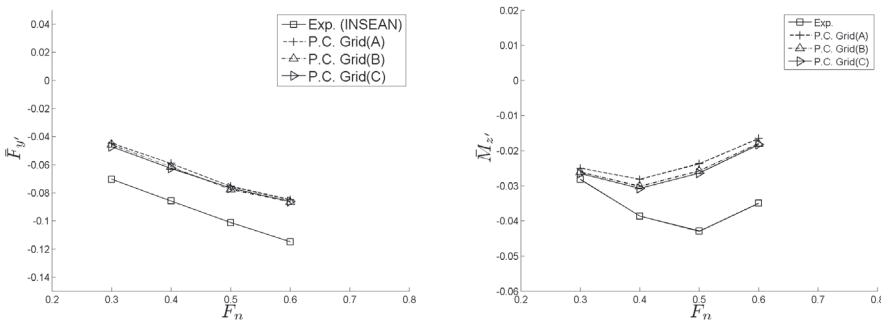


Figure 7.15: Convergence study on the transverse force and yaw moment, $\bar{F}_{y'} = F_{y'} / (0.5\rho U^2 L D)$, $\bar{M}_{z'} = M_{z'} / (0.5\rho U^2 L^2 D)$, $\alpha = 10^\circ$, Exp.: experimental data from Fabbri et al. (2009), P.C.: present computations, grids are defined in Table 7.4.

The viscous frictional drag plays an important role in the vessel's resistance force. However, in the present method only the residual resistance forces were considered. The ITTC formula in Eqs. (2.41) and (2.42) for calculating the frictional resistance factor (C_F) was used to estimate the frictional resistance of the vessel. Based on Eq. (2.42), a form factor must be chosen for the vessel. Molland et al. (1994) presented a series of form factors for semi-displacement vessels. A form factor was chosen by interpolating the form factor of similar vessels, using the present vessel's main dimensions. Although, it is usually assumed that form factors are not Froude number dependent, in reality this is not entirely true. For instance, the fact that the transom is wet for stern Froude number less than 2.5 influences the form factor. Moreover, the change in vessel's heel, trim, and sinkage contribute to the form factor. These influences were neglected here for simplicity.

Figure 7.16 shows the comparison between the non-dimensional resistance force, from calculations and experiments, for different Froude numbers. The frictional force was added to the present potential results using Eq. (2.42), together with the form factor $k = 0.28$. The potential-flow values seem to follow the similar trend

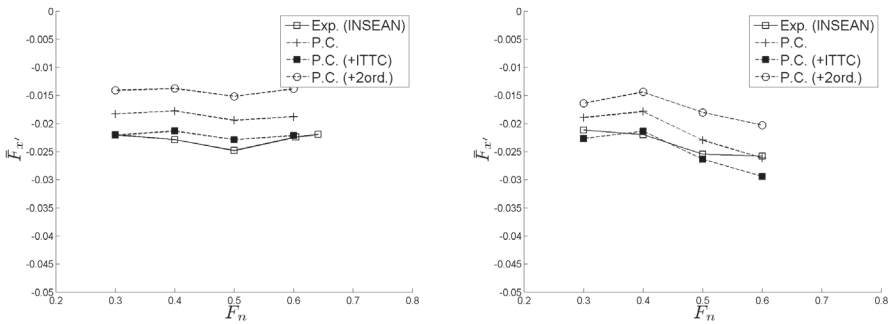


Figure 7.16: The longitudinal Force on a semi-displacement vessel with a drift angle, $\bar{F}_{x'} = F_{x'}/(0.5\rho U^2 LD)$, Left: $\alpha = 5^\circ$, Right: $\alpha = 10^\circ$, Exp.: experimental data from Fabbri et al. (2009), P.C.: present computations, ITTC: correction by ITTC formula, 2ord: correction due to second order force.

as the experiments. The viscous correction was able to qualitatively fill the gap between the two sets of results. The difference between the linear and second order force from Eq. (2.56) is large and increasing with Froude number and the drift angle. The second order force is in incomplete form and calculated from the first order potential by neglecting the second-order potential (see Section 2.9 for more details). This difference is much smaller for the zero drift angle. Although the second order force's sign is negative, it is not possible to conclude the role of this component. A solution of the velocity potential up to the second order is needed to clarify this matter. On the other hand, the magnitude of this force shows that the nonlinearities matter for higher Froude numbers and drift angles.

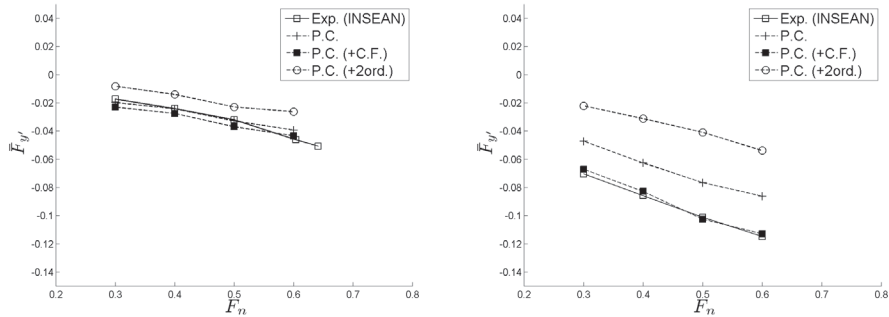


Figure 7.17: The transverse Force on a semi-displacement vessel with a drift angle, Left: $\alpha = 5^\circ$, Right: $\alpha = 10^\circ$, Exp.: experimental data from Fabbri et al. (2009), P.C.: present computations, C.F.: correction by cross-flow drag model, 2ord: correction due to second order force.

Figure 7.17 shows a similar comparison for the transverse force. The increase

in the importance of nonlinearities, with increase in the drift angle, is easier to see. For a drift angle of 5 degrees, the potential-flow values follow the experiments closely and the viscous flow correction, although small, shifts the values away from experiments, except for $Fn = 0.6$. However, the viscous correction by the cross-flow 2D+t method seems to explain the difference between the numerical and experimental results for 10 degrees drift angle much better than for 5 degrees. The predictions for the yaw moment in Figure 7.18 are less satisfactory for both 5 and 10 degrees drift angles. In the present numerical results, the behavior of the yaw moment against Froude number is qualitatively the same for both drift angles, while it is different for the experiments. The yaw moment for 5 degrees drift angle increases with Froude number almost linearly, while for 10 degrees it raises and falls with the peak value around $Fn = 0.5$ (Figure 7.18). This behavior is similar to the calculated yaw moment for 5 and 10 degrees, except that in the calculations the peak values are around $Fn = 0.4$.

It is possible that the difference in the behavior of the yaw moment for 5 degrees drift angle, is due to the viscous moment, which increases with Froude number and was neglected here. However, the calculated yaw moment by the 2D+t viscous cross-flow around a cylinder was small, similar to what was reported in Section 6.3 for a flat plate, and therefore it was not plotted in Figure 7.18. It must be noted that the influence of the free surface and the asymmetry of the ship sections due to the heel angle were neglected in the calculation of viscous cross-flow force. These effects, in addition to the non-linearities such as water run-up at the bow, can be the possible sources of difference between the numerical calculations and the experimental results.

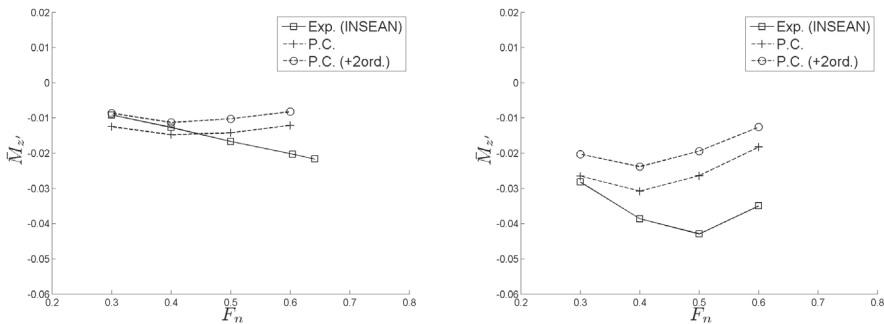


Figure 7.18: The yaw moment on a semi-displacement vessel with a drift angle, Left: $\alpha = 5^\circ$, Right: $\alpha = 10^\circ$, Exp.: experimental data from Fabbri et al. (2009), P.C.: present computations, 2ord: correction due to second order moment.

Based on these comparisons, the overall agreement of the numerical results and experiments are satisfactory. The viscous corrections for the resistance and transverse force seem to explain the differences between the numerical and experimental values. The cross-flow viscous correction for the yaw moment, according to the presented method, is negligible. While the behavior of the transverse force is rea-

sonably predicted, the behavior of the yaw moment is difficult to capture. The importance of non-linearities and 3D viscous flow are believed to be among the reasons

7.4 Heave oscillations

The unsteady forces due to forced heave oscillations of the semi-displacement vessel presented in Section 7.2.2 are investigated here. Keuning (1988) measured the vertical unsteady forces in terms of the added mass and damping in heave. The same segmented model, as in Section 7.2.2, was used to obtain the distribution of hydrodynamic coefficients along the vessel's length.

First, the steady forward motion was solved using the steady-state solver. The solution method was identical to the one presented in Section 7.2. The obtained solution was then used as the initial condition for the time-domain solver. The general procedure for formulating the problem in the time-domain is similar to the method presented in Section 5.6. The main difference is due to the presence of the transom stern. The hollow body model, as introduced in Section 2.10.2 and used in Section 7.2, was adopted here to capture the flow separation from the transom stern. A dry transom stern condition was assumed.

The main challenge in adopting the hollow-body model for the oscillatory problem is related to the boundary condition on the hollow surface. Due to forced oscillations of the vessel, the shape of the hollow changes with time. Therefore, the steady surface of the hollow no-longer represents the free surface behind the transom at all time instances. This means that satisfying the hollow boundary conditions in Eq. (7.1) is not equivalent to the free surface boundary condition. Reshaping the surface of the hollow requires iteration, re-gridding, and recalculation of the coefficient matrix every time-step. However, if small amplitude oscillations are assumed, the changes in hollow shape can be considered to be of second order. Therefore, a form of linearization of the time-varying hollow surface around the steady surface can be adopted.

The linearized form of the free-surface boundary condition about a known, non-flat surface was presented in Eq. (2.4.1). Here, the base velocity potential and the base free-surface elevation can be substituted by the steady velocity potential and the steady hollow shape behind the vessel. Then the hollow surface must be treated as a part of the free surface in the unsteady solution.

A simplified approach is adopted here. The second order terms of the steady velocity potential on the hollow surface are assumed to be small and neglected. It must be noted that this assumption is inconsistent with the linearization assumption used in the steady solution for the transom stern hollow. The hollow-body model by itself is an indirect extension of the linearized model to account for the high non-linearity behind the transom stern. After linearization and using the fact that the steady velocity potential satisfies the free-surface boundary condition on the hollow, the Neumann-Kelvin free-surface boundary condition for the unsteady velocity potential is obtained, which must be satisfied on the steady hollow surface.

$$\phi_{tt} + 2U\phi_{xt} + U^2\phi_{xx} + g\phi_z = 0 \quad \text{on} \quad z = 0 \quad (7.5)$$

Due to the heave oscillations, the hollow surface will change shape in vertical direction. If we linearize this unsteady shape around the steady shape, the normal velocity on the steady surface is no longer zero. The deviation from zero mostly comes from the change in the vertical component of the velocity. The linearized free-surface condition in Eq. (7.5) gives an estimation of this vertical velocity. Using the hollow body boundary condition in Eq. (7.1) and the linearized free-surface condition in Eq. (7.5) an iterative procedure was adopted.

The procedure was started by assuming the hollow surface to act as a solid wall, which moves with the body. The ϕ_n on the surface then was calculated using the linearized body boundary condition in Eq. (2.36), which means no flow through the surface. After solving the boundary integral formulation, the distribution of the velocity potential on the hollow surface was obtained. Using Eq. (7.5) a value for the vertical velocity of the water at the hollow was obtained. As a result of the heave oscillations, this value was different from the vertical component of ϕ_n . Then $\phi_n n_3$ was corrected by the obtained ϕ_z and the procedure was repeated until the convergence was achieved. The solution was time-stepped forward and new iterative procedure was started. The rate of convergence depends on the time-step and oscillation frequency. However, with suitable choice of conditions, convergence is generally fast and it is usually possible to be achieved with in a few iterations. The aforementioned iterative procedure acts as a correction to the

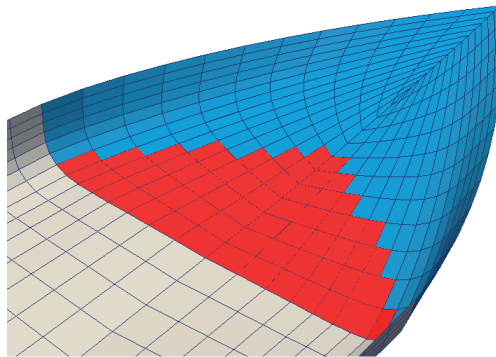


Figure 7.19: Hollow-body grid for satisfying the boundary conditions in heave oscillations, Blue part: hollow-body behind the transom stern, Red part: part of the hollow-body which is almost a horizontal flat surface.

solid body boundary condition on the hollow surface, which lets the flow to pass the linearized surface. This correction is more important where the hollow surface shape is closer to a flat surface. In addition, the influence of the flow behind the transom stern on the forces is larger closer to the vessel. Therefore, for heave oscillations, the correction could be limited only to a group of flat elements adjacent to the transom stern as shown by red color in Figure 7.19.

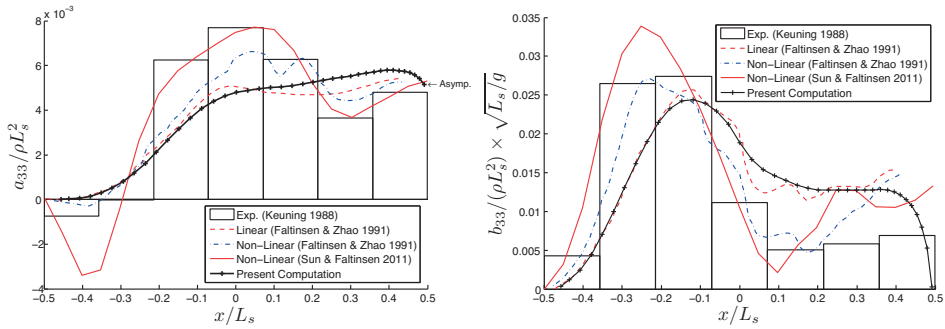


Figure 7.20: The sectional vertical added mass and damping for a heaving semi-displacement vessel, $Fn = 1.14$, $Trim = 1.62^\circ$, $\omega\sqrt{L_s/g} = 4.97$

The unsteady forces due to forced heave oscillations, in terms of the heave added mass and damping, were calculated and presented in Figure 7.20. Here, the frequency of heave oscillations is 11 rad/sec , $\omega\sqrt{L_s/g} = 4.97$, and the amplitude is 0.01 m . The Froude number is 1.14 and the sinkage and trim of 0.004 m and 1.14° suggested by Sun and Faltinsen (2010) are adopted. The accuracy of the present method is similar to the linear 2D+t results from Faltinsen and Zhao (1991), except for the last section close to the stern. The nonlinear 2D+t results with non-viscous separation from the vessel's round bilge, presented by Sun and Faltinsen (2011), show the importance of nonlinearities in capturing the correct values along the vessel. However, as mentioned by Faltinsen and Zhao (1991), we expect the sum of the added mass force per unit length and the restoring force per unit length to go to zero at the transom, as well as the damping, as a result of having an atmospheric pressure behind the dry transom stern. These asymptotic values, which are shown in Figure 7.20, are not reached at the stern in the 2D+t calculations. After imposing the transom stern effects on the upstream flow, through using a 3D solver, a sharp change towards the asymptotic values were observed. This behavior had been also anticipated before by Faltinsen and Zhao (1991).

The results for the same case at different frequency (15 rad/sec , $\omega\sqrt{L_s/g} = 6.77$) are presented in Figure 7.21. Similar conclusions can be drawn for this frequency as well. In addition, the linear results show smaller deviations from the non-linear results along the body at higher frequencies. It can be expected that the linearization assumption is closer to physics at higher frequencies. The attempts to solve the problem for lower frequencies confirmed this matter. The deviations became larger and larger, for smaller frequencies. Corrections due to a change in the vessel's wetted area may be important to include for lower frequencies as suggested by Sun and Faltinsen (2012). Again, the asymptotic values at the transom stern were only reached by the present 3D model. Maybe it would be interesting to point out that for the current selection of Froude numbers and oscillation frequencies, the corrections to the solid boundary condition on the hollow surface were appeared to be almost a constant factor every where. If we consider $[\phi_z]_{\text{corrected}} = \alpha[\phi_z]_{\text{solid boundary}}$, the correction factor α was about 0.97 to 0.99

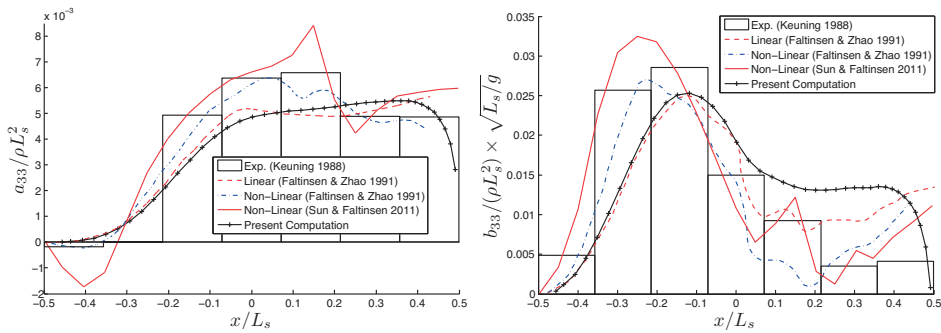


Figure 7.21: Sectional vertical added mass and damping for heaving semi-displacement vessel, $Fn = 1.14$, $\text{Trim} = 1.62^\circ$, $\omega\sqrt{L_s/g} = 6.77$

depending on the frequency.

The sharp change in the forces close to the transom stern can be important, for instance, in calculating the yaw and pitch moment. Due to the distance between the transom stern and the vessel's center of gravity, neglecting this rapid change may result in an incorrect moment. Using the present tools, it seems that the most suitable answer will be achieved by combining the Sun and Faltinsen (2011) method along the vessel and the present method close to the transom stern.

7.5 Conclusions

Hydrodynamics of semi-displacement mono-hull vessels were addressed in this chapter using linear theory. The non-linearities in the flow behind a dry transom stern were handled using hollow-body model. The steady vertical force and free-surface elevation along a semi-displacement vessel with forward speed were calculated and compared to experimental and numerical data. It was shown that the present simple hollow-body model can capture the complex flow behind a dry transom stern with a reasonable accuracy. Moreover, the transverse force and yaw moment on a semi-displacement vessel with drift angle were studied using an asymmetric hollow-body model. A viscous cross-flow drag model was able to explain the differences between the numerical and experimental results for the transverse force qualitatively. This was not possible for the yaw moment.

At the end, the unsteady forces on a heaving semi-displacement vessel were studied. It was shown that the hollow-body method can be used to satisfy the atmospheric pressure condition behind a heaving dry transom stern. The method was shown to be promising for handling the dry transom stern condition behind a semi-displacement vessel in an oscillatory motion. This can be useful in establishing accurate hydrodynamic models of such vessels in sway, roll, and yaw, which can be used in a dynamic stability analysis, for instance, to predict a calm-water broaching dynamic instability.

Chapter 8

Dynamic Stability Analysis

8.1 Introduction

Dynamic stability of high-speed marine vehicles plays an important role in determining their operational limits. Among different types of instabilities, "calm water broaching" is important for semi-displacement vessels operating at high Froude numbers. Faltinsen (2005) defines calm water broaching as, a non-oscillatory instability, which generally starts by a sudden list due to loss of the steady restoring moment in heel, at high Froude numbers. This sudden change of list angle follows by a violent yaw angle to one side which may lead to capsizing. Lavis (1980) mentioned this type of instability as the main reason why round-bilge monohull vessels must not operate at a Froude number higher than 1.2. Müller-Graf (1997) also reports this type of instability and suggests increasing the steady metacentric height as a solution. It seems reasonable to assume a similar type of instability can be initiated by a small change in the vessel drift/yaw angle. This will induce a roll moment which may lead to calm water broaching as mentioned above. Müller-Graf (1997) referred to this type of instability as *yaw-roll* instability, which can be induced by waves or inadvertent rudder actions.

An attempt is made in this chapter to investigate this type of dynamic instability for a semi-displacement round-bilge monohull. Linear dynamic stability analysis is performed to determine the unstable state of the linear dynamic model. A semi-displacement vessel with documented instability issues has been chosen for investigation. Coupled equations of motion in sway-yaw and also sway-roll-yaw are considered. The hydrodynamic coefficients needed for establishing the dynamic model have been calculated by simplifying the problem to a surface piercing flat plate, using the method outlined in Chapter 3 and investigated in Chapters 6 and (7). The main reasons behind this simplification are numerical complications and lack of experimental data for validation of the complete problem. Sensitivity study has been performed in order to assess the uncertainties due to geometrical simplifications and linearization. Moreover, the influence of variation in the vessel's main parameters, such as longitudinal position of center of gravity, are investigated. The goal is to find out to what degree the linear theory can be used in predicting this

type of instability for high-speed vessels.

8.2 A case with observed dynamic instability

In order to see if linear theory can be used to predict the dynamic instability in semi-displacement mono-hulls, a vessel with observed dynamic instability issue was selected. The vessel and available experimental data, as well as hydrodynamic simplifications of the problem, are presented in this section.

8.2.1 A model semi-displacement vessel

The semi-displacement vessel presented in Section 7.2.1 was chosen for evaluation. The properties of the vessel, including the assumed values for a dynamic stability analysis were reported in Table 8.1.

Table 8.1: Parameters for the semi-displacement vessel from Lugni et al. (2004).

Parameter		Value for vessel
L	(m)	25.0
Beam, B	(m)	1.75
Draft D	(m)	2.0
Displaced volume	(m^3)	40.48
LCG	(m)	1.7
\overline{KM}	(m)	1.44
* \overline{KG}	(m)	1.35
* \overline{GM}	(m)	0.09
* r_{44}	(m)	0.35 B
r_{55}	(m)	0.26 L
* r_{66}	(m)	0.26 L
* r_{46}, r_{64}	(m)	0
Model scale λ	(m)	6.25
* Assumed values.		

It must be noted that these properties belong to a catamaran demi-hull and not a semi-displacement monohull. Therefore, as mentioned by Lugni et al. (2004), the monohull with these properties will have a finer shape than existing semi-displacement vessels. Naturally, from dynamic stability point of view, it can be expected that this vessel has lower maximum operational Froude number than a conventional semi-displacement vessel. This vessel, however, would present a good case for the purpose of the current study. Müller-Graf (1997) suggests that for a semi-displacement monohull with $30(m)$ length, \overline{GM} must be higher than $0.8(m)$. The \overline{GM} value in Table 8.1 was chosen in a way that the center of gravity stays between the center of buoyancy and the metacenter in the vertical direction. The low \overline{GM} is also linked to the fact that this vessel is a demi-hull and not a

conventional semi-displacement hull. A sensitivity study for the \overline{GM} -value was performed which will be presented in the following sections.

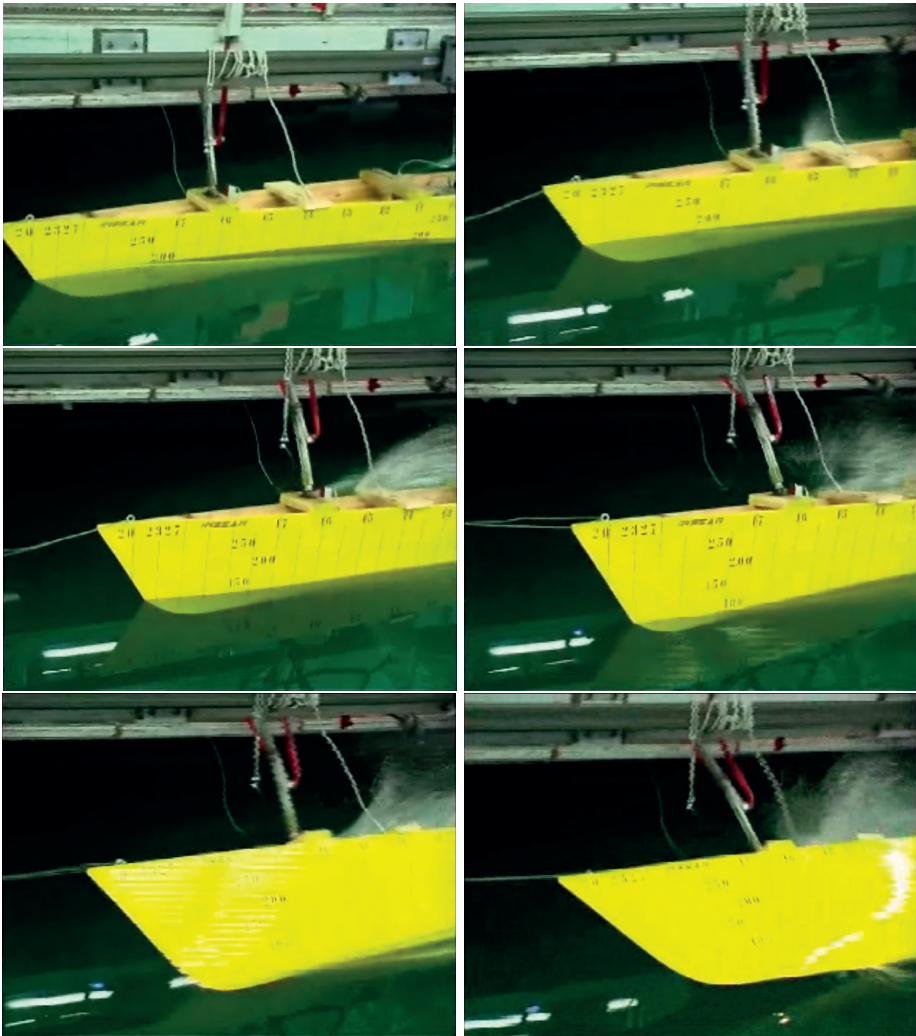


Figure 8.1: Experimental pictures from the broaching process, (Lugni *et al.* 2003, private communications). $F_n=0.9$. The process takes 3 seconds in model scale with scale ratio $\lambda = 6.25$.

The main reason for choosing the aforementioned vessel was an observed dynamic instability issue at Froude number 0.9, during a set of experiments realized at INSEAN towing tank in 2003 (Lugni *et al.* private communications). The focus of the experiments was on measuring the free-surface elevation around the semi-displacement demi-hull, while it was towed with the catamaran draft (Lugni *et al.*, 2004). Therefore, the weight of the demi-hull and its center of gravity were modi-

fied in a way to achieve the target draft, as well as to ensure the stability in roll. The vessel was mounted to the carriage at two points and it was free to roll. The two mounting points along the vessel made the vessel slightly restrained in yaw. Although this could have delayed the dynamic instability, it could not prevent it at Froude number of 0.9.

The observed instability can be categorized as calm-water broaching. Figure 8.1 shows snapshots of the instability process. Although, small changes in the drift and heel angle of the vessel at the beginning of the process are detectable, it is difficult to say which one comes first. The motion was followed by a continuous increase in drift and heel angle, as well as shift of the vessel to the port side. Unfortunately there is no data available for the lateral motions but the violent yaw and heel angles are very clear in the recorded video.

8.2.2 Hydrodynamic modeling

As presented in Chapter 7, attempts were made to solve the complicated flow around semi-displacement vessels with dry transom stern using the linear potential-flow theory. Although the hollow-body model proved to be promising in the solution of the flow around an oscillating vessel, solving for the sway and yaw oscillations were still challenging. Therefore, a simplified approach was adopted here by transferring the body boundary condition to the center plane. In other words, the ship's surface was simplified as a flat plate with constant aspect ratio of 0.1. Although, for the vessel presented in Section 8.2.1, the correct aspect ratio would be 0.08, the aspect ratio of 0.1 was chosen in order to make use of the existing experimental data.

Kashiwagi (1984) presented numerical and experimental data for the hydrodynamic coefficients of an advancing and oscillating surface-piercing plate. These values were used to validate the calculations, as well as to obtain estimations of the expected numerical inaccuracies. These estimations can work as a guide lines in sensitivity study of dynamic stability.

The procedure outlined in Section 6.4 was adopted here. Hydrodynamic coefficients in sway, roll, and yaw were calculated for a series of frequencies at different Froude numbers. The seakeeping coordinate system, presented in Section 2.1, was used for calculations. The center of gravity of the plate was assumed to be in the middle. Figures 8.2 to 8.4 show comparisons for the added mass and damping coefficients in sway, roll, and yaw at Froude number of 0.3, respectively. The experimental data from Kashiwagi (1984), as well as the numerical data by Chapman's 2D+t method, and the two procedures outlined in Kashiwagi (1984), are presented (procedures are called Pro.1. and Pro.2. similar to the original report). The overall agreement of the results are acceptable. The results of the procedure-one from Kashiwagi (1984) predicts a singularity at $\tau = \omega U/g = 1/4$, which does not exist in the reported experimental values. The calculations from the other numerical methods, including the present method, agreed with the experimental data and do not show the singular behavior. Interested readers are referred to the discussions presented in Sections 6.3 and 6.4 regarding the importance of the cross-flow drag, when the oscillation frequency approaches zero.

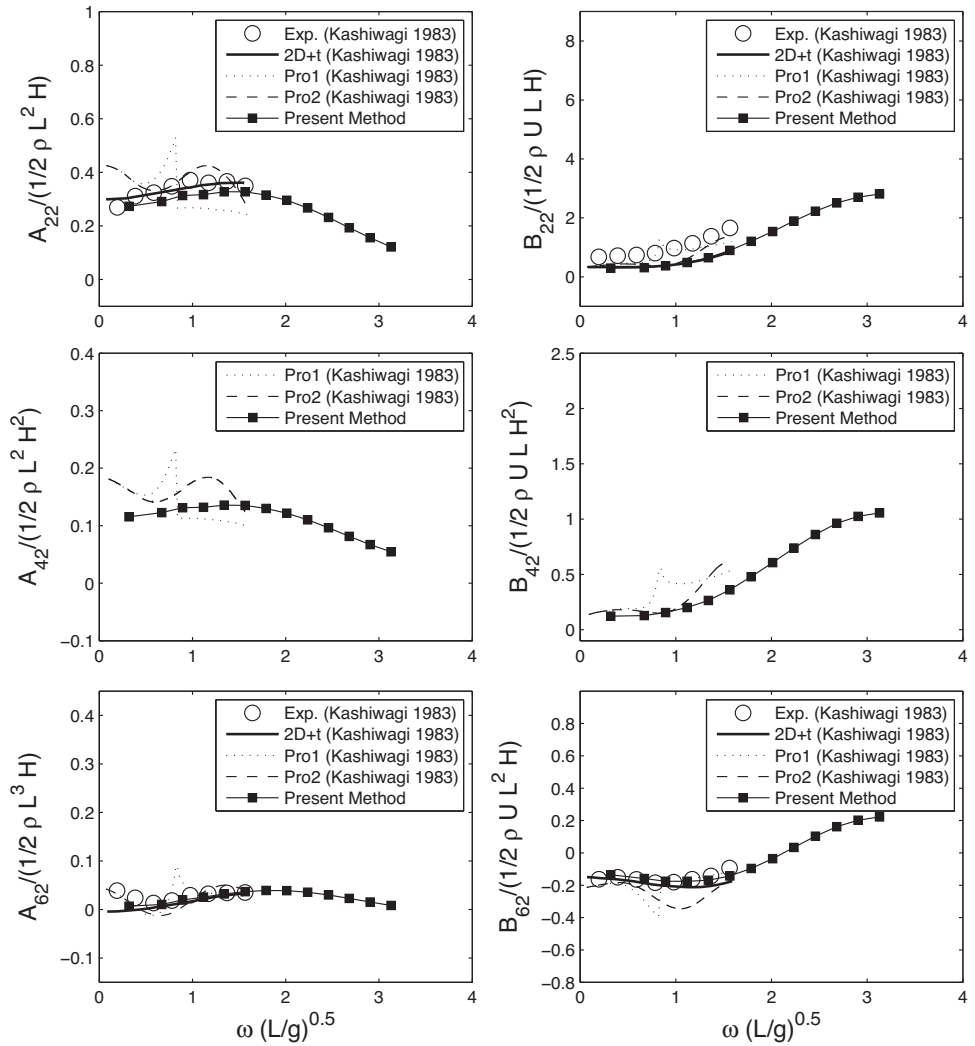


Figure 8.2: Hydrodynamic coefficients for a plate in sway oscillations, Aspect ratio $\Lambda = H/L = 0.1$, $Fn = 0.3$. The differences between Kashiwagi (1983) and the present coordinate systems must be noted. The values were transferred to the present seakeeping coordinate system in Section 2.1.

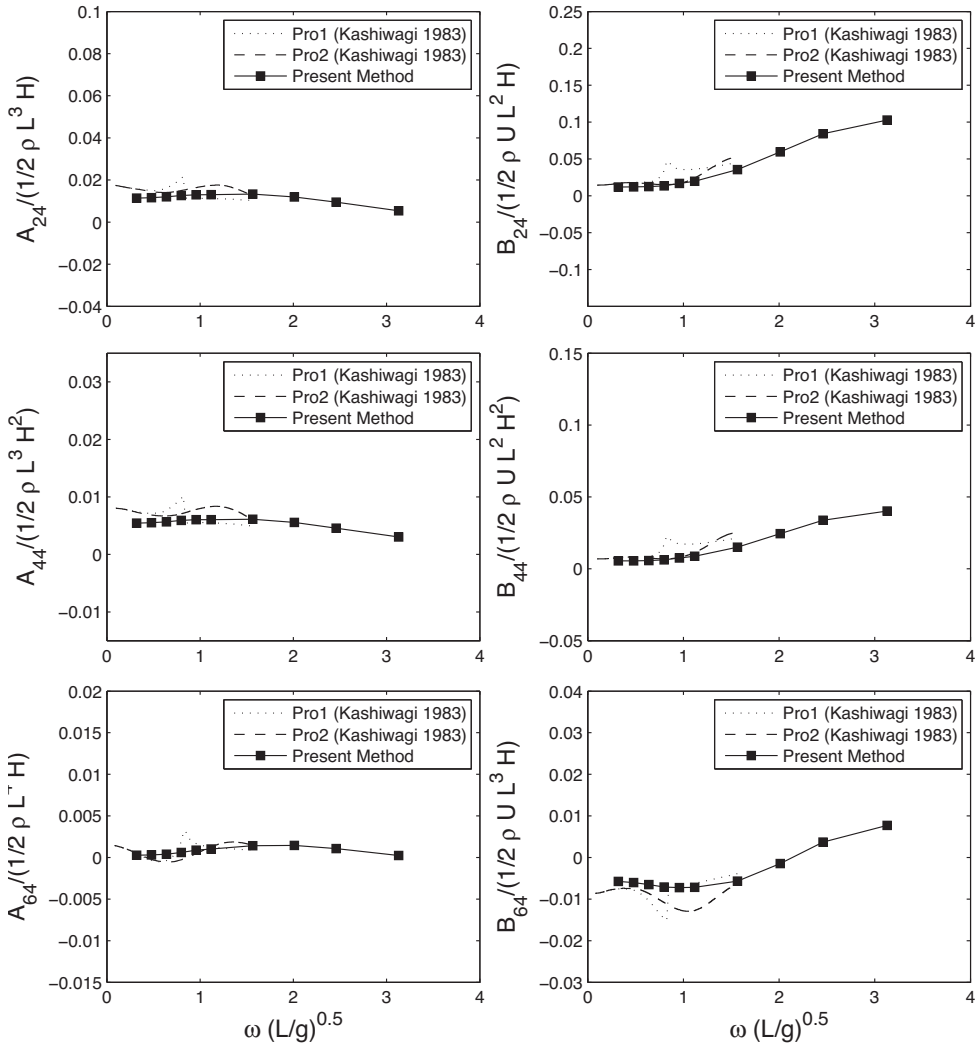


Figure 8.3: Hydrodynamic coefficients for a plate in roll oscillations, Aspect ratio $\Lambda = H/L = 0.1$, $Fn = 0.3$. The differences between Kashiwagi (1983) and the present coordinate systems must be noted. The values were transferred to the present seakeeping coordinate system in Section 2.1.

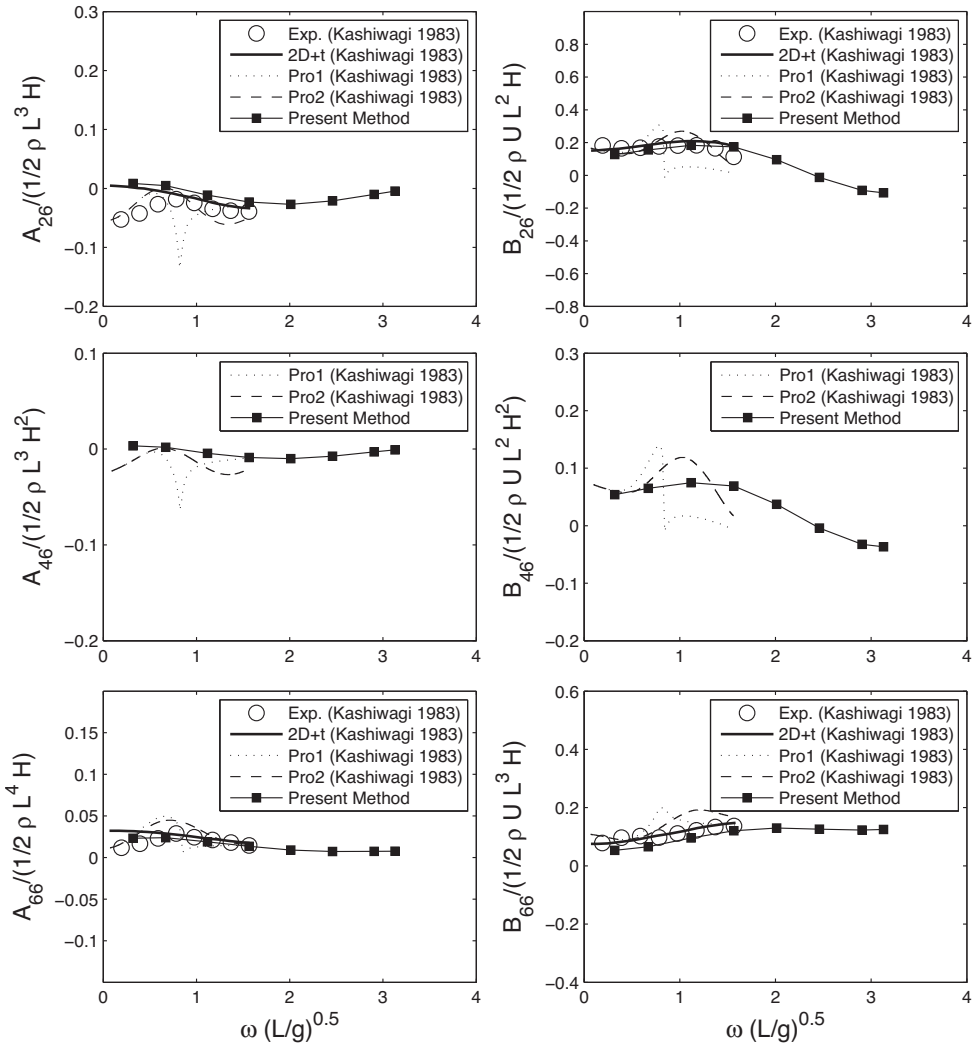


Figure 8.4: Hydrodynamic coefficients for a plate in yaw oscillations, Aspect ratio $\Lambda = H/L = 0.1$, $Fn = 0.3$. The differences between Kashiwagi (1983) and the present coordinate systems must be noted. The values were transferred to the present seakeeping coordinate system in Section 2.1.

Figures 8.5 to 8.7 show the variation of the hydrodynamic coefficients with Froude number and frequency. It must be noted that calculating the coefficients for low oscillation frequencies was difficult due to numerical problems. Low frequency oscillations generate long waves. As discussed in Section 3.7.2, this leads to a demand to increase the size of the free-surface domain and the damping zone, in order to absorb the waves at the boundaries. Therefore, the values at zero

frequency presented in Figures 8.5 to 8.7 were calculated by linearly extrapolating the last computational points. It can be interesting to note that at higher Froude numbers the hydrodynamic coefficients become frequency-independent, while at lower Froude numbers their values can vary strongly with the oscillation frequency (see Figure 8.7).

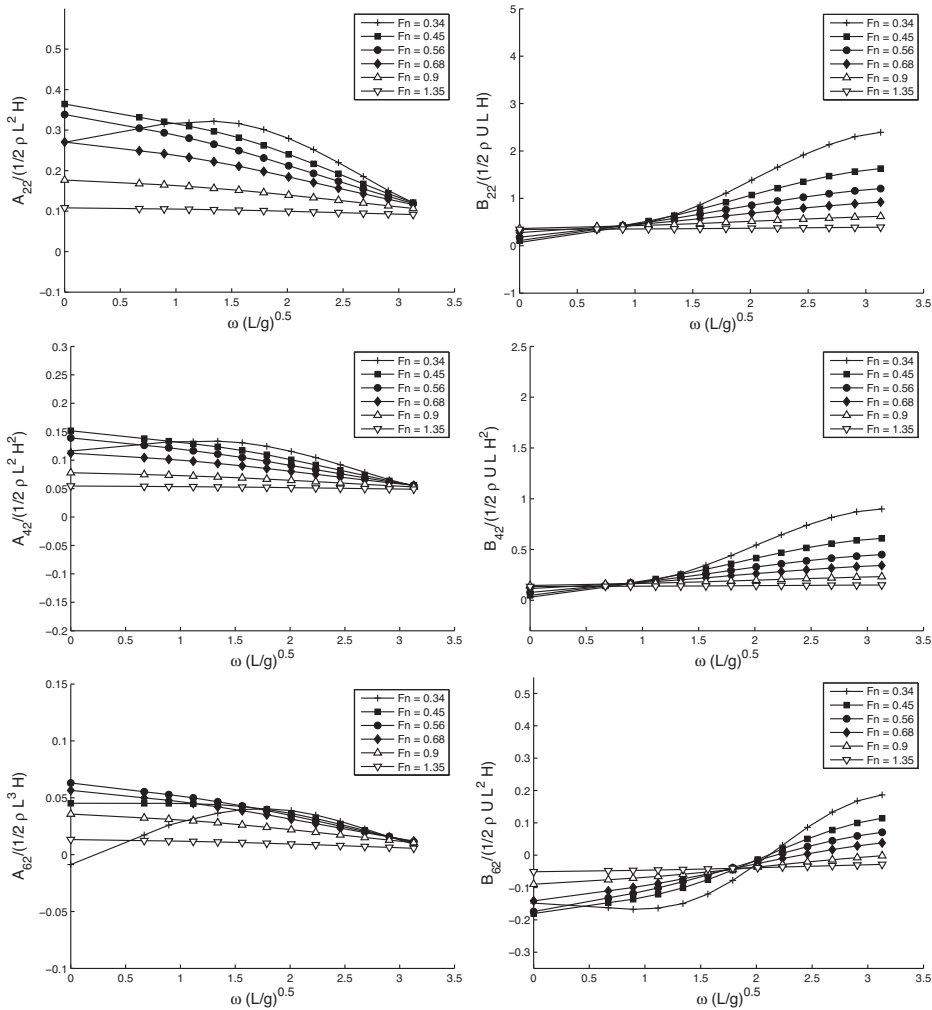


Figure 8.5: Variation of hydrodynamic coefficients with Froude number for a plate in sway oscillations, Aspect ratio $\Lambda = H/L = 0.1$. The values for zero frequency were obtained by extrapolation.

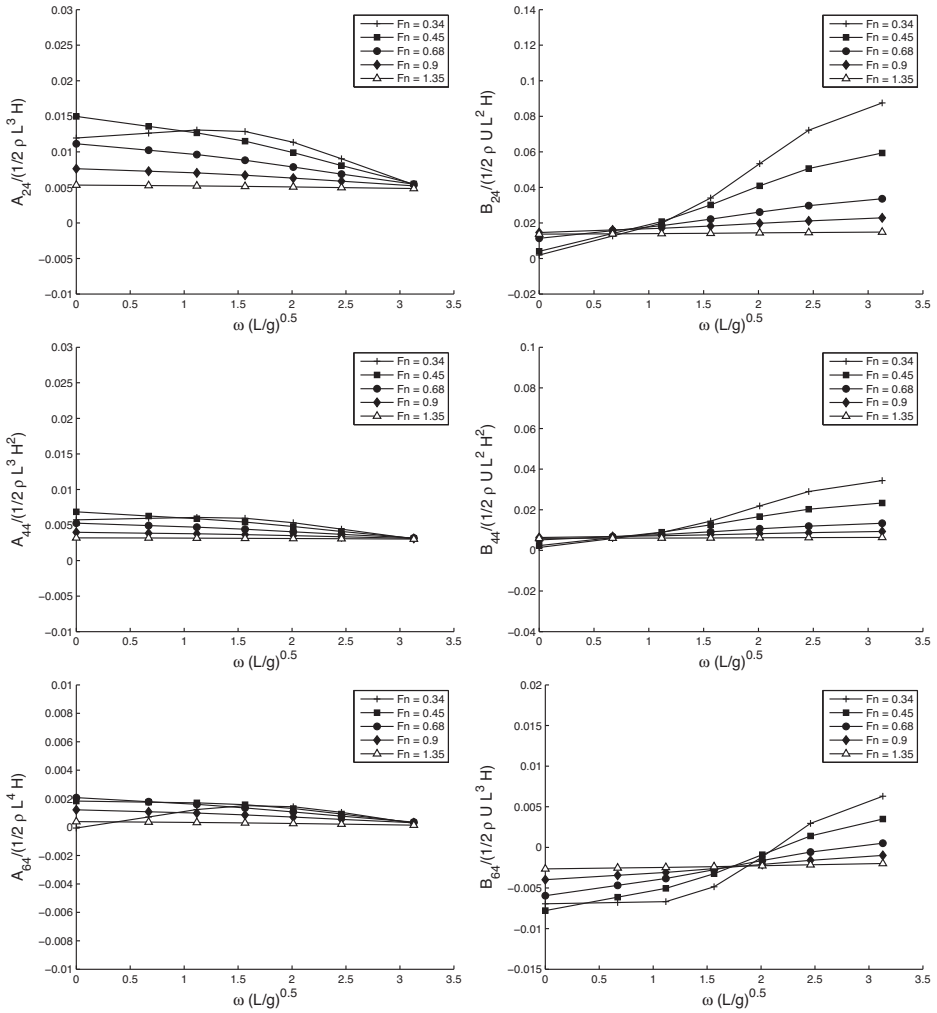


Figure 8.6: Variation of hydrodynamic coefficients with Froude number for a plate in roll oscillations, Aspect ratio $\Lambda = H/L = 0.1$. The values for zero frequency were obtained by extrapolation.

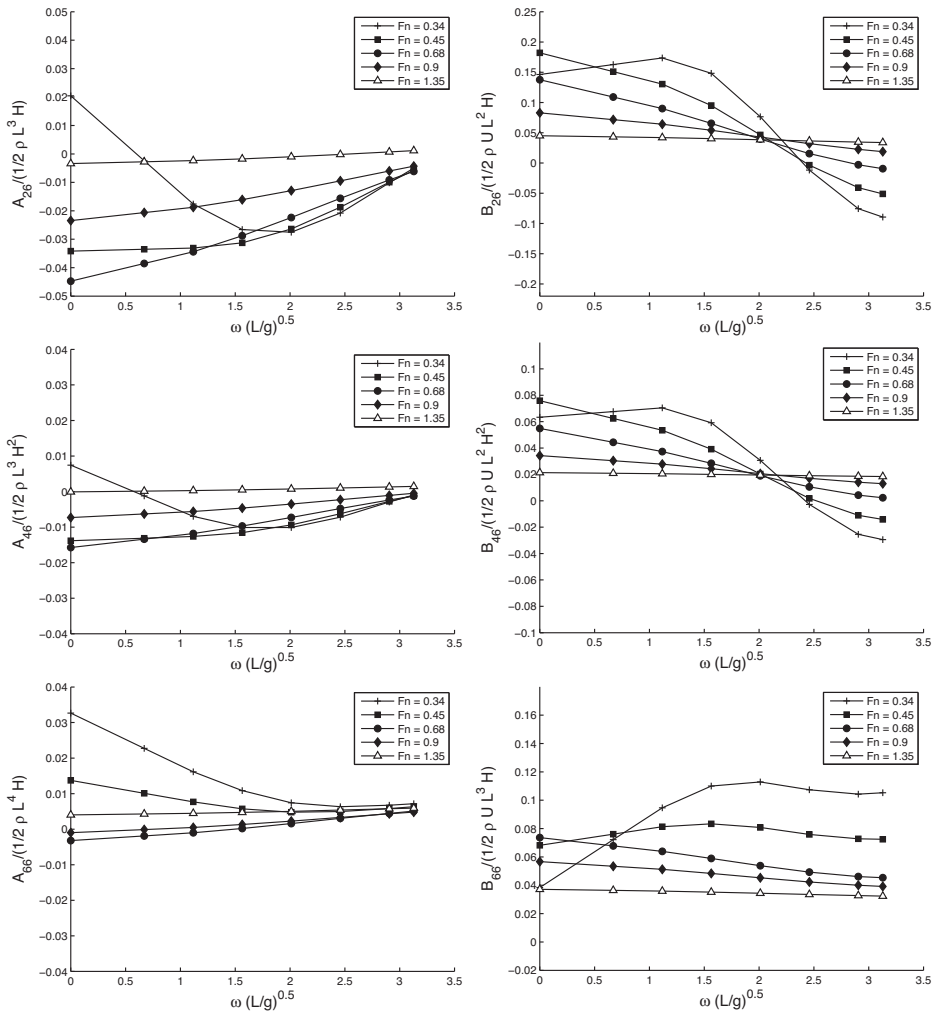


Figure 8.7: Variation of hydrodynamic coefficients with Froude number for a plate in yaw oscillations, Aspect ratio $\Lambda = H/L = 0.1$. The values for zero frequency were obtained by extrapolation.

As mentioned before, the hydrodynamic coefficients presented in Figures 8.6 and 8.7 were used to represent the hydrodynamic of the vessel presented in Section 8.2.1. The chosen plate has constant draft along the length. This means that the changes in the ship sections' drafts were neglected. Moreover, due to sinkage and trim induced by the forward speed, the local draft will change along the ship, which was also neglected here. A plate with a taper angle may represent these effects better (see Figure 6.5). In analogy to slender body theory, the body boundary conditions were transferred to the center plane. This means that a small beam to draft ratio was assumed. This is not generally true for semi-displacement vessels.

In the semi-displacement vessel studied here, however, this ratio is 0.875, which makes the assumption more reasonable. For conventional semi-displacements, this value can be between 5 to 7.

In order to study dynamic-stability, a dynamic model of the vessel must be created, which requires hydrodynamic coefficients. A series of B-splines were fitted on the computed hydrodynamic coefficients. In this way, the added mass and damping coefficients were represented in the form of smooth two-variable functions as $A_{ij} = f_{ij}(Fn, \omega)$ and $B_{ij} = g_{ij}(Fn, \omega)$. The variation of these functions with frequency and Froude number are presented for A_{66} and B_{66} as an example. From these functions, a series of hydrodynamic coefficients was obtained for each frequency and Froude number pair. Then, a dynamic model for that pair was established.

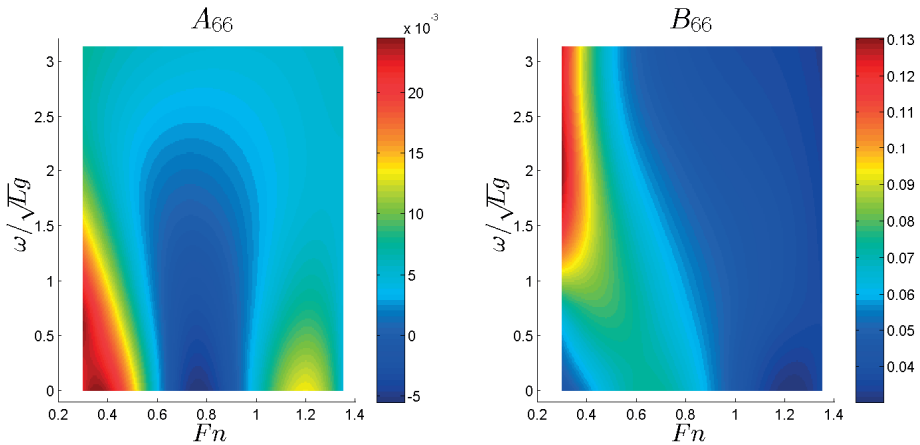


Figure 8.8: Variation of A_{66} and B_{66} with frequency and Froude number for a surface piercing plate, Aspect ratio $\Lambda = H/L = 0.1$, B-spline fitting was used to interpolate the results in Figure 8.7.

8.3 Sway-yaw dynamic stability analysis

We start the dynamic stability analysis by looking at the coupled sway and yaw equations of motion.

8.3.1 Formulation

From Eq. (2.46) the coupled equations of motion, in sway and yaw, can be obtained as shown in Eq. (8.1) below. These equations are written about the center of the seakeeping coordinate system described in Section 2.1. A special attention must be paid to $-MU\dot{\eta}_2$ term. This term comes from the fact that our original equation system is written in a non-inertial coordinate system. By transferring it to the

inertial coordinate system, the sway acceleration term ($\dot{\eta}_2$) is modified by $-U\dot{\eta}_6$ (see Section 10.3.2 in Faltinsen (2005) for more details).

$$\begin{aligned} (M + A_{22}) \frac{d^2 \eta_2}{dt^2} + B_{22} \frac{d\eta_2}{dt} + A_{26} \frac{d^2 \eta_6}{dt^2} + (-MU + B_{26}) \frac{d\eta_6}{dt} &= F_2 \\ A_{62} \frac{d^2 \eta_2}{dt^2} + B_{62} \frac{d\eta_2}{dt} + (I_{66} + A_{66}) \frac{d^2 \eta_6}{dt^2} + B_{66} \frac{d\eta_6}{dt} &= F_6 \end{aligned} \quad (8.1)$$

The dynamic stability of a system can be studied by assuming a zero external forcing, i.e. $F_2 = F_6 = 0$, and a solution form e^{st} , where s is a complex number. This means that we can write $\dot{\eta}_2 = \dot{\eta}_{2a}e^{st}$ and $\dot{\eta}_6 = \dot{\eta}_{6a}e^{st}$, where dot represents the time derivative, and subscript a refers to the amplitude. Substituting these into Eq. (8.1), the following equation system for sway and yaw velocity amplitudes is obtained.

$$\begin{bmatrix} (M + A_{22})s + B_{22} & A_{26}s + (-MU + B_{26}) \\ A_{62}s + B_{62} & (I_{66} + A_{66})s + B_{66} \end{bmatrix} \begin{bmatrix} \dot{\eta}_{2a} \\ \dot{\eta}_{6a} \end{bmatrix} = \begin{bmatrix} 0 \\ 0 \end{bmatrix} \quad (8.2)$$

The non-trivial solutions of the above equations are obtained by putting the determinant of the coefficients matrix to zero. This results in a second order equation in s .

$$C_2 s^2 + C_1 s + C_0 = 0 \quad (8.3)$$

where,

$$\begin{aligned} C_2 &= (M + A_{22})(I_{66} + A_{66}) - A_{26}^2 \\ C_1 &= (M + A_{22})B_{66} + (I_{66} + A_{66})B_{22} - A_{26}B_{62} + A_{62}(MU - B_{26}) \\ C_0 &= B_{22}B_{66} - B_{26}B_{62} + B_{62}MU \end{aligned} \quad (8.4)$$

The roots of Eq. (8.3) determine the system's dynamic stability. The real part of the roots show how the response amplitude is changing in time. A negative real part means decay, while positive means amplification and consequently instability. On the other hand, the imaginary part of the roots show the vessel's free-system's response frequency.

8.3.2 Analysis

In order to study the roots of Eq. (8.3), the hydrodynamic coefficients in sway and yaw are needed in addition to the mass, second moment of inertia in yaw, and the vessel's velocity. The model presented in Section 8.2.1 was simplified to a flat plate and studied here. The Froude number and frequency dependent hydrodynamic coefficients were presented in Section 8.2.2. These hydrodynamic coefficients were calculated about the center of the plate in the free surface. The vessel's center of gravity is not, however, necessarily in the middle and it can be changed. Let us assume two coordinate systems, xyz which corresponds to the defined seakeeping coordinate system, and $x'y'z'$ which is parallel to xyz but with the center in the

middle of the vessel (see Figure 8.9). The hydrodynamic coefficients in Section 8.2.2 are actually in $x'y'z'$ coordinate system. In order to use them in Eq. (8.3) they must be transferred to xyz coordinate system using the transformations shown in Eq. (8.5).

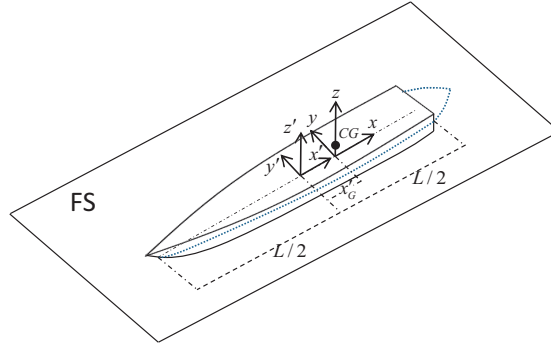


Figure 8.9: Coordinate system transformation for hydrodynamic coefficients, x'_G : Longitudinal position of the center of gravity in $x'y'z'$ coordinate system, note: the shift of the center of gravity towards stern was exaggerated for clarity.

After transferring the hydrodynamic coefficients to the xyz coordinate system, the roots of Eq. (8.3) can be obtained. For each Froude number and frequency pair a series of hydrodynamic coefficients are obtained which form a unique dynamic system. Then, for each system two complex roots are obtained. If the real parts of the two complex roots are negative, we can say that the linear dynamic stability analysis predicts a stable system. Moreover, the imaginary parts of the roots, which are complex conjugate, give the free-system's response frequency. This means that if we remove the forcing function, the vessel's response will have that frequency. It must be noted that the hydrodynamic coefficients are frequency dependent. As a consequence, for different frequencies, we have different values in the equation system, which leads to different roots. Therefore, the imaginary part of a root represents the free-system's response frequency only if it belongs to a system constructed for that frequency. An iterative procedure was adopted to find these roots at each Froude number.

$$\begin{aligned}
 A_{26} &= A'_{26} - x'_G A'_{22} & B_{26} &= B'_{26} - x'_G B'_{22} \\
 A_{62} &= A'_{62} - x'_G A'_{22} & B_{62} &= B'_{62} - x'_G B'_{22} \\
 A_{66} &= A'_{66} - x'_G A'_{62} - x'_G (A'_{26} - x'_G A'_{22}) \\
 B_{66} &= B'_{66} - x'_G B'_{62} - x'_G (B'_{26} - x'_G B'_{22})
 \end{aligned} \tag{8.5}$$

Figure 8.10 shows the stability graph (left), as well as the root locus plot (right), for the vessel presented in Section 8.2.1, with the hydrodynamic coefficients from Section 8.2.2. The white area in the stability graph corresponds to the Froude number and frequency pair in which the system has no root with a positive real

part, i.e. a stable system. The dashed lines are showing the actual computational domain for the hydrodynamic coefficients. This domain was extrapolated towards zero frequency as discussed in Section 8.2.2. Having no black area in the stability graph means that the linear dynamic stability analysis predicted a stable system everywhere. The circles are the imaginary parts of the roots, which correspond to the free-system's response frequencies. The root locus plot for these roots is shown in Figure 8.10 as well. We see that both branches are on the left hand side of the imaginary axis, which corresponds to roots with negative real parts and consequently a stable system. The numbers on the branches represents the vessel's Froude number. Similar root-locus plots were presented by Lewandowski (2003) for a planing hull using frequency-independent empirical hydrodynamic coefficients.

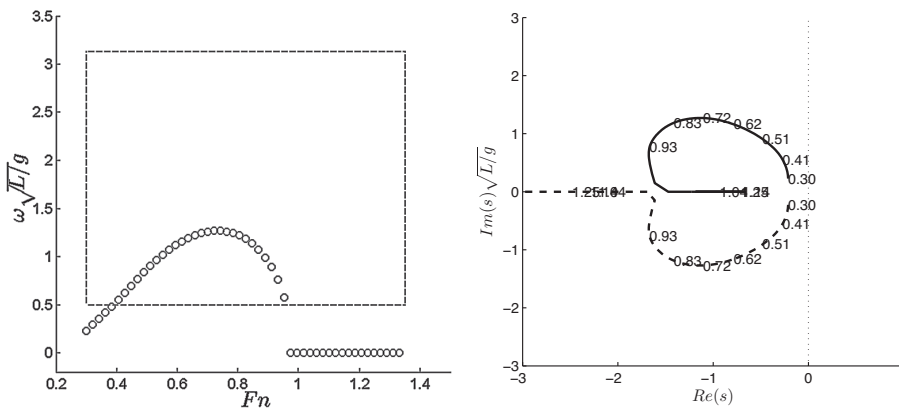


Figure 8.10: (Left): Sway-yaw dynamic stability graph for the studied semi-displacement vessel, Black area: unstable, White area: stable (stable every where), Dashed lines: computational domain, Circles: free-system's response frequencies. (Right): Root locus plot for the sway-yaw system, s : root of the dynamic system's characteristic equation, Froude numbers are shown on the curve.

It is interesting to see that free-system's response frequency was zero for the Froude number approximately higher than 1.0. It means that, in this range of Froude numbers, the response of the freely moving system in sway-yaw was non-oscillatory. Calm water broaching was detected in the experiments for a Froude number 0.9. However, the present linear dynamic stability analysis predicted no instability in sway-yaw for this Froude number. It must be mentioned that Haarhoff and Sharma (2000) links the dynamic instability to the change of the metacentric height due to forward speed, while here these changes were not considered since the calculations do not include the roll motion. Moreover, it is known that the instability predictions by a linearized model of a non-linear system can be inaccurate, if the poles are close to the imaginary axes (e.g. Khalil (2001)). Further investigations are needed in order to evaluate the accuracy of the linear stability predictions in relation to the actual non-linear model

8.3.3 Sensitivity study

A sensitivity study is pursued here in order to investigate the dependency of the vessel’s dynamic stability to each of the parameters. In reality most of the parameters can not be changed independent of the others. However, the independent influence of each parameter was considered and the couplings between them were neglected. The changes are presented in terms of the percentage of the initial calculated values. For instance +20% change means $P_{new} = P_{init} + 0.2 * |P_{init}|$, where P is the parameter of study. Therefore, +20% means increase or decrease, depending on the sign of the initial value. Hereafter, the positive percentage is referred to as increase and negative percentage as decrease in an absolute sense. The added mass coefficients, the damping coefficients and the other parameters related to the vessel’s mass distribution are studied separately in the following sections.

Added mass coefficients

Figure 8.11 shows the instability prediction by changing the added mass coefficients in Eq. (8.3), where the black squares means the system has at least one unstable root in the $Fn - \omega$ plane. Based on Figure 8.11, varying the added mass coefficients up to 40% of their original values does not introduce unstable roots into the system. On the other hand, reducing A_{22} by high percentage such as 60% leads to an unstable system.

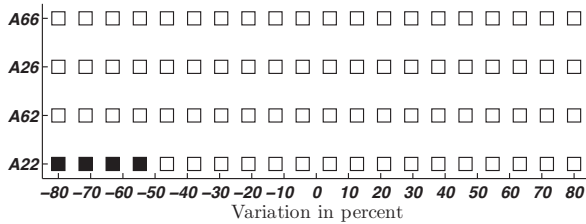


Figure 8.11: Influence of the added mass coefficients on dynamic stability in sway-yaw, Black squares: an unstable system, White squares: a stable system.

More details on the influence of the added mass coefficients can be obtained by looking at how the root locus plots are changing by varying these coefficients. Figure 8.12 shows how free-system’s response frequencies (right) and the corresponding root locus plot (left) are changing by varying A_{22} . It is shown that reducing A_{22} pushes the branches away from the real axis. Moreover, increasing A_{22} reduces the free-system’s response frequencies and push the branches towards the real axes. The stability graph and the corresponding root locus plots for 60% reduction in A_{22} are shown in Figure 8.13. Despite the fact that both branches are on the left hand side of the imaginary axis an unstable area exists for a Froude number between 0.6 to 0.8 at frequencies close to zero. This means that the dynamic system, which was constructed using these pairs of $Fn - \omega$, has an unstable root. However, the imaginary part of this unstable root does not correspond to the free-system’s response frequency at that Froude number.

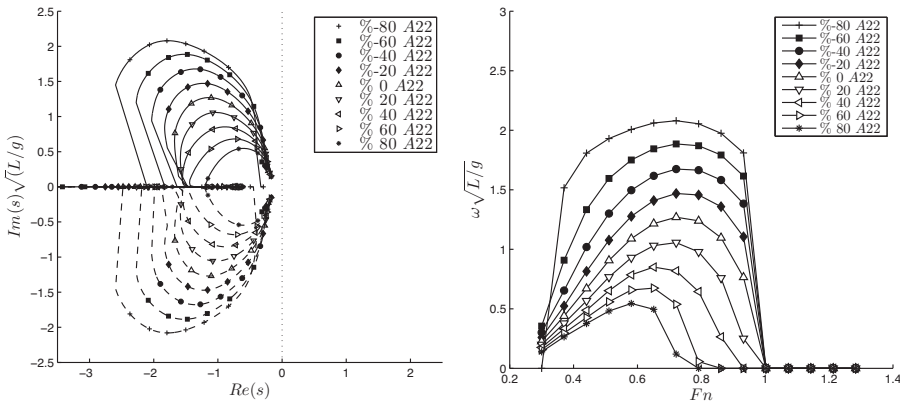


Figure 8.12: Influence of A_{22} on dynamic stability in sway-yaw, (Left): Root locus plot, s : root of the dynamic system's characteristic equation, (Right): Free-system's response frequencies.

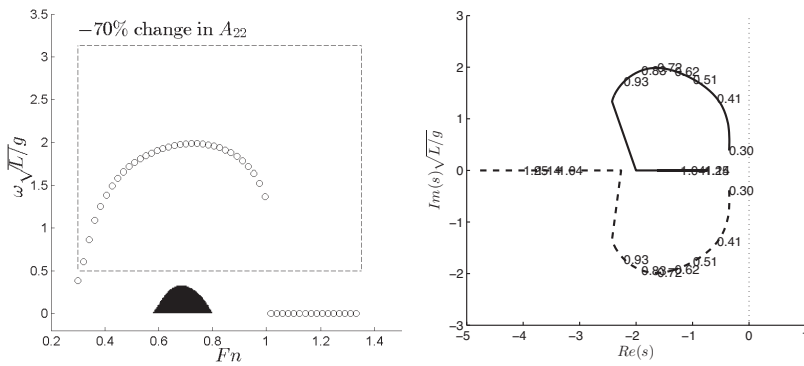


Figure 8.13: Influence of A_{22} on sway-yaw dynamic stability, (Left): Dynamic stability graph, Black area: unstable, White area: stable, Dashed lines: computational domain, Circles: free-system's response frequencies. (Right): The corresponding root locus plots, Froude numbers are shown on the curve, s : root of the dynamic system's characteristic equation.

If a linear system is disturbed with an external forcing with a certain frequency, by removing the disturbance, the system response will move towards the free-system's response frequency. For instance, if the vessel is disturbed by an external force with non-dimensional frequency around 0.2, while moving with $Fn = 0.7$, it would be in the unstable region. However, after the forcing has been removed the vessel response will move towards the frequency of freely oscillating vessel, which is in the stable region. Furthermore, a disturbance in reality consist of many frequencies, which can be viewed through the spectrum of disturbance. How these frequencies interact and the motion develops in time, and how it can effect the

dynamic stability, need further investigations. Since here we are limited by the linear dynamic stability analysis in the frequency domain, we have to say, if an instability exists for a Froude number in any frequency, the system is unstable for that Froude number.

Damping coefficients

Figure 8.14 shows the instability prediction by changing the damping coefficients in Eq. (8.3), where the black squares means the system has at least one unstable root in $F_n - \omega$ plane. Based on Figure 8.14, varying the damping coefficients up to 30% of their original values dose not introduce unstable roots into the system. On the other hand, reducing B_{66} by 40% leads to an unstable system.

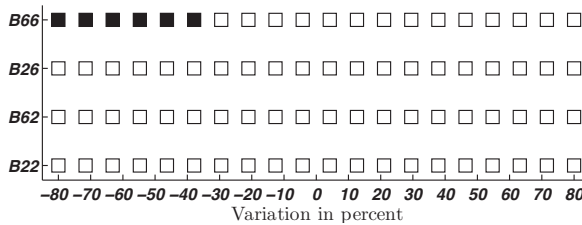


Figure 8.14: Influence of the damping coefficients on dynamic stability in sway-yaw, Black squares: an unstable system, White squares: a stable system.

Figure 8.15 shows how the free-system’s response frequencies (right) and the root locus plots (left) are changing by varying B_{22} . As expected from Figure 8.14, no unstable roots are detected. Unlike A_{22} , increasing B_{22} increases the free-system’s response frequencies, and pushes the root locus branches away from each other and the real axis. Figure 8.16 shows similar plots for B_{66} . Decreasing B_{66} increases the free-system’s response frequencies only up to a certain point. Beyond that point, the frequencies are reduced and the beaches bend towards the imaginary axis, and into the positive side, which leads to instability.

Let us take a closer look to see what happens when the branches cross the imaginary axis into the right hand side. Figure 8.17 shows stability graph, as well as root locus plot, for 60% decrease in B_{66} . In this case, it is possible to see an unstable area in the stability graph. Unlike the results for A_{22} in Figure 8.13, now the unstable area collides with the free-system’s response frequencies. This means that a group of unstable roots, with imaginary parts equal to the free-system’s resonance frequency, exist. Therefore, the branches in the root locus plots are crossing the imaginary axis.

Location of the center of gravity

The influence of the longitudinal location of the center of gravity on the dynamic stability in sway and yaw is investigated here. Figure 8.18 shows the variation of the free-system’s response frequencies (right), and the corresponding root locus

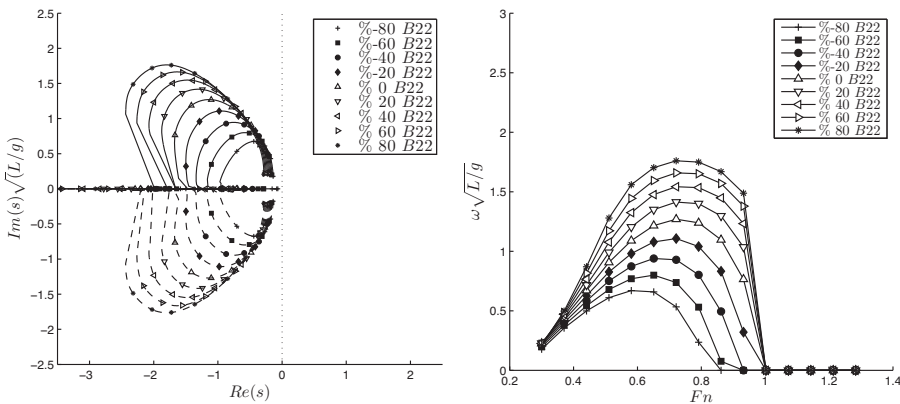


Figure 8.15: Influence of B_{22} on dynamic stability in sway-yaw, (Left): Root locus plot, s : root of the dynamic system's characteristic equation, (Right):Free-system's response frequencies.

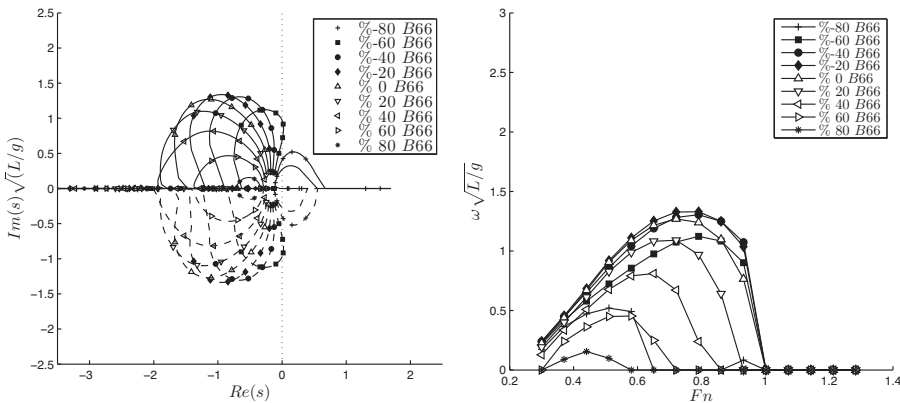


Figure 8.16: Influence of B_{66} on dynamic stability in sway-yaw, (Left): Root locus plot, s : root of the dynamic system's characteristic equation, (Right):Free-system's response frequencies.

branches (left), by varying x'_G , which is the longitudinal position of the center of gravity from mid-ship, positive towards the vessel's aft. Moving the center of gravity towards the bow decreases the response frequencies rapidly. Moreover, the root locus branches are getting closer to the imaginary axis by moving the center towards the aft, and finally crosses the axis for $x'_G/L = 0.36$ and the system becomes unstable. As mentioned before, the instability predictions by a linearized model of a non-linear system can be inaccurate, if the poles are close to the imaginary axes (e.g. Khalil (2001)). Therefore, shifting the roots towards the imaginary axis increases the risk of dynamic instability in general.

Let us take a look at the dynamic stability criteria obtained from a simplified

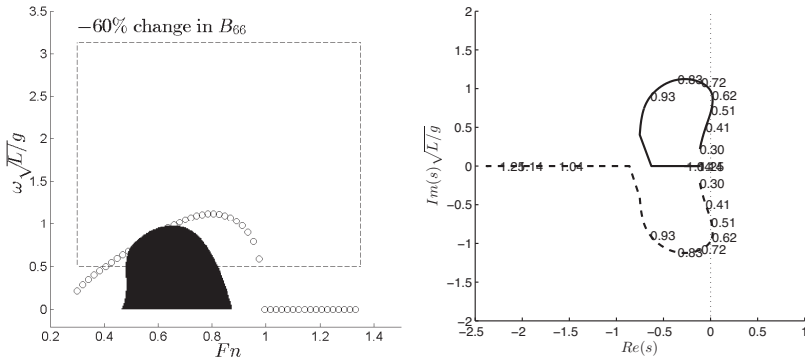


Figure 8.17: Influence of B_{66} on sway-yaw dynamic stability, (Left): Dynamic stability graph, Black area: unstable, White area: stable, Dashed lines: computational domain, Circles: free-system’s response frequencies. (Left): Corresponding root locus plot, s : root of the dynamic system’s characteristic equation, Froude numbers are shown on the curve.

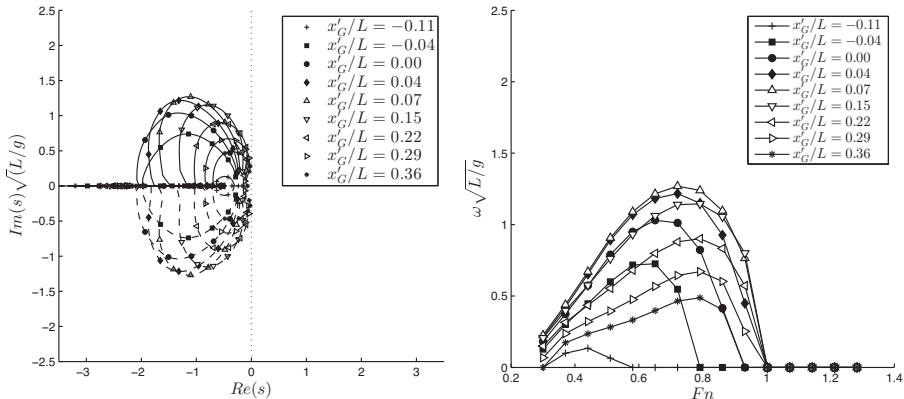


Figure 8.18: Influence of x_G on dynamic stability in sway-yaw, (Left): Root locus plot, s : root of the dynamic system’s characteristic equation, (Right): Free-system’s response frequencies, x'_G : longitudinal position of the center of gravity from the mid-ship, positive towards the vessel’s aft.

analysis by Faltinsen (2005), and also by Newman (1977). In this analysis, C_2 and C_1 in Eq. (8.4) were assumed to be positive, and the center of gravity to be at the mid-ship. Moreover A_{26} was assumed to be negligible. The obtained condition is then governed by the sign of C_0 . Moreover, it was possible to represent the damping values in C_0 in terms of the added mass coefficients. The relation between the damping and added mass coefficients in this analysis are presented in Eq. (8.6).

$$\begin{aligned}
B_{22} &= Ua_{22}(x_T) & B_{62} &= -UA_{22} + Ux_T a_{22}(x_T) \\
B_{26} &= Ux_T a_{22}(x_T) & B_{66} &= -UA_{62} + Ux_T^2 a_{22}(x_T)
\end{aligned} \tag{8.6}$$

Here, x_T is the longitudinal coordinate of the stern and a_{22} is the two dimensional added mass in sway for the stern section. Then, the stability criteria can be written as shown in Eq. (8.7). Based on this analysis, moving the center of gravity towards bow improves the dynamic stability of the system. On the other hand, moving the center towards stern may lead to instability.

$$x_T a_{22}(x_T) > \frac{MA_{22}}{M + A_{22}} \tag{8.7}$$

A similar conclusion can be obtained from Figure 8.18 for the present sway-yaw dynamic stability analysis. Moving the center of gravity towards the stern bends the branches towards the imaginary axis. Getting closer to the imaginary axis means a higher risk of instability. It must be noted that in this analysis, the longitudinal location of the center of gravity was changed independently. Therefore, it was assumed that this variation dose not change the shape of the under water part, and the second moment of inertia in yaw, which is not possible in practice.

8.4 Sway-roll-yaw dynamic stability

The stability analysis presented in Section 8.3 is extended in this section by adding the roll motion.

8.4.1 Formulation

From Eq. (2.46), the coupled equation of motion is sway, roll, and yaw can be obtain as shown in Eqs. (8.8) to (8.10) below. Similar to Eq. (8.1), these equations were written about the origin of the seakeeping coordinate system described in Section 2.1. The vertical position of the center of gravity is taken into consideration using the generalized mass matrix defined in Eq. (2.47). More details on deriving these equations can be found in Section 10.9.3 of Faltinsen (2005).

$$\begin{aligned}
(M + A_{22}) \frac{d^2 \eta_2}{dt^2} + B_{22} \frac{d\eta_2}{dt} + (-Mz_G + A_{24}) \frac{d^2 \eta_4}{dt^2} + \\
B_{24} \frac{d\eta_4}{dt} + A_{26} \frac{d^2 \eta_6}{dt^2} + (-MU + B_{26}) \frac{d\eta_6}{dt} = F_2
\end{aligned} \tag{8.8}$$

$$\begin{aligned}
(-Mz_G + A_{42}) \frac{d^2 \eta_2}{dt^2} + B_{42} \frac{d\eta_2}{dt} + (I_{44} + A_{44}) \frac{d^2 \eta_4}{dt^2} + B_{44} \frac{d\eta_4}{dt} + \\
C_{44} \eta_4 + (-I_{46} + A_{46}) \frac{d^2 \eta_6}{dt^2} + (Mz_G U + B_{46}) \frac{d\eta_6}{dt} = F_4
\end{aligned} \tag{8.9}$$

$$\begin{aligned}
& A_{62} \frac{d^2 \eta_2}{dt^2} + B_{62} \frac{d\eta_2}{dt} + (-I_{64} + A_{24}) \frac{d^2 \eta_4}{dt^2} + \\
& B_{64} \frac{d\eta_4}{dt} + (I_{66} + A_{66}) \frac{d^2 \eta_6}{dt^2} + B_{66} \frac{d\eta_6}{dt} = F_6
\end{aligned} \tag{8.10}$$

It must be noted that $C_{44} = \rho g \nabla \overline{GM}$ only represents the hydrostatic restoring moment in roll, where ∇ is the under water volume of the vessel, and \overline{GM} is the transverse metacentric height. The hydrodynamic restoring coefficients were accounted for through the added mass coefficients in the present calculation method. Therefore, C_{24} and C_{64} were set to zero.

Following the procedure presented in Section 8.3.1, we assume zero excitation forces and a e^{st} solution form, where s is a complex number. Then, we can write $\dot{\eta}_2 = \dot{\eta}_{2a} e^{st}$, $\eta_4 = \eta_{4a} e^{st}$, and $\dot{\eta}_6 = \dot{\eta}_{6a} e^{st}$, where subscript a represents the amplitude of the quantity. By substituting these into Eqs. (8.8) to (8.10), the following equation system for sway, roll, and yaw is obtained.

$$\begin{aligned}
& \left[\begin{array}{ccc}
(M + A_{22})s + B_{22} & (-Mz_G + A_{24})s^2 + B_{24}s & \dots \\
(-Mz_G + A_{42})s + B_{42} & (I_{44} + A_{44})s^2 + B_{44}s + C_{44} & \dots \\
A_{62}s + B_{62} & (-I_{64} + A_{64})s^2 + B_{64}s & \dots \\
\dots & A_{26}s + (-MU + B_{26}) & \\
\dots & (-I_{46} + A_{26})s + (Mz_G U + B_{46}) & \\
\dots & (I_{66} + A_{66})s + B_{66} &
\end{array} \right] \begin{bmatrix} \dot{\eta}_{2a} \\ \eta_{4a} \\ \dot{\eta}_{6a} \end{bmatrix} = \begin{bmatrix} 0 \\ 0 \\ 0 \end{bmatrix}
\end{aligned} \tag{8.11}$$

Setting the determinant of Eq. (8.11) to zero results in a fourth order polynomial, which is called the dynamic system's characteristic polynomial or the stability polynomial (Eq. (8.12)). The roots of this polynomial describes the dynamic stability of the system.

$$C_4 s^4 + C_3 s^3 + C_2 s^2 + C_1 s + C_0 = 0 \tag{8.12}$$

Similar to Eq. (8.3), if a complex root has a positive real part, then the response of the system grows with time, which leads to instability. On the other hand, if the real part of all the four possible roots are negative, it means that the amplitude of the response decays with time, and the freely oscillating system is stable. Then, the possible free-system's response frequencies are dictated by the imaginary parts of this polynomial's roots. Since the polynomial is of fourth order, two pairs of complex conjugate roots, and consequently two different frequencies, are expected. A discussion on the consequences of having two free-system's response frequency is presented in the following section.

8.4.2 Analysis

As discussed in Section 8.3.2, the hydrodynamic coefficients must be transferred to the seakeeping coordinate system of the vessel, considering the longitudinal location

of the center of gravity. Using the notation presented in Figure 8.9, the transformed coefficients are presented in Eq. (8.13).

$$\begin{aligned}
 A_{26} &= A'_{26} - x'_G A'_{22} & B_{26} &= B'_{26} - x'_G B'_{22} \\
 A_{46} &= A'_{46} - x'_G A'_{42} & B_{46} &= B'_{46} - x'_G B'_{42} \\
 A_{62} &= A'_{62} - x'_G A'_{22} & B_{62} &= B'_{62} - x'_G B'_{22} \\
 A_{64} &= A'_{64} - x'_G A'_{24} & B_{64} &= B'_{64} - x'_G B'_{24} \\
 A_{66} &= A'_{66} - x'_G A'_{62} - x'_G (A'_{26} - x'_G A'_{22}) \\
 B_{66} &= B'_{66} - x'_G B'_{62} - x'_G (B'_{26} - x'_G B'_{22})
 \end{aligned}
 \tag{8.13}$$

Figure 8.19 shows the stability graph (left) and the root locus plot (right) for the semi-displacement model presented in Section 8.2.1, using a coupled sway, roll, and yaw dynamic stability analysis. Similar to the sway-yaw analysis, the present simplified model predicts no instability for the assumed system. As discussed for

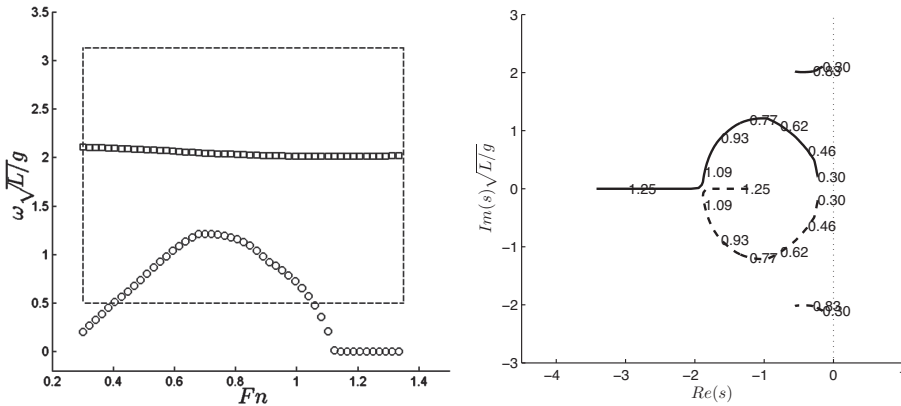


Figure 8.19: (Left): Sway-roll-yaw dynamic stability graph for the sample semi-displacement vessel, Black area: unstable, White area: stable (stable every where), Dashed lines: computational domain, Circles: free-system’s response frequency governed by the first root(sway-yaw), Squares: free-system’s response frequency governed by the second root(roll). (Right): Corresponding root locus plots, s : root of the dynamic system’s characteristic equation, Froude numbers are shown on the curve.

the sway-yaw analysis, the dynamic system’s characteristics depend on the response frequency. This means that in reality, the free dynamic system responds in the frequency, which is used for determining the hydrodynamic coefficients. In the sway-yaw analysis, this frequency was unique at each Froude number and has been found by an iterative procedure. However, as mentioned in Section 8.4.1, two different frequencies are obtained from the roots of the polynomial in Eq. (8.12). Therefore, in a sway-roll-yaw analysis, two values are obtained for a frequency at each Froude number. Therefore, the present analysis in the frequency domain can

not be used to capture the response of the free-system due to the coupling between these two frequencies (or roots). A time-domain analysis, using the convolution integrals, must be used instead. Here, we shall continue with our frequency domain analysis by assuming a linear decomposition of the free-system's responses. Two separate iterative procedures were used to calculate the free-system's response frequencies from the two roots. Then, the presented values refer to the free-system's response frequency, if it is governed by the first or the second root only.

The two response frequencies for the free-system is presented with circles and squares in Figure 8.19. The circles, which correspond to the imaginary parts of the first roots, follow the pattern of the sway-yaw dynamic system by changing the Froude number. However, the imaginary parts of the second roots, represented by squares, is almost independent of the Froude number and have higher values. Comparing these two sets of frequencies, it is possible to conclude that the first set of frequencies (circles) is related to the oscillatory motion in sway and yaw, while the second set (squares) refers to the oscillatory motion in roll. This is in agreement with the results presented by Lewandowski (2003) for the frequencies of a planing vessel, using frequency-independent empirical hydrodynamic coefficients.

8.4.3 Sensitivity study

Following the procedure used in Section 8.3.3, a sensitivity study was performed for the parameters involved in a coupled sway-roll-yaw dynamic system. The coupling of the hydrodynamic coefficients were neglected here in order to simplify the problem. The analysis presented here is very limited due to complexity of the problem. Further investigations are required on this matter, considering the dependencies of the parameters, in order to clarify the roles of each parameter on the dynamic stability of a realistic vessel.

Added mass coefficients

Figure 8.20 shows the instability predictions by changing the added mass coefficients, where the black squares means the system has at least one unstable root in the $F_n - \omega$ plane. Based on the data in Figure 8.20, varying the added mass coefficients up to 10% of their original values does not introduce unstable roots into the system. The dynamic stability seems to be sensitive to the added mass terms in roll and sway, as well as their cross coupling terms. Moreover, the increase in the system's sensitivity to A_{22} is interesting to point out. While in the sway-yaw analysis, the system did not become unstable with 20% reduction in A_{22} , the present sway-roll-yaw analysis suggests otherwise. This can be related to the importance of the roll induced instability. An investigation on the role of each added mass coefficient is left for the future studies.

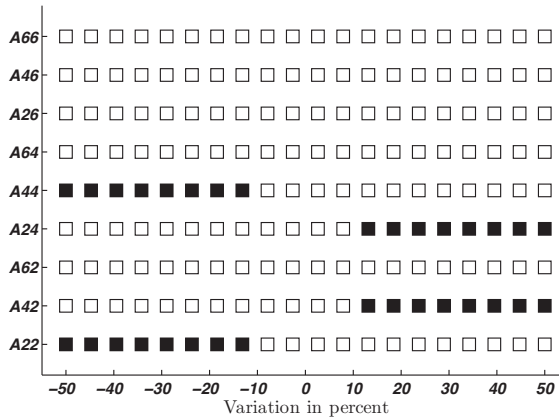


Figure 8.20: Influence of the added mass coefficients on dynamic stability in sway-roll-yaw, Black squares: an unstable system, White squares: a stable system.

Damping coefficients

A preliminary analysis on the influence of the damping coefficients is presented here. Figure 8.21 shows the instability predictions by changing the damping coefficients, where the black squares means the system has at least one unstable root in the $Fn - \omega$ plane. The sensitivity of the system's dynamic stability to the damping coefficients presented in Figure 8.21 suggests a complicated picture. The importance of the cross coupling terms in sway-roll and yaw-roll are interesting to notice.

Figure 8.21 suggests that reducing B_{22} by as little as 8% makes the system unstable. However, by looking at Figure 8.2, it is possible to conclude that the present numerical method, like other potential flow solutions, already under-predicts B_{22} . It was shown in Section 6.3 that at zero-frequency limit, these differences can be associated with the linearized cross-flow drag. This effect was neglected in the present analysis. Increasing Froude number, reduces the importance of this effect. It must be noted that the variation of the damping coefficients are presented independently, while the coupling of the coefficients can be important. For instance, by improving the calculation of the damping coefficients, not only B_{22} will be changed, but B_{66} , B_{44} and other relevant damping terms will also be modified.

Another important damping term is B_{44} . Although it is of second-order, the influence of the viscosity is important in determining the damping coefficients in roll. Moreover, a discrepancy between B_{44} of a vessel and a flat plate is expected. Figure 8.22 shows how the free-system's response frequencies, and the root locus plots, are changing by varying B_{44} . As expected, the influence of this variation on the response frequencies in sway and yaw are negligible. However, the roll response frequency is decreasing by increasing B_{44} . The root locus plot shows that by decreasing B_{44} , the short branch related to the roll motion crosses the

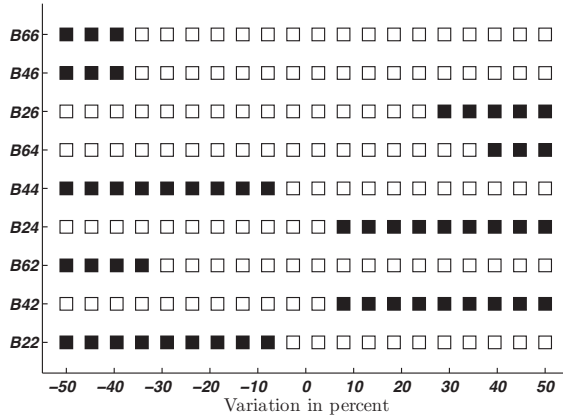


Figure 8.21: Influence of the damping coefficients on dynamic stability in sway-roll-yaw, Black squares: an unstable system, White squares: a stable system.

imaginary axis into the right hand side, which leads to instability. On the other hand, by increasing B_{44} this branch lengthens and bends towards the real axis, while crossing the branches related to the sway-yaw motion. Lewandowski (2003) showed that for a realistic planing hull, the roll-related branches bend towards and connect to the real axis, somewhere after the connection of the sway-yaw branches. As will be presented in the next section, the connection point of the roll-motion branches to the real axis, which is related to the maximum roll response frequency, can be moved by changing the vertical location of the vessel’s center of gravity.

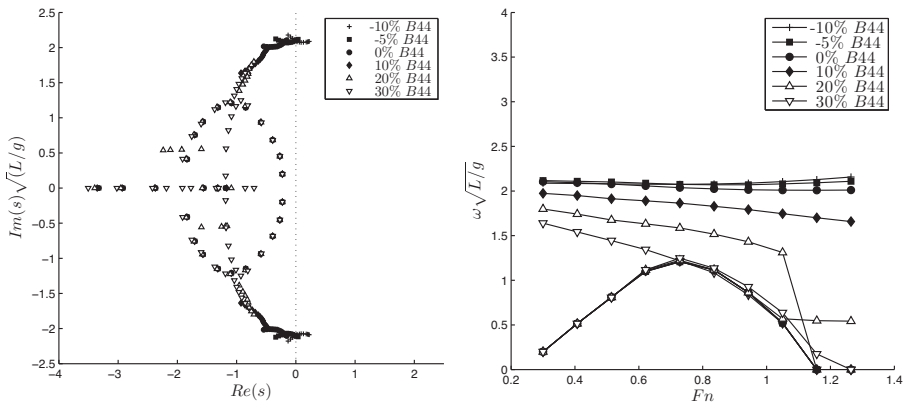


Figure 8.22: Influence of B_{44} on dynamic stability in sway-roll-yaw, (Left): Root locus plot, s : root of the dynamic system’s characteristic equation, (Right): Free-system’s response frequencies.

Location of the center of gravity

A preliminary investigation on the longitudinal and vertical position of the center of gravity, as well as metacentric height, is presented here. At first the influence of the longitudinal position of the center of gravity was investigated independently. Figure 8.23 shows the variation of the free-system's response frequencies and the root locus branches, by moving the center of gravity longitudinally. As expected, the changes in the roll-related frequencies are negligible. However, the sway-yaw related frequencies are changing considerably by moving the center of gravity, especially towards the stern. Similar to the sway-yaw analysis, moving the vessel's center of gravity towards the bow improves the dynamic stability.

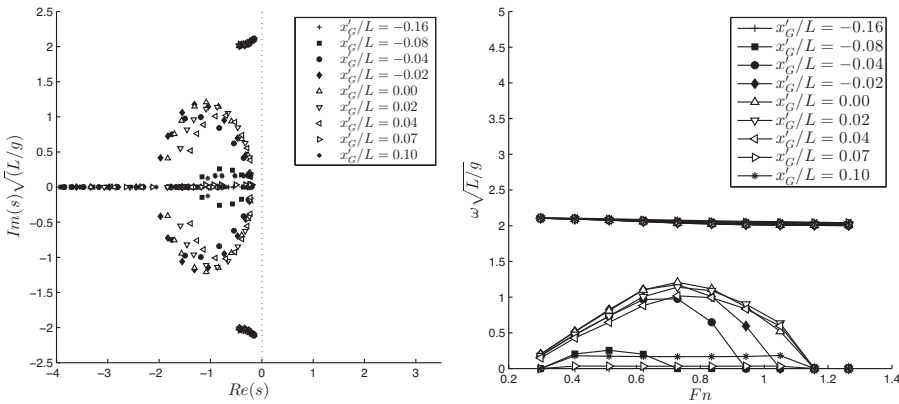


Figure 8.23: Influence of the longitudinal location of the center of gravity on sway-roll-yaw dynamic stability. (Left): Root locus plot, s : root of the dynamic system's characteristic equation, (Right): Free-system's response frequencies. x'_G : longitudinal position of the center of gravity from mid-ship, positive towards vessel's aft.

Investigating the influence of the other parameters, such as \overline{GM} (metacentric height), is important; especially when the roll motion is included. Metacentric height is defined as the vertical distance between the vessel's metacenter and the center of gravity. The vertical position of the center of gravity is usually defined by the distance from the vessel's keel (\overline{KG}). If we define the vertical distance of the metacenter from the keel to be \overline{KM} , we can write,

$$\overline{GM} = \overline{KM} - \overline{KG} \quad (8.14)$$

Then, the restoring moment in roll for a small heel angle θ , can be defined as below.

$$F_4 = \rho g \nabla \overline{GM} \sin \theta \quad (8.15)$$

A positive \overline{GM} is required for a system to be statically stable in roll. The restoring coefficient in roll is obtained by linearizing Eq. (8.15) for small heel angles.

Then, \overline{GM} and z_G in Eq. (8.11) for sway-roll-yaw dynamic stability analysis can be written in terms of \overline{KM} and \overline{KG} as follows,

$$C_{44} = g\rho \nabla (\overline{KM} - \overline{KG}) \quad z_G = \overline{KG} - D \quad (8.16)$$

where D is the vessel's draft. The influence of these parameters on the system's dynamic stability can be studied by varying \overline{KM} and \overline{KG} . \overline{KG} can be varied independently, except from I_{44} , as it represents the mass distribution in the vertical direction. For the height of metacenter from the vessel's keel, we can write,

$$\overline{KM} = \frac{I_w}{\nabla} + \overline{KB} \quad (8.17)$$

where I_w is the second transverse moment of the water plane area, and \overline{BM} is the vertical distance of the center of buoyancy from the vessel's keel. Therefore, changes in \overline{KM} represent changes in the shape and size of the vessel's submerged volume, which may affect the hydrodynamic terms as well. In the simplified analysis presented here, the hydrodynamics of the problem was simplified to be similar to the flow around a flat plate. Therefore, this dependency was neglected. However, the mass of the vessel was kept constant. Therefore, the total submerged volume was assumed to be constant. Allowing for a change in the vessel's submerged volume is directly linked to the changes in vessel's total mass and draft, which can not be neglected (see Section 6.4.3).

Figure 8.24 shows how the free-system's response frequencies and the root locus plots are changing by varying \overline{KM} . The original value for \overline{KM} is $1.44(m)$ in full scale. Decreasing \overline{KM} to less than \overline{KG} immediately introduces roots into the right hand side of the imaginary axis. This is expected, since the system becomes statically unstable. Increasing \overline{KM} up to two times the original value does not change the sway-yaw related frequencies. However, increasing \overline{KM} makes the system more stiff in roll by increasing C_{44} . Then, in analogy to a simple mass-spring-damper system, the roll-related free-system's response frequencies are increased as well.

Figure 8.25 shows similar graphs for varying \overline{KG} . The original values for \overline{KG} was assumed to be $1.35(m)$. Reducing \overline{KG} increases \overline{GM} , and consequently makes the system more stiff in roll (see Eq. (8.14)). Having a high enough \overline{GM} is suggested in practice, in order to reduce the chance of dynamic instability induced by a sudden list due to dynamic loss of \overline{GM} (see Müller-Graf (1997)). Similar results to what has been presented in Figure 8.24 are expected. Again the sway-yaw related stability and the free-system's response frequencies are not changing. However, higher frequencies in roll are obtained for a lower \overline{KG} . In addition, it seems that increasing \overline{KG} bends the roll-related branches towards the real axis. No instability is predicted, by the root locus plots, due to variation of \overline{KG} . However, the results presented in Figure 8.26 suggest otherwise.

The stability graphs for $\overline{KG} = 0.95m$ and $1.0m$ are presented in Figure 8.26. An unstable region between the Froude numbers of 0.8 and 1 is shown, which grows by reducing \overline{KG} . The linear extrapolation of values seems to create a smooth expansion of the unstable area outside the computational domain and towards

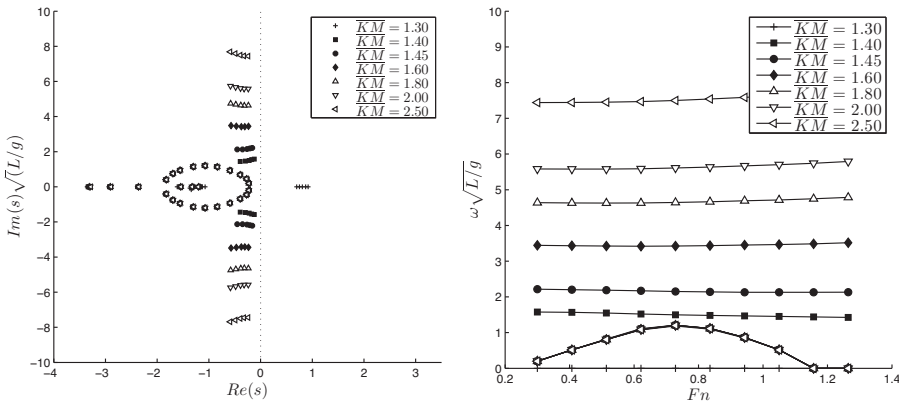


Figure 8.24: Influence of \overline{KM} on sway-roll-yaw dynamic stability. (Left): Root locus plot, s : root of the dynamic system's characteristic equation, (Right):Free-system's response frequencies.

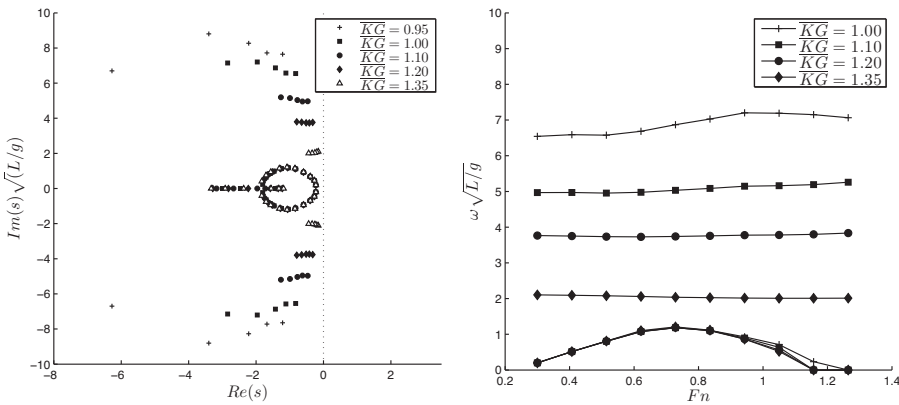


Figure 8.25: Influence of \overline{KG} on sway-roll-yaw dynamic stability. (Left): Root locus plot, s : root of the dynamic system's characteristic equation, (Right):Free-system's response frequencies.

the zero-frequency. Encountering instability by increasing \overline{GM} is strange, since based on the previous studies (e.g. Haarhoff and Sharma (2000) and Eda (1980)) increasing the metacentric height must lead to a more stable system. Looking at Figure 8.26, it seems that the vessel becomes stable again after Froude number of 1.0. This possible scenario has been mentioned before by Haarhoff and Sharma (2000).

Let us take a closer look at the unstable region using the stability graph and root locus plot presented in Figure 8.27. The stability graph is extended to higher frequencies in order to include the free-system's response frequencies in roll. No instability is predicted by the root locus plot. The instability belongs to a system

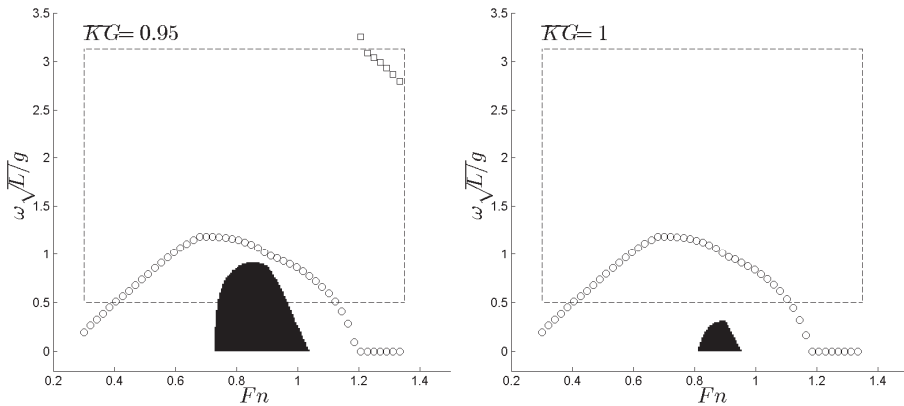


Figure 8.26: Stability graphs showing the influence of \overline{KG} on sway-roll-yaw dynamic stability. Black area: unstable, White area: stable, Dashed lines: computational domain, Circles: free-system's response frequency governed by the first root (sway-yaw), Squares: free-system's response frequency governed by the second root (roll).

constructed for a Froude number around 0.9 and an approximate non-dimensional Frequency below 0.5. However, the imaginary parts of the unstable roots have much higher frequencies. The narrow black area close to the roll-related frequencies in Figure 8.27, shows the frequency of the unstable roots. In other words, the unstable roots belong to a low frequency system, while their imaginary parts are close to the high roll-related frequencies. This suggests that the instability is introduced into the low-frequency sway-yaw due to the stiff dynamics of the system in roll. Therefore, it is possible that this instability represents a non-oscillatory instability in sway-roll, which is induced by an oscillatory motion in roll. In other words, this analysis suggests that increasing \overline{GM} by lowering the center of gravity can have adverse effects on dynamic stability, as well as too low \overline{GM} . However, it is not possible to conclude about the system's response in this condition. Further investigations using a time-domain analysis are required to confirm this observation, by considering the coupling between vessel's modes of motion.

In the experiments introduced in Section 8.2.1, a calm water broaching incident was reported at Froude number of 0.9. However, since exact vertical location of the center of gravity in the experiments is not known, it is not possible to make an exact comparison. The maximum stable Froude number predicted here is be lower than 0.9. However, the restriction in the yaw motion during the experiments maybe the reason why an instability has not been detected at lower Froude numbers. A new set of experiments is needed to clarify this matter. Although, no exact comparison is possible, capturing an instability using the present linear analysis with its simplified hydrodynamic model is promising.

Calm water broaching is the type of non-oscillatory instability which was reported for instance by Müller-Graf (1997) and Eda (1980) to occur at high Froude

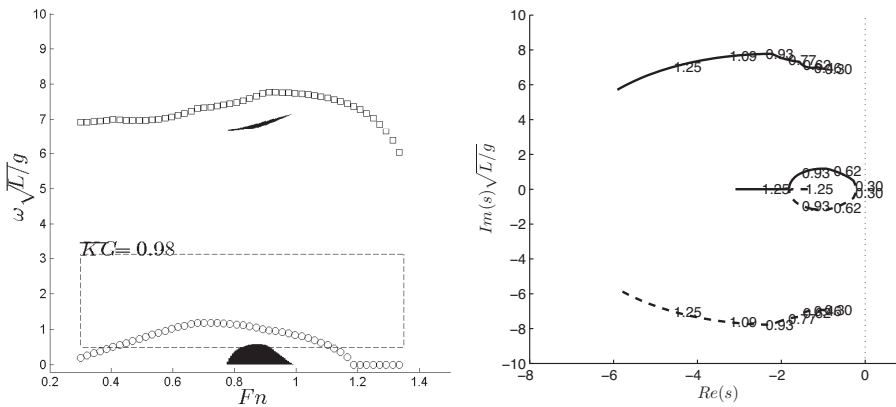


Figure 8.27: Influence of \overline{KG} on sway-roll-yaw dynamic stability. (Left): Stability graphs, Black area: unstable, White area: stable, Dashed lines: computational domain, Circles: free-system's response frequency governed by the first root (sway-yaw), Squares: free-system's response frequency governed by the second root (roll). (Right): Root locus plot, s : root of the dynamic system's characteristic equation, Froude numbers are shown on the branches.

number, due to low \overline{GM} . From the results presented in Figures 8.24 and 8.25, it seems that the expected coupling between the roll motion and the sway-yaw motion, which was mentioned by Eda (1980) and Haarhoff and Sharma (2000) for conventional vessels, can not be captured by this analysis. By taking a closer look at the values, it became clear that as soon as the system becomes statically unstable in roll, i.e. zero or negative \overline{GM} , the sway-roll-yaw stability analysis predicts instability for all the Froude numbers. However, as long as the system was statically stable in roll, reducing \overline{GM} was not changing the predicted instability. It must be noted that the instability scenario described for instance by Eda (1980) is started due to a large heel angle, which comes from a small restoring moment in roll. For high-speed vessels, the initial restoring moment can be reduced due to hydrodynamic pressure. This reduction comes from the change in the shape of the vessel's submerged volume due to trim and lift/sinkage. Then, the vessel's list angle must be increased in order to provide the system with enough roll restoring moment (see Werenskiold (1993)).

Eda (1980) mentioned the importance of the roll-induced yaw moment in roll-induced dynamic instability. Using a hull-form-camber-line method, he showed that the roll-induced yaw moment increases by increasing the roll angle. Although the linear hydrodynamic coupling terms of roll in yaw and sway were considered here, it seems that the problem must be solved by considering the changes in the hydrodynamic coefficients due to a constant heel angle. It has been observed, also during the investigations presented in Section 7.3, that for a semi-displacement vessel, the changes of the submerged volume due to heel angle are important in calculation of the hydrodynamic forces. However, the dependency of the hydrodynamic coefficients in sway and yaw, to the variations of the vessel's submerged

volume due to heeling, were neglected here. Moreover, the influence of trim and sinkage must not be forgotten. On the other hand, the simplified model of a flat plate can not be used to capture these couplings and a detailed representation of the vessel's surface is required. In addition, as Faltinsen (2005) mentions, when the ship speed increases, the importance of the hydrodynamic restoring coefficients will increase. In the present calculations, these coefficients are hidden in the relevant added mass terms. However, correct estimations of these values require solving the flow around the actual ship and not the simplified flat plate.

8.5 Conclusions

A simplified dynamic stability analysis of a monohull semi-displacement vessel was presented in this chapter. Both coupled sway-yaw and sway-roll-yaw equations of motions were considered. It was shown that the linear dynamic stability analysis, even by simplifying the vessel's hydrodynamics to a plate, can predict the existence of the dynamic instability similar to what has been observed in the experiments. However, an exact comparison was not possible due to lack of data. Improvements of the hydrodynamic modeling by considering the changes in the vessel's draft due to variation of keel-line, sinkage, and trim can be important. However, replacing the simplified model of a flat plate with the actual semi-displacement vessel needs further investigations. A series of attempts on this matter was presented in Chapter 7.

Sway-yaw dynamic stability analysis for the selected semi-displacement vessel did not predict an instability. An uncoupled sensitivity study was performed in order to investigate the dependency of the system's dynamic stability on different hydrodynamic coefficients. A series of stability graphs and root locus plots were presented. It was shown that the added mass and damping coefficients have important influence on the free-system's response frequencies. The influence of the longitudinal position of the center of gravity on dynamic stability was investigated. The present simplified analysis confirmed that moving the center of gravity towards bow improves the system's dynamic stability. Further sensitivity investigations by considering the couplings between the hydrodynamic coefficients were left for future work.

Sway-roll-yaw dynamic stability analysis of the assumed system showed no sign of instability either. Two sets of free-system's response frequencies were obtained, by independent iteration of the roots for sway-yaw and roll motion. Sensitivity study for the added mass and damping coefficients showed a complicated picture, especially for the cross-coupling damping terms. The influence of the longitudinal position of the center of gravity was shown to be similar to the one from sway-yaw analysis.

The sensitivity study on \overline{KM} showed that increasing \overline{KM} increases the free-system's response frequencies in roll. Moreover, increasing \overline{GM} by decreasing \overline{KG} creates an unstable region in the $Fn - \omega$ plane. The unstable roots belonged to a system with low frequency, however, their imaginary parts were close to the free-system's response frequencies in roll, which were much higher. This suggested a

possible low-frequency or non-oscillatory instability in sway-yaw, which was induced by a motion in roll of a stiff system. This was not expected, since the loss of steady restoring moment in roll was believed to be the main reason behind the instability problem. Further systematic investigations on the properties of the equation system's roots are required to confirm the validity of these observations. Moreover, the coupling between the two free-system's response frequencies must be investigated by means of convolution methods in the time-domain. In addition, the coupling between the hydrodynamic coefficients must be considered for a practical sensitivity analysis, as well as, a complete representation of the vessel's submerged volume including the vessel's sinkage, trim, and heel angle.

Chapter 9

Summary and Future Works

Sea-keeping -in particular dynamic stability- is an important issue in the design and operation of high-speed vessels. Among other types of instabilities, monohull semi-displacement vessels can suffer from a non-oscillatory dynamic instability in sway, roll, and yaw known as calm water broaching. This type of instability is characterized by a large roll and yaw angles, which may lead to capsizing. According to Müller-Graf (1997), this type of instability may be initiated by a change in the roll or yaw angle. If the instability is initiated by the roll angle, it is associated with the loss of static restoring moment in roll due to hydrodynamic effects, as reported by Eda (1980) and discussed by Haarhoff and Sharma (2000). Predicting this type of instability was a goal of the present study.

9.1 Summary and conclusions

The linear dynamic stability of coupled equations in sway-yaw and sway-roll-yaw was chosen for investigating the calm water broaching instability of monohull semi-displacement vessels at high forward speed. The hydrodynamics of semi-displacement vessels had to be solved first in order to obtain the required hydrodynamic coefficients for establishing the dynamic model.

Mathematical Formulation

Linear potential theory was used for calculating the hydrodynamic coefficients. A linearized mathematical representation of the potential-flow problem about mean forward speed was presented in the seakeeping coordinate system. The body and free-surface boundary conditions were linearized about the mean free-surface and body position. Linearized equations of motion for the vessel in six degrees of freedom were presented. Hydrodynamic forces were calculated by pressure integration, and the force was presented in terms of linearized added mass and damping coefficients. Selected viscous effects were included in the potential-flow calculations indirectly when their roles were significant. The numerical calculations are based on the boundary integral method.

Numerical Implementation

A three-dimensional potential flow solver based on the Rankine panel method was developed for solving steady-state and time-varying problems. Different discretization methods, such as constant and Lagrangian shape functions, were implemented. A newly-developed computer program made the solution of the discretized boundary integral formulations possible in an abstract form, independent of the discretization scheme. In this way, potential flow problems with different boundary integral formulations could be implemented easily. Moreover, different discretization schemes could be used alternatively in solving a problem, which made the comparison of different methods practical.

Methods for satisfying the radiation boundary condition and handling the free-surface truncation were presented. It was argued that, for higher forward speeds, the problem could be viewed as a hyperbolic problem with elliptic dependency. Therefore, the direction of differentiation had to be in agreement with the direction of the physical data flow. Upstream differentiation was considered as a method which can be helpful in obtaining physical and stable results by satisfying this condition. Damping zones were used to absorb the waves generated by the vessel's oscillations at lower Froude numbers. Numerical grid generation methods for controlling the grid point distribution and the discretization of the boundary surfaces were presented. It was discussed that the elements' shapes and the density of the collocation points are important in obtaining a reliable and efficient solution.

Evaluation of Discretization Methods

The numerical properties of different discretization methods were systematically investigated using semi-discrete Fourier analysis. Propagation of a wave on a discretized surface with uniform elements was studied. The numerical dispersion and damping of different numerical schemes were discussed by comparing the continuous and discrete forms of dispersion relation. Problems with and without forward speed were considered. The combinations of discrete-space continuous-time, continuous-space discrete-time, and discrete-time and space were considered in order to investigate the influence of each discretization separately. It was shown that different numerical and differentiation schemes may be suitable for different problems. Moreover, the presence and magnitude of the forward speed was important for choosing the correct numerical scheme. In addition, the nature of the numerical instabilities in boundary integral methods was to some degree governed by the forward speed. The present numerical scheme was investigated using the aforementioned method, and estimates of expected damping and dispersion errors are obtained.

Non-separated Flows

The problem of a heaving semi-submerged sphere was solved in time-domain by means of linear theory. Infinite water depth was assumed. The values of heave added mass and damping were obtained by Fourier transform of the time-domain results for different frequencies and compared to the semi-analytical results by

Hulme (1982). A damping zone was introduced around the circular free-surface domain in order to absorb the generated waves. The agreement of the results was satisfactory. Then, the diffraction problem of a vertical circular cylinder in waves was solved using the time-domain solver. The damping zone and circular free-surface domain were adopted. The results for diffraction potential and free-surface elevation gave satisfactory agreement with the analytical method by Havelock (1940).

The velocity potential induced by a Kelvin source traveling under the free-surface was solved using the steady-state solver and compared with the existing analytical results. Additionally, the computed free-surface elevation around an advancing Wigley hull was compared to existing numerical and experimental data. Forced heave oscillations of an advancing Wigley hull and Series-60 vessel were solved in the time domain. The results were compared with existing numerical and experimental data in terms of heave added mass and damping. The performance and accuracy of the present numerical scheme was then established to be satisfactory, within the limitations of a linearized formulation.

Tail-separated Flows

The trailing edge flow separation was included using a linearized vortex sheet. The flow around a high aspect ratio foil in infinite fluid was solved. The Kutta condition was satisfied at the trailing edge using the method presented by Faltinsen and Pettersen (1983) and later used by Kristiansen (2009). The pressure coefficient around the mid-section was compared to experimental values for a 2D foil. Although linear pressure was used for satisfying the Kutta condition, the second order pressure terms played an important role, especially around the leading edge.

The steady problem of an advancing surface-piercing flat plate with a small drift angle was studied next. The Kutta condition at the plate's trailing edge was satisfied using a linearized vortex sheet. The inconsistency between the linearized free-surface boundary condition and the Kutta condition at the intersection of the free-surface and the plate's trailing edge was addressed. The hydrodynamic transverse force and yaw moment were calculated and compared with existing numerical and experimental data. The difference between the experimental data and the present computations was associated with the cross-flow separation. The wave-making and viscous forces in the transverse direction were separated, in analogy to the Froude hypothesis. A 2D+t cross-flow drag model was used to calculate the transverse force due to bottom-tip flow separation. The free-surface boundary condition was simplified by using a rigid wall condition in the 2D+t method, i.e. the cross-flow vortex and free-surface wave interactions were neglected. A constant increase in the non-dimensional transverse force was obtained using this method. Comparisons suggested that the present assumptions yield good agreement with the experimental data up to a relatively high Froude number ($Fn = 1$). Moreover, the influence of cross-flow drag on yaw moment was shown to be negligible. The influence of plate thickness, taper angle, and draft were studied. In addition, the importance of non-linearities was investigated by comparing the first and second order transverse force and yaw moment.

Next, the unsteady problem of a swaying and yawing surface-piercing flat plate in forward motion was considered. The time-varying vortices generated at the plate's tail were propagating along a linearized vortex sheet. The hydrodynamic forces and coefficients were calculated and compared with existing numerical and experimental data. The dependence of the coefficients on Froude number and oscillation frequency were investigated. It was confirmed that the coefficients are frequency dependent for lower Froude numbers, and independent of frequency for higher speeds. The cross-flow drag seemed to be important, especially at the lower frequencies and Froude numbers, while its relative importance decreases at higher frequencies and Froude numbers. The present results were in acceptable agreement with experimental data. The present 3D results with vortex sheet were also in good agreement with Chapman (1975) calculations using a 2D+t method. The downstream flow does not have any effect on the upstream solution in the 2D+t method, while the correct propagation of the generated vortices to the downstream was essential for an acceptable solution in the present 3D method.

Hydrodynamics of Semi-displacement Vessels

The flow behind the dry transom stern of a semi-displacement vessel was solved using a hollow-body model. The two-dimensional semi-analytical solution by Faltinsen (2005) for the flow in the vicinity of a dry transom stern was combined with numerical grid generation methods and developed for three-dimensional flows. An iterative scheme was used to minimize the pressure and capture the free surface behind the dry transom stern. The model was validated by solving for the steady forward motion of a semi-displacement vessel and comparing the free-surface elevation and distribution of the vertical force along the vessel. It was shown that the present model can capture the drop in the steady vertical force at the transom stern due to atmospheric pressure. This was not possible in the previous studies based on the 2D+t method due to the nature of the numerical scheme.

The forces on a semi-displacement vessel with fixed drift angle on a straight course were considered. The hollow-body model was further developed to capture the asymmetric free-surface shape behind the dry transom stern of a monohull semi-displacement vessel with fixed drift angle. The vessel's heel, trim, and sinkage were included in the calculations from the experimental data. A sensitivity study was performed on the transom stern hollow iteration parameter as well as measured heel, trim, and sinkage. Varying trim, heel, and sinkage of the vessel, considering the order of magnitude of the measurements' accuracy, had no significant influence on the resulting force and yaw moment. The same conclusion was drawn for the hollow iteration parameter. Corrections due to viscous effects are added to the transverse force using a 2D+t cross-flow drag model. The ship hull was simplified to have circular cross-sections. A rigid free-surface condition was assumed. The cross-flow separation captured by this simplified model was shown to be able to explain the difference between experimental and numerical data. However, capturing the correct yaw moment turned out to be difficult. A more detailed cross-flow model, including the actual form of the ship sections, was needed to improve the estimations. Moreover, the cross-flow vortex and free-surface interactions, as well

as flow non-linearities, may matter at higher Froude numbers and drift angles.

Heave oscillations of a monohull semi-displacement vessel with high forward speed was solved in the time domain. The hollow-body model was used to satisfy the free-surface boundary condition behind the transom stern. The unsteady flow was linearized around the obtained steady hollow surface. The boundary condition on the hollow surface was modified to allow the oscillatory flow to pass. The free-surface boundary condition for oscillatory flow was satisfied by means of an iterative scheme. The distribution of heave added mass and damping was calculated and compared to existing experimental and numerical data. The present 3D model was able to capture the sharp change in the values of these quantities close to the transom stern. Capturing this behavior at lower frequencies was, however, troublesome due to the increased unsteady variation of the hollow body's shape.

Dynamic Stability Analysis

A preliminary dynamic stability analysis for a monohull semi-displacement vessel in sway and yaw was presented. Hydrodynamics of the semi-displacement vessel were simplified to be similar to a flat plate. Then, the forces acting on a free-surface-piercing flat plate in forced sway, roll, and yaw oscillations were presented in terms of added mass and damping coefficients. Using these obtained coefficients, the coupled dynamic equations in sway and yaw were established for each frequency and Froude number pair. The roots of the free dynamic system were then studied in order to investigate the vessel's dynamic stability.

A narrow monohull semi-displacement vessel with reported dynamic instability issues in sway-roll-yaw was chosen for validation. It was shown that the simplified sway-yaw analysis did not predict a dynamic instability. On the other hand, the sway-roll-yaw analysis predicted a dynamic instability in the vicinity of the Froude number where the instability has been observed in the experiments. It was shown that the unstable roots belonged to a system with low frequency, while their imaginary parts were close to the free-system's frequencies in roll, which were much higher. This suggested a possible low-frequency or non-oscillatory instability in sway-yaw, which was induced by the roll motion of a stiff system. However, based on the presented linear analysis in the frequency domain, it was not possible to conclude about the behavior of the system. Moreover, the exact vertical location of the center of gravity (\overline{KG}) in experiments was needed to confirm this observation.

In the experiments, no instability was reported at $Fn = 0.8$, while the analysis suggested that the vessel may become unstable even at lower Froude numbers depending on \overline{KG} . The delay in the onset of instability might be associated with the slight yaw restraints in the experiments. Independent sensitivity analysis showed that the instability and the free-system's response frequencies were sensitive to the added mass and damping coefficients. The cross-coupling damping terms in sway-roll and sway-yaw were particularly important in sway-roll-yaw analysis. Varying the longitudinal position of the center of gravity confirmed that moving the center of gravity towards the bow improves the vessel's dynamic stability. The sensitivity study on \overline{KM} did not suggest that the dynamic instability in sway-yaw was sensitive to the value of \overline{GM} as long as it was positive; this result might be due to

the simplification in hydrodynamics from a semi-displacement vessel to a flat plate. The dependence of the sway and yaw hydrodynamic coefficients on the quasi-steady heel angle was needed for more investigations.

9.2 Suggestions for future works

The present studies can be pursued further in many different areas; several are presented here.

- The semi-discrete Fourier analysis can be developed further in order to include non-uniform grids. This is important in investigating the influence of grid non-uniformities on the numerical properties of a discretization method. Moreover, the influence of an external forcing function such as a surface-piercing body can be studied. Further numerical simulations for validating the findings of the Fourier analysis would be interesting.
- Higher-order boundary conditions can be implemented using the current numerical tool. In particular, a fully non-linear steady problem and linearization of the unsteady flow around the non-linear steady flow can be pursued.
- The transient drag coefficient on a plate in start-up flow with and without free surface needs further study using a 2D time-domain Navier-Stokes solver. The findings of such a study can be combined with the present 3D potential flow solution to obtain better cross-flow drag estimations using a 2D+t cross-flow model.
- The bottom-tip flow separation can be included using a linearized horizontal vortex sheet in both the steady and unsteady problems.
- The 2D+t cross-flow calculations for a semi-displacement vessel can be further developed using a 2D time-domain Navier-Stokes solver. In this way, the exact shape and transient change of ship sections can be taken into consideration.
- An iterative body-dynamic solver can be added to the program in order to find the equilibrium position of the vessel based on the calculated hydrodynamic forces.
- The development of the hollow-body model for capturing the dry transom stern effects must be pursued further in order to include sway and yaw oscillations. An experimental investigation of the sway and yaw added mass and damping of a semi-displacement vessel with forward speed can be very valuable in this regard.
- The coupling between quasi-steady heel angle and hydrodynamic forces in sway and yaw must be investigated in order to obtain a better model for the roll-induced dynamic instability. The actual shape of the vessel may be an important factor to take into account.

-
- A more detailed sensitivity study considering the couplings between vessel geometry and hydrodynamic coefficients can be pursued. One could examine the dependence of hydrodynamic coefficients on changes in the vessel's geometrical parameters, how these changes can be realized in practice, and the consequences of them.
 - Further improvements of a vessel's dynamic stability using stabilizers or control of steering units can be suggested for further investigations. A maneuvering and control model can be added to the dynamic system in order to assess the dynamic stability properties of a more realistic model. Moreover, one could make an attempt to identify the destabilization process.

Bibliography

- Alexandrescu, A. (2001), *Modern C++ Design: Generic Programming and Design Patterns Applied*, 1 edn, Addison Wesley.
- Alnaes, M., Logg, A., Mardal, K.-A., Skavhaug, O. and Langtangen, H. (2009), “Unified framework for finite element assembly”, *International Journal of Computational Science and Engineering*, Vol. 4, pp. 231 – 244.
- Baba, E., Asai, S. and Toki, N. (1982), A simulation study on swa-roll-yaw coupled instability of semi-displacement type high speed craft, in ‘Proceedings of the second international Conference on Stability of Ships and Ocean Vehicles’, Tokyo, Japan.
- Bassetti, F., Davis, K. and Quinlan, D. (1998), C++ expression template performance issues in scientific computing, in ‘Parallel Processing Symposium, 1998’, pp. 635 –639.
- Beck, R., Cao, Y. and Lee, T. (1993), Fully nonlinear water wave computations using the desingularized method, in ‘Proceedings of the Sixth International Conference on Numerical Ship Hydrodynamics’, pp. 3–20.
- Büchmann, B. (2000), “Accuracy and stability of a set of free-surface time-domain boundary element models based on b-splines”, *International Journal for Numerical Methods in Fluids*, Vol. 33 of *Int. J. Numer. Methods Fluids (UK)*, pp. 125–55.
- Büchmann, B. (2001), “Theory and applications in stability of free-surface time-domain boundary element models”, *International Journal for Numerical Methods in Fluids*, Vol. 37, pp. 321–339.
- Bunnik, T. (1999), Seakeeping Calculations for Ships, taking into Account the Non-linear Steady Waves, PhD thesis, Delft University of Technology.
- Cao, Y., Schultz, W. and Beck, R. (1991), “Three-dimensional desingularized boundary integral methods for potential problems”, *International Journal for Numerical Methods in Fluids*, Vol. 12 of *Int. J. Numer. Methods Fluids (UK)*, pp. 785–803.
- Chapman, R. (1975), Numerical solution for hydrodynamic forces on a surface-piercing plate oscillating in yaw and sway, in ‘Proc. 1st International Conference on Numerical Ship hydrodynamics’, Bethesda, MD, USA, pp. 330–350.
- Chapman, R. B. (1976), “Free-surface effects for yawed surface-piercing plates”, *Journal of Ship Research*, Vol. 20.
- Cohen, S. and Blount, D. (1986), “Research plan for the investigation of dynamic instability of small high-speed craft”, Vol. 94, pp. 197–214.
- Cox, M. G. (1972), “The numerical evaluation of B-Splines”, *IMA Journal of Applied Mathematics*, Vol. 10, pp. 134–149.

- Dawson, C. (1977), A practical computer method for solving ship wave problems, in 'Proceedings of the 2nd International Conference on Numerical Ship Hydromechanics', Berkely, USA., pp. 30–38.
- de Boor, C. (1972), "On calculating with b-splines", *Journal of Approximation Theory*, Vol. 6, pp. 50–62.
- de Jong, P. (2011), Seakeeping Behaviour of High Speed Ships: An Experimental and Numerical Study, PhD thesis, Delft University of Technology, Delft.
- Doctors, L. (2007), "A numerical study of the resistance of transom-stern monohulls", *Ship Technology Research*, Vol. 54 of *Ship Technol. Res. (Germany)*, pp. 134–44.
- Doctors, L. and Day, A. (2001), Steady-State hydrodynamics of High-Speed vessels with a transom stern, pp. 191–205.
- Dommermuth, D. G. and Yue, D. K. (1987), "Numerical simulations of nonlinear axisymmetric flows with a free surface", *Journal of Fluid Mechanics*, Vol. 178, pp. 195–219.
- Drazen, D. A., Fullerton, A. M., Fu, T. C., Beale, K. L., O'Shea, T. T., Brucker, K. A., Dommermuth, D. G., Wyatt, D. C., Bhushan, S., Carrica, P. M. and Stern, F. (2010), A comparison of model-scale experimental measurements and computational predictions for a large transom-stern wave, in '28th Symposium on Naval Hydrodynamics', Pasadena, CA, USA.
- Eatock Taylor, R. and Chau, F. (1992), "Wave diffraction theory - some developments in linear and nonlinear theory", *Journal of Offshore Mechanics and Arctic Engineering*, Vol. 114, pp. 185–194.
- Eda, H. (1980), Rolling and steering performance of high speed ships simulation studies of yaw-roll-rudder coupled instability, in '13th Symposium on Naval Hydrodynamics', Defense Technical Information Center, Tokyo, Japan.
- Fabbri, L., Di Memmo, A., Palini, M. and Lugni, C. (2009), Prova di manovrabilità su uno scafo semidislocante, Technical Report 2009-084rt, INSEAN, Rome, Italy.
- Faltinsen, O. (1977), Numerical solution of transient nonlinear free-surface motion outside or inside moving bodies, in 'Proceedings 2nd Int. Conf. on Num. Ship Hydrodynamics, UC Berkeley', pp. 257–266.
- Faltinsen, O. M. (1990), *Sea Loads on Ships and Offshore Structures*, Cambridge University Press.
- Faltinsen, O. M. (2005), *Hydrodynamics of High-Speed Marine Vehicles*, Cambridge University Press.
- Faltinsen, O. M. and Pettersen, B. (1983), Vortex shedding around two-dimensional bodies at high reynolds number., in '14th Symposium - Naval Hydrodynamics', Natl. Acad. Press, Ann Arbor, Mich, USA, pp. 1171–1213.
- Faltinsen, O. and Pettersen, B. (1987), "Application of a vortex tracking method to separated flow around marine structures", *Journal of Fluids and Structures*, Vol. 1, pp. 217–237.
- Faltinsen, O. and Zhao, R. (1991), "Numerical predictions of ship motions at high forward speed", *Philosophical Transactions: Physical Sciences and Engineering*, Vol. 334.
- Fink, P. and Soh, W. (1974), Calculation of vortex sheets in unsteady flow and applications in ship hydrodynamics, in 'Proceedings of the 10th symposium on Naval Hydrodynamics', Cambridge, Massachusetts,.
- Fossen, T. I. (1994), *Guidance and Control of Ocean Vehicles*, Wiley.
- Garme, K. (2005), "Improved time domain simulation of planing hulls in waves by correction of the near-transom lift", *International Shipbuilding Progress*, Vol. 52, pp. 201–230.

- Gerritsma, J. and Beukelman, W. (1965), The distribution of the hydrodynamic forces on a heaving and pitching shipmodel, with zero forward speed in still water,, Technical Report 22, Delft University of Technology, Ship Hydromechanics Laboratory.
- Gregory, N. and O'Reilly, C. L. (1973), Low-Speed aerodynamic characteristics of NACA 0012 aerofoil section, including the effects of Upper-Surface roughness simulating hoar frost, Technical Report 3726, Aerodynamics Division N.P.L., London.
- Haarhoff, S. and Sharma, S. D. (2000), A note on the influence of speed and metacentric height on the yaw-rate stability of displacement ships, in 'Proceedings of Intern. workshop on ship maneuvering at Hamburg ship model basin', Hamburg, Germany, October 10-11.
- Havelock, T. (1940), "The pressure of water waves upon a fixed obstacle", *Proceedings of the Royal Society of London, Series A (Mathematical and Physical Sciences)*, Vol. 175, pp. 409–421.
- Hayami, K. and Matsumoto, H. (1994), "A numerical quadrature for nearly singular boundary element integrals", *Engineering Analysis with Boundary Elements*, Vol. 13, pp. 143–154.
- Hess, J. L. (1979), A higher order panel method for three-dimensional potential flow, Technical Report MDC-J8519, Warminster, Penn.
- Hess, J. L. (1990), "Panel methods in computational fluid dynamics", *Annual Review of Fluid Mechanics*, Vol. 22, pp. 255–274.
- Hess, J. and Smith, A. (1967), Calculation of potential flow about arbitrary bodies, in 'Progress in Aeronautical Sciences', Vol. Vol. 8, pp. viii + 431 pp.
- Hsin, C., Kerwin, J. and Newman, J. (1993), A higher-order panel method based on b-splines, in 'Proceedings of the Sixth International Conference on Numerical Ship Hydrodynamics', Iowa, USA, pp. 133–151.
- Hughes, M. and Bertram, V. (1995), A higher-order panel method for 3-d free surface flows, Technical Report 558, Institut fur Schiffbau der Universitat Hamburg.
- Hulme, A. (1982), "The wave forces acting on a floating hemisphere undergoing forced periodic oscillations", *Journal of Fluid Mechanics Digital Archive*, Vol. 121, pp. 443–463.
- Israeli, M. and Orszag, S. A. (1981), "Approximation of radiation boundary conditions", *Journal of Computational Physics*, Vol. 41, pp. 115–135.
- Jensen, G., Mi, Z. and Söding, H. (1986), Rankine source methods for numerical solutions of the steady wave resistance problem, in 'Sixteenth Symposium on Naval Hydrodynamics: Ship Wakes; Large Amplitude Waves; Real Fluid Effects in Ship Hydrodynamics; Fluid-Structure Interaction; Frontier Problems in Hydrodynamics.', Natl Acad Press, Berkeley, CA, USA, pp. 575–582.
- Jensen, P. S. (1987), "On the numerical radiation condition in the steady-state ship wave problem", *Journal of ship research*, Vol. 31, pp. 14–22.
- Journée, J. (1992), Experiments and calculations on 4 wigley hull forms in head waves, Technical report, Delft University of Technology.
- June Bai, K. and McCarthy, J. H. (1979), *Proceedings on the workshop on Ship wave resistance computations*, David W. Taylor Naval Ship Research and Development Center, Bethesda Maryland, USA.
- Kashiwagi, M. (1983), "On the stability derivatives of high speed ships oscillating in low frequency", *J. of Kansai Soc. of Naval Arch.* .
- Kashiwagi, M. (1984), Study on Maneuvering Hydrodynamic Forces on a Ship Advancing in Following Seas, PhD thesis, Osaka University, Department of Naval Architecture and Ocean Engineering, Osaka, Japan.

- Keuning, J. (1988), Distribution of added mass and damping along the length of a ship moving at high forward speed, Technical Report No.817-P, Delft University of Technology, Ship Hydromechanics Laboratory, Delft.
- Keuning, J. A. and Pinkster, J. (1995), Optimisation of the seakeeping behaviour of a fast monohull, in 'Proceeding of the 3th International Conference on Fast Sea Transportation'.
- Keuning, J., Toxopeus, S. and Pinkster, J. (2001), The effect of bowshape on the seakeeping performance of a fast monohull, in 'Proceedings of the 6th International Conference on Fast Sea Transportation', pp. 197–212.
- Khalil, H. K. (2001), *Nonlinear Systems*, 3 edn, Prentice Hall.
- Kim, B. and Shin, Y. S. (2003), "A NURBS panel method for three-dimensional radiation and diffraction problems", *Journal of Ship Research*, Vol. 47, pp. 177–186.
- Kim, Y., Kring, D. and Sclavounos, P. (1997), "Linear and nonlinear interactions of surface waves with bodies by a three-dimensional rankine panel method", *Applied Ocean Research*, Vol. 19, pp. 235–249.
- Kim, Y., Yue, D. K. and Connell, B. S. (2005), "Numerical dispersion and damping on steady waves with forward speed", *Applied Ocean Research*, Vol. 27, pp. 107–125.
- King, B., Beck, R. and Magee, A. (1988), Seakeeping calculations with forward speed using time-domain analysis, in '17th Symposium on Naval Hydrodynamics', The Hague, Netherlands, pp. 577–596.
- Koumoutsakos, P. and Shiels, D. (1996), "Simulations of the viscous flow normal to an impulsively started and uniformly accelerated flat plate", *Journal of Fluid Mechanics*, Vol. 328, pp. 177–227.
- Kring, D. C. (1994), Time domain ship motions by a three-dimensional rankine panel method, PhD thesis, Massachusetts Institute of Technology, USA.
- Kristiansen, T. (2009), Two-dimensional numerical and experimental studies of piston-mode resonance, PhD thesis, Norwegian University of Science and Technology, Department of Marine Technology, Trondheim.
- Landrini, M. and Campana, E. (1996), "Steady waves and forces about a yawing flat plate", *Journal of Ship Research*, Vol. 40, pp. 179–192.
- Lavis, D. R. (1980), The development of stability standards for dynamically supported craft, a progress report., in 'In Proc. of the High Speed Surface Craft Exhibition and Conference', Kalerghi Publications, Brighton, Sussex, UK, pp. 384–94.
- Lee, C. and Newman, J. (1991), "First- and second-order wave effects on a submerged spheroid", *Journal of Ship Research*, Vol. 35, pp. 183 – 190.
- Lewandowski, E. M. (2003), *The Dynamics of Marine Craft: Maneuvering and Seakeeping*, 1st edn, World Scientific Pub Co Inc.
- Li, H., Han, G. and Mang, H. A. (1985), "A new method for evaluating singular integrals in stress analysis of solids by the direct boundary element method", *International Journal for Numerical Methods in Engineering*, Vol. 21, pp. 2071–2098.
- Liapis, S. and Beck, R. (1985), Seakeeping computations using time-domain analysis, National Academy of Sciences, pp. 34–56.
- Lighthill, M. (1960), "Studies on magneto-hydrodynamic waves and other anisotropic wave motions", *Royal Society – Philosophical Transactions Series A*, Vol. 252, pp. 397–430.

- Lin, W. M. and Yue, D. K. P. (1990), Numerical solutions for large-amplitude ship motions in the time domain, in 'Proceedings of the 18th Symposium on Naval Hydromechanics', Ann Arbor, Mich, USA, pp. 41–65.
- Liu, Y., Kim, C. and Lu, X. (1991), "Comparison of higher-order boundary element and constant panel methods for hydrodynamic loadings", *International Journal of Offshore and Polar Engineering*, Vol. 1, pp. 8–17.
- Liu, Y. and Lu, X.-s. (1988), "Polar coordinate transformation approach for treatment of singular integrals in boundary element methods", *Applied Mathematics and Mechanics*, Vol. 9, pp. 959–967.
- Longuet-Higgins, M. and Cokelet, E. (1976), "The deformation of steep surface waves on water. i. a numerical method of computation", *Proceedings of the Royal Society of London, Series A (Mathematical and Physical Sciences)*, Vol. 350 of *Proc. R. Soc. Lond. A, Math. Phys. Sci. (UK)*, pp. 1–26.
- Longuet-Higgins, M. and Cokelet, E. (1978), "The deformation of steep surface waves on water. II. growth of normal-mode instabilities", *Proceedings of the Royal Society of London, Series A (Mathematical and Physical Sciences)*, Vol. 364 of *Proc. R. Soc. Lond. A, Math. Phys. Sci. (UK)*, pp. 1–28.
- Lugni, C., Colagrossi, A., Landrini, M. and Faltinsen, O. (2004), Experimental and numerical study of semi-displacement mono-hull and catamaran in calm water and incident waves, in 'Proc. of 25th Symposium on Naval Hydrodynamics', Canada.
- MacCamy, R. and Fuchs, R. (1954), Wave force on a pile: A diffraction theory, Tech. Memo 69, US Army Corps of Engineers Beach Erosion Board, Washington DC.
- Maki, K. J., Doctors, L. J., Beck, R. F. and Troesch, A. W. (2005), Transom-stern flow for high-speed craft, in 'Eighth International Conference on Fast Sea Transportation', Saint Petersburg, Russia.
- Maniar, H. D. (1995), A three dimensional higher order panel method based on B-splines, Thesis, Massachusetts Institute of Technology, USA. Thesis (Ph. D.)—Massachusetts Institute of Technology, Dept. of Ocean Engineering, 1995.
- Maniar, H. D., Newman, J. N. and Xü, H. (1990), Free-Surface effects on a yawed Surface-Piercing plate, in 'Eighteenth Symposium on Naval Hydrodynamics', Ann Arbor, Mich.
- Mantic, V. (1993), "A new formula for the c-matrix in the somigliana identity", *Journal of Elasticity*, Vol. 33, pp. 191–201.
- Mei, C., Stiassnie, M. and Yue, D. K. P. (2005), *Theory and applications of ocean surface waves*, Vol. 23 of *Advanced series on ocean engineering*, expanded ed edn, World Scientific Publishing Company.
- Molland, A. F., Wellicome, J. F. and Couser, P. R. (1994), Resistance experiments on a systematic series of high speed displacement catamaran forms: variation of length-displacement ratio and breadth-draught ratio, Technical Report 71, University of Southampton.
- Morino, L. and Kao, C. (1974), "Subsonic potential aerodynamics for complex configurations: a general theory", *AIAA Journal*, Vol. 12 of *AIAA J. (USA)*, pp. 191–7.
- Müller-Graf, B. (1997), Dynamic stability of high speed small craft, in 'WEGEMT Association Twenty-Fifth School Craft Technology', Athens. Greece: Dept. of Nav. Arch, and Mar. Eng. National Technical University of Athens.
- Müller-Graf, B. and Schmiechen, M. (1982), On the stability of semidisplacement craft, in 'In Proc. of Second Intern. Conf. on Stability of Ships and Ocean Vehicles', Tokyo, Japan, pp. 67–76.

- Nakos, D. (1990), Ship wave patterns and motions by a three dimensional Rankine Panel Method, PhD thesis, Massachusetts Institute of Technology, USA.
- Nakos, D. E. and Sclavounos, P. D. (1990), "On steady and unsteady ship wave patterns", *Journal of Fluid Mechanics*, Vol. 215, p. 263.
- Nakos, D., Kring, D. and Sclavounos, P. (1993), Rankine panel methods for transient Free-Surface flows, in 'Proceedings of the Sixth International Conference on Numerical Ship Hydrodynamics', Iowa City, pp. 613–632.
- Nakos, D. and Sclavounos, P. (1994), "Kelvin wakes and wave resistance of cruiser- and transom-stern ships", *Journal of Ship Research*, Vol. 38, pp. 9–29.
- Newman, J. (1986), "Distributions of sources and normal dipoles over a quadrilateral panel", *Journal of Engineering Mathematics*, Vol. 20, pp. 113–126.
- Newman, J. (1987a), "Evaluation of the wave-resistance green function: part 1 - the double integral.", *Journal of Ship Research*, Vol. 31, pp. 79–90.
- Newman, J. (1987b), "Evaluation of the wave-resistance green function: part 2 - the single integral on the centerplane.", *Journal of Ship Research*, Vol. 31, pp. 145–150.
- Newman, J. N. (1977), *Marine Hydrodynamics*, Cambridge: The MIT Press.
- Newman, J. N. (1978), The theory of ship motions., in 'Advances in Applied Mechanics', Vol. 18, United States, p. 65p.
- Ogilvie, T. F. and Tuck, E. O. (1962), A rational strip theory of ship motions - part 1, Technical Report 013, Department of Naval Architecture and Marine Engineering, University of Michigan, USA.
- OpenFOAM* (n.d.).
URL: <http://www.openfoam.com/>
- Qiao, H. (2006), "Object-oriented programming for the boundary element method in two-dimensional heat transfer analysis", *Advances in Engineering Software*, Vol. 37, pp. 248–259.
- Raven, H. (1988), Variations on a theme by dawson, in 'Seventeenth Symposium on Naval Hydrodynamics', Hague, Netherlands.
- Raven, H. (1993), Nonlinear ship wave calculations using the RAPID method, in 'Proceedings of the Sixth International Conference on Numerical Ship Hydrodynamics', Iowa, USA, pp. 95–118.
- Raven, H. (1996), A solution method for the nonlinear ship wave resistance problem, PhD thesis, Delft University of Thechnology.
- Reed, A., Telste, J. and Scragg, C. (1991), Analysis of transom stern flows, in 'Proceedings of the Eighteenth Symposium on Naval Hydrodynamics', pp. 207–219.
- Rogers, D. F. and Adams, J. A. (1989), *Mathematical Elements for Computer Graphics*, 2 edn, McGraw-Hill Science/Engineering/Math.
- Romate, J. (1992), "Absorbing boundary conditions for free surface waves", *Journal of Computational Physics*, Vol. 99, pp. 135–145.
- Romate, J. E. (1989), The numerical simulation of nonlinear gravity waves in three dimensions using a higher order panel method, PhD thesis, Universiteit Twente, Enschede, Netherlands.
- Salvesen, N., Tuck, E. O. and Faltinsen, O. M. (1970), "Ship motions and sea loads", Vol. 78 of *Trans. SNAME*, pp. 250–78.

- Sarpkaya, T. (1966), "Separated flow about lifting bodies and impulsive flow about cylinders", *AIAA Journal*, Vol. 44, pp. 414–420.
- Saunders, H. E. (1957), *Hydrodynamics in Ship Design*, Vol. 2, Society of Naval Architects and Marine Engineers.
- Savitsky, D. (1988), Wake shapes behind planing hull forms, in 'Proceedings International High-Performance Vehicle Conference', Vol. VII, Springer-Verlag, Shanghai: The Chinese Society of Naval Architecture and Marine Engineering, pp. 1–15.
- Schoenberg, I. J. (1946), "Contributions to the problem of approximation of equidistant data by analytic functions", Vol. 4, pp. 45–99;112–141.
- Sclavounos, P. D. and Nakos, D. (1988), Stability analysis of panel methods for Free-Surface flows with forward speed., in 'Proceedings of the 17th symposium on Naval Hydrodynamics', Hague, Netherlands.
- Shao, Y. (2010), Numerical potential-flow studies on weakly-nonlinear wave-body interactions with/without small forward speeds, PhD thesis, Norwegian University of Science and Technology, Department of Marine Technology, Trondheim.
- Shao, Y. and Faltinsen, O. M. (2010), "Use of body-fixed coordinate system in analysis of weakly nonlinear wave-body problems", *Applied Ocean Research*, Vol. 32, pp. 20–33.
- Shao, Y.-L. and Faltinsen, O. (2012), "Linear seakeeping and added resistance analysis by means of body-fixed coordinate system", *Journal of Marine Science and Technology*, Springer Japan, pp. 1–18.
- Sierevogel, L. (1998), Time-domain calculations of ship motions, PhD thesis, Delft University of Technology.
- Skourup, J., Cheung, K. F., Bingham, H. B. and Büchmann, B. (2000), "Loads on a 3D body due to second-order waves and a current", *Ocean Engineering*, Vol. 27, pp. 707–727.
- Starke, B., Raven, H. and van der Ploeg, A. (2007), Computation of transom-stern flows using a steady free-surface fitting RANS method, in '9th International Conference on Numerical Ship Hydrodynamics', Ann Arbor, Michigan.
- Sun, H. (2007), A Boundary Element Method Applied to Strongly Nonlinear Wave-Body Interaction Problems, PhD thesis, Norwegian University of Science and Technology, Department of Marine Technology.
- Sun, H. and Faltinsen, O. (2010), Numerical study of a Semi-Displacement ship at High-Speed, in 'Proceedings of the 29th International Conference on Ocean, Offshore and Arctic Engineering', Shanghai, China.
- Sun, H. and Faltinsen, O. (2011), Hydrodynamic forces on high-speed ships in forced vertical motions, in 'Proceedings of the Eleventh International Conference on Fast Sea Transportation', Honolulu, Hawaii, USA.
- Sun, H. and Faltinsen, O. M. (2012), "Hydrodynamic forces on a semi-displacement ship at high speed", *Applied Ocean Research*, Vol. 34, pp. 68–77.
- Tanizawa, K. (2000), The state of the art on numerical wave tank, in '4th Osaka Colloquium on Seakeeping Performance of Ships', Osaka, Japan, pp. 95–114.
- Teng, B., Gou, Y. and Ning, D. (2006), "A higher order BEM for Wave-Current action on Structures-Direct computation of Free-Term coefficient and CPV integrals", Vol. 20, pp. 395–410.

- Thompson, J. F., Soni, B. K. and Weatherill, N. P. (1999), *Handbook of grid generation*, CRC Press.
- Timman, R. and Newman, J. N. (1962), "The coupled damping coefficients of a symmetric ship", *Journal of Ship Research*, Vol. 5, pp. 1–7.
- Tønnessen, R. (1999), A finite element method applied to unsteady viscous flow around 2D blunt bodies with sharp corners, PhD thesis, Norwegian University of Science and Technology, Department of Marine Technology, Trondheim.
- Vada, T. and Nakos, D. E. (1993), Time-marching schemes for ship motion simulations, in 'Int. Workshop on Water Waves and Floating Bodies', St John's, Newfoundland, Canada.
- van den Brug, J. B., Beukelman, w. and Prins, G. J. (1971), Hydrodynamic forces on a surface piercing flat plate, Technical Report 325, Delft University of Technology, Ship Building Laboratory.
- van Walree, F. (2002), Development, validation and application of a time domain seakeeping method for high speed craft with a ride control system, in 'Proceedings of the 24th Symposium on Naval Hydrodynamics', Fukuoka, Japan, pp. 475–490.
- Veldhuizen, T. (1995), "Expression templates", *C++ Report*, Vol. 7, pp. 26–31.
- Veldhuizen, T. (2006), 'Blitz++ manual'.
- Veldhuizen, T. and Jernigan, M. (1997), Will c++ be faster than fortran?, in Y. Ishikawa, R. Oldenhoeft, J. Reynders and M. Tholburn, eds, 'Scientific Computing in Object-Oriented Parallel Environments', Vol. 1343 of *Lecture Notes in Computer Science*, Springer Berlin / Heidelberg, pp. 49–56.
- Vugts, J. (1970), The hydrodynamic forces and ship motions in waves., PhD thesis, Uitgeverij Waltman, Delft.
- Wehausen, J. V. and Laitone, E. V. (1960), *Surface Waves*, Vol. IX of *Encyclopaedia of Physics*, Springer.
- Werenskiold, P. (1993), Methods for regulatory and design assessment of planning craft dynamic stability, in 'FAST93', Vol. 1, The Society of Naval Architects of Japan, Tokyo, Japan, pp. 883–94.
- Wong, H. L. and Calisal, S. M. (1996), "Numerical algorithms for slender bodies with vortex shedding and density stratification", *Journal of ship research*, Vol. 40, pp. 11–21.
- Wyatt, D., Fu, T., Taylor, G., Terrill, E., Xing, T., Bhushan, S., O'Shea, T. and Dommermuth, D. (2008), A comparison of full-scale experimental measurements and computational predictions of the transom-stern wave of the R/V/ Athena I, in 'Twenty-Seventh Symposium on Naval Hydrodynamics', Seoul, Korea, pp. 5–10.
- Xü, H. (1991), "Potential flow solution for a yawed surface-piercing plate", *Journal of Fluid Mechanics*, Vol. 226 of *Journal of Fluid Mechanics*, pp. 291–317.
- Xü, H. (1992), Numerical study of fully nonlinear water waves in three dimensions, Thesis. Thesis (Sc. D.), Massachusetts Institute of Technology, Dept. of Ocean Engineering.
- Yang, D. (2000), *C++ and Object Oriented Numeric Computing for Scientists and Engineers*, Springer-Verlag New York Inc.
- Zhao, R. and Faltinsen, O. (1989), A discussion of the m-terms in the wave-body interaction problem., in 'Int. Workshop on Water Waves and Floating Bodies', Oystese, Norway.

- Zhao, R. and Faltinsen, O. (1990), Interaction between current, waves and marine structures, *in* 'The proceedings: Fifth International Conference on Numerical Ship Hydrodynamics', Hiroshima, Japan.
- Zhu, W. and Faltinsen, O. M. (2007), Towards numerical dynamic stability predictions of Semi-Displacement vessels, *in* 'Proceedings of the Ninth International Conference on Fast Sea Transportation', Shanghai, China.
- Zienkiewicz, O. C., Taylor, R. L. and Zhu, J. (2005), *The Finite Element Method: Its Basis and Fundamentals, Sixth Edition*, 6 edn, Butterworth-Heinemann.

Appendices

Appendix A

Lagrangian polynomials and shape functions

A.1 4-points linear elements

$$\mathcal{N}_j(\xi, \eta) = \frac{1}{4}(1 + \xi_j \xi)(1 + \eta_j \eta) \quad (\text{A.1})$$

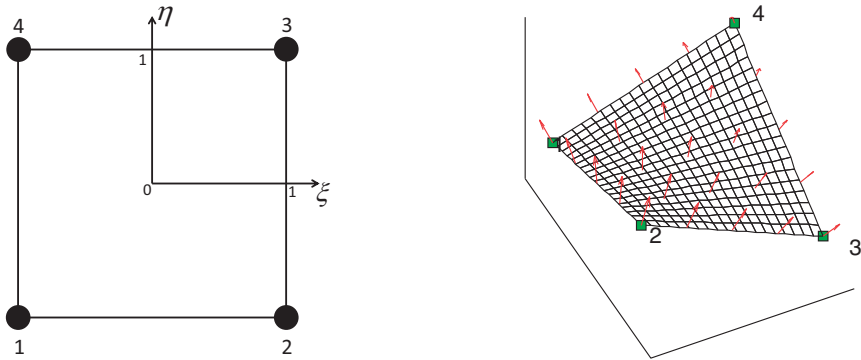


Figure A.1: 4-points linear panel

A.2 8-points quadratic elements

$$\begin{aligned} \mathcal{N}_j(\xi, \eta) &= \frac{1}{4}(1 + \xi_j \xi)(1 + \eta_j \eta)(-1 + \xi_j \xi + \eta_j \eta) && \text{for } j = 1, 3, 5, 7 \\ \mathcal{N}_j(\xi, \eta) &= \frac{1}{2}(1 + \xi_j \xi + \eta_j \eta)(1 - \xi_j^2 \eta^2 - \eta_j^2 \xi^2) && \text{for } j = 2, 4, 6, 8 \end{aligned} \quad (\text{A.2})$$

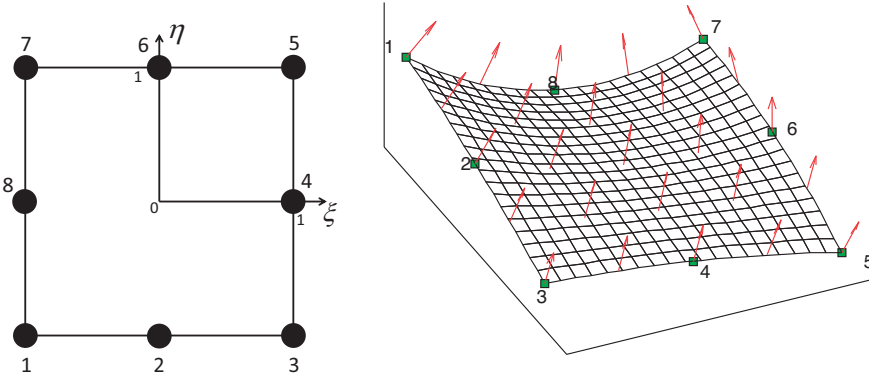


Figure A.2: 8-points quadratic panel

A.3 9-points quadratic elements

$$\begin{aligned}
 \mathcal{N}_j(\xi, \eta) &= \frac{1}{4}(\xi + \xi_j)(\eta + \eta_j)\xi\eta && \text{for } j = 1, 3, 5, 7 \\
 \mathcal{N}_j(\xi, \eta) &= \frac{1}{2} (1 - \xi_j^2\eta^2 - \eta_j^2\xi^2) && \\
 &(\eta_j\eta(1 + \eta_j\eta) + \xi_j\xi(1 + \xi_j\xi)) && \text{for } j = 2, 4, 6, 8 \\
 \mathcal{N}_j(\xi, \eta) &= (1 - \xi^2) (1 - \eta^2) && \text{for } j = 9
 \end{aligned}
 \tag{A.3}$$

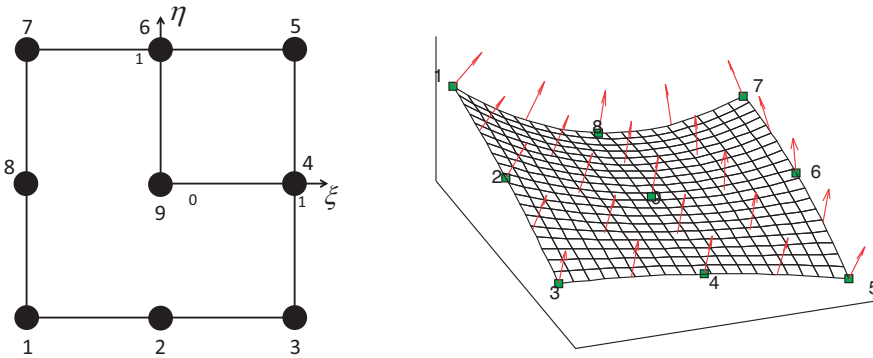


Figure A.3: 9-points quadratic panel

A.4 12-points cubic elements

$$\begin{aligned}
 \mathcal{N}_j(\xi, \eta) &= \frac{1}{32}(1 + \xi_j\xi)(1 + \eta_j\eta) (9(\xi^2 + \eta^2) - 10) && \text{for } j = 1, 4, 7, 10 \\
 \mathcal{N}_j(\xi, \eta) &= \frac{9}{32}(1 + \eta_j\eta)(1 - \xi^2) \cdot (1 + 9\xi_j\xi) && \text{for } j = 2, 3, 8, 9 \\
 \mathcal{N}_j(\xi, \eta) &= \frac{9}{32}(1 + \xi_j\xi)(1 - \eta^2)(1 + 9\eta_j\eta) && \text{for } j = 5, 6, 11, 12
 \end{aligned}
 \tag{A.4}$$

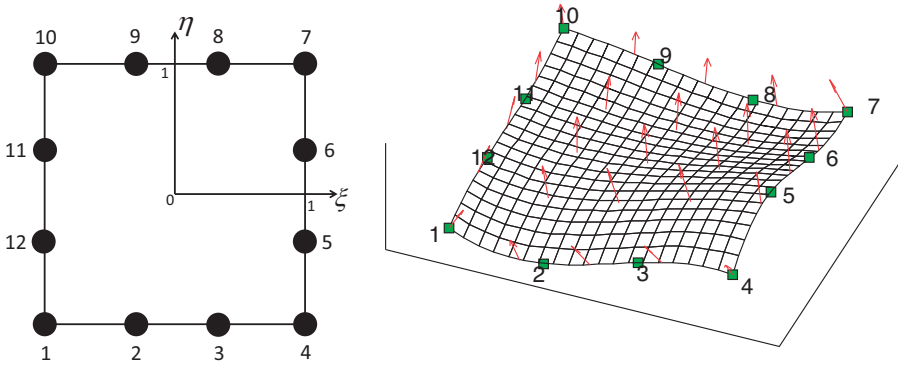


Figure A.4: 12-points cubic panel

Appendix B

Fourier transformations

In this appendix the definitions and mathematical formulations needed for the analysis in Chapter 4 are presented.

B.1 Analytical solution for propagating waves in 3D

The velocity potential for a linear propagating wave in three-dimensional space and in deep water can be presented as shown in Eq. (B.1) below.

$$\phi = \frac{g\zeta_a}{\omega} e^{|k|z} e^{-i(\omega t - kx \cos \theta - ky \sin \theta)} \quad (\text{B.1})$$

Here ζ_a is the wave amplitude, ω is the wave frequency and k is the wave number defined as $k = \frac{2\pi}{\lambda}$, where λ is the wave length. If a propagating wave in arbitrary direction on free surface is assumed, two wave numbers in x and y directions can be defined. Let us choose θ to be the direction of wave propagation. Then the components of wave number in x and y can be obtained as $u = k \cos \theta$ and $v = k \sin \theta$ respectively. By substituting the velocity potential from Eq. (B.1) in Neumann-Kelvin free-surface boundary condition Eq. (2.33) the so-called *dispersion relation* is obtained.

$$g|k| - \omega^2 + 2U\omega k \cos \theta - U^2 k^2 \cos^2 \theta = 0 \quad (\text{B.2})$$

Here U can be seen as a current in Earth-fixed or a forward velocity of a ship in sea-keeping coordinate system. The roots of Eq. (B.2) represent the possible existing waves on the surface. The analytical solutions for Eq. (B.2) for $k > 0$, i.e. downstream waves is,

$$k = \frac{g}{2U^2 \cos^2 \theta} \left(1 + 2\tau \cos \theta \pm \sqrt{1 + 4\tau \cos \theta} \right) \quad (\text{B.3})$$

and for $k < 0$, i.e. upstream waves,

$$k = \frac{g}{2U^2 \cos^2 \theta} \left(-1 + 2\tau \cos \theta \pm \sqrt{1 - 4\tau \cos \theta} \right) \quad (\text{B.4})$$

where $\tau = U\omega/g$. From Eq. (B.4) one can conclude that upstream waves only exist when $\tau < 1/(4\cos\theta)$. In absence of forward speed or current the dispersion relation simplifies to Eq. (B.5) below.

$$g|k| - \omega^2 = 0 \quad (\text{B.5})$$

For the waves generated by a moving disturbance with oscillations the dispersion relation becomes,

$$g|k| - U^2k^2 \cos^2\theta = 0 \quad (\text{B.6})$$

The roots of dispersion relation in this case are,

$$|k| = \frac{g}{U^2 \cos^2\theta} \quad (\text{B.7})$$

Although the mathematical solution gives positive and negative wave numbers (i.e. down- and upstream waves) in reality only downstream waves can exist. This is known as radiation condition which must be added to the problem in order to get the physical solution.

B.2 Fourier analysis

A summary of the tools needed for Fourier analysis is presented here.

B.2.1 Continuous Fourier transform

Continuous Fourier transform and its inverse is presented in Eqs. (B.8) and (B.9) respectively.

$$\tilde{\phi}(k, \theta, \omega) = \mathcal{F}[\phi] = \int_{-\infty}^{\infty} \int_{-\infty}^{\infty} \int_{-\infty}^{\infty} \phi(x, y, t) e^{-i(\omega t - kx \cos\theta - ky \sin\theta)} dx dy dt \quad (\text{B.8})$$

$$\phi(x, y, t) = \mathcal{F}^{-1}[\tilde{\phi}] = \frac{1}{8\pi^3} \int_{-\infty}^{\infty} \int_{-\pi}^{\pi} \int_0^{\infty} \tilde{\phi}(k, \theta, \omega) e^{i(\omega t - kx \cos\theta - ky \sin\theta)} k dk d\theta d\omega \quad (\text{B.9})$$

B.2.2 Semi-discrete Fourier transform

Fourier transform on discrete flat surface extended to infinity and time is presented in Eq. (B.10).

$$\hat{\phi}(k, \theta, \omega) = \hat{\mathcal{F}}[\phi] = \Delta x \Delta y \Delta t \sum_{I=-\infty}^{\infty} \sum_{J=-\infty}^{\infty} \sum_{K=-\infty}^{\infty} \phi(I\Delta x, J\Delta y, K\Delta t) e^{-i(\omega K\Delta t - kI\Delta x \cos\theta - kJ\Delta y \sin\theta)} \quad (\text{B.10})$$

Here Δx and Δy are the element's span in x and y directions. Δt is time-step. I, J, K are the indices of summation.

B.2.3 Convolution theorem

Two-dimensional continuous convolution between two functions f and g defined on a flat surface in xy -plane extending to infinity defined as shown in Eq. (B.11) below.

$$(f * g)(\mathbf{x}) = \iint_{-\infty}^{+\infty} f(\boldsymbol{\xi})g(\mathbf{x} - \boldsymbol{\xi}) d\xi d\eta \quad (\text{B.11})$$

Here $\boldsymbol{\xi}$ is the integral dummy variable. The discrete convolution is,

$$(f \otimes g)(\mathbf{x}_i) = \Delta x \Delta y \sum_{j=-\infty}^{\infty} f(\mathbf{x}_j)g(\mathbf{x}_i - \mathbf{x}_j) \quad (\text{B.12})$$

Convolution theorem states,

$$\tilde{\mathcal{F}}[(f * g)(\mathbf{x})] = \tilde{f}(u, v)\tilde{g}(u, v) \quad (\text{B.13})$$

$$\hat{\mathcal{F}}[(f \otimes g)(\mathbf{x}_i)] = \hat{f}(u, v)\hat{g}(u, v) \quad (\text{B.14})$$

B.2.4 Aliasing theorem

$$\hat{f}(u, v) = \sum_{K, L=-\infty}^{\infty} \tilde{f}\left(u + \frac{2\pi K}{\Delta x}, v + \frac{2\pi L}{\Delta y}\right) \quad (\text{B.15})$$

\hat{f} approaches \tilde{f} when $\Delta x, \Delta y \rightarrow 0$.

B.2.5 Fourier transform of the Rankine source function

The Rankine source function which used as the Green function in this analysis is,

$$G(\mathbf{x}, \boldsymbol{\xi}) = \frac{1}{\sqrt{(x - \xi)^2 + (y - \eta)^2 + (z - \zeta)^2}} \quad (\text{B.16})$$

It is possible to write the above function as a function of the distance between the two inputs as shown in Eq. (B.17). This form can be used to rewrite equations in convolution form as will be shown later.

$$G(\mathbf{x}, \boldsymbol{\xi}) = \mathcal{G}(\mathbf{x} - \boldsymbol{\xi}) = \frac{1}{|\mathbf{x} - \boldsymbol{\xi}|} \quad (\text{B.17})$$

\mathcal{G} is identical to G except for the inputs. The two input variables of G combined into one in \mathcal{G} . Here we will not consider this difference and use G to refer to both functions keeping in mind that when convolution properties are needed the second

form is used. Fourier transform of the source function is required for evaluation of boundary element formulation. The transformation of Rankine source function is,

$$\tilde{\mathcal{F}}[G(\mathbf{x} - \boldsymbol{\xi})] = \int_{-\infty}^{\infty} \int_{-\infty}^{\infty} \frac{1}{\sqrt{(x - \xi)^2 + (y - \eta)^2 + (z - \zeta)^2}} e^{iu(x - \xi) + iv(y - \eta)} d(x - \xi) d(y - \eta) \quad (\text{B.18})$$

Here u and v are the wave numbers in x and y direction respectively. Then $\mathbf{k} = (u, v)$ is the wave number vector and $|k| = \sqrt{u^2 + v^2}$ is the magnitude of wave number. The absolute value is an indication that the wave number itself could be positive or negative which indicates the propagation direction of wave. By use of the following coordinate transformation,

$$x - \xi = r \cos \theta \quad y - \eta = r \sin \theta \quad (\text{B.19})$$

Eq. (B.18) can be written as,

$$\tilde{\mathcal{F}}[G(\mathbf{x} - \boldsymbol{\xi})] = \int_0^{\infty} \int_0^{2\pi} \frac{1}{\sqrt{r^2 + (z - \zeta)^2}} e^{iur \cos \theta + ivr \sin \theta} r dr d\theta \quad (\text{B.20})$$

We start by integrating the θ -dependent part. Let us define an auxiliary angle α which satisfies,

$$\cos \alpha = \frac{u}{\sqrt{u^2 + v^2}} \quad \sin \alpha = \frac{v}{\sqrt{u^2 + v^2}} \quad (\text{B.21})$$

Substituting α in θ -dependent part of the integral in Eq. (B.20) we obtain,

$$\int_0^{2\pi} e^{ir\sqrt{u^2 + v^2}(\cos \alpha \cos \theta + \sin \alpha \sin \theta)} d\theta = \int_0^{2\pi} e^{ir\sqrt{u^2 + v^2} \cos(\theta - \alpha)} d\theta \quad (\text{B.22})$$

It is known that,

$$\int_0^{2\pi} e^{ir\sqrt{u^2 + v^2} \cos(\theta - \alpha)} d\theta = 2\pi J_0 \left(r\sqrt{u^2 + v^2} \right) \quad (\text{B.23})$$

where J_0 is the Bessel function of zero order. Then,

$$\tilde{\mathcal{F}}[G(\mathbf{x} - \boldsymbol{\xi})] = 2\pi \int_0^{\infty} \frac{r}{\sqrt{r^2 + (z - \zeta)^2}} J_0 \left(r\sqrt{u^2 + v^2} \right) dr \quad (\text{B.24})$$

Moreover,

$$\int_0^{\infty} \frac{r}{\sqrt{r^2 + a^2}} J_0(cr) dr = \frac{1}{c} e^{-|a|c} \quad (\text{B.25})$$

Therefore,

$$\tilde{\mathcal{F}}[G(\mathbf{x} - \boldsymbol{\xi})] = \frac{2\pi}{\sqrt{u^2 + v^2}} e^{-|z-\zeta|\sqrt{u^2+v^2}} \quad (\text{B.26})$$

If the Fourier transform is done in \mathbf{x} instead of $\mathbf{x} - \boldsymbol{\xi}$ we obtain,

$$\tilde{\mathcal{F}}[G(\mathbf{x} - \boldsymbol{\xi})] = \frac{2\pi}{\sqrt{u^2 + v^2}} e^{-|z-\zeta|\sqrt{u^2+v^2}} e^{iu\xi + iv\eta} \quad (\text{B.27})$$

Here the term $e^{iu\xi + iv\eta}$ comes from the change in the reference system for defining the wave-like behaviour of the function. This can also represent the collocation point shift in Fourier transform based on $\mathbf{x} - \boldsymbol{\xi}$ (by defining the collocation shift as $\mathbf{x} + \boldsymbol{\epsilon} - \boldsymbol{\xi}$). $|z - \zeta|$ can be interpreted as the distance for desingularization or raised panels (Raven (1996) and Bunnik (1999)). A flat sea-bed can be added to the formulation using $|z - \zeta|$ as well (see Kim et al. (2005)). Assuming no collocation shift or desingularization,

$$\tilde{G} = \frac{2\pi}{\sqrt{u^2 + v^2}} = \frac{2\pi}{|k|} \quad (\text{B.28})$$

B.2.6 Fourier transforms of B-spline base functions

The centered B-spline bases functions (Eqs. (B.29) and (B.30)) are chosen for this study due to their convolution properties. As discussed before B-spline elements with $b^{(1)}$ is identical to the uniform quadrilateral constant elements. Moreover $b^{(2)}$ relates to uniform linear elements using Lagrangian polynomials (HOBEM elements) and coordinate transformation. Relating higher order Lagrangian-based and B-spline-based elements is not straight forward. However, the study of higher-order B-spline elements can be of interest to gain more insight regarding the importance of discretization order.

$$b^{(1)}(\xi) = \begin{cases} 1 & |\xi| \leq \frac{\Delta x}{2} \\ 0 & \text{otherwise} \end{cases} \quad (\text{B.29})$$

$$b^{(m)}(\xi) = \frac{1}{\Delta x} b^{(m-1)}(\xi) * b^{(1)}(\xi) = \frac{1}{\Delta x} \int_{-\infty}^{+\infty} b^{(m-1)}(\tau) b^{(1)}(\xi - \tau) d\tau \quad (\text{B.30})$$

Here τ is the integral dummy variable. Using continuous convolution theorem (Eq. (B.13)) the Fourier transform of $b^{(m)}$ becomes,

$$\tilde{b}^{(m)} = \frac{1}{\Delta x} \tilde{b}^{(m-1)} \tilde{b}^{(1)} \quad (\text{B.31})$$

while for the first order base function we have,

$$\tilde{b}^{(1)}(u) = \Delta x \frac{\sin \frac{u\Delta x}{2}}{\frac{u\Delta x}{2}} \quad (\text{B.32})$$

therefore,

$$\tilde{b}^{(m)}(u) = \Delta x \left(\frac{\sin \frac{u\Delta x}{2}}{\frac{u\Delta x}{2}} \right)^m \quad (\text{B.33})$$

The non-dimensional form of the Fourier transform of the base function is obtained by substituting $\bar{u} = \frac{u\Delta x}{2\pi}$ as follows.

$$\tilde{b}^{(m)}(\bar{u}) = \Delta x \left(\frac{\sin \pi \bar{u}}{\pi \bar{u}} \right)^m \quad (\text{B.34})$$

For a 2D shape function of orders m and n we have,

$$B^{(m,n)}(\xi, \eta) = b^{(m)}(\xi)b^{(n)}(\eta) \quad (\text{B.35})$$

The Fourier transform of the two-dimensional base function becomes,

$$\tilde{B}^{(m,n)}(u, v) = \Delta x \Delta y \left(\frac{\sin \frac{u\Delta x}{2}}{\frac{u\Delta x}{2}} \right)^m \left(\frac{\sin \frac{v\Delta y}{2}}{\frac{v\Delta y}{2}} \right)^n \quad (\text{B.36})$$

The non-dimensional form can be obtained by defining, $\bar{u} = \frac{u\Delta x}{2\pi}$ and $\bar{v} = \frac{v\Delta y}{2\pi}$ while $\Lambda = \Delta y/\Delta x$ is the element's aspect ratio.

$$\tilde{B}^{(m,n)}(\bar{u}, \bar{v}) = \Delta x^2 \Lambda \left(\frac{\sin \pi \bar{u}}{\pi \bar{u}} \right)^m \left(\frac{\sin \pi \bar{v}}{\pi \bar{v}} \right)^n \quad (\text{B.37})$$

The discrete version of Eq. (B.36) can be obtained using the semi-discrete Fourier transform and aliasing theorem as follows.

$$\hat{B}^{(m,n)}(u, v) = \Delta x \Delta y \sum_{K,L=-\infty}^{\infty} \left(\frac{\sin \frac{u_K \Delta x}{2}}{\frac{u_K \Delta x}{2}} \right)^m \left(\frac{\sin \frac{v_L \Delta y}{2}}{\frac{v_L \Delta y}{2}} \right)^n \quad (\text{B.38})$$

Here,

$$\begin{aligned} u_K &= u + \frac{2\pi K}{\Delta x} \\ v_L &= v + \frac{2\pi L}{\Delta y} \end{aligned} \quad (\text{B.39})$$

where K and L are integer indices for summation. Following Nakos (1990) the semi-discrete Fourier transform of two-dimensional B-spline base function in non-dimensional form is obtained as shown in Eq. (B.40) below.

$$\hat{B}^{(m,n)}(\bar{u}, \bar{v}) = \frac{\Delta x^2 \Lambda}{\pi^2} \sin^m(\pi \bar{u}) \sin^n(\pi \bar{v}) \sum_{K,L=-\infty}^{\infty} \frac{(-1)^{mK+nL}}{(\bar{u} + K)^m (\bar{v} + L)^n} \quad (\text{B.40})$$

B.2.7 Fourier transform of differential operators

Continuous operators

Derivatives can be calculated analytically if the unknown representation is smooth enough. In this case the continuous Fourier transform of the differentiation operators are,

$$\mathcal{F} \left[\frac{\partial}{\partial x} f(x, y, t) \right] = iu \tilde{f}(u, v, \omega) \quad \mathcal{F} \left[\frac{\partial}{\partial t} f(x, y, t) \right] = -i\omega \tilde{f}(u, v, \omega) \quad (\text{B.41})$$

Finite difference operators

In a case of discrete functions, finite difference operators can be used to calculate derivatives numerically. It is possible to write Finite difference operator of various orders in summation form as presented in Eq. (B.42) below.

$$\begin{aligned} \left. \frac{\partial f(\mathbf{x}, t)}{\partial x} \right|_{\mathbf{x}_i} &= \sum_{j=-\infty}^{\infty} d_j^{(x)} f(\mathbf{x}_i - \mathbf{x}_j, t) \\ \left. \frac{\partial f(\mathbf{x}, t)}{\partial t} \right|_{t_i} &= \sum_{j=-\infty}^{\infty} d_j^{(t)} f(\mathbf{x}, t_i - t_j) \\ \left. \frac{\partial^2 f(\mathbf{x}, t)}{\partial x^2} \right|_{\mathbf{x}_i} &= \sum_{j=-\infty}^{\infty} d_j^{(xx)} f(\mathbf{x}_i - \mathbf{x}_j) \\ \left. \frac{\partial^2 f(\mathbf{x}, t)}{\partial t^2} \right|_{t_i} &= \sum_{j=-\infty}^{\infty} d_j^{(tt)} f(\mathbf{x}, t_i - t_j) \\ \left. \frac{\partial^2 f(\mathbf{x}, t)}{\partial x \partial t} \right|_{\mathbf{x}_i, t_n} &= \sum_{k=-\infty}^{\infty} d_k^{(t)} \sum_{j=-\infty}^{\infty} d_j^{(x)} f(\mathbf{x}_i - \mathbf{x}_j, t_n - t_k) \end{aligned} \quad (\text{B.42})$$

The coefficients d_j for different operators are summarized in Table B.1. It is important to note that the finite difference operators in Eq. (B.42) have discrete convolution form. Therefore, it is possible to calculate semi-discrete Fourier transform of finite difference operators using discrete convolution theorem as follows.

$$\widehat{\mathcal{F}} \left[\frac{\partial f(\mathbf{x}, t)}{\partial x} \right] = \widehat{\mathcal{F}} \left[\frac{1}{\Delta x} d^{(x)} \otimes f \right] = \frac{1}{\Delta x} \widehat{d}^{(x)} \widehat{f} \quad (\text{B.43})$$

Here $\widehat{d}^{(x)}$ includes the element's span parameter $1/\Delta x$ as listed in Table B.1. Let us defined,

$$\widehat{D}^{(x)} = \frac{1}{\Delta x} \widehat{d}^{(x)} = \sum_{j=-\infty}^{\infty} d_j^{(x)} e^{ij\Delta x u} \quad (\text{B.44})$$

Table B.1: Coefficients for upstream Finite difference operators. For instance $D_1^{(x)}$ means first-order upstream finite difference operator in x .

FD Scheme		d_4	d_3	d_2	d_1	d_0	d_{-1}
$D_1^{(x)}$	$\frac{1}{\Delta x} \times$	0	0	0	-1	1	0
$D_2^{(x)}$	$\frac{1}{\Delta x} \times$	0	0	1/2	-2	3/2	0
$D_3^{(x)}$	$\frac{1}{\Delta x} \times$	0	-1/3	3/2	-3	11/6	0
$D_1^{(t)}$	$\frac{1}{\Delta t} \times$	0	0	0	-1	1	0
$D_2^{(t)}$	$\frac{1}{\Delta t} \times$	0	0	1/2	-2	3/2	0
$D_3^{(t)}$	$\frac{1}{\Delta t} \times$	0	-1/3	3/2	-3	11/6	0
$D_1^{(xx)}$	$\frac{1}{\Delta x^2} \times$	0	0	1	-2	1	0
$D_2^{(xx)}$	$\frac{1}{\Delta x^2} \times$	1/4	-2	11/2	-6	9/4	0
$D_3^{(xx)}$	$\frac{1}{\Delta x^2} \times$	35/12	-26/3	19/2	-56/12	11/12	0
$D_1^{(tt)}$	$\frac{1}{\Delta t^2} \times$	0	0	1	-2	1	0
$D_2^{(tt)}$	$\frac{1}{\Delta t^2} \times$	0	2	-5	4	-1	0
$D_3^{(tt)}$	$\frac{1}{\Delta t^2} \times$	35/12	-26/3	19/2	-56/12	11/12	0

Then the semi-discrete Fourier transform of differentiation operators become,

$$\begin{aligned}
 \widehat{\mathcal{F}} \left[\frac{\partial f(\mathbf{x}, t)}{\partial x} \right] &= \widehat{D}^{(x)} \widehat{f} = \left[\sum_{j=-\infty}^{\infty} d_j^{(x)} e^{ij\Delta x u} \right] \widehat{f} \\
 \widehat{\mathcal{F}} \left[\frac{\partial f(\mathbf{x}, t)}{\partial t} \right] &= \widehat{D}^{(t)} \widehat{f} = \left[\sum_{j=-\infty}^{\infty} d_j^{(t)} e^{-ij\Delta t \omega} \right] \widehat{f} \\
 \widehat{\mathcal{F}} \left[\frac{\partial^2 f(\mathbf{x}, t)}{\partial x^2} \right] &= \widehat{D}^{(xx)} \widehat{f} = \left[\sum_{j=-\infty}^{\infty} d_j^{(xx)} e^{ij\Delta x u} \right] \widehat{f} \\
 \widehat{\mathcal{F}} \left[\frac{\partial^2 f(\mathbf{x}, t)}{\partial t^2} \right] &= \widehat{D}^{(tt)} \widehat{f} = \left[\sum_{j=-\infty}^{\infty} d_j^{(tt)} e^{-ij\Delta t \omega} \right] \widehat{f} \\
 \widehat{\mathcal{F}} \left[\frac{\partial^2 f(\mathbf{x}, t)}{\partial x \partial t} \right] &= \widehat{D}^{(x)} \widehat{D}^{(t)} \widehat{f} = \\
 &\left[\sum_{j=-\infty}^{\infty} d_j^{(x)} e^{ij\Delta x u} \right] \left[\sum_{j=-\infty}^{\infty} d_j^{(t)} e^{-ij\Delta t \omega} \right] \widehat{f}
 \end{aligned}
 \tag{B.45}$$

B.3 Boundary integral formulation

Let us consider the linearized Neumann-Kelvin problem in boundary integral form as presented in Eq. (4.3). Assuming the velocity potential to be represented by

two-parameter B-spline base functions on a discrete free surface we obtain,

$$\begin{aligned}
 & 2\pi \sum_{j=-\infty}^{\infty} \phi_j(t) B_j(\mathbf{x}_i)^{(m)} + \frac{1}{g} \iint_{-\infty}^{\infty} \left[\frac{\partial^2}{\partial t^2} \sum_{j=-\infty}^{\infty} \phi_j(t) B_j(\boldsymbol{\xi})^{(m)} \right] G(\mathbf{x}_i, \boldsymbol{\xi}) \, d\xi \, d\eta + \\
 & \frac{2U}{g} \iint_{-\infty}^{\infty} \left[\frac{\partial^2}{\partial t \partial \xi} \sum_{j=-\infty}^{\infty} \phi_j(t) B_j(\boldsymbol{\xi})^{(m)} \right] G(\mathbf{x}_i, \boldsymbol{\xi}) \, d\xi \, d\eta + \\
 & \frac{U^2}{g} \iint_{-\infty}^{\infty} \left[\frac{\partial^2}{\partial \xi^2} \sum_{j=-\infty}^{\infty} \phi_j(t) B_j(\boldsymbol{\xi})^{(m)} \right] G(\mathbf{x}_i, \boldsymbol{\xi}) \, d\xi \, d\eta = F
 \end{aligned} \tag{B.46}$$

The derivatives in Eq. (B.46) must be dealt with in order to proceed further. If a known time dependency is assumed for the velocity potential (for instance, $\phi_j(t) = e^{-i\omega t}$) then time derivatives can be calculated analytically. In any case the time derivative operators can be moved outside the integrals and dealt with later. On the other hand the spatial derivatives can be calculated using numerical and analytical methods. For instance the B-spline base function can be analytically differentiated in-order to spatial derivatives. In this case the order of base function (m) must be large than the order of the requested derivative. Using the fact that the integral's kernel vanishes at infinity, the $\frac{\partial}{\partial \xi}$ can be moved to source function and be calculated analytically (Eq. (B.47)). Moreover, using the symmetry properties of the source function, $\frac{\partial}{\partial \xi}$ can be exchanged with $\frac{\partial}{\partial x}$ and moved outside the integral (Eq. (B.47)). Finite difference operators can be used to calculate derivatives in this case.

$$\begin{aligned}
 & \iint_{-\infty}^{\infty} \left[\frac{\partial}{\partial \xi} \phi(\boldsymbol{\xi}, t) \right] G(\mathbf{x}, \boldsymbol{\xi}) \, d\xi \, d\eta = - \iint_{-\infty}^{\infty} \phi(\boldsymbol{\xi}, t) \left[\frac{\partial}{\partial \xi} G(\mathbf{x}, \boldsymbol{\xi}) \right] \, d\xi \, d\eta \\
 & \frac{\partial}{\partial \xi} G(\mathbf{x}, \boldsymbol{\xi}) = - \frac{\partial}{\partial x} G(\mathbf{x}, \boldsymbol{\xi})
 \end{aligned} \tag{B.47}$$

If numerical calculation is chosen for all the derivatives in Eq. (B.46), we can write

$$\begin{aligned}
 & 2\pi \sum_{j=-\infty}^{\infty} \phi_j(t) B_j(\mathbf{x}_i)^{(m)} + \frac{1}{g} \left[\frac{\partial^2}{\partial t^2} \right] \sum_{j=-\infty}^{\infty} \phi_j(t) \mathcal{S}_j^{(m)}(\mathbf{x}_i) + \\
 & \frac{2U}{g} \left[\frac{\partial}{\partial t} \right] \left[\frac{\partial}{\partial x} \right] \sum_{j=-\infty}^{\infty} \phi_j(t) \mathcal{S}_j^{(m)}(\mathbf{x}_i) + \\
 & \frac{U^2}{g} \left[\frac{\partial^2}{\partial x^2} \right] \sum_{j=-\infty}^{\infty} \phi_j(t) \mathcal{S}_j^{(m)}(\mathbf{x}_i) = F
 \end{aligned} \tag{B.48}$$

where,

$$\mathcal{S}_j^{(m)}(\mathbf{x}_i) = \iint_{-\infty}^{\infty} B_j^{(m)}(\boldsymbol{\xi}) G(\mathbf{x}_i - \boldsymbol{\xi}) d\xi d\eta \quad (\text{B.49})$$

If a uniform grid is assumed, the base functions of different elements will be identical except for a translation. Therefore we can write, $B_{i-j}^{(m)} = B_o^{(m)}(\mathbf{x}_i - \mathbf{x}_j)$ where $B_o^{(m)}$ is the B-spline base function at the origin. Using the translation $(\mathbf{x}_i - \mathbf{x}_j)$ the base function at vertex j is related to the base function at origin by moving the coordinate system from $(0, 0)$ to \mathbf{x}_j . Then Eq. (B.48) takes the following form,

$$\begin{aligned} & 2\pi \sum_{j=-\infty}^{\infty} \phi_j(t) B_{i-j}^{(m)} + \frac{1}{g} \left[\frac{\partial^2}{\partial t^2} \right] \sum_{j=-\infty}^{\infty} \phi_j(t) \mathcal{S}_{i-j}^{(m)} + \\ & \frac{2U}{g} \left[\frac{\partial}{\partial t} \right] \left[\frac{\partial}{\partial x} \right] \sum_{j=-\infty}^{\infty} \phi_j(t) \mathcal{S}_{i-j}^{(m)} + \\ & \frac{U^2}{g} \left[\frac{\partial^2}{\partial \xi^2} \right] \sum_{j=-\infty}^{\infty} \phi_j(t) \mathcal{S}_{i-j}^{(m)} = F \end{aligned} \quad (\text{B.50})$$

where,

$$\mathcal{S}_{i-j}^{(m)} = \mathcal{S}_j^{(m)}(\mathbf{x}_i - \mathbf{x}_j) = \iint_{-\infty}^{\infty} B_o^{(m)}(\boldsymbol{\xi}) G(\mathbf{x}_i - \mathbf{x}_j - \boldsymbol{\xi}) d\xi d\eta \quad (\text{B.51})$$

The differentiation operators in Eq. (B.50) can be replaced by the summations for finite difference operators as shown in Eq. (B.42). The terms in Eq. (B.50) have the form of discrete convolution (Eq. (B.12)). This suggests the use of the semi-discrete Fourier transform. Applying the semi-discrete Fourier transform defined in Eq. (B.10) and using the discrete convolution theorem we obtain,

$$\left[2\pi \widehat{B}_o^{(m)} + \widehat{D}^{(tt)} \widehat{\mathcal{S}} + \frac{2U}{g} \widehat{D}^{(t)} \widehat{D}^{(x)} \widehat{\mathcal{S}} + \frac{U^2}{g} \widehat{D}^{(xx)} \widehat{\mathcal{S}} \right] \widehat{\phi} = \widehat{F} \quad (\text{B.52})$$

Therefore the discrete dispersion relation becomes,

$$\widehat{W} = 2\pi g \widehat{B}_o^{(m)} + \widehat{D}^{(tt)} \widehat{\mathcal{S}} + 2U \widehat{D}^{(t)} \widehat{D}^{(x)} \widehat{\mathcal{S}} + U^2 \widehat{D}^{(xx)} \widehat{\mathcal{S}} = 0 \quad (\text{B.53})$$

The semi-discrete Fourier transform of differential operators are presented in Section B.2.7. On the other hand the semi-discrete Fourier transform of \mathcal{S} and B can be calculated from their continuous Fourier transform by the aliasing theorem as follows (see Section B.2.4).

$$\begin{aligned} \widehat{\mathcal{S}} &= \sum_{K,L=-\infty}^{\infty} \widetilde{\mathcal{S}}\left(u + \frac{2\pi K}{\Delta x}, v + \frac{2\pi L}{\Delta y}\right) \\ \widehat{B}_o^{(m)} &= \sum_{K,L=-\infty}^{\infty} \widetilde{B}_o^{(m)}\left(u + \frac{2\pi K}{\Delta x}, v + \frac{2\pi L}{\Delta y}\right) \end{aligned} \quad (\text{B.54})$$

Moreover, using the continuous convolution theorem,

$$\tilde{\mathcal{S}}(u, v) = \tilde{B}_o^{(m)}(u, v)\tilde{G}(u, v) \quad (\text{B.55})$$

therefore,

$$\hat{\mathcal{S}} = \sum_{K,L=-\infty}^{\infty} \tilde{B}_o^{(m)}\left(u + \frac{2\pi K}{\Delta x}, v + \frac{2\pi L}{\Delta y}\right) \tilde{G}\left(u + \frac{2\pi K}{\Delta x}, v + \frac{2\pi L}{\Delta y}\right) \quad (\text{B.56})$$

Here, expressions for \tilde{G} and $\tilde{B}_o^{(m)}$ are given in Eqs. (B.28) and (B.40) respectively. It is important to mention that if analytical differentiation is used to calculate spatial derivatives, the differentiation operator will appear inside the summation of Eq. (B.56). For instance, if analytical differentiation is used to calculate one of the spatial derivatives the discrete dispersion relation will be,

$$\widehat{\mathcal{W}} = 2\pi g \widehat{B}_o^{(m)} + \widehat{D}^{(tt)} \widehat{\mathcal{S}} + 2U \widehat{D}^{(t)} \widehat{\mathcal{S}}_x + U^2 \widehat{D}^{(x)} \widehat{\mathcal{S}}_x = 0 \quad (\text{B.57})$$

where,

$$\widehat{\mathcal{S}}_x = \sum_{K,L=-\infty}^{\infty} i \left[u + \frac{2\pi K}{\Delta x} \right] \tilde{B}_o^{(m)}\left(u + \frac{2\pi K}{\Delta x}, v + \frac{2\pi L}{\Delta y}\right) \tilde{G}\left(u + \frac{2\pi K}{\Delta x}, v + \frac{2\pi L}{\Delta y}\right) \quad (\text{B.58})$$

and for both spatial derivatives we have,

$$\widehat{\mathcal{W}} = 2\pi g \widehat{B}_o^{(m)} + \widehat{D}^{(tt)} \widehat{\mathcal{S}} + 2U \widehat{D}^{(t)} \widehat{\mathcal{S}}_x + U^2 \widehat{\mathcal{S}}_{xx} = 0 \quad (\text{B.59})$$

where,

$$\widehat{\mathcal{S}}_{xx} = \sum_{K,L=-\infty}^{\infty} - \left[u + \frac{2\pi K}{\Delta x} \right]^2 \tilde{B}_o^{(m)}\left(u + \frac{2\pi K}{\Delta x}, v + \frac{2\pi L}{\Delta y}\right) \tilde{G}\left(u + \frac{2\pi K}{\Delta x}, v + \frac{2\pi L}{\Delta y}\right) \quad (\text{B.60})$$

This is the case, for instance, when derivatives are calculated from differentiation of the smooth B-spline base functions, or the Rankine source function G , instead of using the finite difference operators.

**Previous PhD theses published at the Departement of Marine Technology
(earlier: Faculty of Marine Technology)
NORWEGIAN UNIVERSITY OF SCIENCE AND TECHNOLOGY**

Report No.	Author	Title
	Kavlie, Dag	Optimization of Plane Elastic Grillages, 1967
	Hansen, Hans R.	Man-Machine Communication and Data-Storage Methods in Ship Structural Design, 1971
	Gisvold, Kaare M.	A Method for non-linear mixed -integer programming and its Application to Design Problems, 1971
	Lund, Sverre	Tanker Frame Optimalization by means of SUMT-Transformation and Behaviour Models, 1971
	Vinje, Tor	On Vibration of Spherical Shells Interacting with Fluid, 1972
	Lorentz, Jan D.	Tank Arrangement for Crude Oil Carriers in Accordance with the new Anti-Pollution Regulations, 1975
	Carlsen, Carl A.	Computer-Aided Design of Tanker Structures, 1975
	Larsen, Carl M.	Static and Dynamic Analysis of Offshore Pipelines during Installation, 1976
UR-79-01	Brigt Hatlestad, MK	The finite element method used in a fatigue evaluation of fixed offshore platforms. (Dr.Ing. Thesis)
UR-79-02	Erik Pettersen, MK	Analysis and design of cellular structures. (Dr.Ing. Thesis)
UR-79-03	Sverre Valsgård, MK	Finite difference and finite element methods applied to nonlinear analysis of plated structures. (Dr.Ing. Thesis)
UR-79-04	Nils T. Nordsve, MK	Finite element collapse analysis of structural members considering imperfections and stresses due to fabrication. (Dr.Ing. Thesis)
UR-79-05	Ivar J. Fylling, MK	Analysis of towline forces in ocean towing systems. (Dr.Ing. Thesis)
UR-80-06	Nils Sandsmark, MM	Analysis of Stationary and Transient Heat Conduction by the Use of the Finite Element Method. (Dr.Ing. Thesis)
UR-80-09	Sverre Haver, MK	Analysis of uncertainties related to the stochastic modeling of ocean waves. (Dr.Ing. Thesis)
UR-81-15	Odland, Jonas	On the Strength of welded Ring stiffened cylindrical Shells primarily subjected to axial Compression

UR-82-17	Engesvik, Knut	Analysis of Uncertainties in the fatigue Capacity of Welded Joints
R-82-18	Rye, Henrik	Ocean wave groups
UR-83-30	Eide, Oddvar Inge	On Cumulative Fatigue Damage in Steel Welded Joints
UR-83-33	Mo, Olav	Stochastic Time Domain Analysis of Slender Offshore Structures
UR-83-34	Amdahl, Jørgen	Energy absorption in Ship-platform impacts
UR-84-37	Mørch, Morten	Motions and mooring forces of semi submersibles as determined by full-scale measurements and theoretical analysis
UR-84-38	Soares, C. Guedes	Probabilistic models for load effects in ship structures
UR-84-39	Aarsnes, Jan V.	Current forces on ships
UR-84-40	Czujko, Jerzy	Collapse Analysis of Plates subjected to Biaxial Compression and Lateral Load
UR-85-46	Alf G. Engseth, MK	Finite element collapse analysis of tubular steel offshore structures. (Dr.Ing. Thesis)
UR-86-47	Dengody Sheshappa, MP	A Computer Design Model for Optimizing Fishing Vessel Designs Based on Techno-Economic Analysis. (Dr.Ing. Thesis)
UR-86-48	Vidar Aanesland, MH	A Theoretical and Numerical Study of Ship Wave Resistance. (Dr.Ing. Thesis)
UR-86-49	Heinz-Joachim Wessel, MK	Fracture Mechanics Analysis of Crack Growth in Plate Girders. (Dr.Ing. Thesis)
UR-86-50	Jon Taby, MK	Ultimate and Post-ultimate Strength of Dented Tubular Members. (Dr.Ing. Thesis)
UR-86-51	Walter Lian, MH	A Numerical Study of Two-Dimensional Separated Flow Past Bluff Bodies at Moderate KC-Numbers. (Dr.Ing. Thesis)
UR-86-52	Bjørn Sortland, MH	Force Measurements in Oscillating Flow on Ship Sections and Circular Cylinders in a U-Tube Water Tank. (Dr.Ing. Thesis)
UR-86-53	Kurt Strand, MM	A System Dynamic Approach to One-dimensional Fluid Flow. (Dr.Ing. Thesis)
UR-86-54	Arne Edvin Løken, MH	Three Dimensional Second Order Hydrodynamic Effects on Ocean Structures in Waves. (Dr.Ing. Thesis)
UR-86-55	Sigurd Falch, MH	A Numerical Study of Slamming of Two-Dimensional Bodies. (Dr.Ing. Thesis)
UR-87-56	Arne Braathen, MH	Application of a Vortex Tracking Method to the Prediction of Roll Damping of a Two-Dimension

		Floating Body. (Dr.Ing. Thesis)
UR-87-57	Bernt Leira, MK	Gaussian Vector Processes for Reliability Analysis involving Wave-Induced Load Effects. (Dr.Ing. Thesis)
UR-87-58	Magnus Småvik, MM	Thermal Load and Process Characteristics in a Two-Stroke Diesel Engine with Thermal Barriers (in Norwegian). (Dr.Ing. Thesis)
MTA-88-59	Bernt Arild Bremdal, MP	An Investigation of Marine Installation Processes – A Knowledge - Based Planning Approach. (Dr.Ing. Thesis)
MTA-88-60	Xu Jun, MK	Non-linear Dynamic Analysis of Space-framed Offshore Structures. (Dr.Ing. Thesis)
MTA-89-61	Gang Miao, MH	Hydrodynamic Forces and Dynamic Responses of Circular Cylinders in Wave Zones. (Dr.Ing. Thesis)
MTA-89-62	Martin Greenhow, MH	Linear and Non-Linear Studies of Waves and Floating Bodies. Part I and Part II. (Dr.Techn. Thesis)
MTA-89-63	Chang Li, MH	Force Coefficients of Spheres and Cubes in Oscillatory Flow with and without Current. (Dr.Ing. Thesis)
MTA-89-64	Hu Ying, MP	A Study of Marketing and Design in Development of Marine Transport Systems. (Dr.Ing. Thesis)
MTA-89-65	Arild Jæger, MH	Seakeeping, Dynamic Stability and Performance of a Wedge Shaped Planing Hull. (Dr.Ing. Thesis)
MTA-89-66	Chan Siu Hung, MM	The dynamic characteristics of tilting-pad bearings
MTA-89-67	Kim Wikstrøm, MP	Analysis av projekteringen for ett offshore projekt. (Licenciat-avhandling)
MTA-89-68	Jiao Guoyang, MK	Reliability Analysis of Crack Growth under Random Loading, considering Model Updating. (Dr.Ing. Thesis)
MTA-89-69	Arnt Olufsen, MK	Uncertainty and Reliability Analysis of Fixed Offshore Structures. (Dr.Ing. Thesis)
MTA-89-70	Wu Yu-Lin, MR	System Reliability Analyses of Offshore Structures using improved Truss and Beam Models. (Dr.Ing. Thesis)
MTA-90-71	Jan Roger Hoff, MH	Three-dimensional Green function of a vessel with forward speed in waves. (Dr.Ing. Thesis)
MTA-90-72	Rong Zhao, MH	Slow-Drift Motions of a Moored Two-Dimensional Body in Irregular Waves. (Dr.Ing. Thesis)
MTA-90-73	Atle Minsaas, MP	Economical Risk Analysis. (Dr.Ing. Thesis)
MTA-90-74	Knut-Arild Farnes, MK	Long-term Statistics of Response in Non-linear Marine Structures. (Dr.Ing. Thesis)

MTA-90-75	Torbjørn Sotberg, MK	Application of Reliability Methods for Safety Assessment of Submarine Pipelines. (Dr.Ing. Thesis)
MTA-90-76	Zeuthen, Steffen, MP	SEAMAID. A computational model of the design process in a constraint-based logic programming environment. An example from the offshore domain. (Dr.Ing. Thesis)
MTA-91-77	Haagensen, Sven, MM	Fuel Dependant Cyclic Variability in a Spark Ignition Engine - An Optical Approach. (Dr.Ing. Thesis)
MTA-91-78	Løland, Geir, MH	Current forces on and flow through fish farms. (Dr.Ing. Thesis)
MTA-91-79	Hoen, Christopher, MK	System Identification of Structures Excited by Stochastic Load Processes. (Dr.Ing. Thesis)
MTA-91-80	Haugen, Stein, MK	Probabilistic Evaluation of Frequency of Collision between Ships and Offshore Platforms. (Dr.Ing. Thesis)
MTA-91-81	Sødahl, Nils, MK	Methods for Design and Analysis of Flexible Risers. (Dr.Ing. Thesis)
MTA-91-82	Ormberg, Harald, MK	Non-linear Response Analysis of Floating Fish Farm Systems. (Dr.Ing. Thesis)
MTA-91-83	Marley, Mark J., MK	Time Variant Reliability under Fatigue Degradation. (Dr.Ing. Thesis)
MTA-91-84	Krokstad, Jørgen R., MH	Second-order Loads in Multidirectional Seas. (Dr.Ing. Thesis)
MTA-91-85	Molteberg, Gunnar A., MM	The Application of System Identification Techniques to Performance Monitoring of Four Stroke Turbocharged Diesel Engines. (Dr.Ing. Thesis)
MTA-92-86	Mørch, Hans Jørgen Bjelke, MH	Aspects of Hydrofoil Design: with Emphasis on Hydrofoil Interaction in Calm Water. (Dr.Ing. Thesis)
MTA-92-87	Chan Siu Hung, MM	Nonlinear Analysis of Rotordynamic Instabilities in Highspeed Turbomachinery. (Dr.Ing. Thesis)
MTA-92-88	Bessason, Bjarni, MK	Assessment of Earthquake Loading and Response of Seismically Isolated Bridges. (Dr.Ing. Thesis)
MTA-92-89	Langli, Geir, MP	Improving Operational Safety through exploitation of Design Knowledge - an investigation of offshore platform safety. (Dr.Ing. Thesis)
MTA-92-90	Sævik, Svein, MK	On Stresses and Fatigue in Flexible Pipes. (Dr.Ing. Thesis)
MTA-92-91	Ask, Tor Ø., MM	Ignition and Flame Growth in Lean Gas-Air Mixtures. An Experimental Study with a Schlieren System. (Dr.Ing. Thesis)

MTA-86-92	Hessen, Gunnar, MK	Fracture Mechanics Analysis of Stiffened Tubular Members. (Dr.Ing. Thesis)
MTA-93-93	Steinebach, Christian, MM	Knowledge Based Systems for Diagnosis of Rotating Machinery. (Dr.Ing. Thesis)
MTA-93-94	Dalane, Jan Inge, MK	System Reliability in Design and Maintenance of Fixed Offshore Structures. (Dr.Ing. Thesis)
MTA-93-95	Steen, Sverre, MH	Cobblestone Effect on SES. (Dr.Ing. Thesis)
MTA-93-96	Karunakaran, Daniel, MK	Nonlinear Dynamic Response and Reliability Analysis of Drag-dominated Offshore Platforms. (Dr.Ing. Thesis)
MTA-93-97	Hagen, Arnulf, MP	The Framework of a Design Process Language. (Dr.Ing. Thesis)
MTA-93-98	Nordrik, Rune, MM	Investigation of Spark Ignition and Autoignition in Methane and Air Using Computational Fluid Dynamics and Chemical Reaction Kinetics. A Numerical Study of Ignition Processes in Internal Combustion Engines. (Dr.Ing. Thesis)
MTA-94-99	Passano, Elizabeth, MK	Efficient Analysis of Nonlinear Slender Marine Structures. (Dr.Ing. Thesis)
MTA-94-100	Kvålsvold, Jan, MH	Hydroelastic Modelling of Wetdeck Slamming on Multihull Vessels. (Dr.Ing. Thesis)
MTA-94-102	Bech, Sidsel M., MK	Experimental and Numerical Determination of Stiffness and Strength of GRP/PVC Sandwich Structures. (Dr.Ing. Thesis)
MTA-95-103	Paulsen, Hallvard, MM	A Study of Transient Jet and Spray using a Schlieren Method and Digital Image Processing. (Dr.Ing. Thesis)
MTA-95-104	Hovde, Geir Olav, MK	Fatigue and Overload Reliability of Offshore Structural Systems, Considering the Effect of Inspection and Repair. (Dr.Ing. Thesis)
MTA-95-105	Wang, Xiaozhi, MK	Reliability Analysis of Production Ships with Emphasis on Load Combination and Ultimate Strength. (Dr.Ing. Thesis)
MTA-95-106	Ulstein, Tore, MH	Nonlinear Effects of a Flexible Stern Seal Bag on Cobblestone Oscillations of an SES. (Dr.Ing. Thesis)
MTA-95-107	Solaas, Frøydis, MH	Analytical and Numerical Studies of Sloshing in Tanks. (Dr.Ing. Thesis)
MTA-95-108	Hellan, Øyvind, MK	Nonlinear Pushover and Cyclic Analyses in Ultimate Limit State Design and Reassessment of Tubular Steel Offshore Structures. (Dr.Ing. Thesis)
MTA-95-109	Hermundstad, Ole A., MK	Theoretical and Experimental Hydroelastic Analysis of High Speed Vessels. (Dr.Ing. Thesis)
MTA-96-	Bratland, Anne K., MH	Wave-Current Interaction Effects on Large-Volume

110		Bodies in Water of Finite Depth. (Dr.Ing. Thesis)
MTA-96-111	Herfjord, Kjell, MH	A Study of Two-dimensional Separated Flow by a Combination of the Finite Element Method and Navier-Stokes Equations. (Dr.Ing. Thesis)
MTA-96-112	Æsøy, Vilmar, MM	Hot Surface Assisted Compression Ignition in a Direct Injection Natural Gas Engine. (Dr.Ing. Thesis)
MTA-96-113	Eknes, Monika L., MK	Escalation Scenarios Initiated by Gas Explosions on Offshore Installations. (Dr.Ing. Thesis)
MTA-96-114	Erikstad, Stein O., MP	A Decision Support Model for Preliminary Ship Design. (Dr.Ing. Thesis)
MTA-96-115	Pedersen, Egil, MH	A Nautical Study of Towed Marine Seismic Streamer Cable Configurations. (Dr.Ing. Thesis)
MTA-97-116	Moksnes, Paul O., MM	Modelling Two-Phase Thermo-Fluid Systems Using Bond Graphs. (Dr.Ing. Thesis)
MTA-97-117	Halse, Karl H., MK	On Vortex Shedding and Prediction of Vortex-Induced Vibrations of Circular Cylinders. (Dr.Ing. Thesis)
MTA-97-118	Iglund, Ragnar T., MK	Reliability Analysis of Pipelines during Laying, considering Ultimate Strength under Combined Loads. (Dr.Ing. Thesis)
MTA-97-119	Pedersen, Hans-P., MP	Levendefiskteknologi for fiskefartøy. (Dr.Ing. Thesis)
MTA-98-120	Vikestad, Kyrre, MK	Multi-Frequency Response of a Cylinder Subjected to Vortex Shedding and Support Motions. (Dr.Ing. Thesis)
MTA-98-121	Azadi, Mohammad R. E., MK	Analysis of Static and Dynamic Pile-Soil-Jacket Behaviour. (Dr.Ing. Thesis)
MTA-98-122	Ulltang, Terje, MP	A Communication Model for Product Information. (Dr.Ing. Thesis)
MTA-98-123	Torbergsen, Erik, MM	Impeller/Diffuser Interaction Forces in Centrifugal Pumps. (Dr.Ing. Thesis)
MTA-98-124	Hansen, Edmond, MH	A Discrete Element Model to Study Marginal Ice Zone Dynamics and the Behaviour of Vessels Moored in Broken Ice. (Dr.Ing. Thesis)
MTA-98-125	Videiro, Paulo M., MK	Reliability Based Design of Marine Structures. (Dr.Ing. Thesis)
MTA-99-126	Mainçon, Philippe, MK	Fatigue Reliability of Long Welds Application to Titanium Risers. (Dr.Ing. Thesis)
MTA-99-127	Haugen, Elin M., MH	Hydroelastic Analysis of Slamming on Stiffened Plates with Application to Catamaran Wetdecks. (Dr.Ing. Thesis)
MTA-99-	Langhelle, Nina K., MK	Experimental Validation and Calibration of

128		Nonlinear Finite Element Models for Use in Design of Aluminium Structures Exposed to Fire. (Dr.Ing. Thesis)
MTA-99-129	Berstad, Are J., MK	Calculation of Fatigue Damage in Ship Structures. (Dr.Ing. Thesis)
MTA-99-130	Andersen, Trond M., MM	Short Term Maintenance Planning. (Dr.Ing. Thesis)
MTA-99-131	Tveiten, Bård Wathne, MK	Fatigue Assessment of Welded Aluminium Ship Details. (Dr.Ing. Thesis)
MTA-99-132	Søreide, Fredrik, MP	Applications of underwater technology in deep water archaeology. Principles and practice. (Dr.Ing. Thesis)
MTA-99-133	Tønnessen, Rune, MH	A Finite Element Method Applied to Unsteady Viscous Flow Around 2D Blunt Bodies With Sharp Corners. (Dr.Ing. Thesis)
MTA-99-134	Elvekrok, Dag R., MP	Engineering Integration in Field Development Projects in the Norwegian Oil and Gas Industry. The Supplier Management of Norne. (Dr.Ing. Thesis)
MTA-99-135	Fagerholt, Kjetil, MP	Optimeringsbaserte Metoder for Ruteplanlegging innen skipsfart. (Dr.Ing. Thesis)
MTA-99-136	Bysveen, Marie, MM	Visualization in Two Directions on a Dynamic Combustion Rig for Studies of Fuel Quality. (Dr.Ing. Thesis)
MTA-2000-137	Storteig, Eskild, MM	Dynamic characteristics and leakage performance of liquid annular seals in centrifugal pumps. (Dr.Ing. Thesis)
MTA-2000-138	Sagli, Gro, MK	Model uncertainty and simplified estimates of long term extremes of hull girder loads in ships. (Dr.Ing. Thesis)
MTA-2000-139	Tronstad, Harald, MK	Nonlinear analysis and design of cable net structures like fishing gear based on the finite element method. (Dr.Ing. Thesis)
MTA-2000-140	Kroneberg, André, MP	Innovation in shipping by using scenarios. (Dr.Ing. Thesis)
MTA-2000-141	Haslum, Herbjørn Alf, MH	Simplified methods applied to nonlinear motion of spar platforms. (Dr.Ing. Thesis)
MTA-2001-142	Samdal, Ole Johan, MM	Modelling of Degradation Mechanisms and Stressor Interaction on Static Mechanical Equipment Residual Lifetime. (Dr.Ing. Thesis)
MTA-2001-143	Baarholm, Rolf Jarle, MH	Theoretical and experimental studies of wave impact underneath decks of offshore platforms. (Dr.Ing. Thesis)
MTA-2001-144	Wang, Lihua, MK	Probabilistic Analysis of Nonlinear Wave-induced Loads on Ships. (Dr.Ing. Thesis)
MTA-	Kristensen, Odd H. Holt, MK	Ultimate Capacity of Aluminium Plates under

2001-145		Multiple Loads, Considering HAZ Properties. (Dr.Ing. Thesis)
MTA-2001-146	Greco, Marilena, MH	A Two-Dimensional Study of Green-Water Loading. (Dr.Ing. Thesis)
MTA-2001-147	Heggelund, Svein E., MK	Calculation of Global Design Loads and Load Effects in Large High Speed Catamarans. (Dr.Ing. Thesis)
MTA-2001-148	Babalola, Olusegun T., MK	Fatigue Strength of Titanium Risers – Defect Sensitivity. (Dr.Ing. Thesis)
MTA-2001-149	Mohammed, Abuu K., MK	Nonlinear Shell Finite Elements for Ultimate Strength and Collapse Analysis of Ship Structures. (Dr.Ing. Thesis)
MTA-2002-150	Holmedal, Lars E., MH	Wave-current interactions in the vicinity of the sea bed. (Dr.Ing. Thesis)
MTA-2002-151	Rognebakke, Olav F., MH	Sloshing in rectangular tanks and interaction with ship motions. (Dr.Ing. Thesis)
MTA-2002-152	Lader, Pål Furset, MH	Geometry and Kinematics of Breaking Waves. (Dr.Ing. Thesis)
MTA-2002-153	Yang, Qinzhen, MH	Wash and wave resistance of ships in finite water depth. (Dr.Ing. Thesis)
MTA-2002-154	Melhus, Øyvinn, MM	Utilization of VOC in Diesel Engines. Ignition and combustion of VOC released by crude oil tankers. (Dr.Ing. Thesis)
MTA-2002-155	Ronæss, Marit, MH	Wave Induced Motions of Two Ships Advancing on Parallel Course. (Dr.Ing. Thesis)
MTA-2002-156	Økland, Ole D., MK	Numerical and experimental investigation of whipping in twin hull vessels exposed to severe wet deck slamming. (Dr.Ing. Thesis)
MTA-2002-157	Ge, Chunhua, MK	Global Hydroelastic Response of Catamarans due to Wet Deck Slamming. (Dr.Ing. Thesis)
MTA-2002-158	Byklum, Eirik, MK	Nonlinear Shell Finite Elements for Ultimate Strength and Collapse Analysis of Ship Structures. (Dr.Ing. Thesis)
IMT-2003-1	Chen, Haibo, MK	Probabilistic Evaluation of FPSO-Tanker Collision in Tandem Offloading Operation. (Dr.Ing. Thesis)
IMT-2003-2	Skaugset, Kjetil Bjørn, MK	On the Suppression of Vortex Induced Vibrations of Circular Cylinders by Radial Water Jets. (Dr.Ing. Thesis)
IMT-2003-3	Chezian, Muthu	Three-Dimensional Analysis of Slamming. (Dr.Ing. Thesis)
IMT-2003-4	Buhaug, Øyvind	Deposit Formation on Cylinder Liner Surfaces in Medium Speed Engines. (Dr.Ing. Thesis)
IMT-	Tregde, Vidar	Aspects of Ship Design: Optimization of Aft Hull

2003-5		with Inverse Geometry Design. (Dr.Ing. Thesis)
IMT-2003-6	Wist, Hanne Therese	Statistical Properties of Successive Ocean Wave Parameters. (Dr.Ing. Thesis)
IMT-2004-7	Ransau, Samuel	Numerical Methods for Flows with Evolving Interfaces. (Dr.Ing. Thesis)
IMT-2004-8	Soma, Torkel	Blue-Chip or Sub-Standard. A data interrogation approach of identity safety characteristics of shipping organization. (Dr.Ing. Thesis)
IMT-2004-9	Ersdal, Svein	An experimental study of hydrodynamic forces on cylinders and cables in near axial flow. (Dr.Ing. Thesis)
IMT-2005-10	Brodtkorb, Per Andreas	The Probability of Occurrence of Dangerous Wave Situations at Sea. (Dr.Ing. Thesis)
IMT-2005-11	Yttervik, Rune	Ocean current variability in relation to offshore engineering. (Dr.Ing. Thesis)
IMT-2005-12	Fredheim, Arne	Current Forces on Net-Structures. (Dr.Ing. Thesis)
IMT-2005-13	Heggernes, Kjetil	Flow around marine structures. (Dr.Ing. Thesis)
IMT-2005-14	Fouques, Sebastien	Lagrangian Modelling of Ocean Surface Waves and Synthetic Aperture Radar Wave Measurements. (Dr.Ing. Thesis)
IMT-2006-15	Holm, Håvard	Numerical calculation of viscous free surface flow around marine structures. (Dr.Ing. Thesis)
IMT-2006-16	Bjørheim, Lars G.	Failure Assessment of Long Through Thickness Fatigue Cracks in Ship Hulls. (Dr.Ing. Thesis)
IMT-2006-17	Hansson, Lisbeth	Safety Management for Prevention of Occupational Accidents. (Dr.Ing. Thesis)
IMT-2006-18	Zhu, Xinying	Application of the CIP Method to Strongly Nonlinear Wave-Body Interaction Problems. (Dr.Ing. Thesis)
IMT-2006-19	Reite, Karl Johan	Modelling and Control of Trawl Systems. (Dr.Ing. Thesis)
IMT-2006-20	Smogeli, Øyvind Notland	Control of Marine Propellers. From Normal to Extreme Conditions. (Dr.Ing. Thesis)
IMT-2007-21	Storhaug, Gaute	Experimental Investigation of Wave Induced Vibrations and Their Effect on the Fatigue Loading of Ships. (Dr.Ing. Thesis)
IMT-2007-22	Sun, Hui	A Boundary Element Method Applied to Strongly Nonlinear Wave-Body Interaction Problems. (PhD Thesis, CeSOS)
IMT-2007-23	Rustad, Anne Marthine	Modelling and Control of Top Tensioned Risers.

(PhD Thesis, CeSOS)

IMT-2007-24	Johansen, Vegar	Modelling flexible slender system for real-time simulations and control applications
IMT-2007-25	Wroldsen, Anders Sunde	Modelling and control of tensegrity structures. (PhD Thesis, CeSOS)
IMT-2007-26	Aronsen, Kristoffer Høyve	An experimental investigation of in-line and combined inline and cross flow vortex induced vibrations. (Dr. avhandling, IMT)
IMT-2007-27	Gao, Zhen	Stochastic Response Analysis of Mooring Systems with Emphasis on Frequency-domain Analysis of Fatigue due to Wide-band Response Processes (PhD Thesis, CeSOS)
IMT-2007-28	Thorstensen, Tom Anders	Lifetime Profit Modelling of Ageing Systems Utilizing Information about Technical Condition. (Dr.ing. thesis, IMT)
IMT-2008-29	Berntsen, Per Ivar B.	Structural Reliability Based Position Mooring. (PhD-Thesis, IMT)
IMT-2008-30	Ye, Naiquan	Fatigue Assessment of Aluminium Welded Box-stiffener Joints in Ships (Dr.ing. thesis, IMT)
IMT-2008-31	Radan, Damir	Integrated Control of Marine Electrical Power Systems. (PhD-Thesis, IMT)
IMT-2008-32	Thomassen, Paul	Methods for Dynamic Response Analysis and Fatigue Life Estimation of Floating Fish Cages. (Dr.ing. thesis, IMT)
IMT-2008-33	Pákozdi, Csaba	A Smoothed Particle Hydrodynamics Study of Two-dimensional Nonlinear Sloshing in Rectangular Tanks. (Dr.ing.thesis, IMT/ CeSOS)
IMT-2007-34	Grytøyr, Guttorm	A Higher-Order Boundary Element Method and Applications to Marine Hydrodynamics. (Dr.ing.thesis, IMT)
IMT-2008-35	Drummen, Ingo	Experimental and Numerical Investigation of Nonlinear Wave-Induced Load Effects in Containerships considering Hydroelasticity. (PhD thesis, CeSOS)
IMT-2008-36	Skejic, Renato	Maneuvering and Seakeeping of a Singel Ship and of Two Ships in Interaction. (PhD-Thesis, CeSOS)
IMT-2008-37	Harlem, Alf	An Age-Based Replacement Model for Repairable Systems with Attention to High-Speed Marine Diesel Engines. (PhD-Thesis, IMT)
IMT-2008-38	Alsos, Hagbart S.	Ship Grounding. Analysis of Ductile Fracture, Bottom Damage and Hull Girder Response. (PhD-thesis, IMT)
IMT-2008-39	Graczyk, Mateusz	Experimental Investigation of Sloshing Loading and Load Effects in Membrane LNG Tanks Subjected to

Random Excitation. (PhD-thesis, CeSOS)

IMT-2008-40	Taghipour, Reza	Efficient Prediction of Dynamic Response for Flexible and Multi-body Marine Structures. (PhD-thesis, CeSOS)
IMT-2008-41	Ruth, Eivind	Propulsion control and thrust allocation on marine vessels. (PhD thesis, CeSOS)
IMT-2008-42	Nystad, Bent Helge	Technical Condition Indexes and Remaining Useful Life of Aggregated Systems. PhD thesis, IMT
IMT-2008-43	Soni, Prashant Kumar	Hydrodynamic Coefficients for Vortex Induced Vibrations of Flexible Beams, PhD thesis, CeSOS
IMT-2009-43	Amlashi, Hadi K.K.	Ultimate Strength and Reliability-based Design of Ship Hulls with Emphasis on Combined Global and Local Loads. PhD Thesis, IMT
IMT-2009-44	Pedersen, Tom Arne	Bond Graph Modelling of Marine Power Systems. PhD Thesis, IMT
IMT-2009-45	Kristiansen, Trygve	Two-Dimensional Numerical and Experimental Studies of Piston-Mode Resonance. PhD-Thesis, CeSOS
IMT-2009-46	Ong, Muk Chen	Applications of a Standard High Reynolds Number Model and a Stochastic Scour Prediction Model for Marine Structures. PhD-thesis, IMT
IMT-2009-47	Hong, Lin	Simplified Analysis and Design of Ships subjected to Collision and Grounding. PhD-thesis, IMT
IMT-2009-48	Koushan, Kamran	Vortex Induced Vibrations of Free Span Pipelines, PhD thesis, IMT
IMT-2009-49	Korsvik, Jarl Eirik	Heuristic Methods for Ship Routing and Scheduling. PhD-thesis, IMT
IMT-2009-50	Lee, Jihoon	Experimental Investigation and Numerical in Analyzing the Ocean Current Displacement of Longlines. Ph.d.-Thesis, IMT.
IMT-2009-51	Vestbøstad, Tone Gran	A Numerical Study of Wave-in-Deck Impact using a Two-Dimensional Constrained Interpolation Profile Method, Ph.d.thesis, CeSOS.
IMT-2009-52	Bruun, Kristine	Bond Graph Modelling of Fuel Cells for Marine Power Plants. Ph.d.-thesis, IMT
IMT 2009-53	Holstad, Anders	Numerical Investigation of Turbulence in a Skewed Three-Dimensional Channel Flow, Ph.d.-thesis, IMT.
IMT 2009-54	Ayala-Uraga, Efran	Reliability-Based Assessment of Deteriorating Ship-shaped Offshore Structures, Ph.d.-thesis, IMT
IMT 2009-55	Kong, Xiangjun	A Numerical Study of a Damaged Ship in Beam Sea Waves. Ph.d.-thesis, IMT/CeSOS.

IMT 2010-56	Kristiansen, David	Wave Induced Effects on Floaters of Aquaculture Plants, Ph.d.-thesis, CeSOS.
IMT 2010-57	Ludvigsen, Martin	An ROV-Toolbox for Optical and Acoustic Scientific Seabed Investigation. Ph.d.-thesis IMT.
IMT 2010-58	Hals, Jørgen	Modelling and Phase Control of Wave-Energy Converters. Ph.d.thesis, CeSOS.
IMT 2010- 59	Shu, Zhi	Uncertainty Assessment of Wave Loads and Ultimate Strength of Tankers and Bulk Carriers in a Reliability Framework. Ph.d. Thesis, IMT/ CeSOS
IMT 2010-60	Shao, Yanlin	Numerical Potential-Flow Studies on Weakly-Nonlinear Wave-Body Interactions with/without Small Forward Speed, Ph.d.thesis,CeSOS.
IMT 2010-61	Califano, Andrea	Dynamic Loads on Marine Propellers due to Intermittent Ventilation. Ph.d.thesis, IMT.
IMT 2010-62	El Khoury, George	Numerical Simulations of Massively Separated Turbulent Flows, Ph.d.-thesis, IMT
IMT 2010-63	Seim, Knut Sponheim	Mixing Process in Dense Overflows with Emphasis on the Faroe Bank Channel Overflow. Ph.d.thesis, IMT
IMT 2010-64	Jia, Huirong	Structural Analysis of Intact and Damaged Ships in a Collision Risk Analysis Perspective. Ph.d.thesis CeSoS.
IMT 2010-65	Jiao, Linlin	Wave-Induced Effects on a Pontoon-type Very Large Floating Structures (VLFS). Ph.D.-thesis, CeSOS.
IMT 2010-66	Abrahamsen, Bjørn Christian	Sloshing Induced Tank Roof with Entrapped Air Pocket. Ph.d.thesis, CeSOS.
IMT 2011-67	Karimirad, Madjid	Stochastic Dynamic Response Analysis of Spar-Type Wind Turbines with Catenary or Taut Mooring Systems. Ph.d.-thesis, CeSOS.
IMT - 2011-68	Erlend Meland	Condition Monitoring of Safety Critical Valves. Ph.d.-thesis, IMT.
IMT – 2011-69	Yang, Limin	Stochastic Dynamic System Analysis of Wave Energy Converter with Hydraulic Power Take-Off, with Particular Reference to Wear Damage Analysis, Ph.d. Thesis, CeSOS.
IMT – 2011-70	Visscher, Jan	Application of Particle Image Velocimetry on Turbulent Marine Flows, Ph.d.Thesis, IMT.
IMT – 2011-71	Su, Biao	Numerical Predictions of Global and Local Ice Loads on Ships. Ph.d.Thesis, CeSOS.
IMT – 2011-72	Liu, Zhenhui	Analytical and Numerical Analysis of Iceberg Collision with Ship Structures. Ph.d.Thesis, IMT.
IMT – 2011-73	Aarsæther, Karl Gunnar	Modeling and Analysis of Ship Traffic by Observation and Numerical Simulation. Ph.d.Thesis, IMT.

Imt – 2011-74	Wu, Jie	Hydrodynamic Force Identification from Stochastic Vortex Induced Vibration Experiments with Slender Beams. Ph.d.Thesis, IMT.
Imt – 2011-75	Amini, Hamid	Azimuth Propulsors in Off-design Conditions. Ph.d.Thesis, IMT.
IMT – 2011-76	Nguyen, Tan-Hoi	Toward a System of Real-Time Prediction and Monitoring of Bottom Damage Conditions During Ship Grounding. Ph.d.thesis, IMT.
IMT- 2011-77	Tavakoli, Mohammad T.	Assessment of Oil Spill in Ship Collision and Grounding. Ph.d.thesis, IMT.
IMT- 2011-78	Guo, Bingjie	Numerical and Experimental Investigation of Added Resistance in Waves. Ph.d.Thesis, IMT.
IMT- 2011-79	Chen, Qiaofeng	Ultimate Strength of Aluminium Panels, considering HAZ Effects, IMT
IMT- 2012-80	Kota, Ravikiran S.	Wave Loads on Decks of Offshore Structures in Random Seas. Ph.d.thesis, CeSOS.
IMT- 2012-81	Sten, Ronny	Dynamic Simulation of Deep Water Drilling Risers with Heave Compensating System, IMT.
IMT- 2012-82	Berle, Øyvind	Risk and resilience in global maritime supply chains, IMT.
IMT- 2012-83	Fang, Shaoji	Fault Tolerant Position Mooring Control Based on Structural Reliability, CeSOS.
IMT- 2012-84	You, Jikun	Numerical studies on wave forces and moored ship motions in intermediate and shallow water, CeSOS.
IMT- 2012-85	Xiang ,Xu	Maneuvering of two interacting ships in waves, CeSOS
IMT- 2012-86	Dong, Wenbin	Time-domain fatigueresponse and reliability analysis of offshore wind turbines with emphasis on welded tubular joints and gear components, CeSOS
IMT- 2012-87	Zhu, Suji	Investigation of Wave-Induced Nonlinear Load Effects in Open Ships considering Hull Girder Vibrations in Bending and Torsion, CeSOS
IMT- 2012-88	Zhou, Li	Numerical and Experimental Investigation of Station-keeping in Level Ice, CeSOS
IMT- 2012-90	Ushakov, Sergey	Particulate matter emission characteristics from diesel engines operating on conventional and alternative marine fuels, IMT
IMT- 2013-1	Yin, Decao	Experimental and Numerical Analysis of Combined In-line and Cross-flow Vortex Induced Vibrations,

